

**SWEAT MONITORING WITH CMOS COMPATIBLE
TECHNOLOGY: ISFETS AND BEYOND**

Présentée le 24 janvier 2020

à la Faculté des sciences et techniques de l'ingénieur
Laboratoire des dispositifs nanoélectroniques
Programme doctoral en microsystemes et microélectronique

pour l'obtention du grade de Docteur ès Sciences

par

Francesco BELLANDO

Acceptée sur proposition du jury

Dr J.-M. Sallese, président du jury
Prof. M. A. Ionescu, directeur de thèse
Prof. C. Ricciardi, rapporteur
Prof. M. A. Alam, rapporteur
Prof. H. Altug, rapporteuse

An expert is a man who has made all the mistakes
which can be made in very a narrow field.
— Niels Bohr

To my families: the one I was gifted with and the one I chose...

Acknowledgements

I could write a whole other thesis just to mention all the people which have helped me in this journey.

All my gratitude goes to professor Ionescu who decided to trust me with this project and gave me a chance to grow and challenge myself. I just hope my results have repaid you.

I also want to thank my PhD Jury: Jean-Michel Sallese, who is always ready to help when our poor students need a jury president, and professor Ricciardi, Haltug and Alam who, despite their tight schedule, found the time to read my work and provide unvaluable feedbacks to complete or improve it.

I wouldn't have gotten this far without the help of my incredible colleagues, on which I could always count whenever I needed help. In particular I need to thank my office mates: Erick, who saw a frightened rookie and convinced him that it was going to be fine. You made the beginning of this experience so much more fun!

Maneesha, you are a wonderful friend and a beautiful person. If I had gained nothing but your friendship in this four years I would still be happy. Not *completely* happy, but quite happy. I have seen you facing more problems than anyone else in your PhD, and every time you got up and resumed fighting. Your brain got you far, but this attitude will get you anywhere.

Jun-Rui, when you arrived my productivity dropped to zero for two months: you were asking questions non-stop about anything. After those two months, however, you could do most of what I could do, plus everything you were already able to do. You reminded me that being a scientist is more about curiosity than knowledge and you did it before I wandered too far from the path.

Sadegh, you have accomplished so much in one year, and I'm sorry I won't be here to see just how much more you will manage to do. I mean, I could follow your updates in Google Scholar, but we both know that I won't. Still, keep up the great work!

I also need to thank the Xsensio family, which faced with me the hard challenge of bringing together so many branches of science. In particular Fabien Wildhaber and Johan Longo, who have been real mentors during my project. In the last four years, I owed them 50% of my results and 90% of my alcohol intake.

My thanks also go to Karin, Isabelle and Lucie, which have helped me navigating the bureaucratic ocean on which my PhD was floating, and to the CMi staff for the useful discussions on my fabrication processes.

I really want to thank my family as well. Mamma, papà, Lorenzo e nonna Emilia: siete le fondamenta di tutto ciò che ho costruito nella mia vita. Non mi ricordo di una sola sfida

Acknowledgements

in cui mi sia mai sentito solo, persino quando non avevate idea di cosa stessi facendo. Non mi avete mai tirato o spinto verso obiettivi scelti da voi, ma siete sempre stati al mio fianco mentre seguivo i miei, facendo tutto ciò che potevate per liberarmi la strada passo dopo passo e facendo un tifo indiavolato ogni volta che ho dovuto affrontare qualcosa da solo. Non ho parole per ringraziarvi.

Alessandra, a volte mi chiedo se avessi la minima idea di in cosa ti stessi imbarcando, mettendoti con me due settimane prima che iniziassi un dottorato di ricerca. In ogni caso non riesco a immaginare come sarebbe stato tutto questo senza di te: in quattro anni mi sei sempre stata vicina quando il mio progetto cadeva a pezzi, le misure non funzionavano e tutti i miei sforzi sembravano crollare come un castello di carte o, come noi chiamiamo questa situazione nell'ambiente, "mercoledì". Non hai mai sbuffato per le mie lamentele e, a differenza di me, non hai mai dubitato delle mie capacità. Spero che tu sappia che dovresti essere coautrice di ogni articolo che abbia mai scritto.

I didn't mention half of the people who have earned my gratitude, but attempting to make a complete list would be dangerous because I'm sure I would leave somebody important out and, three years from now, I would still be begging the EPFL academic service to let me edit the acknowledgment page. You know who you are, I know who you are, and anyone who doesn't know who you are wouldn't recognize your names even if I wrote them. Rest assured I will remember you.

Lausanne, 2 December 2019

F. B.

Abstract

In recent years, sweat has gained increasing attention from the scientific community as a new analyte for health monitoring. The main advantage with respect to the "Gold Standard" for laboratory analysis, *i.e.* blood, is of course the possibility of performing non-invasive assays, granting the maximum comfort for the user. Sweat contains a wide collection of relevant biomarkers, such as ions (Na^+ , K^+ , Mg^+ , Ca^{++} ...) and biomolecules (lactate, cortisol, cholesterol...). For some of these biomarkers, a direct correspondence between their concentration in sweat and blood has been fully demonstrated; for some others, instead, sweat analysis cannot provide information on their blood concentration. This last set of biomarker, however, has been gaining relevance as the literature on the correlation between sweat composition and health conditions expanded.

The most widespread technology for wearable sweat sensors, as of now, consists in the employ of big electrodes for potentiometric detection of target markers. This strategy, on top of not being CMOS-compatible and therefore harder to integrate in a complex wearable system (*e. g.* a smartwatch), requires a huge amount of sweat, which is produced only under intense heat or physical activity. Ion-Sensitive Field-Effect Transistors (ISFETs), on the other hand, can be made extremely small without reducing their sensing performances, allowing monitoring of sweat composition at very low sweating rates, compatible with at-rest values. In this work, such advantage is pursued *via* the integration of a low-volume capillary microfluidics, with a capacity of just a few hundreds of nanoliters, on a chip containing a set of Fully-Depleted Silicon-On-Insulator FETs (FD SOI FETs) and miniaturized Ag/AgCl Reference Electrodes (mREs). This system, able to host up to four different functionalizations, each for monitoring a specific sweat biomarker, is capable of collecting sweat from the skin of an user at rest, passively driving it in contact with the sensors, and readily transducing the chemical parameters measured by the functionalized gates in an electric signal, which is then analyzed by the read-out system, providing data on the composition of the analyte and, therefore, on the health condition of the wearer.

The fabricated devices showed excellent performances in terms of both electrical characterization and biomarker sensitivity: the FETs characterized with a metal gate have shown an I_{ON}/I_{OFF} ratio of 10^6 , a nearly-ideal Subthreshold Swing (SS) of just 65 mV/dec, an hysteresis-free characteristics and fully ohmic contacts on ultra-thin silicon. The threshold voltage (V_{th}) shifts linked to a tenfold variation in the biomarkers concentrations also reached the

Abstract

nearly-ideal values of 55 to 60 mV/dec, and extremely linear dependence over a wide range of dilutions.

One of the strengths of the ISFET technology is its ability to exploit technological progresses of MOSFETs for computing. For this reason, in the final part of this thesis we have investigated the application to sensors of one of the latest strategies for the improvement of MOSFET performances: the Negative Capacitance (NC).

Addition of a ferroelectric capacitor (Fe-Cap) to the gate stack of our sensors reduced their SS by 21%, therefore improving their current sensitivity by 26%. The measured Current Efficiency also improved. Further experiments employing different sets of Fe-Caps and pulsed mode measurements, moreover, demonstrated a SS six times lower than the one of the baseline ISFETs and three times lower than the thermionic limit, paving the way to a new class of sensors with ideality factor larger than 1.

Keywords: Sweat sensing, Ion-Sensitive Field-Effect Transistors (ISFETs), UTB FD SOI FETs, microfluidics, functionalization, wearable sensors, low-power, label-free sensor, Nernst limit, steep slope, heterogeneous integration, Negative Capacitance.

Riassunto

Negli ultimi anni, il sudore ha ottenuto crescente attenzione da parte della comunità scientifica come nuovo analita per il monitoraggio dello stato di salute. Il principale vantaggio rispetto allo standard di riferimento per le analisi di laboratorio, *i.e.* il sangue, è ovviamente la possibilità di eseguire test non invasivi, assicurando il massimo comfort all'utilizzatore. Il sudore contiene un'ampia gamma di biomarcatori importanti, come ioni (Na^+ , K^+ , Mg^+ , Ca^{++} ...) e biomolecole (acido lattico, cortisolo, colesterolo...). Per alcuni di questi biomarcatori, una corrispondenza diretta tra le loro concentrazioni nel sudore e nel sangue è stata confermata in via definitiva; per altri, invece, l'analisi del sudore non è in grado di fornire informazioni sulle rispettive concentrazioni nel sangue. Questo ultimo gruppo di biomarcatori, comunque, sta guadagnando importanza mentre la letteratura sulla correlazione tra la composizione del sudore e lo stato di salute si espande.

La tecnologia più diffusa per i sensori di sudore indossabili, al momento, consiste nell'impiego di grossi elettrodi per la detezione potenziometrica di marcatori specifici. Questa strategia, oltre a non essere compatibile con la tecnologia CMOS, e quindi di difficile integrazione in un sistema indossabile complesso (come uno smartwatch), richiede una grande quantità di sudore, che viene prodotta solo in condizioni di intenso calore o attività fisica. Gli Ion-Sensitive Field-Effect Transistors (ISFETs), d'altro canto, possono essere fabbricati con dimensioni molto ridotte senza ridurre le loro performance come sensori, permettendo il monitoraggio della composizione del sudore a bassissime velocità di sudorazione, compatibili coi valori a riposo. In questo lavoro, tale vantaggio è conseguito tramite l'integrazione di un sistema microfluidico capillare di volume molto ridotto, con una capacità di solo qualche centinaio di nanolitri, su un chip contenente un set di Fully-Depleted Silicon-On-Insulator FETs (FD SOI FETs) e uno di Reference Electrodes miniaturizzati (mREs) composti di Ag/AgCl. Questo sistema, in grado di ospitare fino a quattro diverse funzionalizzazioni, ognuna preposta per il monitoraggio di uno specifico biomarcatore del sudore, è capace di raccogliere il sudore dalla pelle di un utilizzatore a riposo, condurla passivamente in contatto con i sensori, e trasdurre i parametri chimici misurati dai gate funzionalizzati in un segnale elettrico. Il segnale prodotto viene quindi analizzato dal sistema di read-out, fornendo dati sulla composizione del sudore e, di conseguenza, sullo stato di salute dell'utilizzatore.

I dispositivi fabbricati hanno mostrato eccellenti performance in termini sia di caratterizzazione elettrica che di sensibilità ai biomarcatori: i FET testati con un gate in metallo sono

Abstract

caratterizzati da un rapporto I_{ON}/I_{OFF} di 10^6 , un Subthreshold Swing (SS) quasi ideale di appena 65 mV/dec, una caratteristica priva di isteresi e contatti completamente ohmici su Silicio ultra-sottile. Le variazioni della tensione di soglia (V_{th}) relative a una variazione di un fattore dieci nella concentrazione dei biomarcatori hanno a loro volta raggiunto valori quasi ideali, tra i 55 e i 60 mV/dec, e una dipendenza estremamente lineare su un ampio range di diluizioni.

Uno dei punti di forza della tecnologia ISFET è la sua capacità di sfruttare i progressi tecnologici dei MOSFET usati per la computazione. Per questo motivo, nella parte finale di questa tesi abbiamo investigato l'applicazione ai sensori di una delle ultime strategie per il miglioramento delle performance dei MOSFET: la Negative Capacitance (NC). L'aggiunta di un condensatore ferroelettrico (Fe-Cap) al gate-stack dei nostri sensori ha ridotto il loro SS del 21%, migliorando la loro current sensitivity del 26%. La current efficiency misurata è migliorata a sua volta. Ulteriori esperimenti utilizzando diversi set di Fe-Cap e misure in modalità pulsata, inoltre, hanno dimostrato un SS sei volte più basso di quello dell'ISFET di base e tre volte più basso del limite termionico, aprendo la strada a una nuova classe di sensori con fattore di idealità superiore a 1.

Parole chiave: sensori di sudore, Ion-Sensitive Field-Effect Transistors (ISFETs), UTB FD SOI FETs, microfluidica, funzionalizzazione, sensori indossabili, basso consumo, sensori label-free, limite di Nernst, steep slope, integrazione eterogenea, Negative Capacitance.

Contents

Acknowledgements	v
Abstract (English/Italian)	vii
List of Figures	xii
List of Tables	xviii
List of Symbols	xxi
List of greek letters	xxv
1 Introduction	1
1.1 Sweat as a biological fluid of interest	1
1.2 Sweat sensing: recent history and State of Art	4
1.3 Sweat sensing with computing technology	8
1.3.1 The logic Field-Effect Transistor	8
1.3.2 The Ion-Sensitive Field-Effect Transistor	14
1.3.3 Choice of the FD technology	22
1.4 Summary	23
2 Technological development and characterization of the ribbon-ISFET	25
2.1 TCAD simulations for design and process optimization	25
2.2 Cleanroom process flow for ribbon-FET fabrication	29
2.3 Photolithographic processes	33
2.4 Etching processes	39
2.4.1 Wet etching	39
2.4.2 Plasma etching	41
2.4.3 Physical etching	43
2.5 Oxidation and deposition processes	44
2.5.1 Dry oxidation and gate dielectric deposition processes	44
2.5.2 Deposition processes for dielectric passivation and metal lines	46
2.6 Ohmic contacts on ultra-thin SOI	49
2.7 FD SOI Ribbon-FETs characterization	55
2.8 FD SOI Ribbon-ISFETs characterization	59

Contents

2.9	Summary	63
3	Lab On SkinTM: a fully integrated wearable sweat analyzer	65
3.1	Passive capillary microfluidics	65
3.1.1	Microfluidic pumps	69
3.1.2	Closed microfluidics	70
3.1.3	Capillary inlets	72
3.2	Functionalization	75
3.2.1	Ion-Sensitive crown ether SAM	75
3.2.2	Ion-Selective Membranes	78
3.3	Miniaturized Quasi Reference Electrode	85
3.4	Lab On Skin TM characterization	88
3.5	Summary	91
4	Negative Capacitance ISFET	93
4.1	Negative Capacitance for steep-slope switches.	93
4.2	Experimental demonstration of Negative Capacitance with metal gate FETs. . .	98
4.3	Application of the Negative Capacitance effect to ISFETs.	103
4.3.1	Modeling of the ISFET capacitance for matching	104
4.3.2	Experimental characterization of an NC ISFET	109
4.3.3	Pulsed measurements mode for improved NC	113
4.4	NC ISFET complete modeling.	118
4.5	Summary	121
5	Conclusions and Outlook	123
5.1	Main achievements	123
5.2	Comparison with the State of Art	125
5.3	Outlook	126
5.3.1	Technological improvements for the Lab On Skin TM	126
5.3.2	Technological improvements for the NC ISFET	127
5.3.3	Further functionalizations and new applications	128
5.3.4	Concluding remarks	129
A	Appendices	131
A.1	Appendix A	131
A.2	Appendix B	136
A.3	Appendix C	138
	Bibliography	140
	Curriculum Vitae	153
	List of Publications	155

List of Figures

1.1	Ecrrine glands structure and proportion, adapted from reference [19].	2
1.2	Benito-Lopez <i>et al.</i> Passive microfluidics with pH sensitive element.	4
1.3	Koh <i>et al.</i> Smart patch with four different selectively sensitive areas.	5
1.4	Rose <i>et al.</i> Electrode-based smart patch.	5
1.5	Gao <i>et al.</i> Electrode-based FISA wristband.	6
1.6	Nakata <i>et al.</i> Flexible ISFET-based patch.	6
1.7	Douthwaite <i>et al.</i> Sensing and processing system of the ISFET-based apparatus proposed.	7
1.8	Structure of a typical n-type bulk MOSFET.	9
1.9	Band diagram of a) a typical undoped semiconductor material without bias applied, b) a typical n-p-n transistor without bias applied and c) n-p-n transistor without (black lines) and with (green lines) a positive gate bias applied.	9
1.10	Transfer characteristics of a typical n-type MOSFET. The Off current lies below the noise level of the measurement equipment.	11
1.11	Schematic representation of the sections of a) a finFET, b) a nanowire and c) a FD SOI ribbon-FET.	14
1.12	Structure of a typical n-type bulk ISFET.	14
1.13	HDL model.	15
1.14	Gouy-Chapman Diffuse Layer model.	15
1.15	Stern model.	16
1.16	Sensitivity of an ISFET with an HfO ₂ sensing layer for various NaCl concentrations. 20	
2.1	Simulated effects on the transfer characteristics of varying a) the channel length, b) the S/D doping level, c) the thickness of the HfO ₂ layer and d) the thickness of the SOI.	26
2.2	Doping level simulated with a dose of $2 \times 10^{15} \text{ cm}^{-2}$ and 25 keV of energy.	27
2.3	Phosphorus distribution in the implanted area. The grey area represents the Si layer, while the light blue one the BOx.	27
2.4	Phosphorus distribution for different implantation energies from 25 to 5 keV.	28
2.5	Phosphorus distribution for different implantation doses from 2×10^{15} to 10^{14} cm^{-2}	29
2.6	Silicon thinning to ensure Full Depletion condition.	29
2.7	Phosphorus implantation for the Source and Drain areas.	30

List of Figures

2.8	FETs geometry photolithographic definition with landing on BOx.	30
2.9	Dielectric gate stack formation.	31
2.10	Gate metal deposition.	31
2.11	Source and Drain contact opening and platinum needle deposition.	32
2.12	Silicon dioxide passivation.	33
2.13	Metal lines lift-off and SU-8 passivation.	33
2.14	The set of alignment marks employed in our batches. The same elements are arranged in mirrored position on the two opposite sides of the wafers.	34
2.15	Example of photolithography results.	35
2.16	Lift-off with LOR/AZ-ECI procedure.	35
2.17	Reverse trapezoid shape of the nLOF structures. Sample picture from CMi website.	36
2.18	Effect of different reflective coefficients in a non-optimized SU-8 process.	37
2.19	A UV dose compatible with the SU-8 hardening on silicon is not compatible with the development of small structures on metal.	37
2.20	Rising the UV dose allowed achieving a homogeneous SU-8 layer.	38
2.21	Increasing the critical dimension of the SU-8 openings prevented the unwanted exposure effect.	38
2.22	Deep wet etching of Pyrex in HF. Sample picture from CMi website.	39
2.23	Photoresist detachment due to a short HF etching on a test wafer.	40
2.24	Uneven etching of Pt in aqua regia.	41
2.25	High aspect ratio plasma etching of silicon. Sample picture from CMi website.	42
2.26	a) SEM of a finished device b) TEM of the section of one of the S/D openings.	43
2.27	SEM of a lamella extracted from one of our SOIs, showing that the BOx has been completely removed.	45
2.28	Aluminum erosion after a photolithographic step.	47
2.29	Detrimental effect of X-rays on FD SOI devices during evaporation.	48
2.30	Deposition of sputtered SiO ₂ around the devices.	48
2.31	Band diagram of an ohmic contact, showing that no barrier is created [97].	49
2.32	Band diagram of a tunnel contact, showing the tunneling mechanism [97].	49
2.33	Test structure: doped line featuring large pads for metal connection.	50
2.34	I-V characteristics before annealing.	51
2.35	I-V characteristics after annealing for different length of the doped line with AlSi1% contacts.	51
2.36	Extraction of the parasitic resistance of the AlSi1% contacts.	52
2.37	Output characteristics of a ribbon-FET with poor AlSi1% contacts.	53
2.38	I-V characteristics for different length of the doped line with Pt contacts.	53
2.39	Extraction of the parasitic resistance of the Pt contacts.	54
2.40	Output characteristics of a ribbon-FET with excellent Pt contacts.	54
2.41	Evolution of the output characteristic.	55
2.42	Transfer characteristics in the first batch.	56
2.43	Transfer characteristics of the second batch devices featuring AlSi1% contact lines.	57
2.44	Transfer characteristics of the second batch devices featuring Pt contact lines.	57

2.45	Transfer characteristics comparison for two sets of ribbon-FETs featuring, respectively, individual and common Source contacts. The higher I_{OFF} values of the latter set are due to the sum of individual contributions to the leakage current passing from the bulk, due to implantation-induced damage to the ultra-thin BOX.	58
2.46	Layout of the sensing chip used for producing the Lab-On-Skin TM prototype.	58
2.47	PDMS stamp with microfluidic channels.	59
2.48	Aluminum support structure clamping together sensing chip and PDMS stamp.	60
2.49	Transfer characteristics for pH buffers ranging from 5 to 9. V_{th} shifts to more negative values for higher H^+ concentrations, <i>i.e.</i> lower pH.	60
2.50	V_{th} dependence on the pH for our first ISFET batch.	61
2.51	Transfer characteristics for pH buffers ranging from 5 to 9 for our second ISFET batch.	61
2.52	V_{th} dependence on the pH for our second ISFET batch.	62
2.53	Transfer characteristics for pH buffers ranging from 4 to 8 for our second ISFET batch employing a Pt-coated gate.	62
2.54	V_{th} dependence on the pH for our second ISFET batch employing a Pt-coated gate.	63
3.1	Steps of a capillary filling process.	66
3.2	Hydrophilic (low CA) and hydrophobic (high CA) surfaces.	66
3.3	Position of the water front in the capillary channel as a function of time.	67
3.4	Shape of a droplet deposited in CMi-processed SU-8 GM 1060.	68
3.5	Structure of the first prototype of the passive microfluidics. The channels here are represented by metal lines to be visible.	68
3.6	SU-8 microfluidics pump with varying pitch and pillars size.	69
3.7	Steps of capillary filling of a microfluidic pump.	69
3.8	Filling time-lapse of a microfluidic pump.	70
3.9	Processing of the two wafers. The microfluidics is defined on the ISFET wafer (a and b) while the closing layer is spin-coated on the support wafer (c and d).	71
3.10	Processing of the two wafers. a) Wafer bonding. b) Al anodic dissolution.	71
3.11	Circular inlets and outlets defined with the excimer laser.	72
3.12	Arborescent structure of a capillary inlet (right) able to collect liquid from a wide surface.	72
3.13	Artificial skin sample.	73
3.14	Capture of a droplet from the artificial skin.	73
3.15	Capture and flow of a droplet from the artificial skin.	74
3.16	Microfluidic sample on a sensing chip.	74
3.17	Synthesis of the molecules which will form the SAM.	75
3.18	SAM of sodium-selective molecules.	76

List of Figures

3.19	Transfer characteristics response to variations in the NaCl molar concentration in the analyte for a) a functionalized sensor and b) a control sensor. The differences in the shape of the transfer characteristics of the two graphs are probably due to the high device to device variability observed in our first batch and to partial degradation of the SU-8 passivation layer, but do not hinder the differential measurements.	76
3.20	Response of the functionalized and control sensors to the concentration of NaCl in the solution and extracted non-zero differential sensitivity.	77
3.21	Transfer characteristics response to variations in the pH of the analyte for a) a sensor whose gold gate has been functionalized with a sodium-sensitive SAM and b) a sensor with a clean gold gate.	78
3.22	Response of the functionalized and control sensors to the pH of the solution and extracted differential sensitivity. The near-zero value of the differential sensitivity demonstrates that the SAM functionalization doesn't affect the gold sensitivity to non-specific ions.	78
3.23	Separation of positive (C^+) and negative (A^-) ions of a salt at the interface between two phases, according to their solubility.	79
3.24	ISM embedding ionic sites (R^-) and specific ionophores (black circles). In this figure, a specific salt (KCl) has been taken as an example to underline the role of the different elements.	80
3.25	ISM with ionophores for potassium.	82
3.26	Transfer characteristics response to variations of the sodium (a) or potassium (b) concentration in the analyte measured with the respective ISM. The results of a test with a high concentration of a competitor ion have also been reported.	83
3.27	Threshold voltage dependence of the sodium-selective sensor on the sodium concentration (a) and of the potassium-selective sensor on the potassium concentration (b). Data needed for the error bars of graph (a) have been lost.	83
3.28	Threshold voltage dependences of the sodium-functionalized (a) and potassium-functionalized (b) ISMs to their respective target ions and to competing species.	84
3.29	Real-time monitoring of the concentration of sodium and potassium in a solution with a sodium-functionalized and a potassium-functionalized ISFET.	84
3.30	Drop casting of the ISM on a set of sensors on the chip.	85
3.31	AgCl formation on a 1 μm thick layer of silver sputtered on SU-8. The thin adhesion layer of chromium is also visible.	86
3.32	ISM-functionalized chip featuring a pair of miniaturized RE on the bottom metal seed. The Cl^- -saturated membranes covering them are also visible.	87
3.33	Stability measurement of the membrane-coated miniaturized RE. Over 14 hours of measurement, no appreciable drift has been observed.	87
3.34	Measurement setup for the characterization of the functionalized sensor in real-time measurement mode.	88
3.35	Real-time measurement of (a) sodium and (b) potassium concentration in the LUT.	89

3.36 (a) Transfer characteristics response to variation of the potassium concentration in the analyte, measured with the K-functionalized ISM and the embedded mRE. (b) Threshold voltage dependence of the integrated system on the potassium concentration.	90
3.37 Real-time measurement of potassium concentration in the LUT performed with the K-functionalized ISM and the embedded mRE.	90
4.1 Energy landscape of a ferroelectric material. The two local minimums correspond to the remnant polarization charge Q_0	94
4.2 Relation between the polarization charge of the ferroelectric and the external bias. Q_C is the coercive polarization charge, corresponding to the coercive potential.	95
4.3 Inverted $V_F(Q_F)$ characteristics. The red section points to the region where the capacitance is negative.	96
4.4 Structure of a NC-MOSFET. The FE-Cap can be defined on top of the gate or be a completely separated element with an electrical connection to the gate metal.	97
4.5 Optical image of the polycrystalline PZT FE-Cap chip employed. Different sizes of FE-Cap are visible.	99
4.6 P-V characteristics of the polycrystalline PZT FE-Cap.	99
4.7 Connection scheme and equivalent circuit of our NCFET. FE-Cap and MOSFET are two separate devices connected through micromechanical probes and BNC cables.	100
4.8 Transfer characteristics of our MOSFETs in normal conditions and with the addition of the FE-Cap. The curve steepening due to the NC effect is clearly visible.	100
4.9 Comparison of the SS of the conventional and NC MOSFETs. The NC configuration shows a sub-thermionic SS over more than two decades of current.	101
4.10 Comparison of the current efficiency of the conventional and NC MOSFETs. The NC configuration shows an efficiency $> 40 \text{ V}^{-1}$ over more than two decades of current.	102
4.11 Differential gain of the FE-Cap over the relevant V_G range for the SS. The average value is relevantly bigger than one.	102
4.12 Dependence of the polarization on the externally applied bias, measured during the NCFET operation. Negative capacitance is observed in the marked region.	103
4.13 First configuration of the introduced NC ISFET, with the corresponding equivalent circuit.	104
4.14 Stern model used for the evaluation of C_{LG}	105
4.15 Measured and simulated ISFET transfer characteristics at various pH values.	108
4.16 Dependence of C_{diff} and C_S on the RE bias.	108
4.17 C-V characteristics of the complete ISFET.	109
4.18 P-V characteristics of the single-crystalline PZT FE-Cap.	109
4.19 NC ISFET transfer characteristics extracted at pH 7.	110

List of Figures

4.20 Comparison of transfer characteristics and 10-points smoothed SS of standard and NC-boosted ISFETs.	110
4.21 Comparison of the current efficiency of standard and NC-boosted ISFETs. . . .	111
4.22 Differential gain measured at the two sides of the FE-Cap.	112
4.23 Transfer characteristics extracted at various pH values for the NC ISFET.	112
4.24 Transfer characteristics of the FD SOI MOSFET extracted at various pulses duration.	113
4.25 Second configuration of the introduced NCISFET with the corresponding equivalent circuit.	114
4.26 P-V characteristics of the low (700°C) and high (800°C) temperature annealing Si-doped HfO ₂ FE-Caps.	115
4.27 Transfer characteristics of the NC-ISFET extracted at various pulse durations. .	115
4.28 Characterization of the pH response of a standard ISFET in Pulsed Mode. . . .	116
4.29 Results of five consecutive transfer characteristics measurements employing the low-temperature annealing Si-doped HfO ₂	117
4.30 Transfer characteristics of the NC ISFET extracted at different pH values, together with the failed consistency check.	117
4.31 Transfer characteristics of the high-temperature annealing Si-doped HfO ₂ NC ISFET.	118
4.32 Comparison between the transfer characteristics of the high-temperature annealing Si-doped HfO ₂ NC ISFET and the obtained fitting with the NC ISFET model.	119
4.33 a) Comparison between the total capacitance of the baseline ISFET and of its corresponding NC counterpart for different pH values. b) Potential drop across V_{REF} , showing a marked negative valley in response to positive RE biases. . . .	119
4.34 Band diagram of ISFET and NC ISFET. The ferroelectric component increase the band bending in the silicon channel.	120
4.35 NC ISFET transfer characteristics simulated for pH values ranging from 4 to 8. .	120

List of Tables

1.1	Compliance of the different sensing strategies with the various requirements	8
1.2	Performances requirements and related technology choice.	24
2.1	Fabrication issues and solutions	55
3.1	Lab-On-Skin diagram.	91
4.1	FET performance Boost due to NC effect	103
4.2	ISFET performance Boost due to NC effect	111
5.1	Lab On Skin TM comparison with the SOA	125
5.2	NC ISFET comparison with the SOA	126

List of Symbols

Symbol or Abbreviation	Meaning
$[C^+]_{LUT}$	Cations concentration in the LUT
$[C^+]_{mem}$	Cations concentration in the membrane
$[H^+]_s$	Hydrogen ions concentration at the dielectric interface
$[H^+]_B$	Hydrogen ions concentration in the bulk of the solution
Ag/AgCl	Silver/Silver chloride
a_{Hs^+}	Hydrogen ions activity at the dielectric interface
ALD	Atomic Layer Deposition
AlSi	Aluminum silicide
A_V	Gain of the NC amplifier
b	thickness of the Stern layer
BaTiO ₃	Barium titanate
BHF	Buffered hydrofluoric acid
BOx	Buried Oxide
C ₂ H ₂ Cl ₂	Dichloroethylene
CA	Contact Angle
Ca ⁺⁺	Calcium ion
C_D	Depletion layer capacitance
C_{DE}	Dielectric capacitance
C_{diff}	Density of capacitance of the Diffuse layer
C_{LG}	Density of capacitance of the liquid Gate
C_{FE}	Capacitance of the FE-Cap
C_{it}	Interface trap capacitance
Cl ⁻	Chlorine ion
C_{LG}	Liquid Gate capacitance
CMi	Center of MicroNanoTechnology
CO ₂	Carbon dioxide
C_{OX}	Oxide capacitance
C_S	Density of capacitance of the Stern layer

Symbols

DOS	bis(2-ethylhexyl) sebacate
DSO	Dysprosium Scandium oxide
E	Electric Field
E^0	Portion of EMF independent on $[C^+]_{LUT}$ and $[C^+]_{mem}$
E_C	Conduction band energy
E_F	Fermi energy
E_{Fi}	Intrinsic Fermi energy
EMF	ElectroMotive Force
EOT	Equivalent Oxide Thickness
E_V	Valence band energy
FD	Fully Depleted
FE-Cap	Ferroelectric Capacitor
$FeCl_3$	Iron chloride
FET	Field-Effect Transistor
FISA	Fully Integrated Sensor Array
g_m	Transconductance
H^+	Hydrogen ion
H_2O_2	Hydrogen peroxide
H_2SO_4	Sulphuric acid
HBr	Hydrobromic acid
HCl	Chloridric acid
HDL	Helmholtz Double Layer
HF	Hydrofluoric acid
HfO_2	Hafnium oxide
HNO_3	Nitric acid
IBE	Ion Beam Etching
ICP	Inductively Coupled Plasma
I_D	Drain current
I_{OFF}	OFF current
I_{ON}	ON current
ISFET	Ion-Sensitive FET
ISM	Ion-Selective Membranes
J_{diff}	Density of diffusion current
J_{drift}	Density of drift current
J_{tot}	Density of total current
K^+	Potassium ion
$k_B T$	Thermal energy
K_c	Equilibrium dissociation constant
KCl	Potassium Chloride
KOH	Potassium hydroxide
K_{sp}	Solubility product constant of AgCl
L	Langevin function

LED	Light-Emitting Diode
LOD	Limit of Detection
LOR	Lift-Off Resist
LUT	Liquid Under Test
m	FET ideality factor
Max _S	Theoretical current sensitivity limit of ISFETs
Mg ⁺	Magnesium ion
MOSFET	Metal-Oxide-Semiconductor FET
mRE	Miniaturized RE
MSR	Minimum Sweat Rate
n ₀	Bulk density of ions
n _{0w}	Bulk density of water molecules
N _A	Acceptor-type dopants concentration
Na ⁺	Sodium ion
NaCl	Sodium chloride
Na-TFPB	Sodium tetrakis [3,5-bis(trifluoromethyl)phenyl]borate
Na-TPB	Sodium tetraphenylborate
NC	Negative Capacitance
N _D	Donor-type dopants concentration
NH ₄ ⁺	Ammonium ion
NH ₄ ⁺ F	Ammonium fluoride
NH ₄ ⁺ OH	Ammonium hydroxide
n _i	Intrinsic carrier concentration
NW FET	Nanowire FET
OHP	Outer Helmholtz Plane
P	Polarization of the Stern layer
p ₀	Magnitude of the water external dipole moment
PbTiO ₃	Lead titanate
PDMS	Polydimethylsiloxane
pH _{pzc}	pH corresponding to the PZC of the sensing layer
pH _s	pH at the dielectric interface
PLD	Pulsed Laser Deposition
PMMA	Polymethyl methacrylate
PSA	Pressure Sensitive Adhesive
P _r	Remnant polarization
PVB	Polyvinyl butyral
PVC	Polyvinyl chloride
PZC	Point of Zero Charge
PZT	Lead zirconate titanate
q	Elementary charge
Q ₀	Remnant polarization charge of the ferroelectric without external bias

Symbols

Q_C	Coercive polarization charge of the ferroelectric
Q_D	Charge of the depletion layer
Q_{DE}	Charge of the dielectric capacitor
Q_F	Polarization charge of the ferroelectric
QRE	Quasi-RE
RE	Reference Electrode
SAM	Self-Assembled Monolayer
SEM	Scanning Electron Microscopy
SF ₆	Sulfur esafuoride
SiO ₂	Silicon dioxide
SNR	Signal-to-Noise Ratio
SOI	Silicon-On-Insulator
S_{out}	ISFET ideality factor
SRO	Strontium Ruthenium oxide
SS	Subthreshold Swing
t	Time
TEM	Transission Electron Microscopy
TEMAH	Tetrakis(ethylmethylamido)hafnium(IV)
t_{high-k}	Thickness of the high-k dielectric
U	Free energy of the ferroelectric material
U_{CDE}	Free energy of the dielectric capacitor
V_C	Coercive voltage of the ferroelectric
V_D	Drain voltage
V_{DD}	Supply voltage
V_G	Gate voltage
V_F	Polarization voltage of the ferroelectric
V_{FB}	Flatband voltage
V_{MOS}	Potential applied to the MOSFET
V_{OX}	Oxide voltage
V_{REF}	RE voltage
V_{sens}	Bias variation given by a pH variation of 1 point
V_{th}	Threshold voltage
WF	Workfunction
x_D	Depletion region thickness
$x_{D_{max}}$	Depletion region maximum thickness
z	Valence of the ion being sensed

List of greek letters

Greek letter	Meaning
α	Ideality factor for ion sensing materials
α_{FE}	Anisotropy constant of the ferroelectric
β	Buffer capacitance
β_{FE}	Anisotropy constant of the ferroelectric
β_s	Surface buffer capacitance
δ	Surface reactivity
ϵ_0	Dielectric constant of the vacuum
ϵ_r	Relative dielectric constant
η	Reciprocal of the thermal energy
μ	Mobility
ρ	Frictional inertia of the FE-Cap
σ	Density of charge in the OHP
τ	Time constant related to initial oxide thickness in an oxidation process
Φ_f	Fermi potential
$\Phi(x=b)$	Electric field at the OHP
χ^{sol}	Surface dipole potential of the gate oxide
Ψ	Potential due to pH

1 Introduction

The challenge of continuous, non-invasive health monitoring is bringing together the most different branches of science, from biology, to electronics, to physics, to information technology.

The term "wearable sensor" covers an astoundingly wide range of different devices, as the first choice to be made when designing one (*Which condition should we monitor?*) leads to more decisions to take (*Which biological parameter should we consider for that condition?*) and these as well bring about more and more (*Which technology should we choose? In which kind of device should it be integrated?...*)

Many works have been focusing on extracting physical signals from the body, such as motion, position, heart rate, breath rate, skin temperature and skin conductivity, often integrating multiple assays in the same wearable system [1–12].

The possibility of extracting chemical parameters from the body of the user in real-time, on the other hand, would add a plethora of new information to be used for diagnostic: for this reason a lot of attention has been given to the body-fluids which could undergo such analysis (blood, sweat, saliva, tears, urine...)

In this work, we focus on sweat sensing and, in particular, on the employ of CMOS-compatible ISFETs to achieve a quantitative evaluation of the concentrations of relevant biomarkers.

1.1 Sweat as a biological fluid of interest

Sweat is a biofluid whose main function is the thermal regulation of the body during heat or intense physical activity [13]. Under these conditions, specific heat receptors distributed in different parts of the body (skin, muscles, stomach, central nervous systems and anterior hypothalamus) send a signal to the anterior hypothalamus which, through the sympathetic nervous systems, generates a dilatation of the skin vascular bed, increasing skin blood flow and stimulating sweat.

The sweat glands on the body are generally divided in *eccrine*, in which the sweat is secreted from the cells without a destructive process, and *apocrine*, in which the secretion happens *via*

Chapter 1. Introduction

a pinch-off of the cells outer parts [14]. A third type of sweat glands, the *apoeccrine*, showing traits of both the previously mentioned kinds, can be listed, but for the scope of this work we will only focus on the eccrine glands, which are the most widely spread on the skin [15].

Eccrine sweat glands are active since birth and are distributed on every part of the skin, except the lips, with an average concentration of 200 cm^{-2} . The area with the highest concentration of such glands are the palms and the soles, with an average of 700 per centimeter square, while the lowest concentration is found on the back (64 cm^{-2}).

Eccrine sweat glands (Figure 1.1) are constituted by a single tube with a length ranging from 4 to 8 mm. The superficial part, called *acrosyringium* is a funnel-shaped opening in the skin made of normal epithelial cells, with a depth of about $200 \mu\text{m}$ and a diameter of $150 \mu\text{m}$. The part beneath it, the *dermal duct* is composed by a straight part, about 2 mm long, and a coiled part. During sweating, primary sweat is inserted by the cells inside the dermal duct, whose main function is to reabsorb the excess of ions. The rest of the liquid is expelled on the top of the skin, where it evaporates consuming some of the excess heat of the body. Sweat rates up to one liter per hour are common for adults, allowing the dissipation of 675 W of heat.

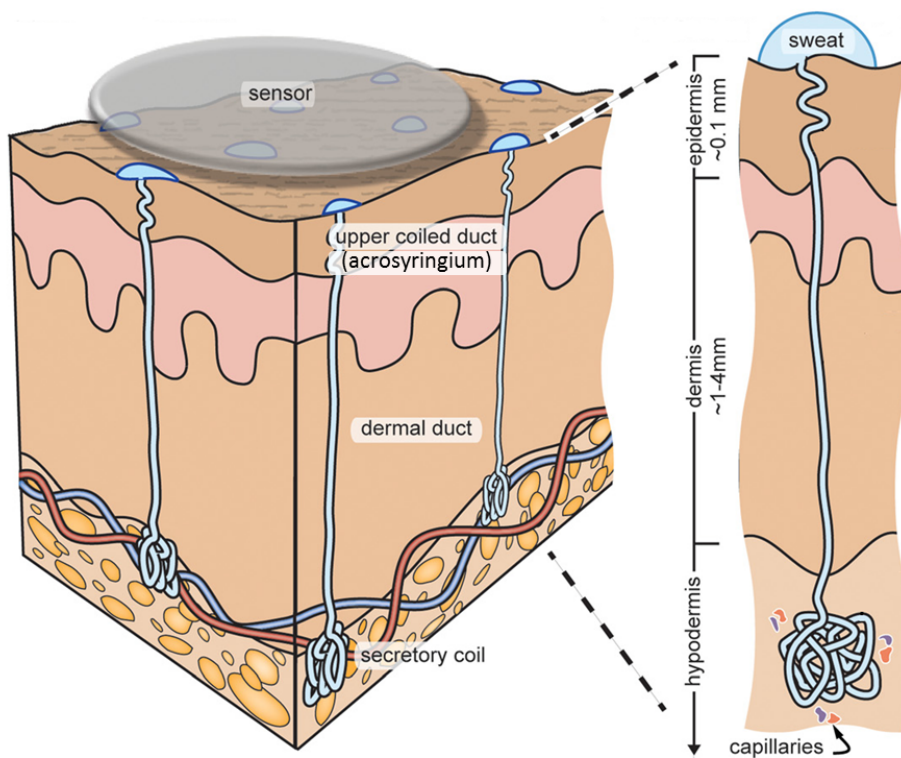


Figure 1.1 – Eccrine glands structure and proportion, adapted from reference [19].

In order to estimate the availability of sweat for a wearable sensor, and therefore the constraints regarding its size and interface with the liquid, we need to know the average sweat rate. The simplest way to evaluate it is to consider the average surface of the human skin (1.8 m^2 [16]) and perform simple calculations, obtaining an average sweat rate of about $1 \mu\text{l cm}^{-2} \text{ min}^{-1}$.

This same order of magnitude is confirmed by other studies [17, 18].

This value, anyhow, refers to sweating rate in exceptional conditions: in order to use this biofluid for continuous health monitoring, it is necessary to adapt our sensors to sweating rates at rest and in normal temperature conditions. Four different studies have been reported by Taylor et al. in [16], in which the average sweat rates for different part of the body of subjects at rest and in thermoneutral conditions are measured. While the ratios between sweat rates in different body parts is almost identical in all the reported papers, the absolute values show differences up to a factor 2 from one work to the other, due to the high variability of these parameters among different subjects. It is however possible to estimate an order of magnitude for the rates, which is around $20 \text{ nl cm}^{-2} \text{ min}^{-1}$ for the forearms and 100 for the palms.

Exploiting such a low production of analyte will require a series of strategies, which will be introduced in Chapter 3.

The relevance of designing a sensor for a specific biofluid depends on its composition and the medical relevance of its components: sweat is composed at 99% by water, in which ions and biomolecules are dissolved.

The most abundant and commonly monitored ions are Na^+ and Cl^- (with a concentration ranging between 10 and 100 mM), K^+ (4-24 mM) and NH_4^+ (0.5-8 mM), while the most relevant macromolecules are lactate (5-60 mM), ethanol (2.5-22.5 mM), urea (2-6 mM) and glucose (10 μM -0.7 mM). Trace-level of many more medically relevant molecules can also be found, such as cortisol (22.1-386 nM), neuropeptide Y (188-682 pM) and interleukin 6 (291-654 pM) [19, 20]. The ability to detect concentrations below a few μM , however, can be achieved at the cost of a lower measurement accuracy on the whole concentration spectrum; therefore, though future works might include the last mentioned molecules in the list of biomarkers of interest, they are out of the scope of this thesis.

The medical relevance of a biomarker concentration in sweat can either come from studies which link it to a physical condition or, more indirectly, from the possibility of using it to evaluate the corresponding concentration in blood, serum or plasma, commonly used as gold standards in most analysis.

With the increasing interest in the use of sweat as biological analyte, many studies have focused on proving or disproving such correlation for the different biomarkers: it was found that no correlation can be observed between the concentration of Na^+ , K^+ , Cl^- and urea in sweat and in plasma [21, 24], while, on the contrary, a strict correlation could be proven for lactate [22], ethanol [23], glucose [25, 26] and NH_4^+ [27].

Na^+ , K^+ and Cl^- are useful biomarkers for sweat-based diagnostics thanks to the effect that different illnesses and physical conditions have on their concentration: Na^+ can be monitored to mark hormonal changes which prelude to ovulation in women [28] or to evaluate the sweat rate [29]. An increase in the ratio between K^+ and Na^+ concentration could be a symptom of renal failure [30] and an increase in that between Cl^- and K^+ a symptom of Cystic Fibrosis [31]. This last sweat test is currently the gold standard for hospital testing.

Since so many ratios are involved, it is clear that the usefulness of the monitoring of these biomarkers increases dramatically when multiple functionalizations are achieved on the same sensor.

1.2 Sweat sensing: recent history and State of Art

In the last years, many different approaches have been presented for monitoring the sweat composition with wearable devices.

Colorimetric detection was one of the first strategies introduced, mostly because of the ease of integration of an hygroscopic material, containing chemical reagents, on a flexible microfluidics.

In 2009, Benito-Lopez *et al.* [32] proposed a system in which sweat was collected with a passive microfluidics made of Polymethyl methacrylate (PMMA) and a Pressure-Sensitive Adhesive (PSA) and flown through a 1 mm long patch containing a pH-sensitive dye (Figure 1.2). In this system, the readout is achieved with two μ -Light-Emitting Diodes (LED), acting respectively as light source and light detector, positioned above and below of the pH-sensitive patch.

Since the readout was based on light detection, the sensor had to be covered by a Velcro belt to avoid environmental noise.

This system, introducing a microfluidics width of only 200 μm , has been a decisive first step towards continuous sweat monitoring and showed the importance of limiting the amount of sweat needed for sensing. Repeatable measurements have been achieved over multiple hours, proving the reliability of this strategy.

Multiple limitations can nevertheless be listed: first of all, this system could only sense pH alone, drastically limiting the medical relevance of the data extracted. Secondly, the two-LEDs system is difficult to integrate in a more complex device. The fact that this device has not been designed for mass production and integration is also apparent from its fabrication procedure, in which the PMMA channel is engraved by a CO₂ laser, the sensing element is manually introduced and the PSA closing layer manually applied. The absorbent material also needs to be manually inserted in the outlet and is not designed to provide a slow, controlled sweat flow. Finally, it has to be underlined that the amount of sweat needed by this architecture ($200 \mu\text{m} \times 80 \mu\text{m} \times 2 \times 10^4 \mu\text{m} = 3.2 \times 10^8 \mu\text{m}^3 = 320 \text{ nl}$) is still not compatible with normal sweating rates at rest, especially if we consider that the inlet opening has a diameter of only 1 mm, from which we are expected to obtain a mere 0.15 nl/minute. This last issue is shared by all the device presented in this section.

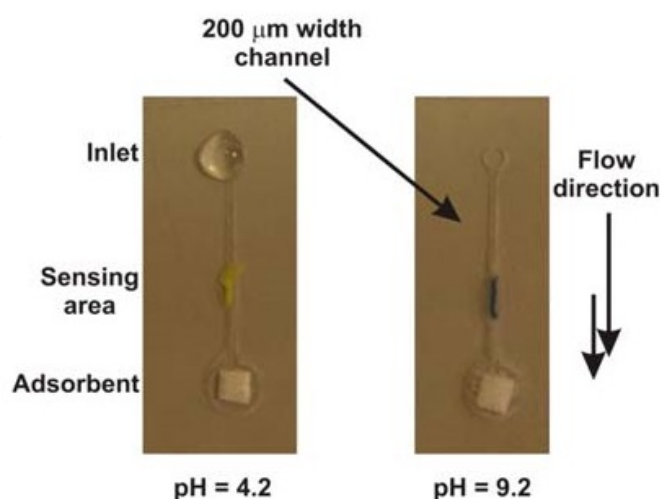


Figure 1.2 – Benito-Lopez *et al.* Passive microfluidics with pH sensitive element.

1.2. Sweat sensing: recent history and State of Art



Figure 1.3 – Koh *et al.* Smart patch with four different selectively sensitive areas.

Colorimetric detection has also been employed later by Koh *et al.* [33]. Their device consisted in a PDMS microfluidics containing a set of four color-responsive materials, each sensitive to a different biomarker concentration (pH, lactate, glucose and chloride) (Figure 1.3). The complete system, flexible, 3 cm wide and only 700 μm thick, was attached on the skin of the user with a biocompatible adhesive.

The read-out was performed inspecting the colors of the sensing areas with an app installed in a smartphone. The system, tested indoor and outdoor during physical exercise sessions, was also able to store the sweat and evaluate the sweat rate.

The amount of sweat needed to fill each of the four cellulose matrices used for sensing, however, was of 5 to 10 μl .

An alternative way to evaluate the concentration of electrically charged biomarkers consists in the employ of potentiometric measurements. In this case, the selective sensing of specific markers can be achieved, for example, with a selectively sensitive membrane containing specific ionophores for the ions of interest.

This strategy has been employed by Rose *et al.* [34] in their adhesive RFID sensor patch (Figure 1.4). The device includes, together with a miniaturized circuitry for read-out, a Na^+ -functionalized electrode and an Ag/AgCl Reference Electrode (RE). This second element is of fundamental importance for any sensor based on the measurement of electrical potential, as it is capable of stabilizing the bias of the Liquid Under Test (LUT) the same way a Ground contact does for a standard electronic circuit. The miniaturization of this element is one of the key challenges to overcome in the design of a potentiometric wearable sensor and will be discussed in section 3.3.

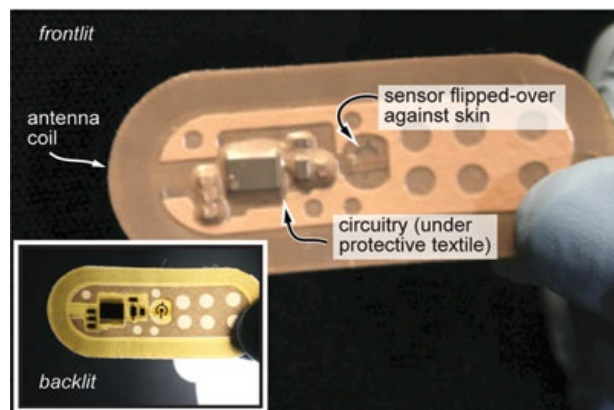


Figure 1.4 – Rose *et al.* Electrode-based smart patch.

One of the key factors limiting the sensitivity of this sensing mechanism is the Nernst limit, which prevents the variation of potential on the sensing layer to grow beyond about 60 mV for

each tenfold variation of the ion concentration, at room temperature. The origin of this limit will be explained in subsection 1.3.2. The sensitivity of this adhesive RFID patch is reportedly of 25 mV/dec for Na^+ .

More recently, Gao *et al.* [35] brought the sensing electrodes technology close to its theoretical limit with their Fully Integrated Sensor Array (FISA) wristband (Figure 1.5). This device is reportedly able to simultaneously measure the sweat concentration of glucose, lactate, Na^+ and K^+ , and the sensitivities to the last two biomarkers have been measured to 64.2 and 61.3 mV/dec, respectively.

In addition to the sensing electrodes, the system also included a temperature sensor, with which it was possible to compensate the heat-related shifts in the measurements.

The sensing electrode technology, however, is not CMOS-compatible and, furthermore,

cannot be used for sensing extremely reduced quantities of liquid, in the range of few tens of nanoliters. This is due to the fact that the sensitivity of extremely miniaturized electrodes is drastically decreased when a standard operational amplifier read-out is employed [36].

These issues can be overcome with the employ of ISFETs, which basically consist in conventional transistors, such as the ones used for computing, in which the metal gate connection is removed and the gate dielectric is put directly in contact with the LUT. An accurate description of these devices is postponed to subsection 1.3.1.



Figure 1.5 – Gao *et al.* Electrode-based FISA wristband.

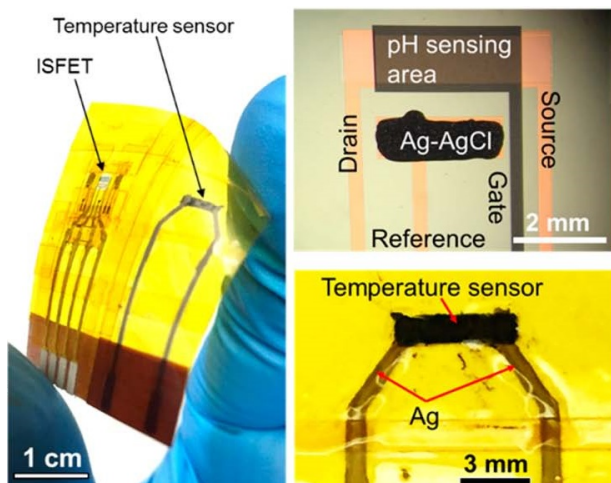


Figure 1.6 – Nakata *et al.* Flexible ISFET-based patch.

A flexible sensing device based on ISFETs has been presented by Nakata *et al.* [37], capable of simultaneously sensing pH and skin temperature (Figure 1.6). The achieved sensitivity reached 50 mV/pH and the temperature dependence of the measurements was efficiently compensated with the temperature sensor. The quality of the ISFET employed, however, due to the challenges in fabricating a transistor on a flexible substrate, was scarce, with a gate-induced current tunability very far from that of ideal devices and dimension hardly im-

1.2. Sweat sensing: recent history and State of Art

proved with respect to simple electrodes.

The system presented in Chapter 3 of this work, among the other improvements, will overcome both of these limitations.

A perhaps more efficient way of exploiting the CMOS-compatibility of this strategy has been presented in [38] by Douthwaite *et al.* In this work, the sensing area is composed by nine ISFET-based pixels (Figure 1.7) whose drain current is averaged and used to feed a ring oscillator.

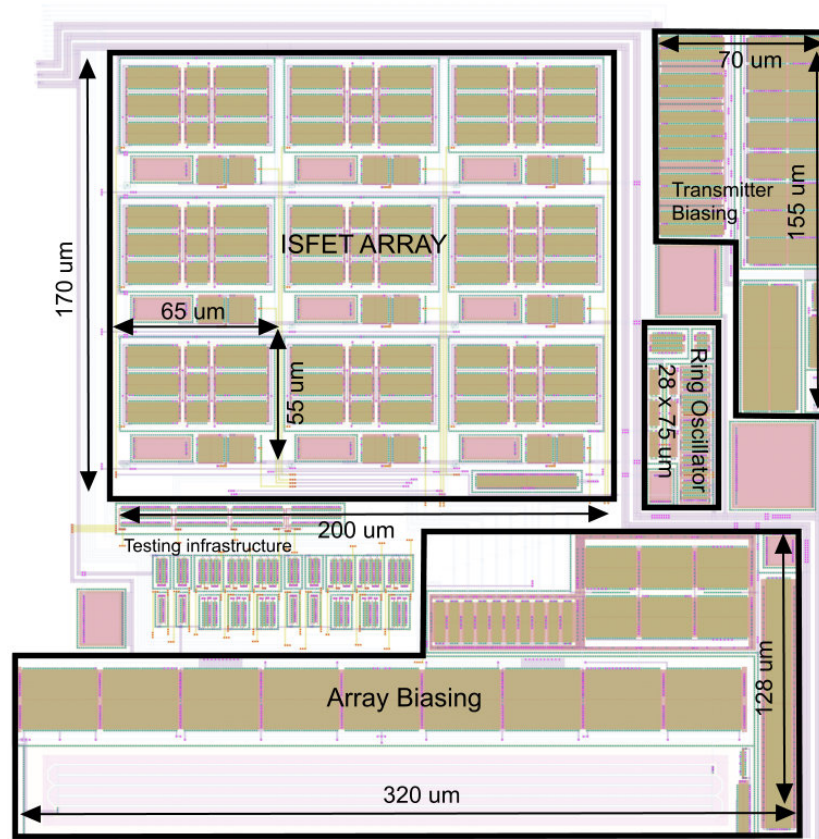


Figure 1.7 – Douthwaite *et al.* Sensing and processing system of the ISFET-based apparatus proposed.

This element, composed by three CMOS inverters, converts the input current in to a frequency, which can readily be transmitted to an external display system with a standard transmitter.

It is easy to see how the employ of ISFETs has made the integration of the sensors with the read-out system completely straightforward: the whole circuit, from biological sensing, to data transduction, is now composed of only one kind of device, the FETs, with minor differences among the ones used in the different stages.

This advantage can easily be exploited to simplify the production of complete systems and increase the integration capabilities with other wearable devices.

In Table 1.1 the strengths and weaknesses of each of the introduced strategies are listed.

	ISFET	ISE	Colorimetric
Low volumes compatibility	VV	X	X
CMOS compatibility	VV	V	X
Mass producible	VV	VV	V
Flexible substrate compatibility	V	VV	VV
Easy prototyping	V	VV	VV
Reusability	VV	VV	V

Table 1.1 – Compliance of the different sensing strategies with the various requirements

1.3 Sweat sensing with computing technology

A Field-Effect Transistor is a three terminal device in which the resistance between two of its contacts (the Source and the Drain) is controlled by the potential applied to the third one (the Gate). Invented in 1959 at the Bell laboratories by Martin M. Atalla and Dawon Kahng, it was intended for logic applications: it constitutes, in fact, the building block of all modern electronics and continuous research is carried on to make them as small, cheap and efficient as possible [39]. In 1970, Piet Bergveld [40] suggested for the first time that the same device structure could be employed for sensing, creating a new technology which, from its very birth, was strong of years of extensive research and know-how.

In this section, we will first present the standard FET device, then we will show how its Ion-Sensitive counterpart differentiates from it and how it can be employed.

1.3.1 The logic Field-Effect Transistor

The FET, and in particular the MOSFET (Metal-Oxide-Semiconductor FET), is a semiconductor-based device which, in the *enhancement mode* described in this thesis, is composed by two heavily doped and highly conductive regions, which constitute the *Source* and the *Drain*, separated by a lowly doped, high resistivity one, called *channel*. The channel region is covered by a dielectric layer, which provides electrical insulation from the metal (or polysilicon) contact which constitutes the *Gate*. A typical MOSFET structure is shown in Figure 1.8.

The semiconductor can be silicon, germanium or a compound of two or more elements taken from the third and fifth column of the periodic table. In this introduction, anyhow, we will assume the transistor to be made of silicon. To understand how the gate bias can influence the conductivity of the channel, it is useful to consider the Band Diagram of the device. Here we are going to treat the case of an n-type MOSFET, *i.e.* a MOSFET in which the Source and Drain regions are heavily n-type doped and the substrate is lightly p-type doped. The p-type case will be exactly dual.

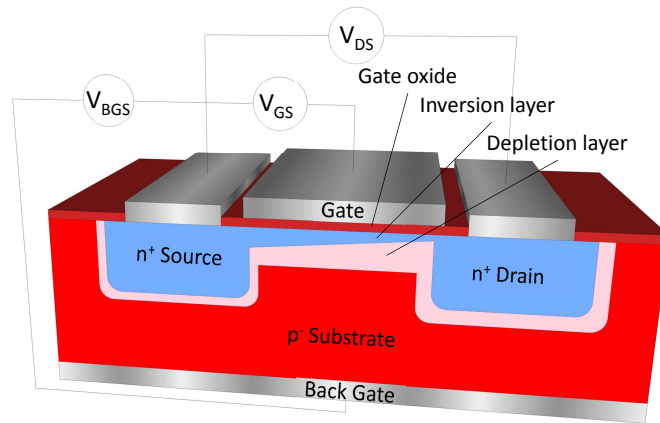


Figure 1.8 – Structure of a typical n-type bulk MOSFET.

To understand the physical operation of this device, a short theoretical presentation of its band diagram is presented [41]. Let us first consider a situation in which no bias and no doping is applied to the semiconductor material (Figure 1.9 a)).

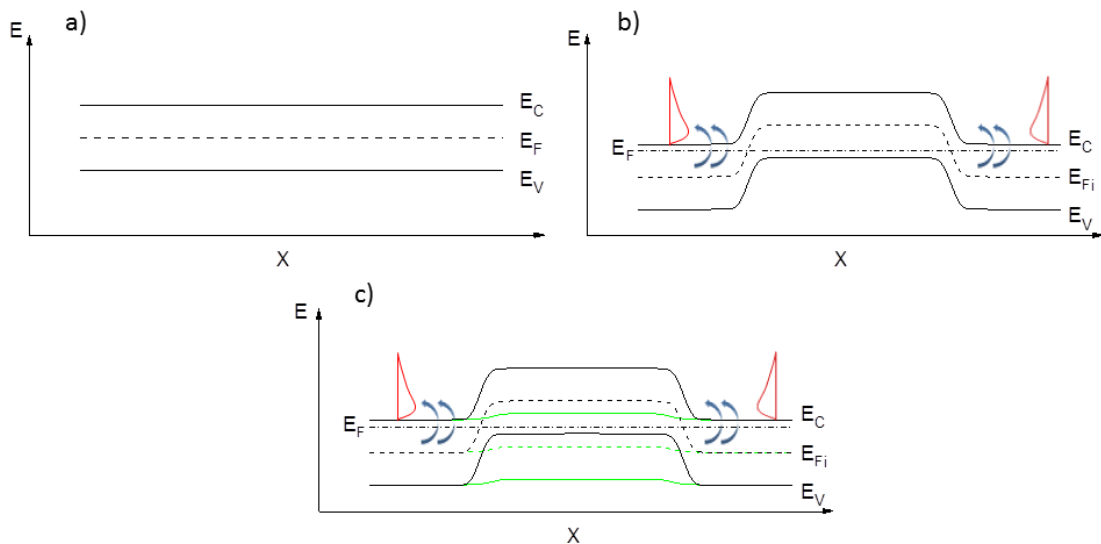


Figure 1.9 – Band diagram of a) a typical undoped semiconductor material without bias applied, b) a typical n-p-n transistor without bias applied and c) n-p-n transistor without (black lines) and with (green lines) a positive gate bias applied.

Since the material is completely homogeneous, the bands are flat. The Fermi level (E_F) lies in the middle of the Band Gap, where no electron state is found, therefore at 0 K all the electrons of the material are found below the Valence Band, where all the available states are occupied. In this condition, the resistance of the material is virtually infinite, since the charges are not able to move. When thermal energy is introduced, some electrons start jumping across the Band Gap; this event enables two conduction mechanism: first of all the electrons on the Conduction Band can freely move from one available state to another and, secondly, an empty

state is created in the Valence Band. This empty state can be filled by a nearby electron, which therefore frees the state which it was previously occupying. The overall effect of this mechanism can be modeled considering this empty state as a fictitious positive charge moving in the opposite direction with respect to the electrons. This charge takes the name of *hole*.

If a bias is applied to the sides of this system, electrons and holes will move in opposite directions, both contributing to the total current. The relationship between applied bias and generated current will be, until heating effects become relevant, perfectly linear.

In order to enable control on the resistivity of the material, we employ, in this case, n-type doping: elements from the fifth column of the periodic table (typically Phosphorus or Arsenic) are inserted, with various techniques, in the Source and Drain region. A high temperature annealing allows the crystal lattice to recover from the amorphization that this extremely energetic process usually generates. During the annealing, some of the inserted atoms can substitute the silicon atoms in the lattice, becoming *activated*. Elements from the fifth column of the periodic table possess an extra electron in their outer electronic shell, compared to the ones in the fourth, therefore, once activated, they effectively increase the number of electrons in the region in which they are inserted. Being E_F , by definition, the energy at which the most energetic electron is found at 0 K, the addition of more electrons to the system causes its rise, reducing the distance to the conduction band (E_C). Quantitatively, the relationship between the dopants concentration and the Fermi level shift is described by Equation 1.1:

$$E_F = E_{Fi} + k_B T \ln(N_D / n_i), \quad (1.1)$$

where E_{Fi} is the Fermi Energy in non-doped (*intrinsic*) conditions, $k_B T$ is the thermal energy, N_D is the concentration of n-type (*donor*) dopants and n_i is the intrinsic carrier concentration of silicon ($1.5 \times 10^{10} \text{ cm}^{-3}$). A typical value for the doping in the S/D region of a MOSFET is between 10^{19} and 10^{20} cm^{-3} .

The electrons of the doped regions now have a smaller energy jump to overcome, in order to reach the Conduction Band (blue arrows in Figure 1.9 b)). The consequent higher concentration of mobile charges will determine a diffusion current towards areas of lower doping, generating an electric field opposing further diffusion. Once the equilibrium between the two forces is achieved, the potential generated at the two junctions will have determined a band bending. The electron distribution in energy (red lines in Figure 1.9 b)) will be given by the combination of the number of available states (growing with the square root of the energy above E_F) and Fermi-Dirac statistics, which foresees an exponential decrease of the occupation probability for higher energy states [42].

In these conditions, even if a positive bias is applied between the Drain and Source contacts, the electrons able to diffuse from Source to Drain are only the ones in the evanescently small distribution tail which surpasses the energy barrier between Source and channel. This weak transport of charges is what will constitute the *Off current* (I_{OFF}) of our MOSFET [43].

In order to switch ON our device, it is necessary to lower the channel barrier. This can be achieved applying a positive bias to it through the Gate. Figure 1.9 c) shows the effect on the Band Diagram.

It is clear that, given a positive Drain bias, a huge amount of carriers would now be able to travel from Source to Drain, giving rise to the *On current* (I_{ON}). Since a high concentration of free electrons from one or both contacts can now flow in the channel, the portion of channel at the interface with the gate dielectric will have a concentration of free electrons superior to that of holes which, given the p-type doping of this region, were previously the majority carriers. For this reason, this interface is called *inversion layer*, as had been shown in Figure 1.8 [44]. The minimum V_G at which the inversion layer is completely formed is called *threshold voltage* (V_{th}) and can be viewed as the gate bias needed to switch on the device. Its value can be extracted from Equation 1.2.

$$V_{th} = 2\Phi_f + V_{FB} + \frac{Q_D}{C_{OX}}, \quad (1.2)$$

where Φ_f is the Fermi potential given by $\Phi_f = \frac{k_B T}{q} \ln(N_A/n_i)$ (N_A being the concentration of p-type dopants and q the elementary charge), V_{FB} is the flatband voltage, *i. e.* the voltage at which the energy bands at the interface between oxide and silicon are flat (given by the difference in work function between silicon and gate metal), Q_D is the charge of the *depletion layer* shown in Figure 1.8 and C_{OX} is the capacitance of the oxide layer. The relation between Drain Current (I_D) and V_G of a transistor takes the name of *transfer characteristics* and is usually plotted in semilogarithmic scale in order to emphasize the sub-threshold regime, *i. e.* the part of the curve characterized by $V_G < V_{th}$. This part of the characteristics is particularly interesting for the characterization of a FET device since many relevant parameters can be extracted from it, as will be shown later. A typical n-type MOSFET transfer characteristics, extracted from one of the devices fabricated for the scope of this work, is shown in Figure 1.10.

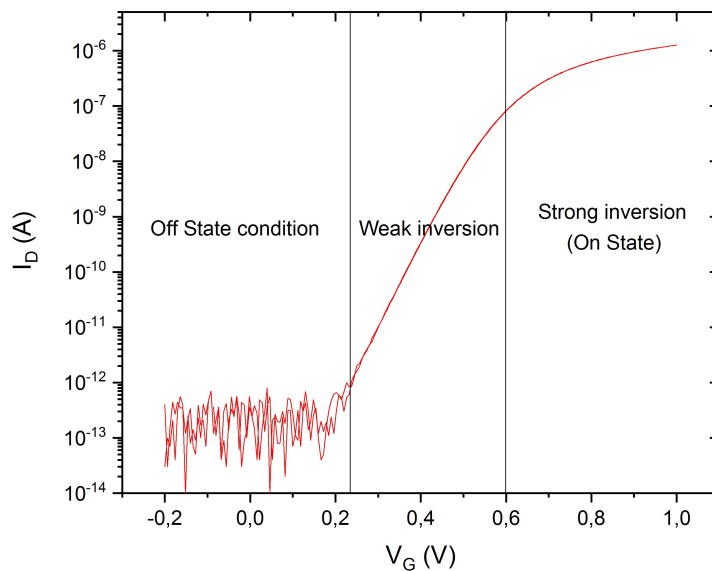


Figure 1.10 – Transfer characteristics of a typical n-type MOSFET. The Off current lies below the noise level of the measurement equipment.

Chapter 1. Introduction

The most important parameters used for evaluating the quality of a MOSFET, both for logic application and for sensing, are the *Subthreshold Swing* (SS) and the I_{ON}/I_{OFF} ratio.

The first parameter, usually expressed in terms of millivolt per decade, represents the steepness of the exponential growth of I_D with V_G in the weak inversion region. For computing, a steep SS is desired as it allows reducing the *supply voltage* (V_{DD}) of a transistor while still keeping a high I_{ON}/I_{OFF} ratio, limiting the power needed to operate a device. For sensing, on top of this advantage, a steep SS increases the current sensitivity of the device, since a more important variation of current is achieved given the same variation of gate potential. The I_{ON}/I_{OFF} ratio is important for computing as a high ratio allows for fast operations and low stand-by power consumption. In sensing, the importance of this parameter comes from the fact that, given a SS, an higher I_{ON}/I_{OFF} ratio means a wider sensing range before the sensor saturates.

The minimum value for the SS, in conventional MOSFETs, equals $\frac{k_B T}{q} \ln(10) \simeq 59 \text{ mV/dec}$. The origin of this limit can be understood from the Band Diagrams in Figure 1.9 b) and c): when the Source-channel barrier is lowered, the increase of the number of electrons which are allowed to diffuse depends on their exponential distribution, whose steepness depends solely on the temperature and not on the physical parameters of the device [45].

Nearing this limit requires achieving a near-optimal gate coupling, *i. e.* optimizing the device so that almost the entirety of the applied gate bias is used to lower the Source-channel barrier. The complete formula describing the value of the SS can be expressed as in Equation 1.3:

$$SS = \frac{k_B T}{q} \ln(10) \left(1 + \frac{C_D + C_{it}}{C_{OX}} \right). \quad (1.3)$$

Here, C_D is the depletion capacitance of the silicon channel and C_{it} is the capacitance given by the trapped charges in the silicon-oxide interface. We can use Equation 1.3 to introduce the *ideality factor* $m \geq 1$ of a MOSFET as

$$m = \left(1 + \frac{C_D + C_{it}}{C_{OX}} \right). \quad (1.4)$$

The strategies for lowering this value by increasing C_{OX} have focused for a long time on the reduction of the SiO_2 thickness, but for the last technology nodes this would have brought to a dielectric thickness below 1 nm, with unacceptable leakage levels. For this reason, high-k dielectrics such as HfO_2 and Al_2O_3 have been introduced [50]. These materials, having a dielectric constant ϵ_r higher than that of silicon oxide (up to 25 for HfO_2 and 9.1 for Al_2O_3 against 3.9 for SiO_2), can provide a higher capacitance with the same thickness. To provide an intuitive indication of the advantage brought by the employ of an high-k material, a new parameter, called *Equivalent Oxide Thickness* (EOT) has been introduced. The EOT expresses what would be the physical thickness of a SiO_2 layer having the same capacitance of the high-k dielectric layer. Its mathematical definition is shown in Equation 1.5.

$$EOT = t_{high-k} \frac{\epsilon_{SiO_2}}{\epsilon_{high-k}}, \quad (1.5)$$

where t_{high-k} is the physical thickness of the high-k dielectric layer and ϵ_{high-k} and ϵ_{SiO_2} are the dielectric constant of the high-k dielectric layer and of the SiO_2 , respectively.

High-k dielectrics are also useful for sensing, since they show a nearly-Nernstian sensitivity to pH, as will be shown later in this chapter.

The reduction of C_{it} relies on fabrication strategies meant to prevent the charge trapping at the silicon-gate dielectric interface and will be discussed in the next chapter.

Reducing the Depletion capacitance is a challenge which has been tackled with the introduction of fully depleted (FD) devices. The depletion region of a MOSFET is a part of the channel near the interface with the gate oxide in which the free charges have been removed. Its thickness (x_D) depends on the doping level of the channel, according to Equation 1.6:

$$x_D = \sqrt{\frac{2\epsilon_{Si}\Phi_s}{qN_A}}. \quad (1.6)$$

Here, ϵ_{Si} is the dielectric constant of silicon and Φ_s is the total potential across the surface. This thickness reaches its maximum value $x_{D_{max}}$ when $\Phi_s = 2\Phi_f$.

Until this condition is not reached, as V_G increases, this region expands and the amount of charge stored in it grows as well; therefore, from the definition of capacitance, we can say, as a first approximation, that $C_D = \delta Q_D / \delta V_G > 0$. Here is where the Full Depletion strategies can intervene: if the physical thickness of the silicon channel is way lower than $x_{D_{max}}$, then increasing V_G does not increase the width of the depletion region and therefore there is no increase in the charge stored in it, which means that $C_D = 0$ [46].

Further publications on the topic [47–49] argued that equation 1.3 cannot be strictly applied to thin film devices and introduced more accurate models for the body factor of these devices. For the purpose of this introductory chapter, however, the presented approximation can hold valid. The full-depletion condition can be achieved with different strategies.

A finFET device (Figure 1.11 a) features a fin-shaped channel with thickness greater than the width. The gate bias is applied from three sides, which in some architectures can be tuned independently, allowing a nearly perfect electrostatic control.

Other architectures require the employ of a particular substrate: the Silicon-On-Insulator (SOI). Substrates of this kind feature an oxide layer, whose thickness can be established during the fabrication phase, sandwiched between two crystalline layers of silicon. The bottom silicon layer will constitute the substrate, while the thinner top layer will be used for fabricating the devices. In addition to allowing reducing the physical thickness of the channel, SOIs also prevent current leakages between Source and Drain of the fabricated devices through the substrate, reducing I_{OFF} . Nanowire FETs (NW-FETs, Figure 1.11 b) are an example of structures which can be built on such substrates. The width and thickness of their channels are comparable and extremely reduced, in the order of few tens of nm or less. They are a special kind of *gate all around* devices, showing exceptional electrostatic control. They can also be fabricated as suspended structures.

The last architecture we are going to mention is the ribbon-FET (Figure 1.11 c): an SOI device

in which the channel is wide but extremely thin, so that the bias applied from front gate and backgate is sufficient to achieve Full Depletion.

The choice of the device employed for sensing will be discussed in subsection 1.3.3.

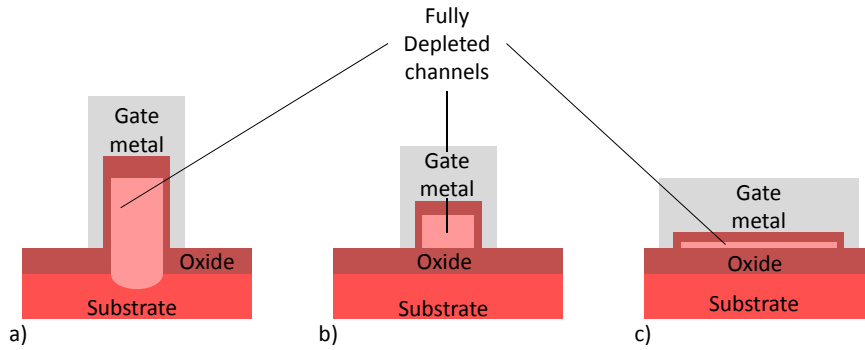


Figure 1.11 – Schematic representation of the sections of a) a finFET, b) a nanowire and c) a FD SOI ribbon-FET.

1.3.2 The Ion-Sensitive Field-Effect Transistor

The ISFET structure, as mentioned before, is fairly similar to that of a conventional MOSFET used for computing. The main difference consists in the fact that, instead of controlling the channel with a metal contact, we employ a *liquid gate*, which is composed by a *Reference Electrode* and the very LUT in which we are interested (Figure 1.12).

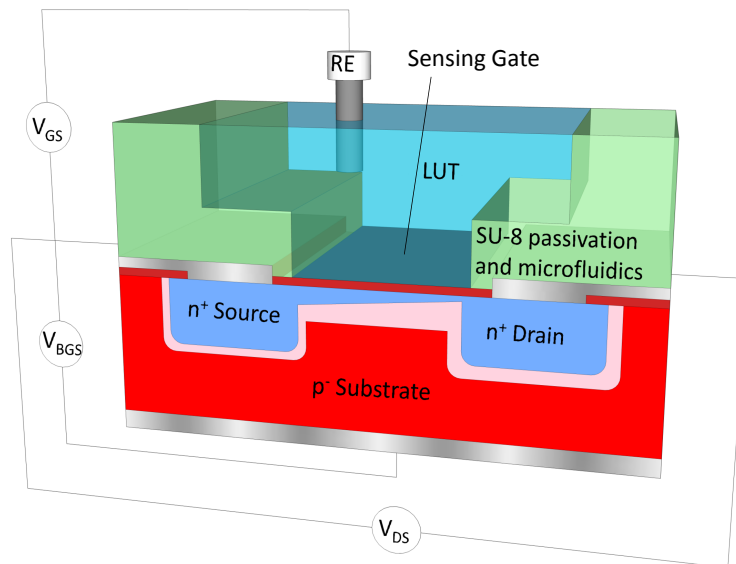


Figure 1.12 – Structure of a typical n-type bulk ISFET.

In this new structure, the charge of the ions in the LUT influences the total gate bias seen from the FET, and will modify its I_D accordingly. This mechanism will be explained in detail later in

this subsection.

Liquid-dielectric interaction at the interface

The interaction between the LUT ions and the gate dielectric, at the oxide-liquid interface, is extremely complex and the models employed to explain it have evolved in time.

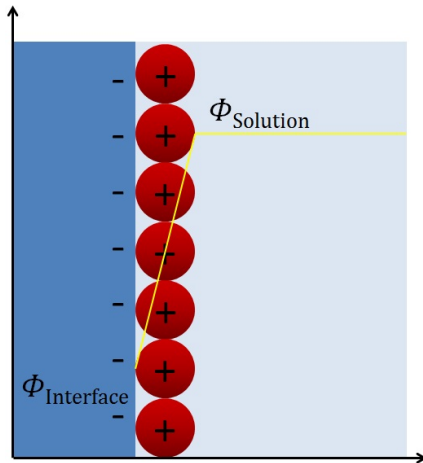


Figure 1.13 – HDL model.

In 1853, Hermann von Helmholtz introduced the *Helmholtz Double Layer* (HDL) model [51], in which it is supposed that the positive charges present in the solution will be adsorbed on the oxide surface (supposed negatively charged because of the strong electronegativity of the Oxygen atoms on the surface) creating a monolayer of immobilized cations called *surface charge layer*, shielding the oxide charge, as shown in Figure 1.13. This component, from a capacitive point of view, can be seen as a dielectric layer over which a linear potential drop is observed. In the rest of the liquid the potential is considered constant.

This model, though introducing some relevant insights on the ion dynamics of a liquid in contact with a charged surface, was not able to accurately describe

the bias-dependent capacitance of the system, as the assumption of complete screening of the oxide potential by the surface charge layer proved to be too strong.

A second description of the behavior of the ions in a liquid at the interface with a charged surface was independently proposed by Louis Georges Gouy in 1910 [52] and David Leonard Chapman in 1913 [53] and takes the name of *Gouy-Chapman model*. In this model, a *diffuse double layer* is introduced, in which the ions of the solution are free to move towards the oxide interface to compensate its charge, arranging themselves in a such a way that the positive charge distribution can be described by the Maxwell-Boltzmann statistics (Figure 1.14). Such distribution will generate an exponential drop of the potential along the liquid, explaining the observed bias-dependent capacitance. In this model, however, the ions are considered point-charges, so that their concentration at the interface can be unphysically high, leading to expected capacitance values far exceeding the experimental measurements.

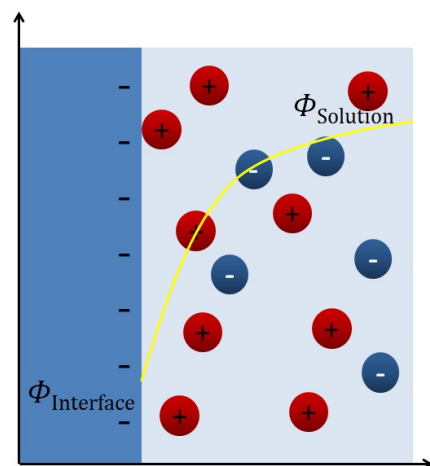


Figure 1.14 – Gouy-Chapman Diffuse Layer model.

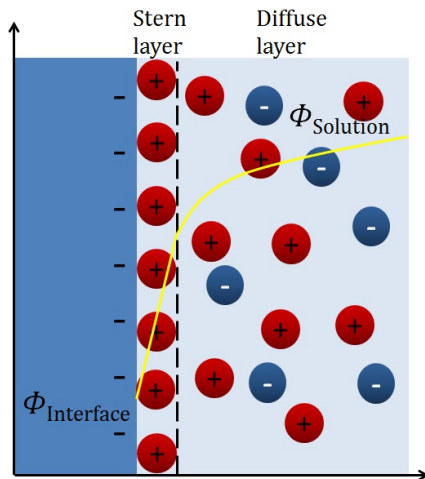


Figure 1.15 – Stern model.

To keep into account the influence of the ionic radius, in 1924 Otto Stern proposed a model encompassing the previous two: the exponential potential drop in the diffuse layer was used to describe the bulk of the liquid, while, at the interface with the oxide, a layer of adsorbed ions similar to the one proposed by Helmholtz was envisaged [54]. The thickness of this layer, which took the name of *Stern Layer* was assumed equal to the ionic radius and its capacitance, which depended on the applied bias, had a typical value of $20 \mu\text{Fcm}^{-2}$. The interface between the Stern layer and the diffuse layer took the name of *Outer Helmholtz Plane* (OHP). Since the liquid is divided in two separate regions with different dynamics, the dependence of its potential on the distance from the interface with the oxide will also

be composed by two different behaviors: as illustrated in Figure 1.15, the first part shows a linear potential drop and the second and exponential one. The total capacitance of the Double Layer (C_{DL}) is therefore evaluated as a series of those of the diffuse layer (C_{diff}) and of the Stern layer (C_S) according to Equation 1.7:

$$C_{DL} = \frac{C_{diff}C_S}{C_{diff} + C_S}. \quad (1.7)$$

The Stern model has its own limitations, such as the fact that the dielectric constant of the diffuse layer is considered homogeneous and independent from external fields and that the ions, excluding the ones in the Stern layer, are still considered point charges.

Though new and more complex theories have followed, the Stern model remains an acceptable approximation for most applications and an excellent basis to understand the ion dynamics mechanism.

It is worth noting that, though a negatively charged oxide layer has been considered to introduce the different models, the same concepts hold for a metal layer as well and that, if the surface immersed in the solution is positively charged, the behavior of positive and negative ions will be simply exchanged.

Ion sensitivity and Nernst limit

The mechanism behind the ion sensing capabilities of a surface relies on its amphoteric nature: the neutral hydroxyl groups are in fact able to be both protonized (*i. e.* adsorb an hydrogen ion and become positively charged) or deprotonized (*i. e.* release an hydrogen ion and become negatively charged). The equilibrium ratio of positively and negatively charged groups depends on the concentration of hydrogen ions in the LUT, and therefore on its pH. For more than two decades after the invention of the ISFET, this surface charge phenomenon has been widely regarded as the direct pH sensing mechanism [55], but the most recent

models [56] state that the role of the amphoteric sites of the sensing surface is rather that of *buffering* the H^+ concentration of the thin layer of liquid in direct contact with it ($[H^+]_s$). The pH of this layer of liquid (pH_s) will therefore be pinned around the *Point of Zero Charge* (PZC) of the sensing surface, *i.e.* around the value of H^+ surface activity (a_{H^+}) at which there is an equal number of positively and negatively charged amphoteric sites [57]. A variation in the bulk concentration of hydrogen ions ($[H^+]_B$), will therefore modify the $[H^+]_B/[H^+]_s$ ratio. As a consequence, the liquid will feature an interface, close to the sensing surface, across which the concentration of H^+ ions is not constant and an electrical potential (Ψ) will build-up, with a magnitude dependent on $[H^+]_B$. It is this potential which is read by the sensor.

The relation between Ψ and the $[H^+]_B/[H^+]_s$ ratio, as already mentioned, will be determined by the *Nernst law*, which takes its name from the chemist Walther Nernst who formulated it in 1888.

It is possible to derive this relation starting from the equations describing the drift and diffusion-driven fluxes of ions across the liquid interface [58]. Though H^+ is the only specie in which we are interested for pH sensing, we will derive the most general formula, valid for any given ion of any valence.

$$J_{diff} = -\mu \frac{k_B T}{q} \frac{\delta[ion^+]}{\delta x}. \quad (1.8)$$

$$J_{drift} = -\mu z [ion^+] \frac{\delta V}{\delta x}. \quad (1.9)$$

Here, μ is the mobility of the ions, z is their valence and $[ion^+]$ is the (positive) ions concentration. Summing these two components together we get:

$$J_{tot} = -\mu \frac{k_B T}{q} \frac{\delta[ion^+]}{\delta x} - \mu z [ion^+] \frac{\delta V}{\delta x}, \quad (1.10)$$

which needs to be equal to 0 at equilibrium. Since μ is a constant, we can then write:

$$-\frac{k_B T}{q} \frac{\delta[ion^+]}{\delta x} = z [ion^+] \frac{\delta V}{\delta x} \quad (1.11)$$

and, therefore,

$$\frac{\delta[ion^+]}{\delta x} = -\frac{zq}{k_B T} [ion^+] \frac{\delta V}{\delta x}. \quad (1.12)$$

We can now separate the variables and integrate both sides.

$$\int_s^B \frac{\delta[ion^+]}{[ion^+]} = -\frac{zq}{k_B T} \int_s^B \delta V. \quad (1.13)$$

The integral limits "s" and "B" refer, respectively, to the the layer of liquid at the interface with the sensing surface and to the bulk liquid. Solving the integrals we obtain:

$$\ln[ion^+]_B - \ln[ion^+]_s = -\frac{zq}{k_B T} (V_B - V_s). \quad (1.14)$$

Exploiting the properties of logarithms, we can get to the final formulation:

$$\Delta V = -\frac{k_B T}{zq} \ln \frac{[ion^+]_B}{[ion^+]_s}. \quad (1.15)$$

This equation states that a tenfold increase (or decrease) in the bulk monovalent ion concentration in the LUT will generate a potential variation of up to $\frac{k_B T}{zq} \ln(10) \simeq 59$ mV, at room temperature. The z at the denominator means that if an ion has a valence bigger than one (e. g. Ca^{++}), the sensitivity will be reduced accordingly.

This value, anyhow, remains an upper limit, and the ability to approach it depends on the efficiency with which the pH_s value can be pinned. This efficiency, in turn, will depend on the properties of the liquid and of the surface of the sensing material.

To understand the dependency of the sensing performances on the surface and liquid parameters, we must consider the phenomenons taking place when the pH of the bulk of the LUT (pH_B) is varied: the sensing surface will be adsorbing or releasing protons in the interface layer to keep its pH (pH_s) constant, and the amount of charges needed to sustain the subsequent variation of potential ($\Delta\Psi$) will depend on the capacitance C_{DL} of the LUT. Achieving a high sensitivity will therefore require a strong release/adsorption of H^+ from the sensing surface and a low C_{DL} . A dimensionless parameter for keeping in to account non-idealities in the sensing mechanism and explain sub-nernstian experimental sensitivities has been introduced in [59]: this parameter, called β is defined as in Equation 1.16:

$$\beta = \frac{q^2 N_s \delta}{C_{DL} k_B T}. \quad (1.16)$$

Here N_s is the density of surface amphoteric sites of the material, *i.e.* the density of sites able to accept or release a charged particle and δ is a parameter keeping into account the equilibrium constants K_a and K_b , describing respectively the adsorption rate of an acceptor site and the release rate of a donor site, as shown in Equation 1.17:

$$\delta = 2\sqrt{K_a K_b}. \quad (1.17)$$

1.3. Sweat sensing with computing technology

The higher is the value of β , the closer to ideal will be the sensitivity of the surface and its linearity. The ideality factor $\alpha \leq 1$ in this case is defined as

$$\alpha = \frac{\beta}{\beta + 1}. \quad (1.18)$$

The real relation between ΔpH_B and $\Delta\Psi$ will then be described by:

$$\Delta\Psi = -2.3\alpha \frac{k_B T}{q} \Delta pH_B. \quad (1.19)$$

The parameter β defined here is related to the full sensing system (sensing layer plus LUT). An alternative but equivalent formulation of the ideality factor α [60] decouples the effects given by the sensing layer buffering effect and by the liquid double layer capacitance, allowing defining a *surface buffer capacitance* (β_s) which describes the quality of the specific material as a pH sensor. The new parameter is defined as

$$\beta_s = \frac{d[B]}{dpH_s} = \frac{d[B]}{d[H^+]_s} \frac{d[H^+]_s}{dpH_s}, \quad (1.20)$$

where B is the net number of charged amphoteric groups on the sensing surface. The final formulation will consequently read

$$\beta_s = N_s \frac{K_a + 4K_a K_b [H^+]_s + K_b [H^+]_s^2}{(K_a + [H^+]_s + K_b [H^+]_s^2)^2} 2.3 [H^+]_s. \quad (1.21)$$

The new definition of the ideality factor α will be:

$$\alpha = \frac{1}{2.3 \frac{k_B T}{q^2} \frac{C_{DL}}{\beta_s} + 1}. \quad (1.22)$$

It has been demonstrated that a correlation exists between the k-value and the β value of a dielectric, so that high-k dielectrics result to be ideal for both the transductions needed in an ISFET [62].

While the buffering capability of the sensing layer only applies to H^+ , the influence of other positively charged species on the measured Ψ is usually not zero. This is due to the fact that a higher concentration of salts in the LUT can decrease the distance needed to screen a net charge, *i. e.* the Debye length. As a consequence, C_{DL} will be increased and α decreased. The dependence of α on the salt concentration in the LUT has two consequences: (i) the sensitivity to pH could be reduced for high molarities of non-hydrogen ions and (ii) the sensing layer could show a parasitic sensitivity to non-hydrogen ions, as the coefficient of ΔpH_B in equation 1.19 will vary. However, given a sufficiently high value of β_s , the effect of the variation of C_{DL} can be neglected and both sensitivity and selectivity of the sensing layer can be maintained. In [60], Bergveld reported a set of measurements showing the response of ISFETs with different sensing layers to a range of NaCl concentration in the LUT. The experimental data demon-

Chapter 1. Introduction

strated that the V_{th} of devices with a Ta_2O_5 gate was almost completely insensitive to changes in the NaCl concentration, while for all the other dielectrics tested (SiO_2 , Si_3N_4 and Al_2O_3) V_{th} was observed to grow for higher NaCl concentrations.

For the fabrication of the devices used in this work, as will be explained in Chapter 2, we employed the facilities of the Center of Microtechnology (CMi) in the EPFL campus, in which Ta_2O_5 is not available. Therefore HfO_2 has been chosen instead. A set of measurements over a range of NaCl concentration from 1 to 100 mM (Figure 1.16) showed that this material featured properties close to those of Ta_2O_5 .

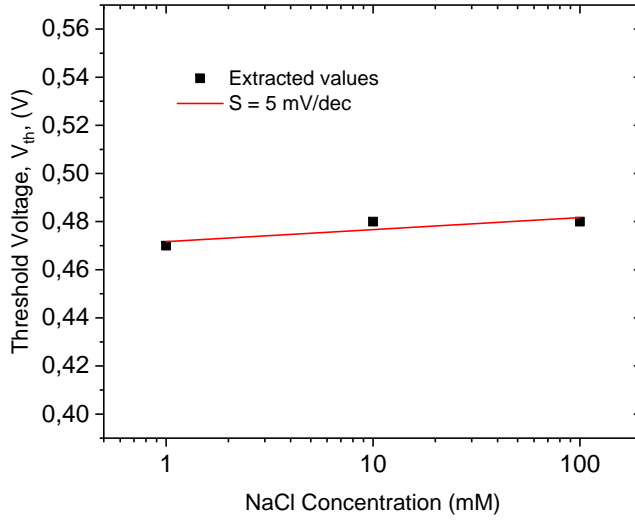


Figure 1.16 – Sensitivity of an ISFET with an HfO_2 sensing layer for various NaCl concentrations.

These results are coherent with those reported in [63], where a NaCl sensitivity close to zero has been reported for HfO_2 even at extremely high molar concentrations (up to 1 M).

If the sensing surface discussed is the gate oxide of a transistor, then we need to modify Equation 1.2 to keep into account the contribution of the ions in the LUT. The new equation will read:

$$V_{th} = V_{REF} - \Psi + \chi^{sol} - 2\Phi_f + V_{FB} + \frac{Q_D}{C_{OX}}, \quad (1.23)$$

where V_{REF} is the potential of the RE shown in Fig 1.12, which will be discussed in more detail later in this subsection, and χ^{sol} is the surface dipole potential of the gate oxide.

Given the theoretical limits of the $\Delta[\text{ion}^+] \Rightarrow \Delta V_{OX}$ and $\Delta V_{OX} \Rightarrow \Delta I_D$ conversions, it is possible to define the cumulative upper sensitivity limit Max_S for the $\Delta[\text{ion}^+] \Rightarrow \Delta I_D$ one. Max_S will be given by the ratio of the thermionic limit and the Nernst limit, as shown in Equation 1.24:

$$Max_S = \frac{59 \text{ mV/pH}}{59 \text{ mV/dec}} = 1 \text{ dec/pH} \quad (1.24)$$

which states that the theoretical maximum sensitivity achievable by an ISFET amounts to a

tenfold variation in I_D for each pH point of variation or, equivalently, for each tenfold variation in the ion concentration. The complete ideality factor $S_{out} \leq 1$, indicating how much a real device approaches this theoretical limit can also be defined from the two ideality factors n and α introduced up to now:

$$S_{out} = \frac{\alpha}{m}. \quad (1.25)$$

S_{out} will be equal to one only if both transduction are ideal. This parameter will be treated again in Chapter 4, where the possibility of reducing m to values smaller than one using Negative Capacitance will be studied.

The Reference Electrode

One of the most challenging tasks when fabricating an ISFET-based sensor is the production of the Reference Electrode.

The RE is an essential component for any sensing device exploiting potentiometry: it is used to apply a definite bias to the LUT. This cannot be done by simply immersing a standard metal electrode (*e. g.* one made of a noble metal to prevent corrosion) in the liquid, because part of the applied potential would drop at the electrode-electrolyte interface, so that the relation between the liquid potential and the applied potential would not be linear.

To solve this issue, special electrodes are employed in which reversible reactions can happen at the surface, so that a current can be generated to compensate the interface potential [61]. In this work, we employed the broadly established Ag/AgCl RE in which, at the surface, the following reaction can be observed:



Regardless this strategy, a simple AgCl electrode wouldn't be able to provide a stable potential in time and for a wide range of Cl^- concentration in the solution. The first issue comes from the AgCl solubility in water: its solubility product constant K_{sp} , defined as the equilibrium dissociation constant K_c multiplied by the number of compound moles in a liter of compound (Equation 1.27), is 1.8×10^{-10} , meaning that about 1.9 mg of AgCl will dissolve in one liter of water at room temperature [64].

$$K_{sp} = K_c[AgCl] = \frac{[Ag^+][Cl^-]}{[AgCl]}[AgCl] = [Ag^+][Cl^-] \quad (1.27)$$

After a certain operation time, the AgCl on the electrode surface would be completely depleted, leaving the bulk silver exposed.

The second issue comes from the fact that the interface potential with the LUT will depend on the concentration of Cl^- ions in the liquid, according to the Nernst equation.

To solve both of these issues, the AgCl electrode is usually immersed in a Cl^- saturated solution. This solution is connected to the LUT through a structure (*e. g.* a porous membrane) able

to allow potential contact while preventing physical mixing, so that the saturated solution doesn't get diluted and the LUT doesn't get contaminated.

A deeper insight on the RE will be reported in Chapter 3, where a miniaturized and fully integrated sweat-sensing system, the *Lab-On-SkinTM*, will be introduced.

1.3.3 Choice of the FD technology

As shown previously, even narrowing down the choice of sensing technology to FD ISFETs, we still have a number of solutions from which we need to determine the most convenient one. The main parameters to be taken in to account when designing a sensor are the sensitivity (therefore SS and gate sensitivity), the sensing range (improved by a high I_{ON}/I_{OFF} ratio), the accuracy (dependent on the stability), the resolution (defined as the inverse of the Signal to Noise Ratio, SNR) and the Limit Of Detection (LOD).

In terms of electrostatic coupling, especially with gate lengths $> 1 \mu\text{m}$, so that no short-channel effect appears, all the systems are pretty much equivalent, all reaching a SS close to the thermionic limit and a satisfying I_{ON}/I_{OFF} ratio $> 10^6$. For what concerns the gate sensitivity, it has been reported [65] that the NW and finFET architectures would offer better performances because of the concave surface formed where the walls of the channels intersect the substrate surface. The theory behind this claim is that the more the liquid surrounds the surface the stronger the detrimental double-layer capacitance screening will be, so that a concave surface is more sensitive than a convex one. Due to the abundant literature on planar FETs reaching nearly-Nernstian sensitivity [66–68] and to the difficulty in finding more works confirming this claim, the weight of this information on our decision has been limited. The literature on the influence of the device geometry on the V_{th} drift is limited and focused on extended gate configurations, for which it has experimentally been found that a large gate area is beneficial [69, 70]. The most widely reported solution for reducing the threshold drift, anyhow, consists in avoiding the employ of SiO_2 and Si_3N_4 as sensing dielectrics, since layers made of these materials tend to absorb the ions of the LUT and slowly change their capacitances, generating a monotonic drift in the current values measured over time [71]. Denser oxides, such as HfO_2 and Al_2O_3 , on top of all the previously mentioned advantages, show a much lower permeability to ions, providing superior stability characteristics. It has also been reported that a gate stack composed by a high quality thermal SiO_2 layer protected by an HfO_2 layer would show the maximum stability in water in terms of dissolution rate, ensuring a long life-time of the wearable device [72].

Given the reduced influence of geometrical properties on the characteristics mentioned so far, the choice of our design has been based solely on the basis of SNR and LOD requirements. Being the sensitivity of the devices, as stated, pretty much independent on their geometry, optimizing the design to increase the SNR consists essentially in minimizing the sources of noise. These can be listed as [73]:

- Thermal noise due to Electrolyte

- FET thermal noise, given by the random motion of electrons in the semiconductor.
- FET flicker noise, related to the number of oxide-trap-induced carriers and to the correlated surface mobility fluctuation mechanism.

In [73] these contributions have been modeled assuming an ideal (noiseless) RE and individually evaluated using HSPICE simulations. All of them showed a decreasing power for wider channels, hinting that, in terms of sensing resolution, ribbon-FETs would make the ideal candidates for our sweat-sensing system. These results have been experimentally confirmed by [74] and [75]. The last requirement to be considered is the LOD of the sensor: we must choose a technology able to detect even the minimum concentration of target markers we can expect to find in our analyte. The LOD dependence on the geometry of the sensing area has been studied by Pradeep Nair and Muhammad Ashraful Alam in [76], giving an intuitive explanation to an already known phenomenon: it is in fact common knowledge in the sensor field that the LOD of nanowires is orders of magnitude lower than that of planar surfaces, for a given measurement time. In [76], this is explained from the point of view of the time statistically needed for a biomarker in a liquid to diffuse to the receptor, and therefore be measured. This time is related to the dimensionality of the sensing area: a suspended nanowire is capable of receiving markers from all directions, while a planar surface benefits only from thermal diffusion in its perpendicular direction. Considering a measurement time compatible with the purpose of health monitoring (about 100 seconds), typical LODs for a nanowire would be in the hundreds of femtomolars, while, for a planar device, the LOD would be around one nanomolar. This order of magnitude, anyhow, is largely compatible with the physiological concentration of most of the relevant biomarkers in sweat: as stated at the beginning of this chapter, Na^+ , K^+ , NH_4^+ , lactate, ethanol, urea and glucose concentrations are all in a range between several μM and several mM, which can easily be detected in less than one second even with a planar sensor. Given the aim of this work, therefore, wide ribbon-FETs have been the technology of choice, sacrificing the lower end of the LOD to achieve a better SNR and therefore a better resolution.

In future works, if other relevant molecules present in trace level in sweat (such as cortisol, neuropeptide Y and interleukin 6) will be targeted, nanowire technology should be considered. The performances requirements which have determined our technology choice are summarized in Table 1.2.

1.4 Summary

In this introductory chapter we have seen how sweat is emerging as an extremely promising fluid of interest for future diagnostic applications, mainly because of its easy accessibility without resorting to invasive testing.

The low secretion rates observed in at-rest and normal temperature conditions, however, are not compatible with colorimetric sensing and electrode-based potentiometric sensing,

Chapter 1. Introduction

Requirement	Advantage	Technological choice
Small footprint	enables at-rest monitoring	ISFETs
High pH sensitivity	strong signal	HfO ₂ as gate dielectric
Low salt sensitivity	low cross-sensitivity	HfO ₂ as gate dielectric
Low drift	good time stability	HfO ₂ as gate dielectric
Steep SS	strong signal	FD technology, long devices
High SNR	good resolution	ribbon-FET technology

Table 1.2 – Performances requirements and related technology choice.

hinting that ISFETs, thanks to their extreme scalability, could represent the best choice for continuous monitoring.

Technological considerations in terms of power consumption, sensing and stability have suggested that the best baseline FET for continuous monitoring of sweat would be a FD SOI ribbon FET featuring an HfO₂ dielectric layer.

In the next chapters of this thesis we will describe:

- The design, fabrication and characterization of a FD SOI ribbon FET adapted for sensing purposes;
- The integration of the fabricated sensor in a complete system embedding functionalization layers, a set of miniaturized REs and a passive capillary microfluidics able to collect sweat from the skin, drive it in contact with the sensing gates of the ISFETs and collect it in a capillary pump, able to regulate the microfluidics flow rate;
- The application to our ISFETs of an emerging strategy for the steepening of the FET SS, with consequent improvement of the current sensitivity S_{out} : the Negative Capacitance.

2 Technological development and characterization of the ribbon-ISFET

The ribbon-FET technology has been chosen in agreement with the constraints and the reasoning exposed in the previous chapter.

The geometry of the envisaged structures is wide enough to be compatible with cheap and fast photolithographic steps, as opposed to finFET or nanowire technology which would have required the employ of e-beam lithography to comply with the nanometric dimensions. The fabrication process remains nevertheless challenging, as the fabrication of highly performant, homogeneous and reliable FETs requires many steps, some of which (especially the high temperature ones) potentially able to degrade the devices beyond recovery. Furthermore, the ultra-thin silicon layer, required to achieve the Full Depletion condition, poses some relevant technological challenges, such as the difficulty in achieving a high doping level and to produce low-resistance ohmic contacts on it. On top of these challenges, our second FET batch employed SOIs featuring an ultra-thin BO_x, required to improve the backgate control, which can be removed if an aggressive procedure is run on the devices while it is exposed, or if the silicon etching is not perfectly controlled.

In this chapter, we are going to present the two FET batches produced for this thesis, underlying the small corrections introduced between the first and the second, to comply with the observed issues. After a first overview on the TCAD simulation performed to design the devices and tune the doping procedure, the main fabrication steps of our process flow will be presented. A more in-depth analysis of the most relevant and challenging steps will follow. Finally, the FETs layout on the chip will be presented and the performances of the two batches compared. All of the fabrication steps, except for the implantation procedures, have been performed in the cleanroom of the Center of MicroNanoTechnology (CMi) in the EPFL campus.

2.1 TCAD simulations for design and process optimization

Sentaurus TCAD has been employed to tune the parameters of the ribbon-FETs: in particular, the effects of varying the length of the channel, the doping level of Source and Drain and the thicknesses of the gate dielectric and of the silicon channel have been investigated. The simulation code is reported in Appendix A.1. In Figure 2.1 the effects on the transfer characteristics

of sweeping the values of each of the mentioned properties are shown.

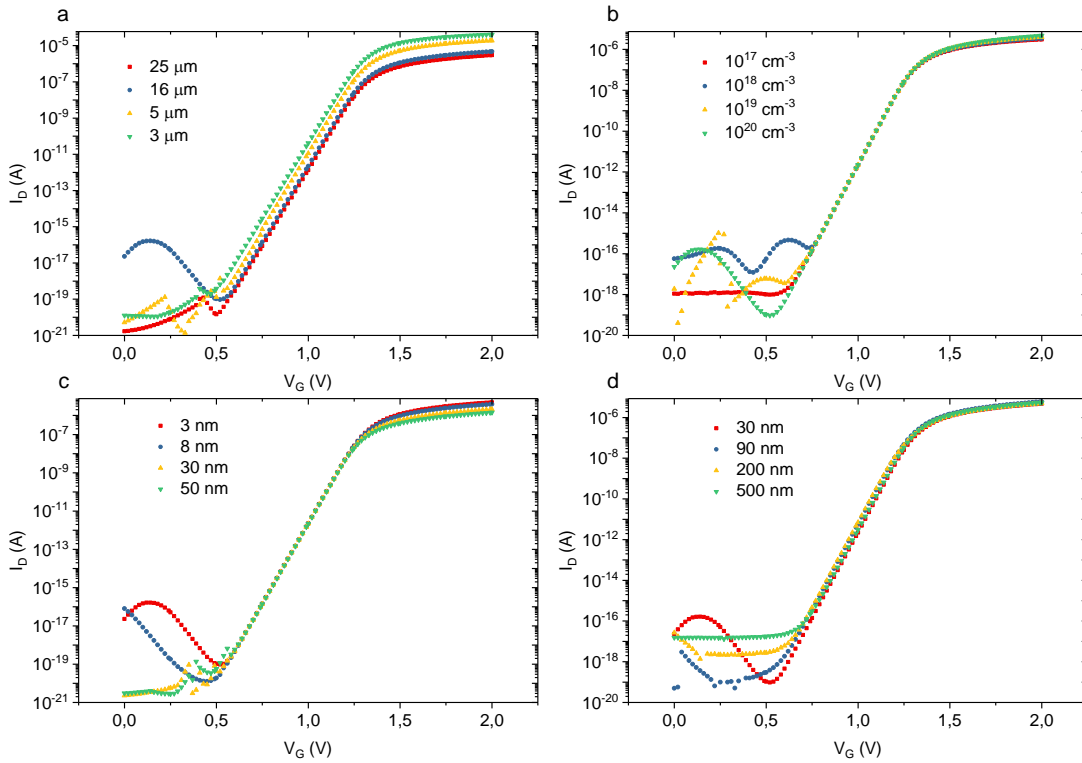


Figure 2.1 – Simulated effects on the transfer characteristics of varying a) the channel length, b) the S/D doping level, c) the thickness of the HfO₂ layer and d) the thickness of the SOI.

It can be noted that, even though some strategies such as thinning the silicon layer, thinning the gate oxide or making a longer device are known to improve the final SS of the device, such effects couldn't be observed in our simulations, were only minor effects, mostly regarding the *ON* current value, are shown: this is because the selected structure, being immune to short channel effects (for a smooth contact with the analyte it is better avoiding sensing areas shorter than a few microns) and leakages through the bulk, can easily achieve a nearly ideal transfer characteristics, beyond which any technological improvement is ineffective. In our fabrication procedure, however, we decided to still implement most of the recommended strategies for device optimization: the silicon layer has been thinned down to 30 nm, the HfO₂ layer deposited by ALD has been limited to 3 nm of thickness and the channels have been made 16 μm long.

These precautions have been taken since the devices simulated by Sentaurus TCAD are supposed ideal, with perfect materials and no fabrication issue, therefore we decided to provide a few expedient to reduce the effects of real-world defects.

TCAD simulations have also been employed to tune the implantation parameters for doping: selecting the right implantation dose and energy, as well as the right doping element, is in fact crucial in order to achieve high doping levels in ultra-thin silicon without compromising its lattice crystalline structure and without damaging the underlying BOX.

2.1. TCAD simulations for design and process optimization

For this kind of simulation, Sentaurus TCAD employs a Markov Chain algorithm [77] in which each implanted ion moves according to a random walk dependent on its mass, its energy and the properties of the material in which it is implanted. Sentaurus is unfortunately not optimized for simulations in such a thin layer of silicon but, given the weak dependence of the device transfer characteristic on the doping level observed before, we decided that an approximation within one order of magnitude of the expected doping level could be suitable for our process. The simulation code is reported in Appendix A.2.

The starting values tested for implantation dose and energy have been the typical ones employed for reaching high doping levels in bulk silicon, therefore $2 \times 10^{15} \text{ cm}^{-2}$ and 25 keV [78] (Figure 2.2).

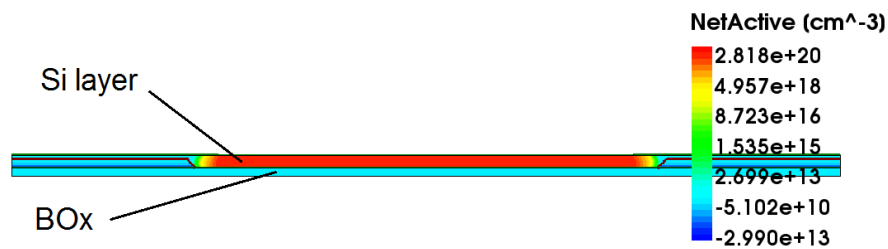


Figure 2.2 – Doping level simulated with a dose of $2 \times 10^{15} \text{ cm}^{-2}$ and 25 keV of energy.

From the output of this simulation, it might look like the parameters for bulk implantation are also appropriate for doping of thin SOI. What is not shown here, however is the damage sustained by the silicon and BOx in the process: to visualize it, we had the simulator plot the distribution of implanted atoms in the full structure, instead of just that of active doping in silicon (Figure 2.3).

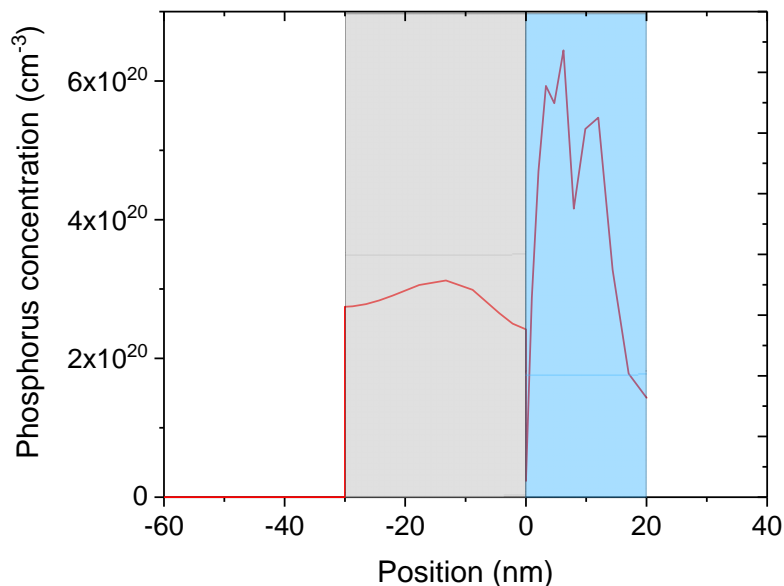


Figure 2.3 – Phosphorus distribution in the implanted area. The grey area represents the Si layer, while the light blue one the BOx.

It is clear from this image that the BOx has sustained great damages from the implantation process: the concentration of phosphorus ions is even higher than in the silicon layer, meaning that:

- The structural integrity of the insulating layer could be compromised, with the effect of allowing high leakages from the S/D contacts to the bulk of the substrate.
- The implanted silicon could be entirely amorphized, so that the lattice damage could not be healed with the annealing step.
- A large amount of charges would be stored in the BOx, possibly degrading the coupling of the backgate and introducing hysteresis in the measurements.

These issues are not unexpected: the parameters employed for this simulation, especially the implantation energy, are meant for a much thicker silicon layer without any BOx to damage underneath. We performed further simulations with decreasing energy to identify the safe energy value for this process (Figure 2.4).

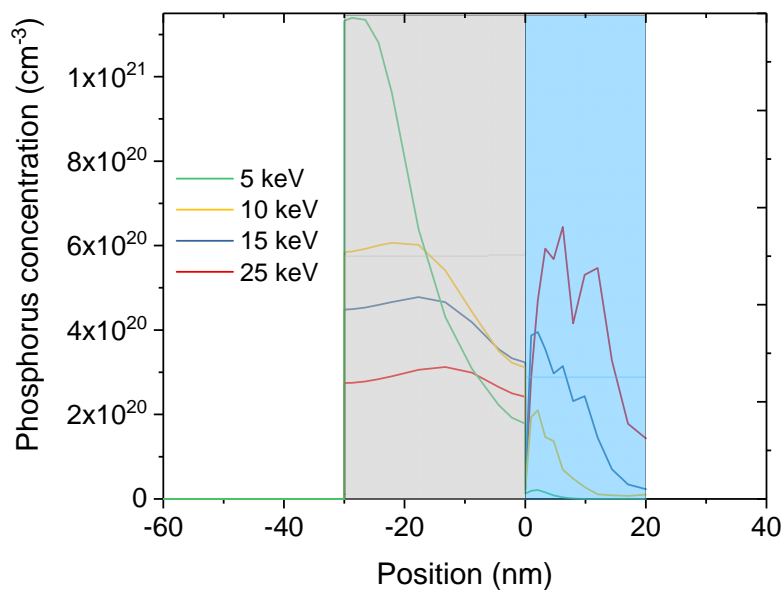


Figure 2.4 – Phosphorus distribution for different implantation energies from 25 to 5 keV.

The concentration of phosphorus ions in the BOx decreases rapidly for lower implantation energies, becoming almost negligible at 5 keV. At the same time we observe a change in the ion distribution inside the silicon layer, with the peak nearing the surface and increasing for lower energies. This is not surprising since, reducing the energy of the ions, fewer of them manage to reach deep positions in the substrate. This creates an unnecessarily high concentration of dopants in the silicon layer, allowing us to employ a safer implantation process by reducing the dose (Figure 2.5).

Reducing the implantation dose we can not only make the process increasingly safe for the

2.2. Cleanroom process flow for ribbon-FET fabrication

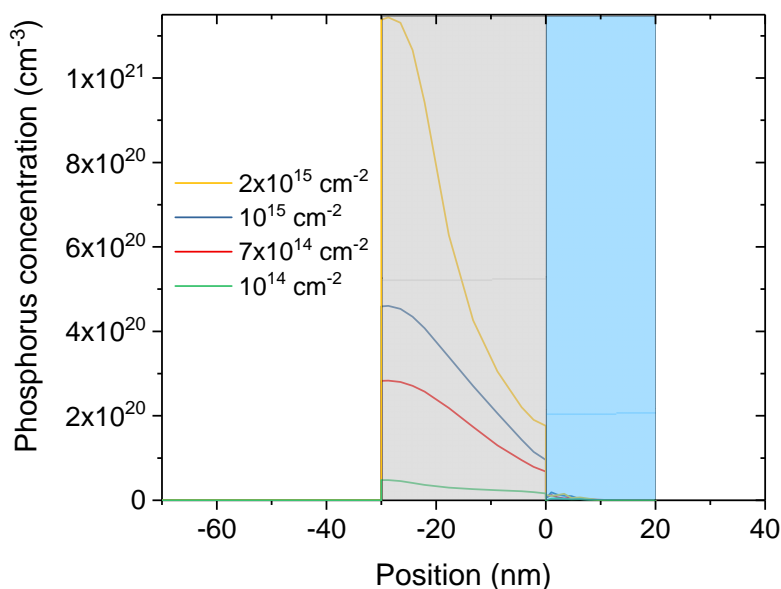


Figure 2.5 – Phosphorus distribution for different implantation doses from 2×10^{15} to 10^{14} cm^{-2} .

BOx, but also obtain a more uniform doping profile in the silicon layer. For this work, we finally decided to employ an implantation dose of 7×10^{14} cm^{-2} with 5 keV of energy. These results are coherent with the parameters reported in [79].

2.2 Cleanroom process flow for ribbon-FET fabrication

The complete process flow can be resumed in 25 steps, with 7 different photolithographic masks. The starting substrate has been an SOI for both batches, but with different parameters: in the first batch we employed an 88 nm thick SOI with a 145 nm thick BOx, while the second run employed a more advanced substrate, with silicon overlayer thickness of 70 nm and BOx thickness of just 20 nm. Both processes started by thinning down the silicon overlayer to 35 nm, through a single-step dry oxidation/wet etching process. The oxide thickness was set to 100 nm for the first batch and to 65 nm for the second and the wet etching has been performed in a 10:1 diluted HF solution (Figure 2.6).

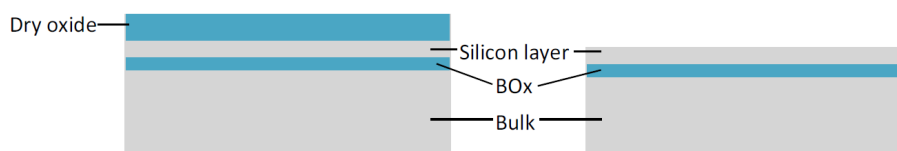


Figure 2.6 – Silicon thinning to ensure Full Depletion condition.

Chapter 2. Technological development and characterization of the ribbon-ISFET

After this step and the photolithographic definition of the alignment marks, the implantation regions have been defined with a second photolithography step (Figure 2.7) and the SOIs have been shipped to IBS in France for the phosphorus implantation, with the parameters established through the TCAD simulations. As expected, the implantation process partially burned and hardened the photoresist mask: the removal required a 20 minute long oxygen plasma etching (Tepla Gigabatch plasma stripper, power: 600 W, O₂ flow: 400 sccm, pressure: 0.8 mbar) followed by a 10 minute wet etching in hot remover 1165 (temperature: 70°C). An annealing step (10 minutes at 600°C followed by 20 seconds at 900°C) has been performed with a Jipelec Jetfirst 200 to recrystallize the implanted silicon and activate the dopants.

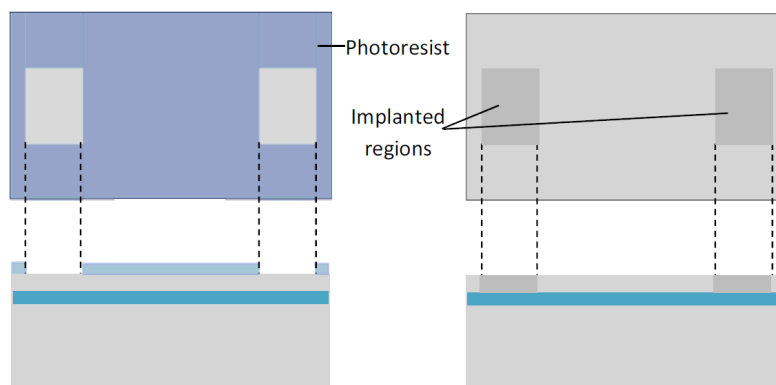


Figure 2.7 – Phosphorus implantation for the Source and Drain areas.

A third photolithographic mask has been used to define the physical ribbon-like shape of the devices (Figure 2.8). For the first batch, the channel width has been ranged from the minimum resolution achievable with standard photolithography in the CMi cleanroom (1 μm) up to 4 μm , while for the second it has been kept to 6 μm for all the devices.

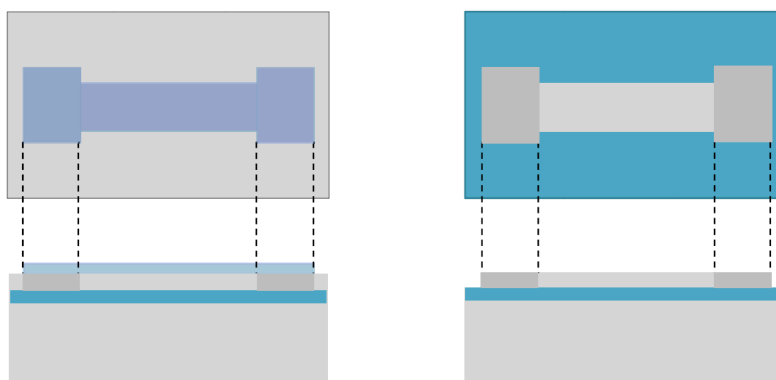


Figure 2.8 – FETs geometry photolithographic definition with landing on BOx.

Etching the thin silicon layer without damaging the BOx required, especially in the second

2.2. Cleanroom process flow for ribbon-FET fabrication

batch, a highly controllable procedure, featuring as well an extreme selectivity for silicon with respect to silicon dioxide. In this work, we employed a plasma etching based on HBr chemistry, which will be discussed in more detail in subsection 2.4.2.

The gate dielectric stack is formed with two separated steps: first a short dry oxidation is used to grow a thin layer of silicon dioxide and then Atomic Layer Deposition (ALD) is used to deposit 3 nm of HfO_2 , an high-k dielectric characterized by excellent electrical and sensing properties (Figure 2.9). The silicon dioxide layer takes the name of *pedestal oxide* and is used to provide a better interface with the hafnium dioxide, reducing the number of trapped charges and improving the performances of the sensor, as will be discussed in subsection 2.5.1.

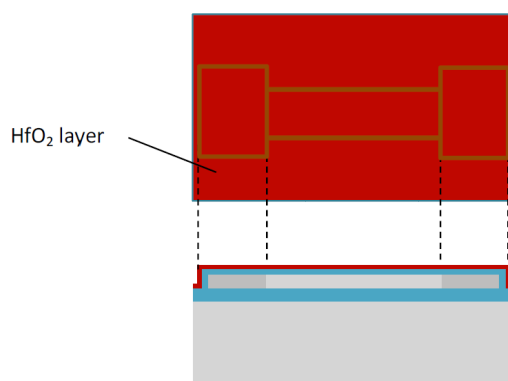


Figure 2.9 – Dielectric gate stack formation.

The main difference between the first and second batch consists in the metals used for the electric contacts: the first batch employed an aluminum alloy containing 1% of silicon for both S/D and Gate, while the second had contacts made of platinum (Figure 2.10). A detailed discussion on the choice of metals will be carried out in section 2.6.

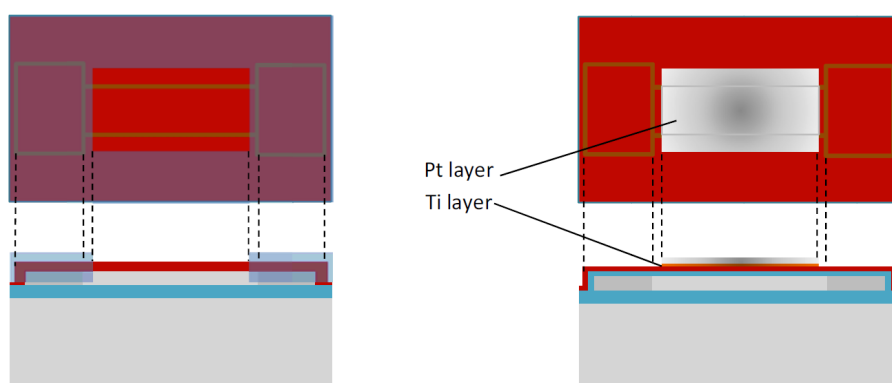


Figure 2.10 – Gate metal deposition.

For the second batch, however, platinum could not be used alone as metal for the gate contact,

as its interface with HfO_2 is poor and test devices fabricated without an interface metal have shown a very high subthreshold swing due to the resulting inefficient gate coupling. For this reason, a thin titanium layer has been sputtered just before the platinum deposition. The sputtering processes have been carried out employing an Alliance-Concept DP 650 sputterer and the structures have been defined by lift-off. A low temperature annealing guaranteed a good contact between metal and dielectric.

In order to form electrical connections with the Source and Drain regions, photolithography has been used to define etching areas on the dielectric layer (Figure 2.11). In order to reduce the contact resistance, the openings are made as big as possible, compatibly with the alignment margin required to avoid the risk of damaging the channel or the BOx. The dielectric etching is performed with an ultra-low Ion Beam Etching (IBE).

After the etching, the same photoresist mask is employed for the lift-off of thin platinum "needles" on the exposed silicon, in order to prevent the growth of oxide during the steps between the dielectric etching and the metal lines deposition. The importance of this strategy will be discussed in section 2.6.

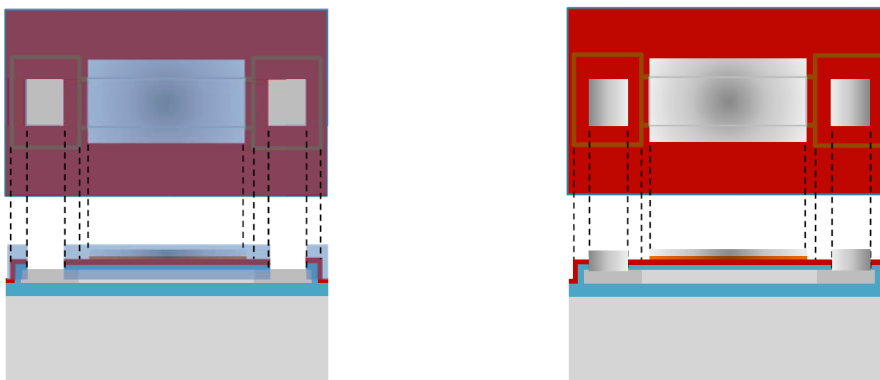


Figure 2.11 – Source and Drain contact opening and platinum needle deposition.

Test devices characterized at this stage, in the second batch, were affected by high leakages, whose origin has been identified in the current passing from the metal lines to the bulk of the SOI. The ultra-thin BOx, in fact, has been weakened by the etching and cleaning steps performed up to this point. In particular, the BHF-based RCA cleaning performed before pedestal oxide growth resulted much more aggressive than foreseen. The metal lines connecting the Source, Drain and Gate contacts of the devices to the external pads of the chip have huge areas, from the standpoint of microelectronics, therefore even the low current leaking through the dielectric layers had a huge influence. To remove this issue, a passivation layer made of sputtered silicon dioxide has been defined via photolithography and lift-off (Figure 2.12). This layer, though only 50 nm thick, has proven extremely effective for suppressing the line leakages.

The aluminum silicide or platinum lines have been deposited by sputtering and lift-off.

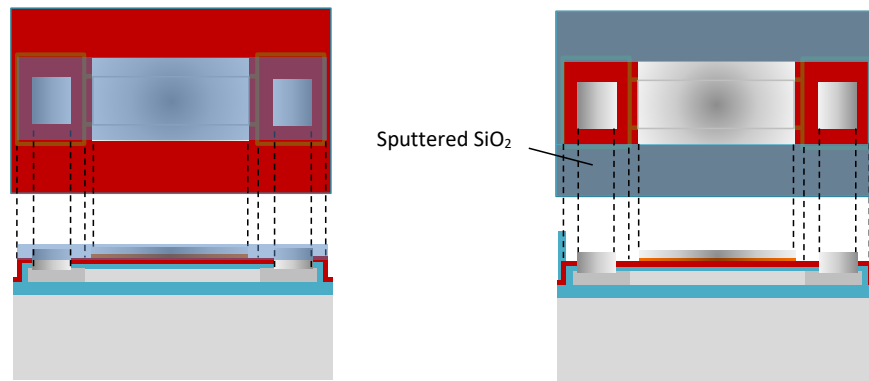


Figure 2.12 – Silicon dioxide passivation.

To conclude the process and allow using the ribbon-FETs as sensor, a passivation layer made of SU-8 has been spin-coated and photolithographically defined (Figure 2.13), so that only the sensing areas, *i.e.* the gates of the FETs, and the contact pads on the sides of the chip are exposed. An hard-baking step at 180°C improved the SU-8 adhesion and concluded the fabrication process.

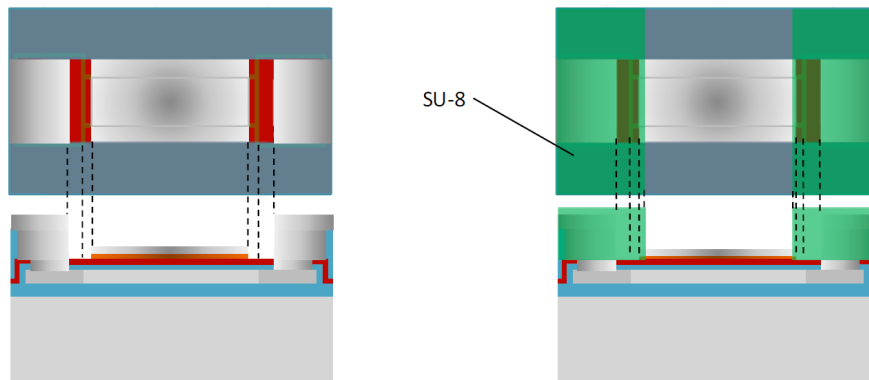


Figure 2.13 – Metal lines lift-off and SU-8 passivation.

2.3 Photolithographic processes

Two different photolithographic procedures are available at CMi: direct laser writing and Cr-mask mediated writing.

The first procedure, based on the *Heidelberg Instruments MLA 150, photoresist laser writer*, employs a laser scanning the wafer and precisely exposing the photoresist (AZ-ECI 3027, in most of the steps performed) in the zones indicated by the GDS file loaded. Developing the exposed photoresist, the areas weakened by the laser are removed and the resulting pattern

can be used for etching or lift-off processes.

The procedure involving a Cr-mask is based on the *Heidelberg Instruments VPG200, photoresist laser writer* and the *Süss MA6/BA6, double side mask aligner and bond aligner* and is somewhat more complex, as the laser doesn't write directly on the working substrate but instead on a mask made of a glass substrate, a chromium layer and a photoresist layer on top. The GDS pattern, created with L-edit software, is inverted, mirrored and transferred on the photoresist of the Cr-mask with a procedure analogous to the one explained before, followed by a Cr wet etching step and by the subsequent removal of the non-exposed photoresist. At this point, the mask can be used as a filter to expose the full working substrate at once with an Hg-lamp. This second process, though less simple, is preferred when many substrates need to undergo the same photolithographic patterning, as it allows performing the time-consuming laser writing only once.

In this work, especially for the second batch, the direct writing has usually been preferred for three reasons: the first is the limited number of wafers to process, which amounted to two for the first batch and to four at the beginning of the second. This made the extra time needed to perform the writing on multiple substrates too small to justify the costs and work related to the fabrication of a Cr-mask. The second reason regards the alignment procedures: when multiple layers need to be written to define a single structure (*e.g.* implantation areas, physical shape, gate metal, S/D openings, oxide passivation, metal lines contacts and SU-8 passivation, as in our case) it is fundamental that all of them are aligned within a well-defined tolerance. This is why one of the very first steps of any fabrication process is the definition of the *alignment marks* (Figure 2.14) which will be used before each photolithographic step to ensure the correct positioning of the photoresist openings.

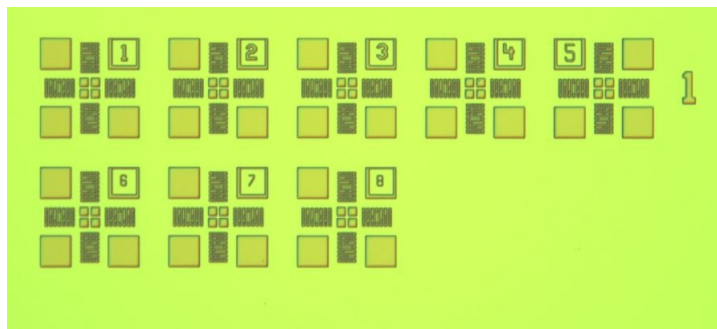


Figure 2.14 – The set of alignment marks employed in our batches. The same elements are arranged in mirrored position on the two opposite sides of the wafers.

The procedure of manually aligning a Cr-mask to these structures can be long and difficult, especially when a sparse design is employed and the mask is consequently mostly opaque, making it challenging to find the alignment marks on the substrate being processed. Alignment on the MLA 150, instead, can be done automatically or with a computer-assisted manual procedure, with advantages in terms of time consumption and precision.

The last reason for which direct writing has been usually preferred is that some steps (especially the ones involving contacts on thin silicon) needed to be tested on a few chips before

processing the full wafer, meaning that some single-use design, featuring lift-off openings only for a set of test devices, had to be employed. After some fine-tuning of the exposure parameters to comply with the SOIs, whose reflective properties are slightly different from the ones of bulk silicon wafers, clean and well-defined structures could be obtained. In Figure 2.15 we can observe photolithographically defined single and triple-channels ribbon-FETs, with dielectric opening and the Pt "needle", together with the photoresist mask which will be employed for the metal lines lift-off. The alignment margin is set to withstand $1\mu\text{m}$ of misalignment per layer (therefore $2\mu\text{m}$ of margin, to comply with the worst case scenario of opposite, maximum misalignment between two layers), but, as can be seen, the actual misalignment achieved with the MLA 150 is far below that limit.

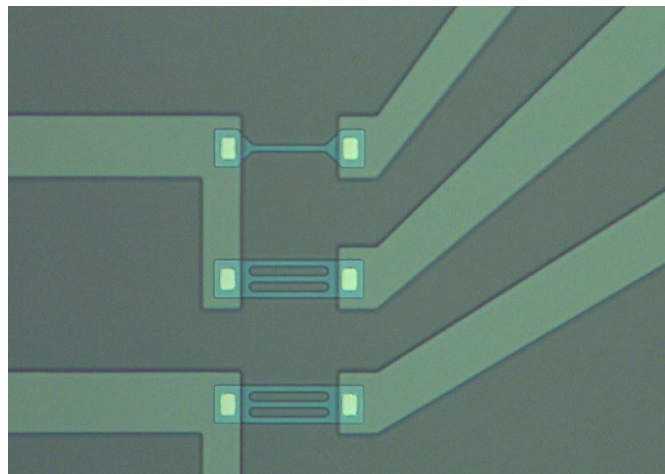


Figure 2.15 – Example of photolithography results.

The photolithographic technique which is usually recommended for lift-off employs a double layer of resist: the first is a non-photosensitive resist called LOR (Lift-Off Resist) 5A while the second is a normal positive resist such as AZ ECI [80]. The exposure and development processes are performed in a similar fashion as for standard photolithography but, during the development, after the exposed photoresist has been removed, the solvent is able to attack the underlying layer of LOR, creating a cavity extending beneath the AZ ECI layer. The resulting "T"-shaped structure allows depositing metal lines precisely and without wall coverage, generating the ideal conditions for lift-off (Figure 2.16).

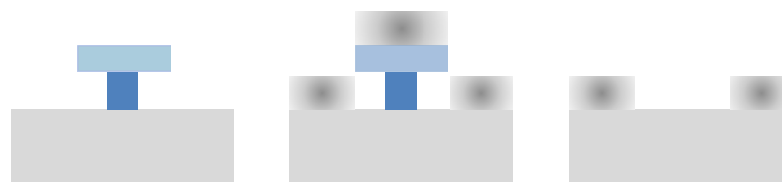


Figure 2.16 – Lift-off with LOR/AZ-ECI procedure.

Chapter 2. Technological development and characterization of the ribbon-ISFET

A downside of this procedure is that, if two lines need to be deposited close to each other, the two under-etches on the LOR could merge together, leaving a suspended layer of photoresist which would undergo delamination. To avoid this risk, throughout our process flow we have always employed standard photolithography for our lift-off photoresist masks. The issue of the resist wall coverage by the deposited metal, which could have prevented its dissolution and therefore made the lift-off procedure impossible, has been solved with the application of ultra-sounds to the Remover 1165 bath, which mechanically weakened the metal layer lying on the resist walls, allowing the solvent to penetrate.

This strategy, however, is not effective when the lift-off of a more rigid material is needed, such as the sputtered SiO_2 used for suppressing the lines leakages. For this step, we employed the nLOF 2020 resist. The advantage of nLOF with respect to AZ-ECI, for this procedure, is that nLOF is a negative resist, as opposed to the AZ-ECI family which is positive. This means that the chemical resiliency of the nLOF is not weakened by the UV light but rather increased, as further cross-linking between the molecules composing it is favored. The result, in terms of processing, is that we need to expose the resist in the areas which need to withstand the developing, instead of those to be removed. Since the resist is absorbing part of the UV light going through it, the bottom part of the exposed areas will be less cross-linked and less chemically resistant to solvent, therefore the etch rate will be higher at the base of the resist, which will create a reverse trapezoid shape, as opposed to the normal trapezoid shape observed in positive resist structures [81] (Figure 2.17).

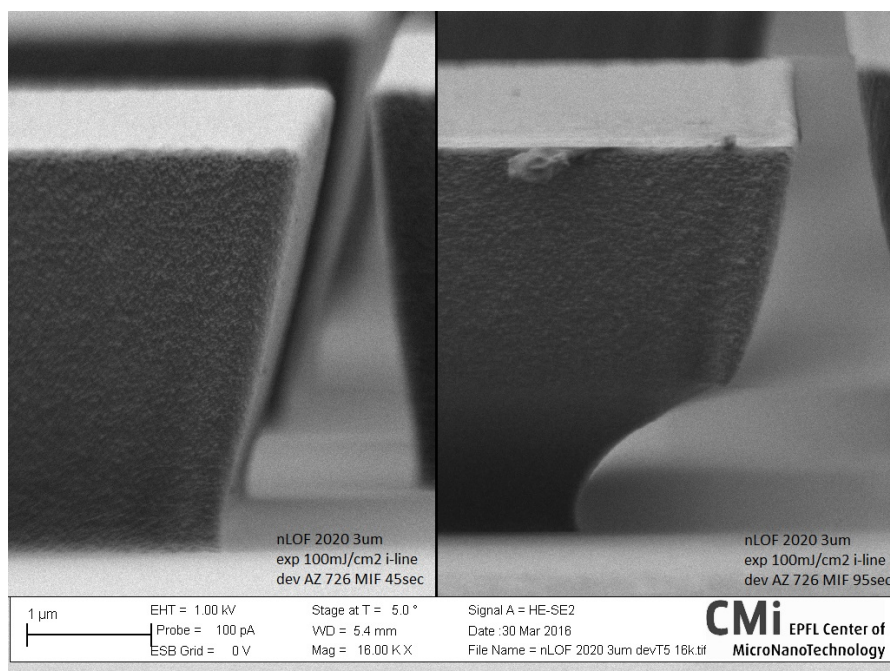


Figure 2.17 – Reverse trapezoid shape of the nLOF structures. Sample picture from CMI website.

This shape acts in the same way as the LOR/AZ-ECI stack, preventing the sputtered material

from covering the walls. Photolithography is used also to define the openings in the SU-8 polymer used for the passivation layer. SU-8 is a negative-type resist as well, therefore it was necessary to expose it everywhere but in the opening regions we wished to develop. Achieving a clean, well defined photoresist mask has proven more challenging when employing SU-8, mainly because, since passivation is performed as the last step of the process, many different materials, featuring different reflective coefficients, are found beneath the resist (Figure 2.18).

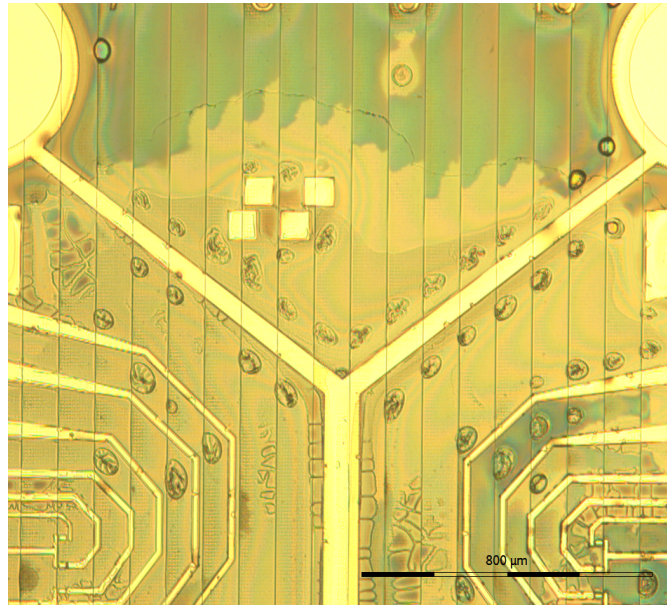


Figure 2.18 – Effect of different reflective coefficients in a non-optimized SU-8 process.

The most detrimental effect of this phenomenon is observed when small openings on platinum pads are needed: the highly reflecting metal is in fact able to deflect a sufficient portion of the UV energy (set to the high values needed for exposing SU-8 on silicon) in the supposedly unexposed areas of the resist. The result is that the minimum feature size in this process is drastically increased, and our smallest openings could not be defined (Figure 2.19).

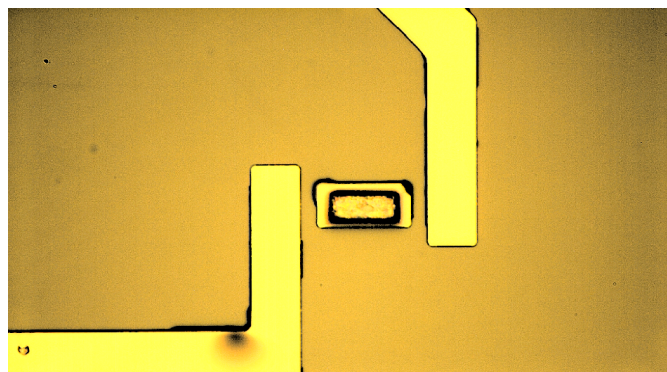


Figure 2.19 – A UV dose compatible with the SU-8 hardening on silicon is not compatible with the development of small structures on metal.

Chapter 2. Technological development and characterization of the ribbon-ISFET

In the end, achieving a stable and resilient SU-8 passivation layer required rising the UV dose, from the initial estimation of 100 mJ/cm², up to 440 mJ/cm² (Figure 2.20) and increasing the SU-8 openings critical dimension to 10 μm (Figure 2.21).

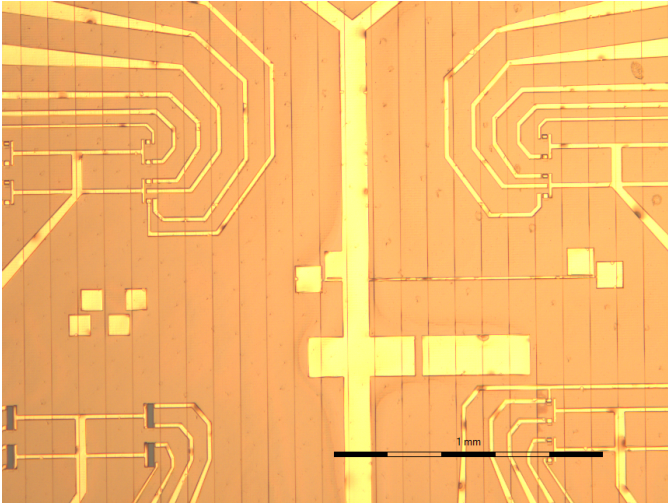


Figure 2.20 – Rising the UV dose allowed achieving a homogeneous SU-8 layer.

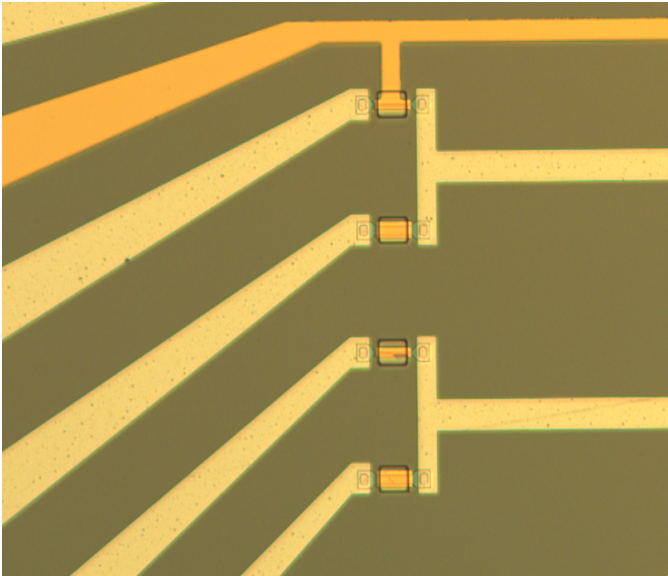


Figure 2.21 – Increasing the critical dimension of the SU-8 openings prevented the unwanted exposure effect.

2.4 Etching processes

Multiple etching steps are needed in the fabrication of our ribbon-FETs: from thinning down the silicon layer, to defining the shape of the devices to opening the deposited dielectric layers for contacts fabrication. Also removing the photoresist masks after each photolithographic step requires some form of etching.

Of the many different strategies for etching, each characterized by some advantages and some limitation, this process flow employs three: wet etching, plasma etching and physical etching. For each etching step, a specific procedure has been chosen according to its particular requirements. In the following subsections we briefly introduce each of them together with the steps in which they have been used.

2.4.1 Wet etching

Wet etching is arguably the simplest form of etching to implement: it consist in putting the material to be removed in contact with an acid, base or solvent able to dissolve it. With the exception of few cases, such as the etching of crystalline silicon in potassium hydroxide (KOH), this kind of etching is isotropic, meaning that the material is etched at the same rate in each region in which a contact with the etchant is provided. The resulting profile is therefore rounded and not fitting for structures requiring deep, vertical holes (Figure 2.22).

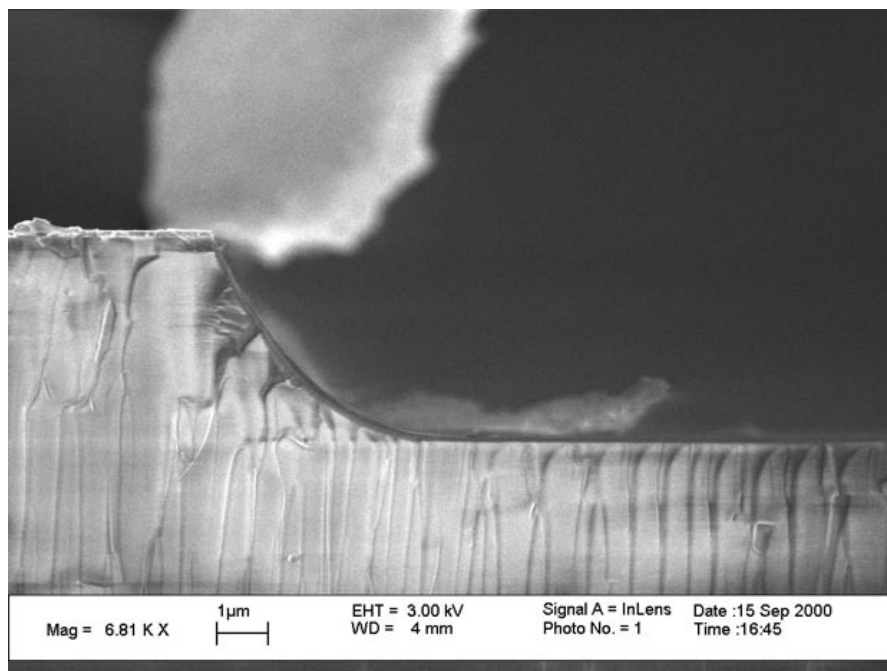


Figure 2.22 – Deep wet etching of Pyrex in HF. Sample picture from CMi website.

On the other hand, wet etching procedures are usually characterized by extreme selectivity between different materials and leave a smoother surface in comparison with both plasma

and physical etching. For these reasons, wet etching has been employed to thin down the silicon layer of the SOI wafers: dry oxidation (as we will see in subsection 2.5.1) is an extremely controllable process and silicon dioxide etching in diluted hydrofluoric acid (HF) leaves a smooth surface without any residual and without attacking at all the silicon.

For a few samples, also the openings on the gate dielectric stack for the definition of the S/D contacts have been produced with wet etching, instead of IBE. This choice, however, requires to keep in mind two issues: first of all, the etch rate of HfO_2 in HF-based baths is much lower than that of SiO_2 . The reported etch rate for dry SiO_2 in a 7:1 diluted Buffered HF (BHF) bath is of 86 nm/min, according to the CMi manual for the *Plade Oxide wet bench*, while our first-hand measurements on the HfO_2 etch rate (performed employing spectroscopic ellipsometry on a HfO_2 test layer before and after a 20 minute long etch) showed that it was of just 1.5 nm/min. The second issue to keep in mind is that diluted HF is not compatible with photoresist masks, as it is able to detach them after few seconds (Figure 2.23). For this reason, the buffered version of this etchant must be employed in this kind of processes, even though the addition of the ammonium fluoride (NH_4F) used as buffer generates a non-zero etch rate towards silicon.

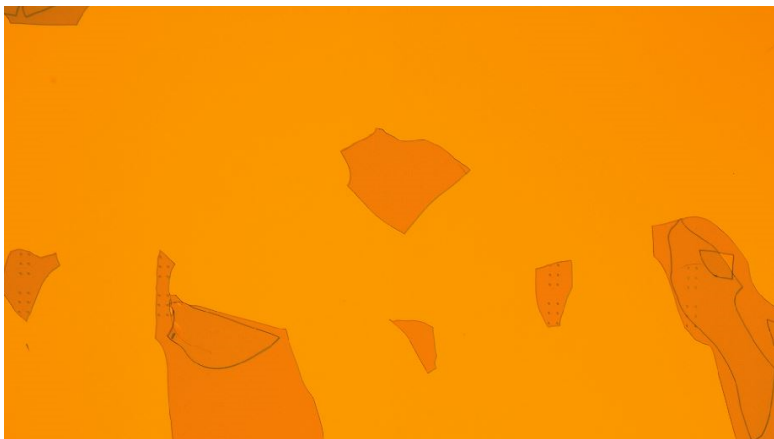


Figure 2.23 – Photoresist detachment due to a short HF etching on a test wafer.

In most cases, wet etching is employed for cleaning procedures. A typical example is the removal of a photoresist mask, which simply requires, as mentioned in section 2.2, a 10 minutes etch in a Remover 1165 bath heated at 70°C. More complex is the case in which a metal contamination has to be treated, such as the case in which inefficient or leaky metal lines need to be removed. This necessity occurred in both our batches, first with the AlSi lines, then with the Pt ones.

The removal of AlSi, being aluminum a soft and chemically reactive metal, is rather easy to achieve, but selectivity towards the other exposed materials has to be carefully kept into account, especially as the AlSi lines have been deposited with a thickness greater than 100 nm, while the other materials constituting our structures (Si, SiO_2 and HfO_2) have thicknesses between 3 and 30 nm. An excellent selectivity [82] can be achieved with a Piranha solution, obtained by carefully adding one part of 30% diluted hydrogen peroxide (H_2O_2) to three parts

of sulfuric acid (H_2SO_4) under strong stirring. The AlSi etching with this mixture is almost instantaneous (in a few seconds the lines are completely removed) and completely safe for the dielectric layers, as the mixture is strongly oxidizing. The removal of Pt lines is sensibly more challenging, as platinum is a noble and mostly chemically inert metal. Its removal requires the employ of a mixture made on purpose for noble metal such as gold, palladium and platinum: the aqua regia [83]. This etchant is composed by three parts of 37% diluted chloridric acid (HCl) and one part of 70% diluted nitric acid (HNO_3), to be poured in this order. Just like the piranha solution, aqua regia is unstable and after preparation is only active for a short time. Etching of Pt lines with aqua regia does not happen at a constant rate and in some cases we have observed complete removal of some sections of the lines before the etching of others could even start (Figure 2.24).

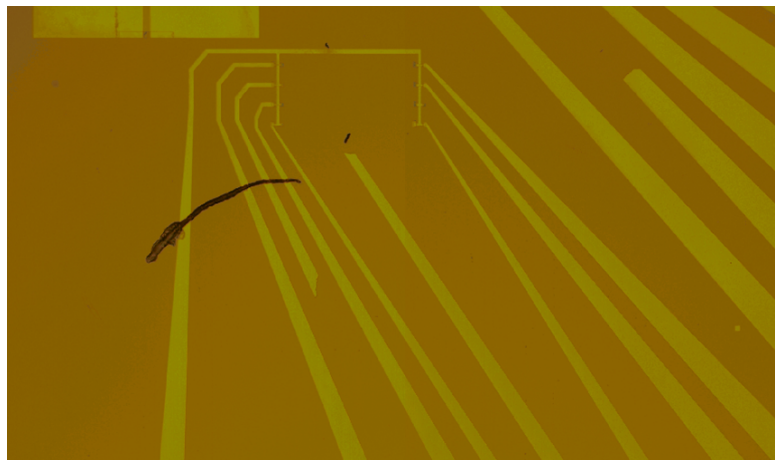


Figure 2.24 – Uneven etching of Pt in aqua regia.

The problem was solved by heating the solution to about 70°C , which led to homogeneous etch of the noble metal. Even though the etching process required several minutes, no etching of the dielectric layer has been observed. On the other hand, leaving such a strong oxidizer in contact with the wafer for a long time had the effect of increasing the thickness of the pedestal oxide beneath the HfO_2 layer, further thinning the SOI layer.

2.4.2 Plasma etching

Plasma etching is a process based on chemical reactions, like the wet etching, and therefore is able to provide selectivity between materials. At the same time, however, the flux of reactive ions can be controlled and directed applying a potential to the surface to be etched, which allows achieving a directional, anisotropic etching profile and therefore vertical walls [84] (Figure 2.25). The Inductively Coupled Plasma (ICP) is generated by an antenna (usually a coil encircling the plasma chamber) generating a radiofrequency electromagnetic signal at 13.56 MHz. This frequency is too fast to influence the heavy nucleus of the species in the chamber, but it can excite the external electrons, removing them from their atoms and making them

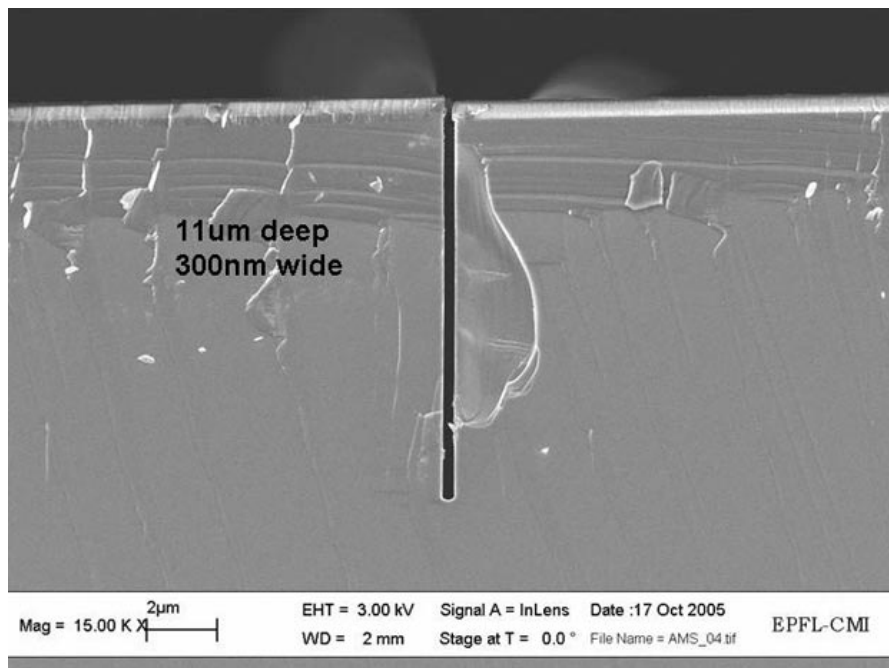


Figure 2.25 – High aspect ratio plasma etching of silicon. Sample picture from CMi website.

collide with the surrounding gas, creating further electron-ion couples. The bias applied to the material to be etched will drive the charged species towards its surface, where adsorption phenomena will take place and, if a chemical reaction producing volatile byproducts is possible, etching will commence.

The possibility of achieving both directional and selective etching has made plasma an irreplaceable tool for microelectronic fabrication but at least two limitations have to be kept into account: first of all, this kind of process is usually meant for deep etching with high etch rates, therefore shallow and controlled etching within a material is challenging. Secondly, the selectivity can not reach the near-to-perfect values shown by wet etching processes, therefore any process requiring to land on a ultra-thin (few nm thick) layer of stopping material is risky. Plasma etching of inorganic material has been employed twice in our process flow: first of all, deep, vertical alignment marks have been etched using a *Alcatel AMS 200 SE, dry etcher, fluorine chemistry*, with a sulfur esafuoride (SF_6) plasma. The geometry of the ribbon-FETs has instead been defined using the *STS Multiplex ICP, dry etcher, chlorine and bromine chemistry*, with a hydrogen bromide (HBr) plasma. Though the etch rate of this recipe for Si (220 nm/min) was extremely high, considering the thickness of the SOI, this plasma features an excellent selectivity, » 50, with respect to SiO_2 , allowing to precisely land on the BOx with limited damages to it.

Another plasma-based process which has often been employed, especially in the first batch, is the oxygen plasma cleaning used to remove the organic photoresist layers after a photolithographic step. In CMi, this process is performed in a *Tepla GiGAbatch, dry etcher, oxygen plasma*. The use of this procedure, however, has been limited since we noticed that, when performed

on silicon, the adsorbed oxygen tends to react forming a compact layer of oxide, with various consequences. Figure 2.26b), in the next subsection, shows the growth of unwanted SiO_2 in the dielectric openings for Source and Drain, which can degrade the electric contact.

2.4.3 Physical etching

Ion Beam Etching (IBE) is a process in which no chemical reaction is required: the etching of the substrate is achieved by simply bombarding the surface with atoms of a noble gas (Ar). The selectivity between materials is obviously much lower than for chemistry-based process and only related to physical properties of the material under etch, so that it can't be engineered by tuning the beam parameters [85].

The procedure offers nevertheless some capabilities which would be harder to achieve with the other methods: IBE features a much higher control on the etch rate, which can be reduced to few nanometers per minute, and, employing a mechanical shutter for instantaneous turn-off of the etching beam, it is possible to perform extremely precise shallow etches.

In CMi, the IBE is performed with a *Veeco Nexus IBE350, ion beam etcher, argon source*, in which the argon ions of an ICP are extracted and accelerated with a three grid system towards the surface to be etched. After acceleration, a plasma bridge neutralizer inserts electrons in the system, turning back the positively charged Ar ions in to neutral atoms, before they impact the surface. This step prevents charging effects which could influence the etching. The substrate is kept tilted so that the etched material is deflected away from the surface, limiting the redeposition effects. A slow rotation is imposed to improve uniformity.

In this process, IBE has been used to etch the SiO_2 - HfO_2 dielectric stack to fabricate the contacts for Source and Drain. Figure 2.26a) shows a Scanning Electron Microscopy (SEM) image of the final device, where the IBE openings are clearly visible. Figure 2.26b) is a Transmission Electron Spectroscopy (TEM) showing the section of one of our contact openings.

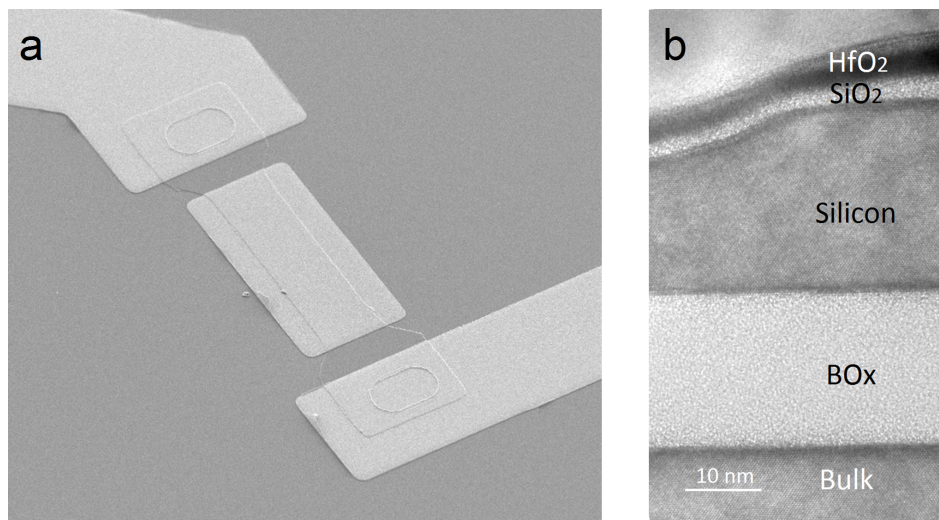


Figure 2.26 – a) SEM of a finished device b) TEM of the section of one of the S/D openings.

2.5 Oxidation and deposition processes

In this section we are going to cover all the procedures used to grow or deposit materials needed for the functioning of the devices. In the first subsection we will explain the processes related to dry oxidation and gate stack definition, mentioning the strategy employed to prevent charge-trapping and hysteresis, while the second will be devoted to an insight in the oxide passivation and metal lines deposition.

2.5.1 Dry oxidation and gate dielectric deposition processes

The most straight-forward method to obtain a dielectric layer on top of a semiconductor is to oxidize its surface, employing an high-temperature process in a controlled atmosphere containing oxygen. One of the main reasons for which silicon has been preferred to germanium as the base material of the semiconductor industry is in fact the high quality of the dielectric produced by its oxidation [86].

The physics behind an oxidation process has been object of intensive studies, which have delivered highly accurate predictive models, allowing the formation of oxide of the exact desired thicknesses by tuning the oxidation parameters [87].

It is now agreed upon that the oxidation mechanism takes place in three steps:

- The oxidant specie reaches the surface of the existing oxide (always present) on the silicon layer.
- The oxidant specie crosses the oxide film and reaches the interface with the silicon.
- The oxidation reaction takes place, creating a new SiO₂ layer.

Each of these processes is characterized by a specific rate, depending on the transport, diffusion and reaction coefficients of the system, as well as on the abundance of oxygen atoms available in the atmosphere. After a brief initial transient, a steady-state is reached and the three rates become equal, which allows creating a system of equations yielding the well know relation 2.1.

$$x_0^2 + Ax_0 = B(t + \tau). \quad (2.1)$$

Here A and B are parameters related to the physical constants of the oxidation reaction, τ is a time constant which accounts for the initial oxide thickness and x_0 and t are, respectively, the thickness of the oxide and the corresponding oxidation time. The oxide growth is generally a very slow process, unless extreme temperatures are employed, and therefore the thickness of the oxide grown is extremely controllable.

Since the growth of the oxide takes place at the expense of the silicon layer, this process can be used for thinning down SOI substrates, as we did.

At CMi, dry oxidation is performed in the *Centrotherm furnaces*, which normally employ

temperatures between 850 and 1050°C. Inside the chamber, on top of the oxygen, is inserted some dichloroethylene ($C_2H_2Cl_2$) which, upon exposure to oxygen at high temperature, burns forming high purity chloridric acid (HCl) and carbon dioxide (CO_2). The HCl helps obtaining a high quality oxide by preventing metal contamination.

The literature points out that the Si consumption amounts to the 44% of the grown oxide thickness, which means that growing 100 nm of oxide would thin down the Si layer by 44 nm. Before processing our expensive substrates, however, we performed a test oxidation/etch run on some SOI scraps, employing spectroscopic ellipsometry (*Sopra GES 5E, spectroscopic ellipsometer*) to measure the thickness of the SiO_2 layer grown and the consequent silicon consumption. It turned out that the thinning effect on our SOIs was higher than expected, resulting *as if* the actual silicon consumption amounted to the 54% of the thickness of the oxide grown. We attributed this phenomenon to the silicon etching due to the employ of a particularly aggressive RCA cleaning step before the oxidation: this procedure, in fact, makes use of a strongly oxidizing mixture of hydrogen peroxide (H_2O_2), water and ammonium hydroxide (NH_4OH) followed by a diluted HF etching, which removes the chemical oxide formed in the first step. The consequent silicon etching could amount to several nanometers, explaining the measurement results.

The same oxidation procedure has been employed for the growth of the pedestal oxide on the channels of the ribbon-FETs, with a specially tuned process featuring a particularly low temperature, down to 600°C. This allowed reaching an oxide thickness of just 5 nm. Unfortunately, the RCA cleaning performed before the oxidation resulted once again more aggressive than expected and the exposed regions of the BOx, for which we had estimated a thinning of the order of 4 nm, were completely removed (Figure 2.27), which made necessary the sputtering and lift-off of the SiO_2 passivation layer.

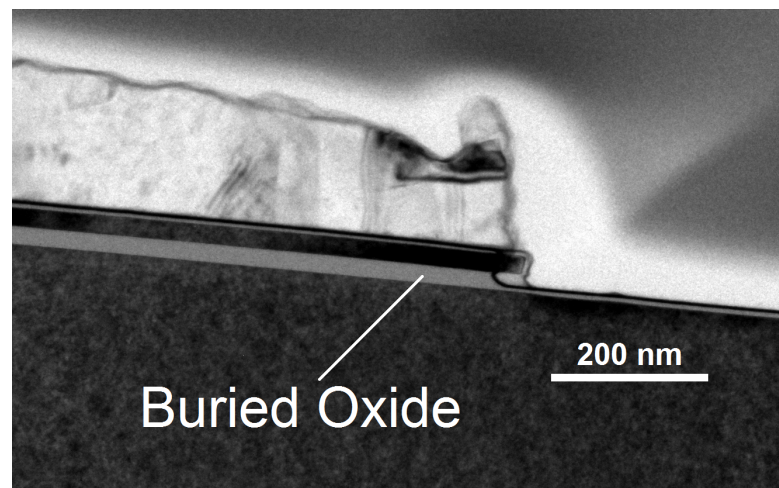


Figure 2.27 – SEM of a lamella extracted from one of our SOIs, showing that the BOx has been completely removed.

The pedestal oxide is nevertheless an essential component of our gate stack: as reported in [88], directly depositing the HfO_2 on the silicon channel would create a poor semiconductor-

dielectric interface, filled with mobile charges which would degrade the gate coupling and generate *hysteresis*.

The hysteresis is a phenomenon which can be observed when the gate bias is switched over a range of values and back: the trapped charges are able to move, influencing the effective electric field seen by the channel and providing a memory effect, which makes the relation between I_D and V_G dependent on the previous V_G values. This property is obviously detrimental, when the devices need to be used as sensors. The pedestal oxide acts against this effect by providing an optimal surface for the high- k dielectric deposition, drastically reducing the number of defects. The deposition of HfO_2 is done through Atomic Layer Deposition (ALD), a technique capable of depositing extremely thin and uniform layers of material by growing one atomic layer at a time [89]. The process for the growth of a monolayer can be resumed in four steps:

- The first precursor is inserted in the chamber containing the substrate and is adsorbed on its surface.
- Nitrogen gas is flown in to the chamber to remove the non-adsorbed precursor.
- The second precursor is inserted in the chamber, where it reacts with the first precursor on the surface of the substrate, creating the first layer of the desired material and a byproduct.
- Nitrogen is flown again to remove the unreacted second precursor and the byproduct

The process can be repeated as many times as needed, until the desired thickness is reached. In CMi, this process is performed with a *BENEQ TFS200*. For the deposition of HfO_2 , the chamber temperature is set to 200°C . The two precursors employed are water and TEMAH (Tetrakis(ethylmethyldamido)hafnium(IV), heated at 80°C). The process is extremely slow, as each deposition cycle takes about 5 s and deposits just 0.1 nm of dielectric. Since in this process flow we only employ 3 nm of HfO_2 , however, this limitation is not an issue.

2.5.2 Deposition processes for dielectric passivation and metal lines

A fast deposition of relatively thick layers of materials can be obtained employing sputtering or evaporation processes. Both these procedures create new layers by extracting material from a source and depositing it on the substrate: the difference between them lies in how the extraction is achieved.

Sputtering processes are based on the ion bombardment of a target, which constitutes the source of material [90]. The ions are usually extracted from a plasma generated by applying a DC bias between an anode (positively charged) and a cathode, which in this technology is the target itself: at high biases (*e.g.* 2000 V) and within a certain range of pressure (1-10 Pa), the electrons emitted by the target can undergo inelastic collision with the atoms present in the chamber (noble gases, usually Argon), potentially ionizing them and freeing more electrons,

which can undergo further inelastic collisions in an avalanche process. The resulting positive ions will be accelerated towards the target surface by the electric field, expelling atoms from its surface. The emitted atoms can be confined with an electromagnetic field by a magnetron, and focused on the surface to be covered. This procedure is not applicable if the target is made of an insulating material, because the electrons leaving its surface to activate the plasma cannot be replaced and a positive charge is quickly built up, preventing further electrons emission and switching off the plasma. To circumvent this problem, an alternating bias is applied, so that, during the semi-cycle in which the target is positively biased, the surface can be replenished of electrons. Sputtering is a versatile technique which allows depositing compound material (such as AlSi1%) without modifying their stoichiometry. The AlSi1% deposited with this method, however, can be easily attacked by even fairly weak chemicals, such as the ones employed for the development of exposed photoresist (Figure 2.28). It is therefore recommendable to limit as much as possible the number of steps between the sputtering of aluminum silicide and its passivation with SU-8.

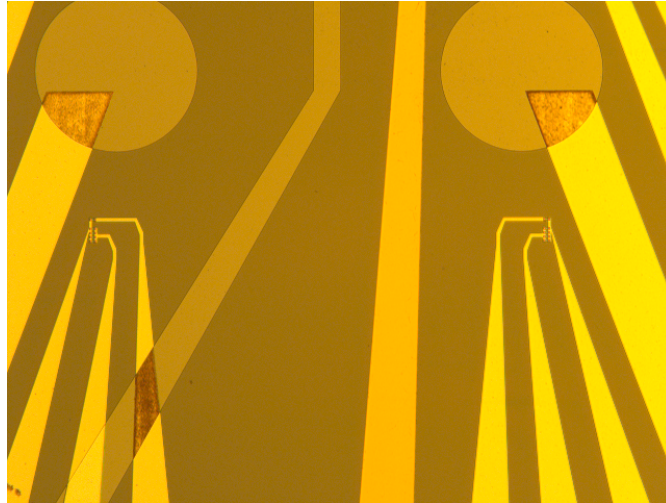


Figure 2.28 – Aluminum erosion after a photolithographic step.

Evaporation processes are divided in two types: evaporation by simple heating of the source and evaporation by superficial heating via an electron beam [91]. The second technique is usually preferred, as it is compatible with materials with high melting temperatures and prevents contamination from the crucible in which the material to evaporate is inserted. This procedure takes place under high vacuum (5×10^{-7} mbar), which allows achieving films of high purity. On the other hand, such high levels of vacuum determine a mean free path for the evaporated atoms in the order of 10^2 to 10^5 cm, meaning that the particles are not be able to scatter and will not reach the substrate with a uniform distribution, such as for sputtering. As a consequence, the coating will be less conformal, even though a rotation can be imposed to mitigate this effect. Furthermore, e-beam evaporation is associated with emission of X-rays, which can damage the surface of the substrate and generate charge trapping in the BOx of FD SOI, degrading the gate coupling and therefore the SS [92]. This effect, unfortunately, has been

directly observed in one of the SOIs of our second batch, when an equipment failure forced us to employ evaporation instead of the usual sputtering process (Figure 2.29).

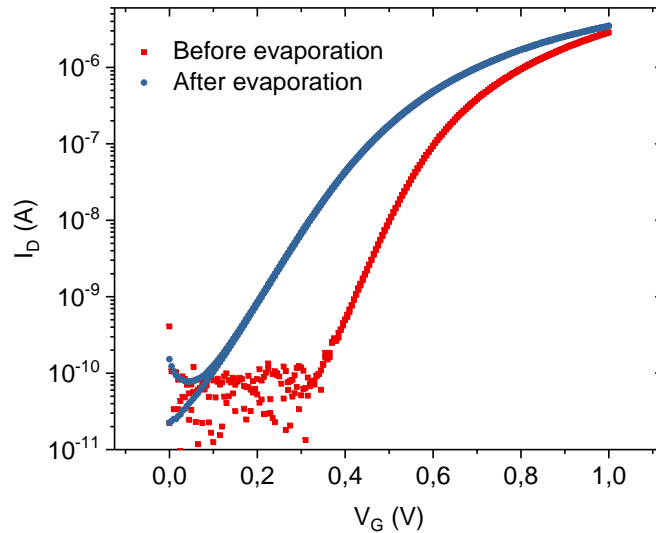


Figure 2.29 – Detrimental effect of X-rays on FD SOI devices during evaporation.

On top of this issue, which alone would be sufficient to discourage the employ of e-beam evaporation on FD SOIs, we need to list the impossibility of evaporating AlSi1% and the poor adhesion properties of evaporated platinum, which hinders the employ of the Pt needle technique by making the lift-off impossible without an adhesion layer.

For all of these reasons, our final recommended process flow features no evaporation steps. The silicon dioxide deposited by a sputtering process has poor electrical properties, when compared to the one produced by thermal oxidation of crystalline silicon [93]. It is possible to improve these properties by finely tuning the sputtering process or through a densification step at high temperatures, but since we didn't have stringent limitations on the silicon dioxide thickness, we decided to simply deposit a thick layer (50 nm, as stated) to solve the issue of leakages to the bulk (Figure 2.30).

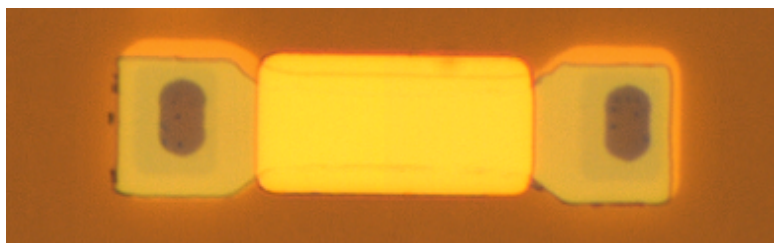


Figure 2.30 – Deposition of sputtered SiO₂ around the devices.

2.6 Ohmic contacts on ultra-thin SOI

The simplest model for the behavior of a metal-semiconductor interface [94] states that the semiconducting material energy levels will undergo bending, according to the work function (WF) of the metal, to achieve a constant Fermi level in the system. Because of this behavior, it should be possible to prevent the formation of a high energy barrier by employing a metal with a low WF (Figure 2.31), coherently with the widely exploited ohmic nature of the aluminum contacts on silicon.

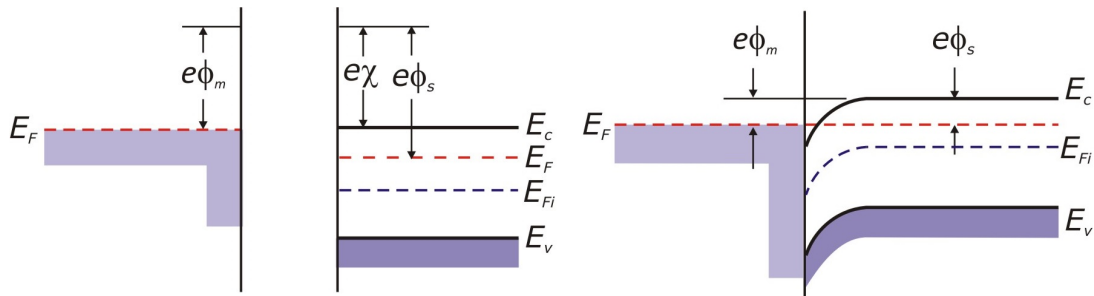


Figure 2.31 – Band diagram of an ohmic contact, showing that no barrier is created [97].

It has soon been found, however, that this model is too simplistic and that numerous experiments directly contradict it [95]. The energy barrier at the metal-semiconductor interface is in fact determined by the *Fermi level pinning* due to the interface states, which makes it basically independent on the WF of the metal. The actual potential barrier for Al contacts is in fact as high as 0.7 eV for normal cleaning and deposition procedures [96] and it further increases to 0.8-0.9 eV after thermal annealing. These results appear to contradict not only the presented model for metal-semiconductor interface, but even the experimental observations which have driven the employ of Al contacts in industry. The explanation of this apparent contradiction resides in another viable carrier transport mechanism across an interface: the barrier tunneling (Figure 2.32).

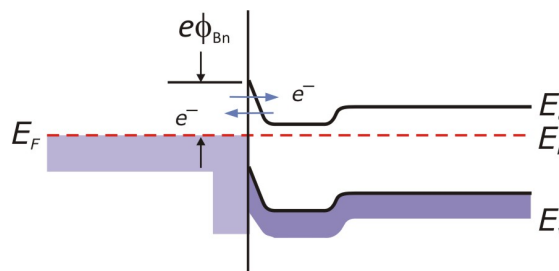


Figure 2.32 – Band diagram of a tunnel contact, showing the tunneling mechanism [97].

The width of the potential barrier at the interface between metal and semiconductor decreases with the square root of the doping level [98, 99], therefore carriers can easily tunnel across a contact on heavily doped silicon ($N_D \geq 10^{19} \text{ cm}^{-3}$), such as in our case.

Sentaurus TCAD simulations for the doping level, as stated, are not completely reliable for

SOIs as thin as ours. However, given the fact that the foreseen values ($3 \times 10^{20} \text{ cm}^{-3}$) is over one order of magnitude higher than required, we can be reasonably sure of the possibility of achieving performant tunneling contacts. In the first batch, the metal lines have been created by sputtering a metal compound made of aluminum and a 1% portion of silicon, followed by lift-off and contact annealing (Centrotherm furnaces, 5 minutes at 445°C followed by 10 minutes at 425°C, in forming gas). The presence of silicon in the compound is needed to saturate its solubility in aluminum: without this expedient, during the thermal annealing the silicon atoms could migrate inside the metal contacts and, given the thinness of our SOIs, create voids [100].

Achieving low-resistance, ohmic contacts with AlSi1% on ultra-thin silicon has proven challenging: on top of the necessity to avoid the growth of oxide due to oxygen plasma cleaning, for which the strategy of the metal needle has been implemented, we also need to consider the silicon precipitation from the alloy to the metal-SOI interface during thermal annealing. This phenomenon can grow an epitaxial layer of amorphous, P-type doped (Al-doped) silicon at the interface, generating a P-N junction with diode-like behavior [101]. Preventing the silicon precipitation requires the presence of a layer of native oxide on top of the SOI [102], making the study of a process flow particularly challenging as a middle situation between a clean surface and the presence of an insulating oxide layer has to be implemented. The layout prepared for the fabrication of the ribbon-FETs contained some test structures (Figure 2.33) made to evaluate the actual doping level and the contact quality through resistance measurements.

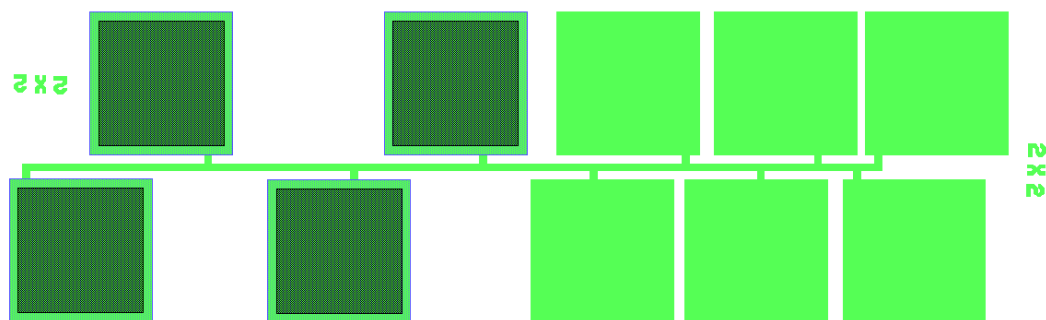


Figure 2.33 – Test structure: doped line featuring large pads for metal connection.

Before the high temperature annealing, the I-V characteristics of these structures is clearly Schottky type (Figure 2.34), with the current remaining at near-zero values for a wide bias range and then increasing exponentially. The asymmetry of the characteristics points out that the two contacts are not completely identical, which is probably due to the non-conformal silicon precipitation from the aluminum contacts on the ion-beam etched silicon openings. After the annealing, the contacts improve and an ohmic behavior is observed. The resistance of the doped line has been measured with different pairs of pads, with growing distance between each-other (Figure 2.35).

It can be observed that not all the characteristics appear perfectly linear, which implies that

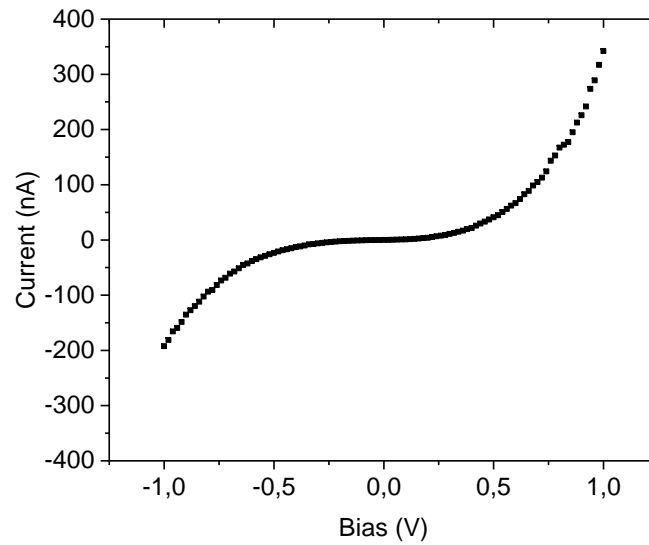


Figure 2.34 – I-V characteristics before annealing.

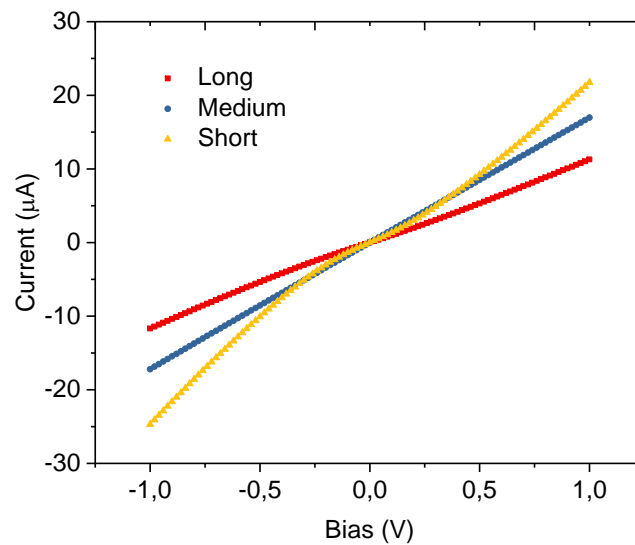


Figure 2.35 – I-V characteristics after annealing for different length of the doped line with AlSi1% contacts.

some variability in the quality of the contacts can still be observed, even between structures close to each other. The value of current obtained at a bias of 1 V can be used to extract the resistance of each line and, plotting the three values together as a function of the test line length, it is possible to find the intercept with the Y axis, representing the parasitic resistance of the contacts. Given the fact that we have only been able to measure three points and that such a big variability exists between the quality of contacts, the estimation is obviously very coarse, but the extracted value of 20 k Ω clearly shows that the quality of the contacts is still

low (Figure 2.36).

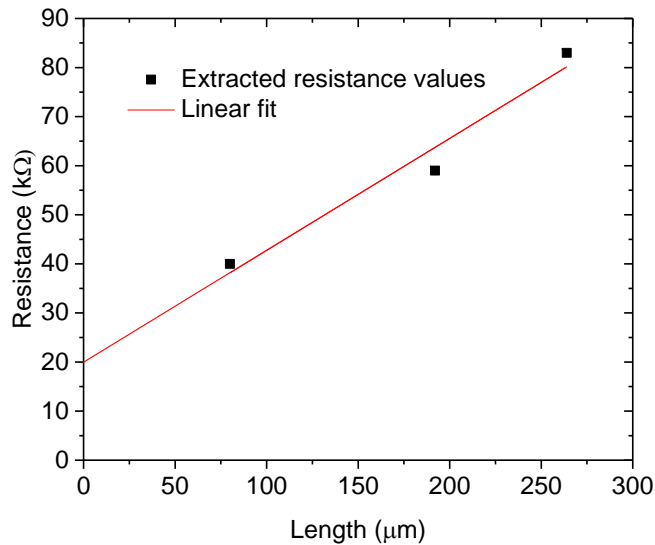


Figure 2.36 – Extraction of the parasitic resistance of the AlSi1% contacts.

The slope of the interpolating line can be used for evaluating the actual doping level from the resistivity of the doped line, even though the variability of the contact resistance limited the precision. The calculated resistance amounts to $237 \Omega/\mu\text{m}$ which, considering the section of the doped line, is equivalent to a resistivity of $2.3 \text{ m}\Omega\text{cm}$. This value, linked to a line made of phosphorus-doped crystalline silicon, indicates a doping level of $2.5 \times 10^{19} \text{ cm}^{-3}$: lower than the simulated one but still largely compatible with the fabrication of a tunnel contact.

The resistive nature of the contacts and their variability appeared even more evident for the actual devices, where the area of contact between metal and semiconductor is two orders of magnitude lower ($48 \mu\text{m}^2$ against $4900 \mu\text{m}^2$). The only way to achieve an acceptable contact to the devices consisted in manually annealing each one of them by forcing a huge bias ($> 10 \text{ V}$) between Source and Drain to heat up the contacts by Joule effect. During this procedure, the gates and the backgates have been left floating to prevent dielectric breakdown.

This procedure allows the production of acceptable devices, but leaves a huge variability amongst the transfer characteristics and is exceptionally time-consuming. Furthermore, sometimes the output characteristics of the devices retain a Schottky-like shape, which makes necessary the employ of high Drain voltages, increasing the power consumption (Figure 2.37). After some literature research [103–106], we found that platinum could constitute a good alternative to AlSi1%. Though this metal doesn't share the low cost, ease of processing and extreme conductivity of aluminum, its stable nature and immunity to spiking and silicon redeposition effects made it an excellent choice for the definition of a tunneling contact by simple deposition.

Platinum lines worked efficiently by simply avoiding the presence of an excessively thick oxide layer at the semiconductor interface, therefore the metal needle strategy granted excellent results, without even the necessity of an annealing step (Figure 2.38).

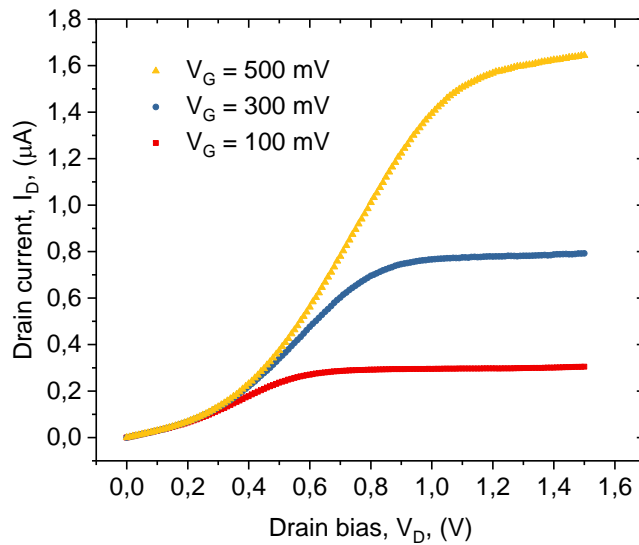


Figure 2.37 – Output characteristics of a ribbon-FET with poor AlSi1% contacts.

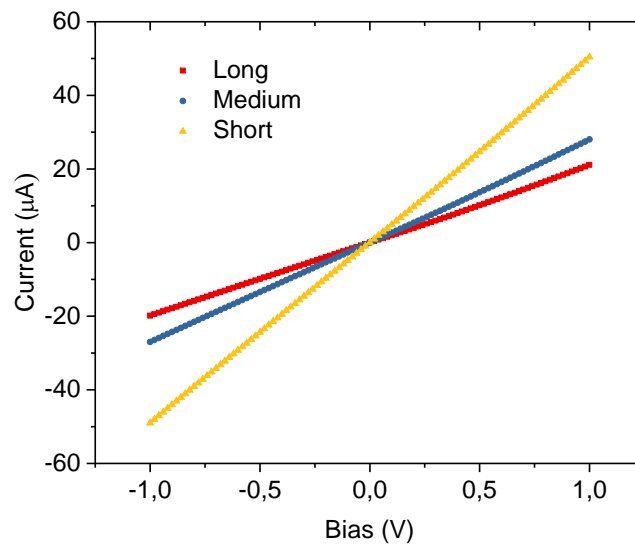


Figure 2.38 – I-V characteristics for different length of the doped line with Pt contacts.

The contacts are now fully ohmic and the higher current levels reached indicate that the contact resistance has diminished. We extracted it with the same strategy employed for the AlSi1% contacts (Figure 2.39)

The dependence of the contact resistance on the length of the line is now more linear, meaning that the behavior of the contacts is almost identical. The extracted contact resistance is slightly negative, indicating that its actual value is now below the precision achievable with these measurements.

The new set of experiment allowed us to extract a more reliable evaluation of the actual doping

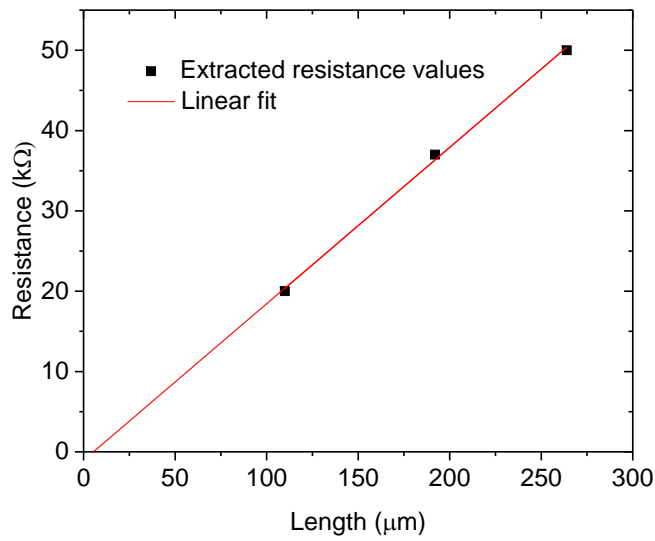


Figure 2.39 – Extraction of the parasitic resistance of the Pt contacts.

level achieved, correcting the previous estimation to $3.1 \times 10^{19} \text{ cm}^{-3}$.

Even the devices featuring small Pt contacts showed excellent output characteristics, meaning that a nearly ideal contact has finally been achieved (Figure 2.40).

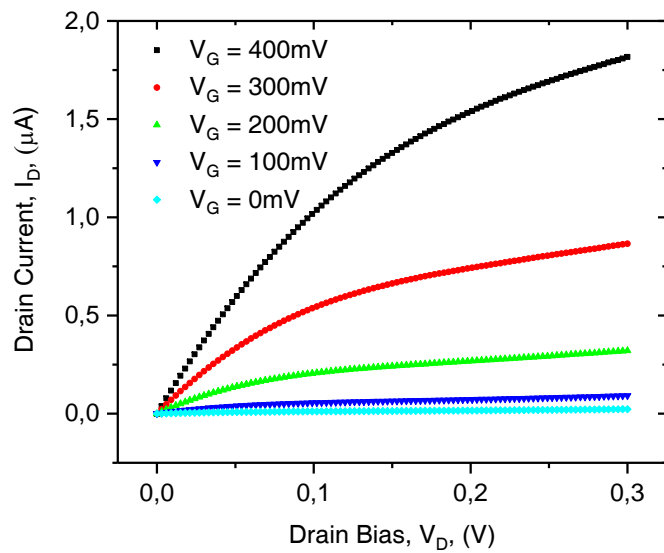


Figure 2.40 – Output characteristics of a ribbon-FET with excellent Pt contacts.

2.7 FD SOI Ribbon-FETs characterization

In this chapter, a number of issues related to the fabrication of ribbon-FETs on UTB FD SOIs have been presented and solved. The main problems encountered and the relative solutions are listed in Table 2.1.

process	issue	solution
Full RCA	removes ultra-thin BOx	sputtering of a SiO ₂ passivation layer
Diluted HF	detaches the photoresist mask	employ of buffered HF
Evaporation	generates X-rays	employ of sputtering alone
PR development	degrades exposed AlSi1%	perform passivation right after
Metal contacts	poor electric performances	metal needle strategy and employ of Pt
SU-8 passivation	openings not defined	bigger SU-8 openings on metal

Table 2.1 – Fabrication issues and solutions

The performances of the devices, in terms of yield, homogeneity of the characteristics, contact resistance and Subthreshold Swing, varied according to the level of optimization of the process flow.

Figure 2.41 shows the evolution of the output characteristics of the devices in time: from the first batch (Figure 2.41 a), to the optimized AlSi1% lines without unwanted oxide from plasma oxygen (Figure 2.41 b) to the final platinum lines (Figure 2.41 c).

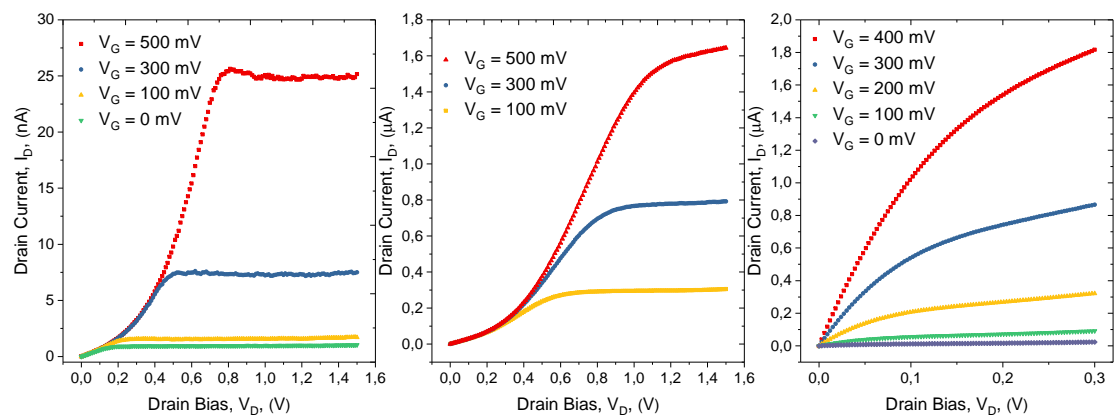


Figure 2.41 – Evolution of the output characteristic.

The Y-axis scale of first graph is in nA, showing the extremely resistive nature of the contact and the X-axis of the last graph only spans from 0 to 300 mV, demonstrating that we can finally switch on the devices at low biases.

The transfer characteristics of the devices have followed the improvements in the quality of the electric contact: the first batch, though showing excellent electrostatic control (since it was never subjected to evaporation processes) and minimal current leakages, had a very low yield, around 20%, and the functioning devices showed high variability, low ON current and an exponential dependence on the Drain bias (Figure 2.42).

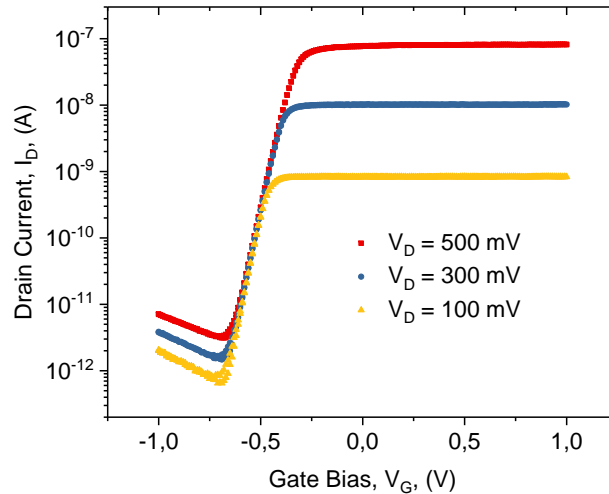


Figure 2.42 – Transfer characteristics in the first batch.

It is clear, from these characteristics, that the Drain current is not showing the gradual saturation described in Figure 1.10 but rather encounters a sudden plateau whose value depends on the Drain bias applied. This behavior can be explained seeing these devices as a series of two variable resistor: the first one, the channel, has a resistance exponentially dependent on the gate bias and the second one, the S/D contacts, has a resistance exponentially dependent on the drain bias. For low values of the gate bias, the overall resistance of the device is dominated by the channel, and is therefore strongly dependent on the gate bias itself. Over a certain value of V_G , however, unless V_D is increased as well, the resistance of the channel falls below that of the contacts and the transfer characteristics becomes suddenly flat. These devices can therefore be employed at low V_D , and therefore at low power, only if the read-out system is able to treat current values well below the nA, which can prove challenging for a wearable device.

In the second batch the problems related to the parasitic oxide growth due to oxygen plasma treatment have been solved with the metal needle strategy but, as we explained, the silicon precipitation at the interface still prevented the achievement of ohmic contacts in most devices. As shown in Figure 2.41, however, the contact resistance has been reduced by the new procedure and the transfer characteristics are now able to achieve much higher current levels and reduce the plateau effect, though an exponential dependence of the I_{ON} value on the Drain bias is still observed (Figure 2.43).

Finally, the definition of tunneling contacts with platinum allowed obtaining low-resistance

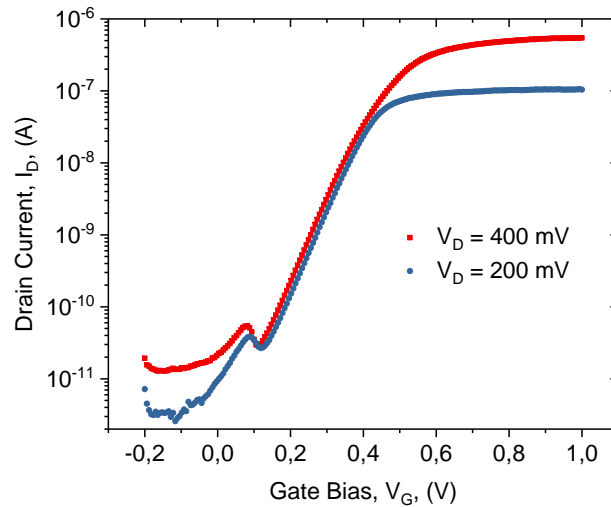


Figure 2.43 – Transfer characteristics of the second batch devices featuring AlSi1% contact lines.

ohmic contacts, featuring the highest I_{ON} levels and complete removal of the plateau effect. These devices had a yield close to 100%. Moreover, they could be operated with a Drain bias of just 100 mV, or lower. The ultra-thin BOx employed in the second batch allowed characterizing these devices for different values of the backgate contact bias, showing that the threshold voltage of these devices is easily tunable (Figure 2.44).

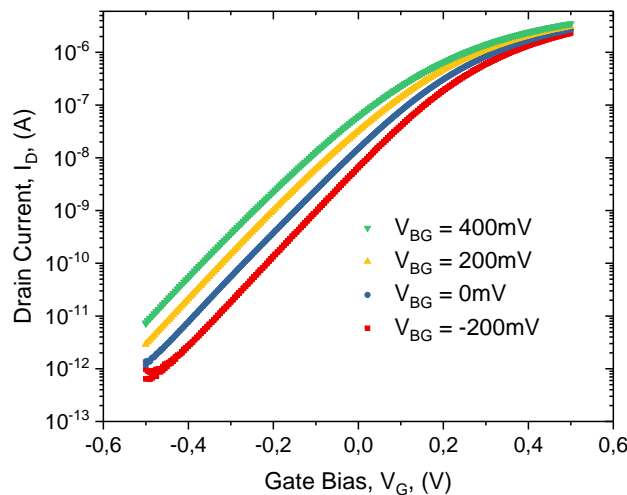


Figure 2.44 – Transfer characteristics of the second batch devices featuring Pt contact lines.

A study of the device-to-device variability has been implemented to determine whether or not a sensor-by-sensor characterization was needed for accuracy. Unsurprisingly, the results, shown in Figure 2.45, demonstrated that the transfer characteristics of these in-house made devices strongly depended on their position on the wafer and on the contact configuration.

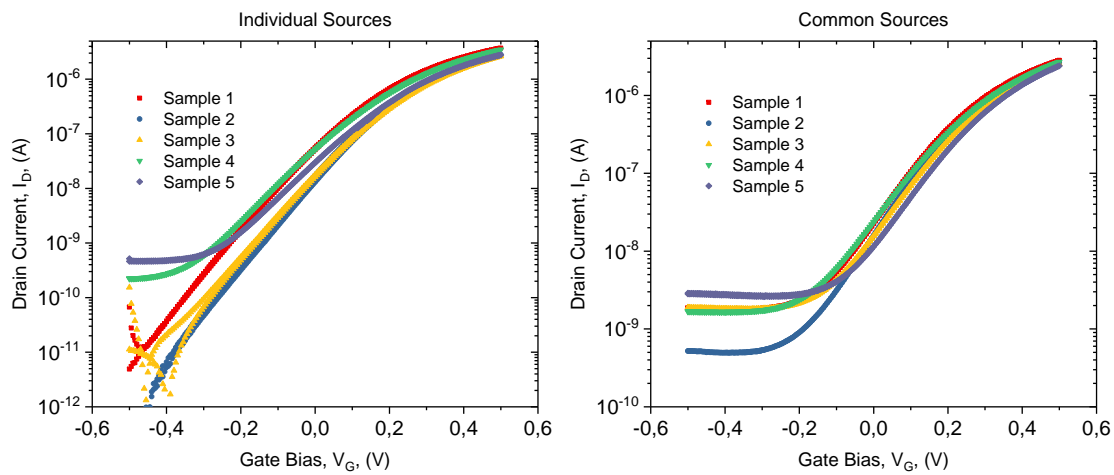


Figure 2.45 – Transfer characteristics comparison for two sets of ribbon-FETs featuring, respectively, individual and common Source contacts. The higher I_{OFF} values of the latter set are due to the sum of individual contributions to the leakage current passing from the bulk, due to implantation-induced damage to the ultra-thin BOx.

Nevertheless, this final version of our ribbon-FETs, with its stability, low power consumption and high I_{ON}/I_{OFF} ratio, proved to be an excellent base device for our experiments.

Figure 2.46 shows the chip which will constitute the base of our Lab-On-SkinTM device.

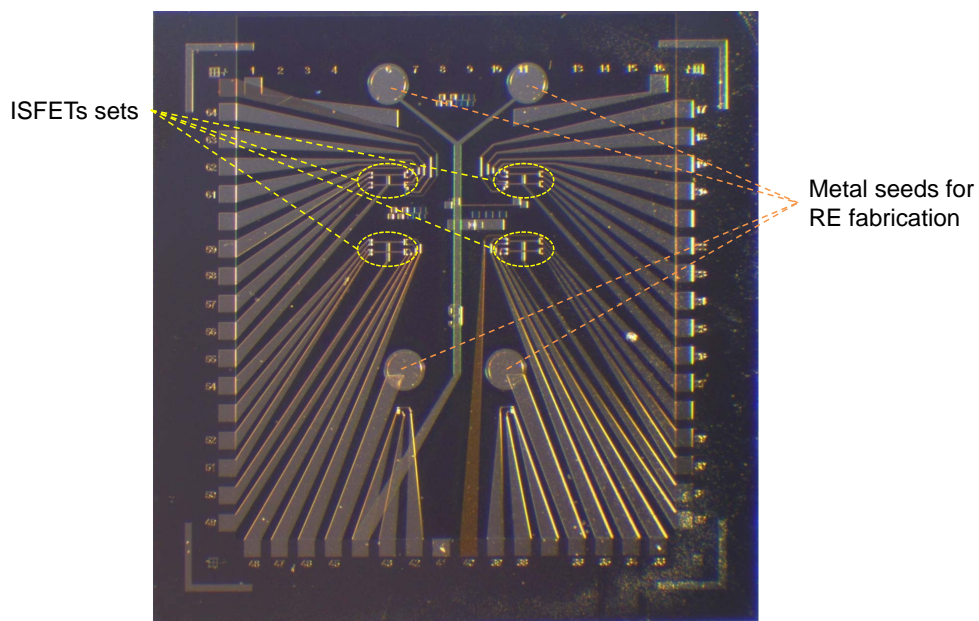


Figure 2.46 – Layout of the sensing chip used for producing the Lab-On-SkinTM prototype.

2.8 FD SOI Ribbon-ISFETs characterization

After completing the electrical characterization of the two batches, each of them has been tested for pH sensing before proceeding with the integration with the other components (Chapter 3).

The sensitivity of both batches to pH has been measured by flowing a set of five different pH buffers on the sensing gates and extracting, for each of them, the corresponding transfer characteristics of the sensor: the binding of positive ions (H^+) on the gate dielectric will shift V_{th} to more negative values according to their concentration, as explained in subsection 1.3.2. The continuous buffer flow has been provided by a 11 Elite Harvard apparatus syringe pump and the bias has been applied to the liquid gate with a commercial flow-through RE (MI-16-701 Microelectrodes Inc.RE). In order to control the flow of liquid on the SU-8 opening, preventing wetting of the exposed metal contact on the sides, a PDMS microfluidics (Figure 2.47) has been fabricated by pouring liquid PDMS on an SU-8 mold and curing it to trigger solidification. Vertical inlets and outlets are defined by keeping a set of four metal needles in contact with the SU-8 structures during curing.



Figure 2.47 – PDMS stamp with microfluidic channels.

In order to keep the PDMS stamp tightly bound to the sensing chip, preventing the liquid from leaking outside of the channels and ensuring that the alignment between channels and SU-8 openings is maintained, a foundry-made aluminum support structure has been designed by Dr. Fabien Wildhaber (Figure 2.48).

The transfer characteristics corresponding to different pH buffers for the first FD UTB SOI ISFET batch are shown in Figure (2.49).

We can clearly observe a constant, homogeneous shift of the transfer characteristics with pH, considering the RE bias (V_{ref}) at which the chosen flag current (10 nA in this case) is reached. From now on, we will refer to the bias value at which the chosen flag current is reached as the V_{th} of our sensors.

The V_{th} measurements become less reliable for lower I_D , as leakages and parasitic effects due

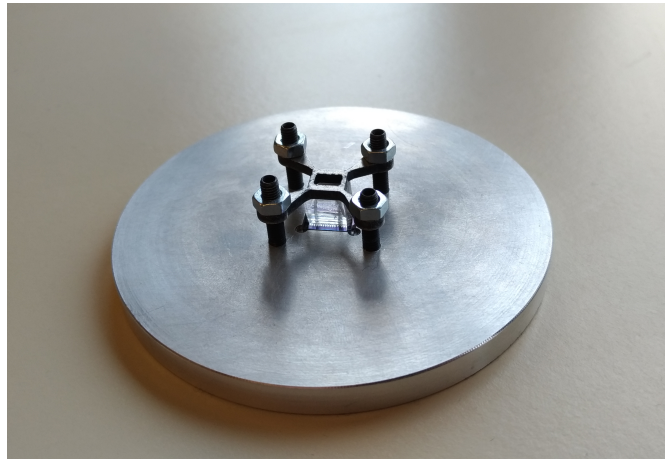


Figure 2.48 – Aluminum support structure clamping together sensing chip and PDMS stamp.

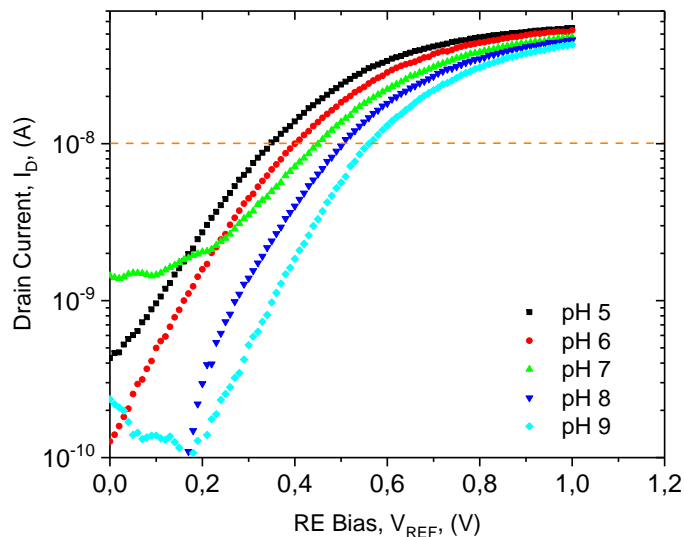


Figure 2.49 – Transfer characteristics for pH buffers ranging from 5 to 9. V_{th} shifts to more negative values for higher H^+ concentrations, *i.e.* lower pH.

to the microfluidic apparatus become more relevant. The low I_{ON} of the devices from our first batch forces us to choose our flag current from a very narrow range. The HfO_2 layer, however, proved to be an excellent sensing material for pH. The sensitivity of these sensor is evaluated extracting V_{th} at the different pH values and plotting them on a graph (Figure 2.50).

As can be observed, the response is extremely linear over the full pH range and the sensitivity is close to the Nernst limit.

The same characterization procedure has been employed for our second ISFET batch, but it was found that the quality of the HfO_2 layer deposited was reduced due to a carbon contamination of the ALD chamber, with the results shown in Figure 2.51.

The measurements appeared to be noisy and the V_{th} shifts are less homogeneous than before. Nevertheless, the transfer characteristics maintained the same shape regardless the pH buffer

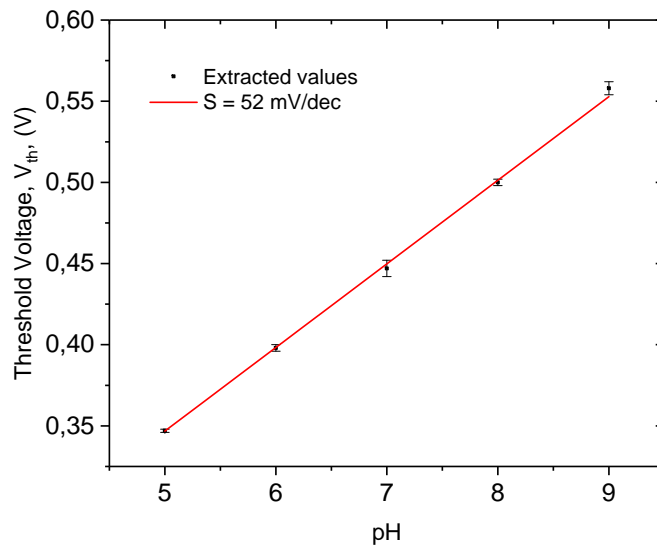


Figure 2.50 – V_{th} dependence on the pH for our first ISFET batch.

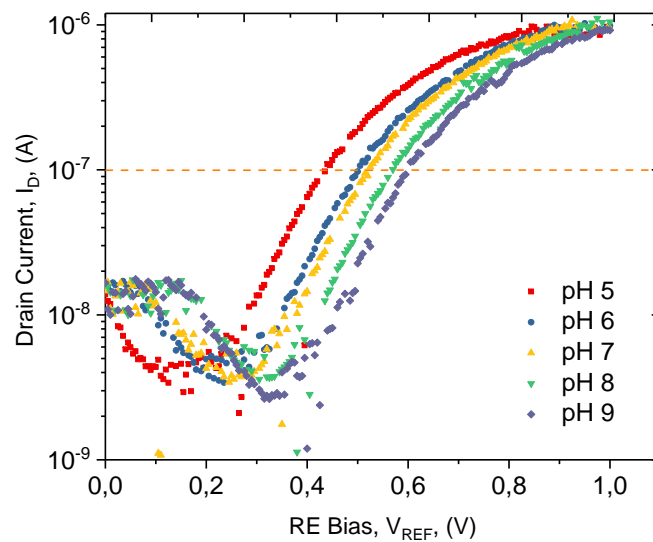


Figure 2.51 – Transfer characteristics for pH buffers ranging from 5 to 9 for our second ISFET batch.

employed, therefore we are now able to freely select our flag I_D over a wider range, adapting our readings to the resolution of the read-out circuit to which our sensor will be connected. The pH sensitivity of this ISFET is plotted in Figure 2.52.

The sensitivity of the new dielectric layer also appeared to be reduced.

For comparison, we have also performed a pH measurement employing one of the sensors featuring a platinum gate. This test was meant not only to investigate the possibility of using platinum as sensing material for pH, but also to determine whether the noise due to the low-quality hafnia could be removed by simply preventing contact with the analyte. The result

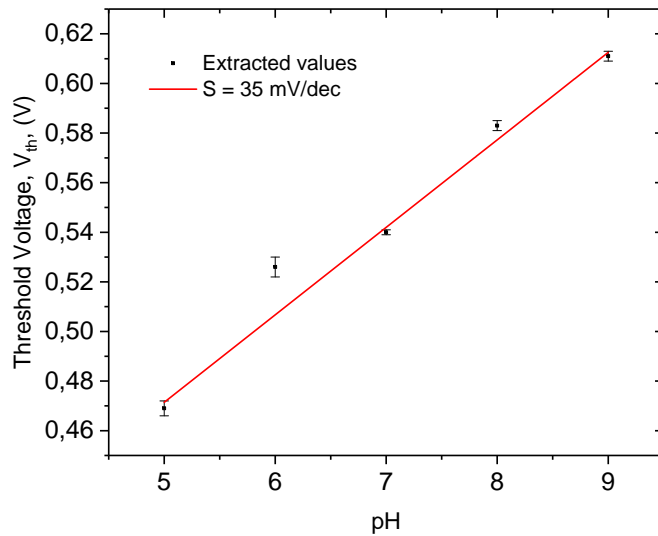


Figure 2.52 – V_{th} dependence on the pH for our second ISFET batch.

of this characterization are shown in Figure 2.53 and 2.54.

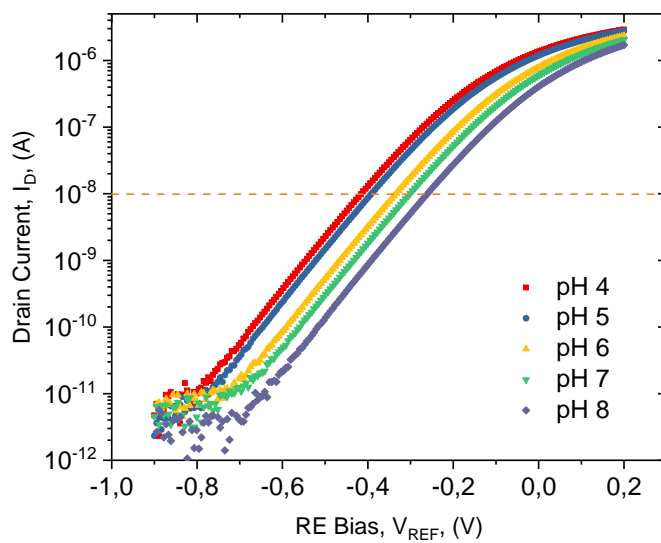


Figure 2.53 – Transfer characteristics for pH buffers ranging from 4 to 8 for our second ISFET batch employing a Pt-coated gate.

Using platinum as sensing layer, the noise observed in Figure 2.51 appears to be removed and the sensitivity increased.

The curves also remain parallel over 5 decades, further increasing the range over which we can select our flag I_D .

For the selective sensing of specific ions, the sensors from our second batch will always employ an Ion-Selective Membrane whose sensitivity, as will be explained in subsection 3.2.2,

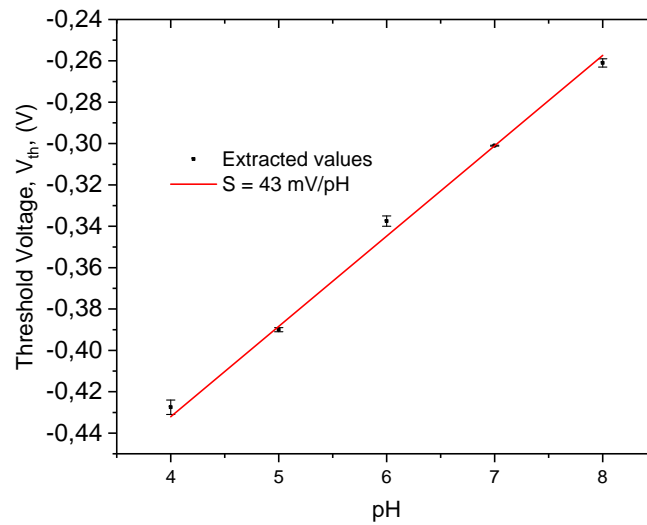


Figure 2.54 – V_{th} dependence on the pH for our second ISFET batch employing a Pt-coated gate.

is completely independent on the underlying layer. For this reason, the only measurement affected by the poor quality of our HfO_2 layer is that of pH.

2.9 Summary

In this section, the most important achievements regarding the fabrication of ribbon FETs are outlined.

- **Technical outcomes:**

- Cleanroom fabrication of ribbon FETs with the following properties:
 - * N-type, fully depleted devices on ultrathin BOx ;
 - * Channel thickness = 30 nm, channel width = 6 μm ;
 - * Gate stack composed by dry SiO_2 (5 nm) and ALD HfO_2 (3 nm);
 - * Pt lines for connections;
 - * Phosphorus doping concentration = 3.1×10^{19} ;
 - * SS down to 64 mV/dec with a metal gate;
 - * SS down to 128 mV/dec with a liquid gate;
 - * I_{ON}/I_{OFF} ratio up to 10^6 with a metal gate;
 - * I_{ON}/I_{OFF} ratio up to 10^5 with a liquid gate;
 - * pH sensitivity up to 54 mV/pH on HfO_2 , up to 40 mV/pH on Pt;
 - * Hysteresis-free characteristics;
 - * Negligible contact resistance.

- **Results highlights:**

In this chapter we have reported the definition of a robust process flow for ultra-thin FD SOI ribbon FETs fabrication, with yield close to 100%. High doping levels are achieved in ultra-thin silicon, employing implantation parameters optimized with TCAD simulations, and a pedestal oxide has been successfully exploited to prevent hysteresis with an HfO₂ gate dielectric. An efficient fabrication procedure for the definition of low-resistance ohmic contacts on ultra-thin silicon has been presented and the Pt is demonstrated as an excellent choice for the metal lines. A set of tests provided the best design and fabrication parameters for the achievement of a conformal and mechanically resistant passivation layer.

The fabricated devices have demonstrated excellent performances, both when tested with a metal gate and when employed as pH sensors.

In the next chapter, we will introduce other important component for sensing and their integration on our sensing chip.

3 Lab On SkinTM: a fully integrated wearable sweat analyzer

In the previous chapter we have presented the fabrication procedure and the characterization results of the ribbon-ISFETs which will act as sensors in our system. The operation of the sensing chip, however, requires the synergy of different components. As anticipated in the introduction, on top of our passivated ribbon-FET chip we need to define:

- a low-volume, passive microfluidics able to collect sweat from the skin of the user, drive it on the sensing gates and store it using a capillary pump, optimized to provide a controlled and constant flow rate with zero power consumption.
- a set of functionalization layers deposited on the sensing gates, in order to provide sensitivity and selectivity for the concentration of one specific kind of ion or molecule.
- a stable, miniaturized QRE, capable of applying a fixed bias on the gates, in order to obtain the stable current measurements required for continuous, long term monitoring of biomarkers in sweat.

The fabrication of these three elements, not trivial in itself, is subject to further constraints due to the compatibility requirements of the fully integrated device. In this chapter, we will first discuss the fabrication and characterization of each of these components alone and then show how they have been integrated together.

3.1 Passive capillary microfluidics

A key feature for any wearable device is the necessity of reducing the power consumption as much as possible. It would have been meaningless to optimize the ribbon-FETs contacts to operate at low V_D , if the transport of sweat was based, for example, on a peristaltic or electrowetting pump.

As already introduced elsewhere [32, 33, 107], capillarity is an ideal solution for the realization of a zero-power microfluidics: this phenomenon is based on the interplay between the adhesion forces of the external molecules of a liquid in a small channel and the cohesion forces

among the internal molecules [108]. The process of capillary filling is shown in Figure 3.1: first, adhesion forces to the walls of the microfluidic channel will lift the external molecules of the liquid, determining the formation of a meniscus. The new shape of the liquid-air interface increases its surface, diminishing the number of hydrogen bonds (in case of water) between the molecules, since fewer water molecules will be found in air. The bulk of the liquid will therefore move upwards to restore the more energetically stable flat surface. The process will then be repeated until complete filling of the channel or until an equilibrium between the dragging forces and the liquid weight and/or viscous friction is reached [109].

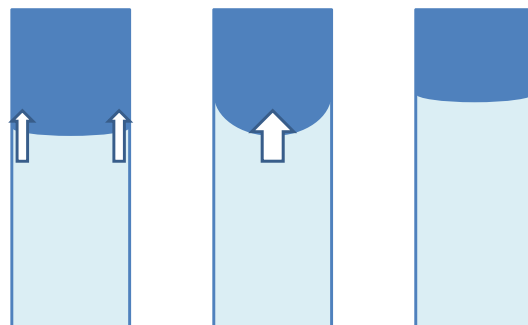


Figure 3.1 – Steps of a capillary filling process.

In order to investigate this phenomenon, a set of simulations have been performed with *Comsol multiphysics*. The aim of these simulation was to obtain a preliminary understanding of the factors determining the probability of achieving complete filling of the channels, as well as of what would have been the time scale of the process.

The first indication given by the simulations was the importance of choosing the right material for the microfluidics channels: capillarity in fact requires the channel to be *hydrophilic*. The hydrophilicity/hydrophobicity of a material is a property vastly dependent on the surface topography and describes the adhesion behavior of said material to water [110]. This property can be evaluated by measuring the *Contact Angle* (CA) between the surface of a small water droplet deposited on the material and the surface of the material itself (Figure 3.2). Conventionally, a material is considered hydrophilic when its CA to water is smaller than 90° and hydrophobic otherwise.

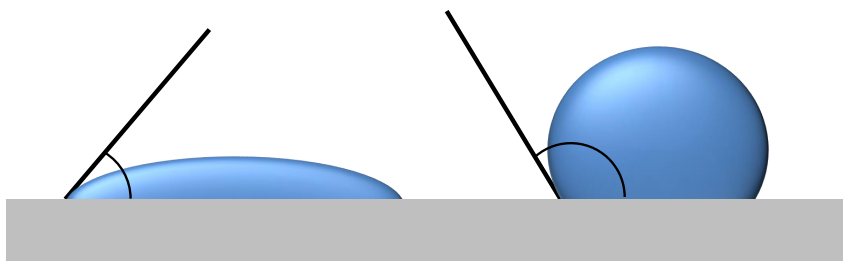


Figure 3.2 – Hydrophilic (low CA) and hydrophobic (high CA) surfaces.

Unsurprisingly, Comsol simulations showed that the filling time was reduced for lower contact angles. The process, however, didn't appear to require superhydrophilic materials (*i.e.* materials with a CA close to 0, as described in [111]): as shown in Figure 3.3, filling a cylindrical channel with a diameter of 30 μm and a length equal to that of the chip (9 mm), considering a CA = 67.5° took only 70 ms of simulated time.

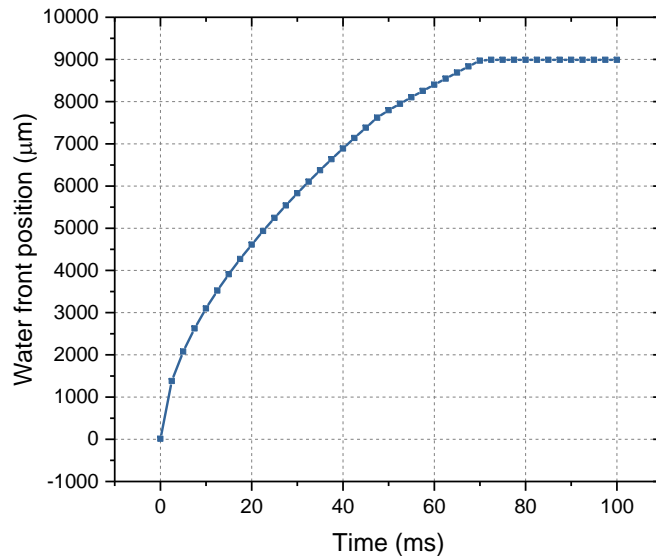


Figure 3.3 – Position of the water front in the capillary channel as a function of time.

On top of the hydrophilicity, we need to consider that the integration of the microfluidics on the sensing chip will require alignment and, furthermore, either a bonding process or its direct fabrication on the chip itself. The second solution, though showing some severe limitations on the fabrication process, especially for what concerns the thermal budget, is more straightforward and easier to upscale, on top of easing the alignment process, and has therefore been preferred. SU-8 has been chosen after testing different solutions, ranging from PMMA, to PDMS to Pressure-Sensitive Adhesives (PSA). The advantages of this structural resin resides in its mechanical durability, high aspect ratio, toughness and high adhesion properties due to its high epoxy content. Another advantage which made it desirable for our process consists, of course, in the possibility to define its shape by a simple photolithographic process [112].

Furthermore, SU-8 has already been subject to in-vitro and in-vivo biocompatibility tests [113] whose results were comparable to those of already FDA approved material such as silicone elastomer and medical steel. The CA of the SU-8 processed in CMi has been measured with a *Kruess DSA-30 Drop Shape Analyzer*, which deposits 3 μl droplets on the surfaces to test and automatically reads the resulting contact angle. The results were as low as 64.1° (Figure 3.4), even lower than what is reported for polymers such as PMMA [114].

The first prototype of the SU-8 microfluidics featured drop-shaped inlets, similar to the ones presented in [32], and a PSA closing layer. Continuous flow after the capillary filling was provided by an absorbent material (absorbing paper). The microchannels were 30 μm wide



Figure 3.4 – Shape of a droplet deposited in CMI-processed SU-8 GM 1060.

and 20 μm thick (Figure 3.5).



Figure 3.5 – Structure of the first prototype of the passive microfluidics. The channels here are represented by metal lines to be visible.

This prototype, in agreement with the Comsol simulations, achieved an almost instantaneous capillary filling which, together with the possibility to be produced easily, at low cost and wafer-scale, made it an excellent proof of concept. Some limitations could nevertheless be listed: the flow rate determined by the absorbing paper was not controllable and in general too fast to be compatible with a reasonable sweat rate. Secondly, the PSA closing layer had to be manually deposited on the channel, preventing upscalability of the fabrication process. Lastly, the design of the inlets limited the area from which sweat could be gathered, requiring at the same time a considerable amount of liquid to be filled. The internal volume of the inlets was in fact orders of magnitude bigger than that of the capillary channels.

These issues have been individually tackled and solved by Dr. Erick Garcia Cordero and Dr. Fabien Wildhaber, with the strategies outlined in the following subsections.

3.1.1 Microfluidic pumps

As mentioned in the introduction, one of the main challenges for health monitoring through sweat analysis consists in the design of a system compatible with the sweat rate of a subject at rest, which is reportedly as low as 20 nl per cm² and per minute. Half of this problem concerns, as stated, the definition of efficient capillary inlets, but it is also necessary to prevent the channels from completely emptying as soon as the capillary filling is complete, otherwise the monitoring would be stopped for lack of analyte and, on top of that, the dry sensors could give meaningless readings. Filtering out these readings would require increasing the complexity of the system and/or of the data analysis.

One possible solution for this issue consists in the definition of a capillary pump made of SU-8 exagonal pillars arranged in a honeycomb structure (Figure 3.6).

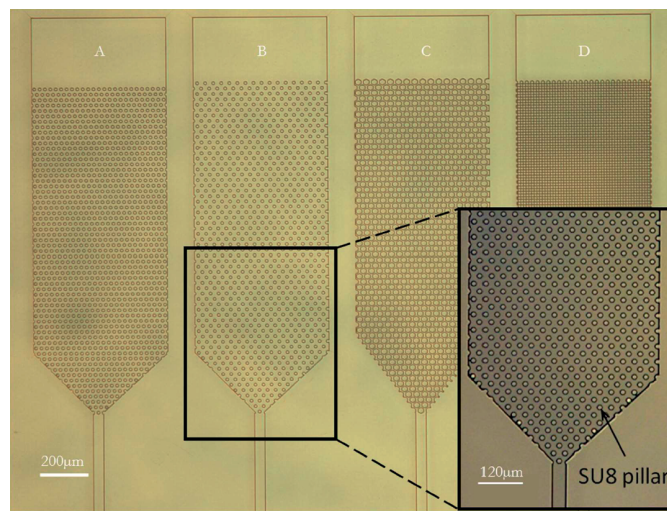


Figure 3.6 – SU-8 microfluidics pump with varying pitch and pillars size.

In this structure, the capillary filling is slowed down, as the progression from one row of pillars to the other requires the liquid to surpass a short empty state, which is only possible after the water fronts has formed a convex meniscus big enough to get in contact with a pillar from the next row (Figure 3.7).

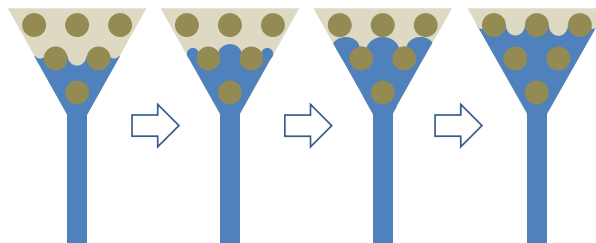


Figure 3.7 – Steps of capillary filling of a microfluidic pump.

The flow rate in the capillary pump can be tuned varying the distance between the pillars or the diameter of the pillars themselves [115, 116]. In this project, pillar sizes of 10 and 20 µm

have been employed. The spacing between adjacent pillar in x and y direction have been varied separately, with distances in the x axis of 10 and 20 μm and distances in the y axis of 0 or 10 μm . The spacing in the y direction is measured as the vertical distance between the top of a pillar in one row and the bottom of a pillar in the row above.

Accurate computer simulations of this structure are made impervious by the influence on the capillary filling of the thickness of the liquid layer: this condition drastically reduces the reliability of 2D simulations, and the computational cost of a 3D capillary filling simulation would be unaffordable. Together with the relative ease of fabrication of these structure, the difficulty in simulating the capillary filling pushed us toward a trial and error approach.

The first test was performed with 10 μm wide pillars and a spacing of 20 μm in the x direction and 10 μm in the y direction, which resulted in a flow rate of 120 pl/minute: a value that resulted actually *too slow* for sweat monitoring applications, as there would be an excessive delay between the production of the sweat and its measurement (Figure 3.8)

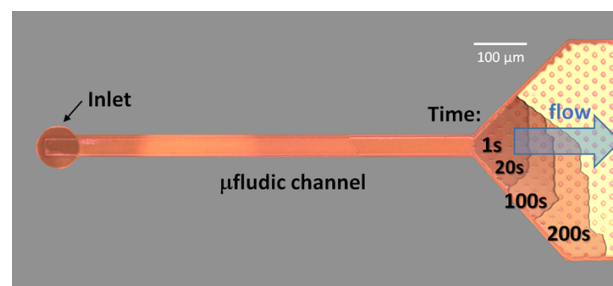


Figure 3.8 – Filling time-lapse of a microfluidic pump.

Doubling the size of the pillars without changing their positioning (*i.e.* reducing the spacing to 10 μm in the x axis and 0 in the y axis) the flow rate increased to 4.2 nl/min, equivalent to the sweat produced by 21 mm^2 of skin in normal conditions.

3.1.2 Closed microfluidics

Creating a closed structure with a bottom-up approach is a challenging task: we cannot directly deposit a closing layer of SU-8 by spin-coating on our open microfluidics without filling the channels. To solve this issue, a two-wafers procedure has been implemented with the following process flow (Figure 3.9): on the first wafer (which in the real process would be the ribbon-FET SOI) were defined the passive channels and the micropillars, realizing an open microfluidics. On the second wafer, instead, a Cr-Al (20 nm - 100 nm) metal stack has been deposited by sputtering and then a 30 μm thick layer of SU-8 has been spin-coated.

The surfaces of the two wafers have been put in contact and heated at 130°C, with an applied pressure of 4.5 bars for 90 minutes. This step was performed in CMi employing a *Süss SB 6, vacuum anodic bonder*.

After this step, the two SU-8 layers are permanently bonded. To remove the second wafer, which has no purpose anymore, anodic dissolution of the Al layer is employed: the two-wafer system is immersed in a 1 M NaCl bath together with a Pt-coated wafer, which acts as counter

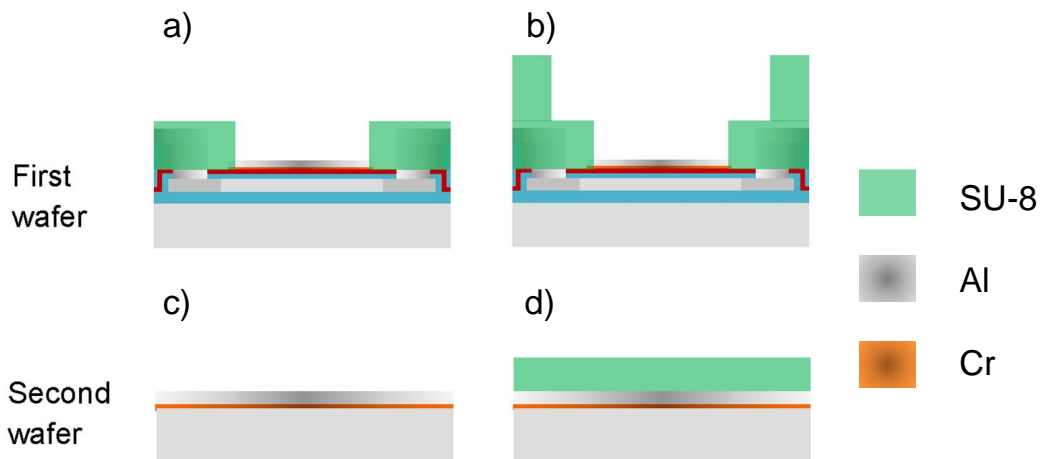


Figure 3.9 – Processing of the two wafers. The microfluidics is defined on the ISFET wafer (a and b) while the closing layer is spin-coated on the support wafer (c and d).

electrode. A bias of 5 V is applied between the backside of the second wafer and the counter electrode, causing the aluminum layer to react with the chlorine ions in the liquid to form aluminum chloride, which dissolves in water. After a few hours, the second wafer is detached, leaving the first wafer with a closed microfluidics on top (Figure 3.10)

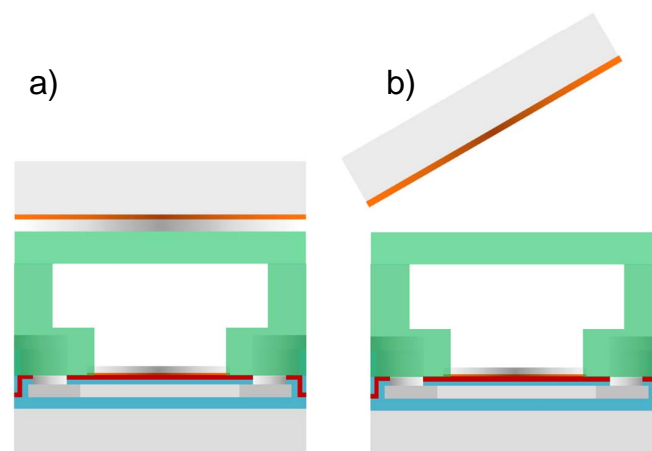


Figure 3.10 – Processing of the two wafers. a) Wafer bonding. b) Al anodic dissolution.

At this point, however, the microfluidics has no inlets or outlets and the only way to open them is the employ of a carefully tuned excimer laser (*OPTEC LSV3*), which poses severe limitations on their design (Figure 3.11).

On top of that, the high-pressure bonding procedure resulted not safe: during the tests some of the dummy wafers employed were cracked. Losing the wafers at this step is an unacceptable risk, given the fabrication time and cost of an SOI ribbon-FET batch.

We found, however, that even an open microfluidics could provide a controlled flow of sweat on the sensors, drastically reducing the complexity and risks of the fabrication procedure

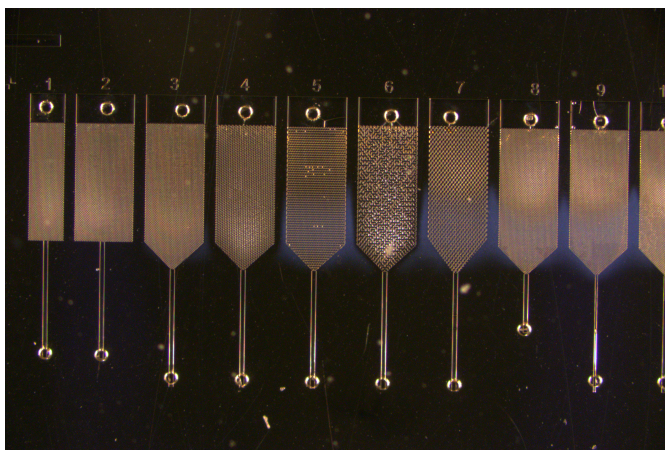


Figure 3.11 – Circular inlets and outlets defined with the excimer laser.

and allowing a more free design of the inlets. The experiments proving these capabilities are outlined in the next subsection.

3.1.3 Capillary inlets

As mentioned, the issues related to the drop-shaped inlets consisted in the limited area from which sweat could be gathered and, at the same time, on their excessive internal volume. The solutions of these two problems look intuitively antithetic, but this is in fact not the case: employing an arborescent structure, with numerous, small capillary channels, it is in fact possible to cover a wide skin area while at the same time reducing the capacity of the inlets, compared to a single bulky chamber such as the one in Figure 3.5. One example of such structures can be seen in Figure 3.12.

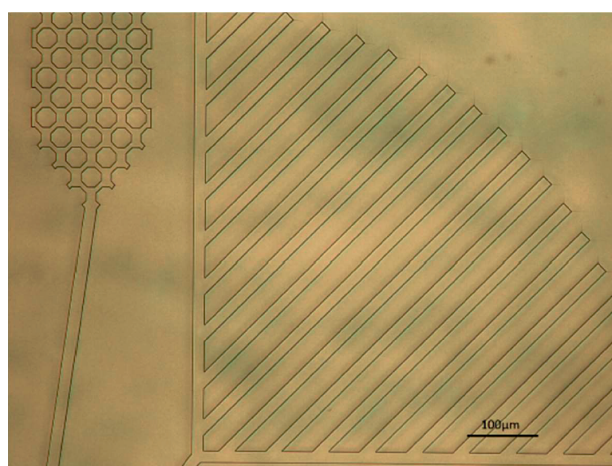


Figure 3.12 – Arborescent structure of a capillary inlet (right) able to collect liquid from a wide surface.

3.1. Passive capillary microfluidics

To test the efficiency of this kind of structure, as well as the functioning of an open capillary microfluidics, an artificial skin (Figure 3.13) has been produced. This element consist of a liquid reservoir encased in an aluminum support structure, with a transparent glass slide on the bottom and on top a molded lens of agarose hydrogel and a 50 μm thick perforated Kapton tape (our artificial skin). The agarose hydrogel is necessary to achieve a homogeneous flow throughout the surface. An inlet and an outlet allow controlling the "sweat" rate with a syringe pump (*11 Elite Harvard apparatus syringe pump*) to simulate different heat or exercise conditions.

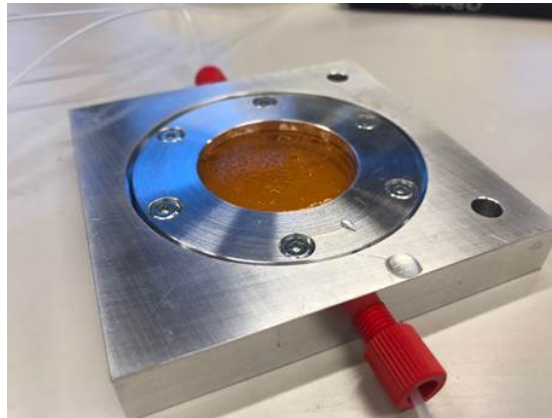


Figure 3.13 – Artificial skin sample.

Thanks to the see-through properties of this system, it is possible to observe the interaction between the artificial skin and the microfluidics samples with a microscope, obtaining some preliminary understanding of the actual gathering and transport processes. Figure 3.14 shows one microfluidic prototype, featuring an arborescent inlet, capturing a droplet forming at a random position beneath its microchannels.

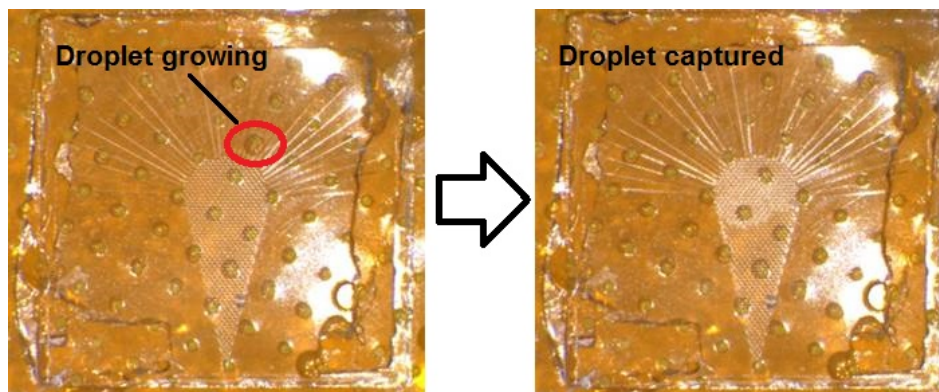


Figure 3.14 – Capture of a droplet from the artificial skin.

Since both the sample fluid and the artificial skin are transparent, however, keeping track of the droplets is not simple. To be able to obtain more precise imaging, to be used for the optimization of the microfluidics design, a fluorescent setup has been defined: the artificial skin system

Chapter 3. Lab On SkinTM: a fully integrated wearable sweat analyzer

has been modified substituting the Kapton layer with an opaque copper-polyimide laminate membrane and employing as sample liquid a solution containing fluorescent rhodamine dye. The microscope has also been equipped with the corresponding filter set. This new setup allowed following with precision the formation, capturing and transport of a liquid droplet, and even to observe the flow velocity with an high-frame-rate camera (Figure 3.15).

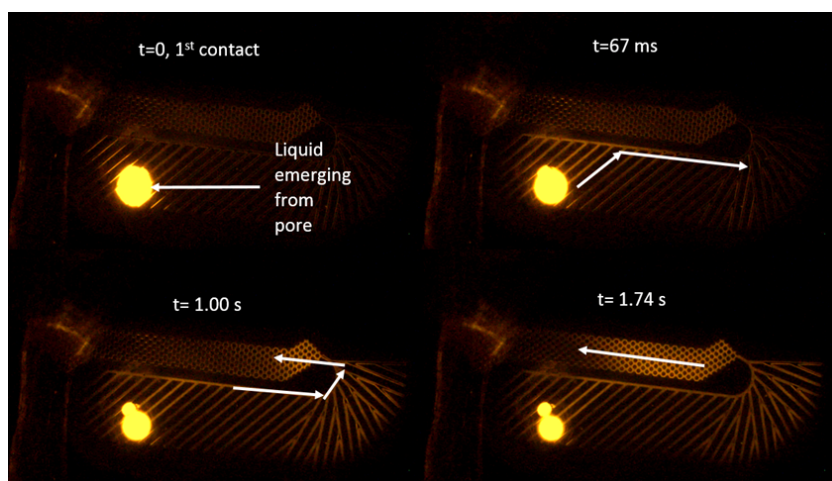


Figure 3.15 – Capture and flow of a droplet from the artificial skin.

This experiment showed clearly that the open microfluidics is capable of capturing, transporting and storing minimum quantities of analyte gathered from a wide area, autonomously and with a tunable flow rate. Figure 3.16 shows the integration of one of the possible microfluidics design on top of our sensing chip. The area from which sweat can be gathered is now wider and the analyte gets to the capillary pumps after contacting the miniaturized QRE and twelve different sensors.

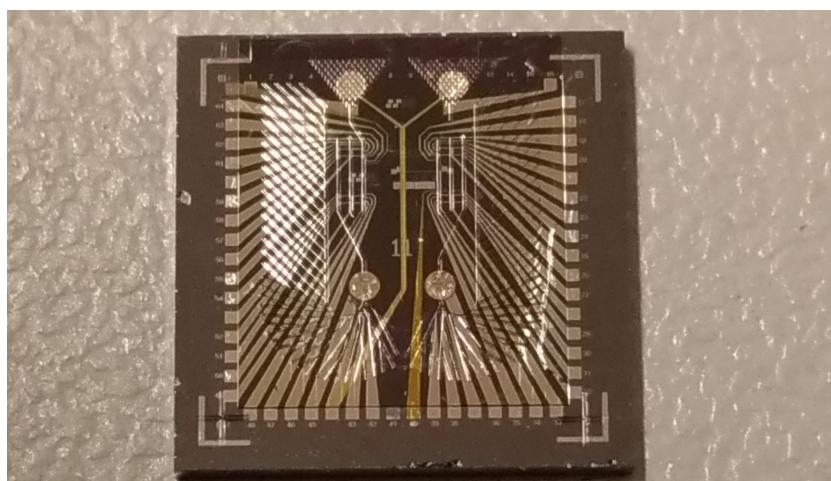


Figure 3.16 – Microfluidic sample on a sensing chip.

3.2 Functionalization

As we have seen in subsection 1.3.2, the sensing gate of a normal ISFET can be used to measure pH thanks to its sensitivity to the hydrogen ions concentration in the analyte. However, the sensing area is not automatically able to selectively sense other ion species, which therefore need the employ of a functionalization layer of some kind. The creation of such layers has been performed by Dr. Negar Moridi, Dr. Johan Longo and Dr. Neil Ebejer.

In this project, two different functionalization procedures have been employed:

1. Self-Assembled Monolayer (SAM) of thiolated ion-sensitive crown ethers deposited on a layer of sputtered gold.
2. Ion-Selective Membrane (ISM) containing ionophores specific for a given ion.

In this section we will present them separately and discuss their respective performances.

3.2.1 Ion-Sensitive crown ether SAM

The name "Self-Assembled Monolayer" comes from the tendency of some long molecules on a solid surface to autonomously arrange themselves in an ordered fashion. This phenomenon is due to the chemical bond formation between the molecules and the surface and to interactions amongst the molecules themselves [117]. In order to create a sensitive self-assembled monolayer on the surface of our sensor, we decided to take benefits of the capability of thiolated molecules to assemble on a gold surface through thiol-gold interaction. For this purpose, we specifically functionalized a commercially available ionophore for Na^+ (15-crown-5-ether) with a thiolated polyethylene glycol (PEG) side-chain. This modification was chosen to improve the capability of the ionophores to self-assemble on the surface as well as adding a degree of freedom to the crown-ether sensitive part, optimizing its interaction with ions. The ionophores have been modified through the reaction of their hydroxyl groups with sulfonide chloride followed by a substitution step using a dithiol-PEG chain. The gold gate of the sensor is then functionalized by dipping in a solution of thiolated ionophores in ethanol for 1 hour, before washing it several times with ethanol to promote the deposition of a homogeneous ion-sensitive SAM on its surface. (Figure 3.17).

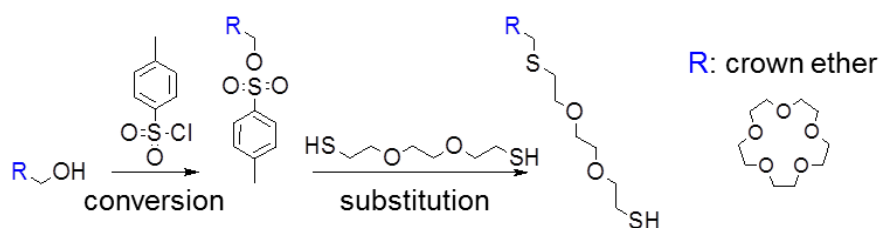


Figure 3.17 – Synthesis of the molecules which will form the SAM.

The obtained monolayer of molecules is schematically represented in Figure 3.18.

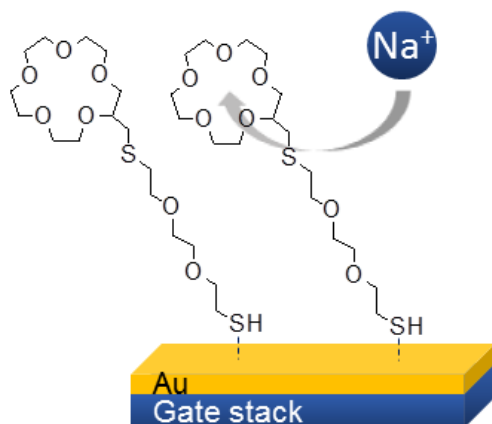


Figure 3.18 – SAM of sodium-selective molecules.

Unfortunately, however dense our SAM can be, the normal sensing properties of the surface won't be completely suppressed: simply depositing such a layer on the gates, hence, would not provide selectivity to our measurements.

A solution to this issue has been proposed in [119]: the surface of gold shows the interesting property of retaining its sensitivity to non-specific ions unchanged after the deposition of a SAM on it, giving the possibility to filter out the non-specific signal with a differential measurement between a functionalized sensor and a non-functionalized one. Figure 3.19 a) and b) show the transfer characteristics response to variations in the NaCl molar concentration in the analyte for the two cases.

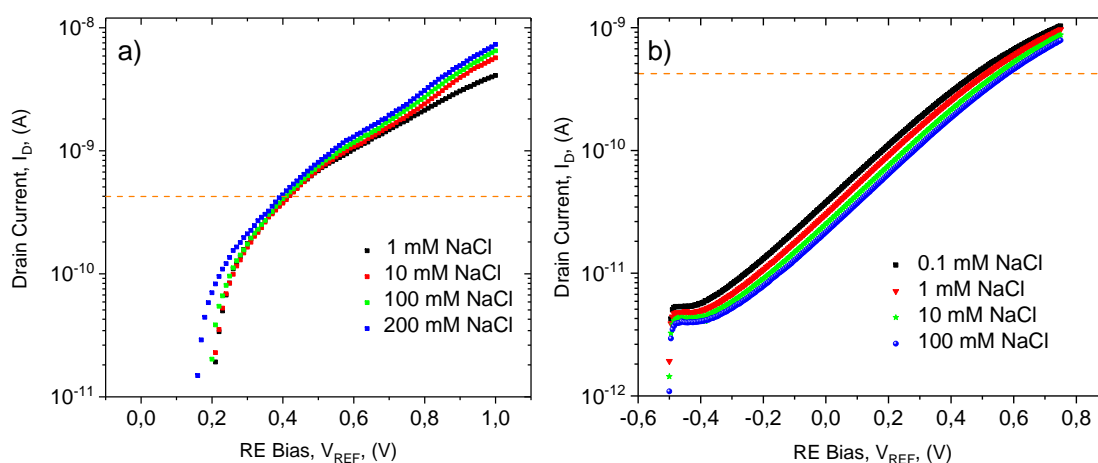


Figure 3.19 – Transfer characteristics response to variations in the NaCl molar concentration in the analyte for a) a functionalized sensor and b) a control sensor. The differences in the shape of the transfer characteristics of the two graphs are probably due to the high device to device variability observed in our first batch and to partial degradation of the SU-8 passivation layer, but do not hinder the differential measurements.

It should be noted that the characteristics of the non-functionalized control sensor are shifting to the right for higher concentrations of NaCl, while the the adsorption of positive ions on the surface is supposed to impose a left-shift, since the actual bias seen by the channel is made more positive. These measurements have been explained in [119] suggesting that the gold surface is adsorbing the negative chlorine ions more efficiently than the positive sodium ones. An alternative, or additional, explanation has been introduced in subsection 1.3.2: the increasing salt concentration could be reducing the sensitivity parameter α , so that a higher V_{th} correspond to the same pH value, as reported for oxides with a limited value of the surface buffer capacitance.

As a consequence, we observe a low response of the functionalized sensor due to the fact that the positive charges of the sodium ions, captured by the crown ethers, are compensating the positive shift given by a higher salt concentration.

To find the differential sensitivity to the concentration of sodium, we extract the V_{th} dependence of the two devices on the ion concentration and subtract the control signal from the functionalized one (Figure 3.20).

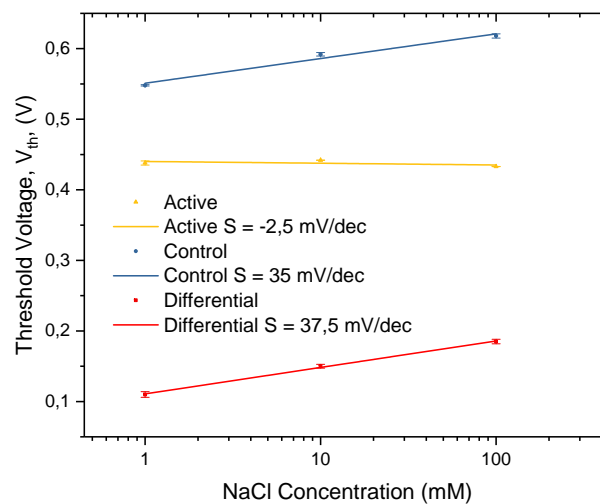


Figure 3.20 – Response of the functionalized and control sensors to the concentration of NaCl in the solution and extracted non-zero differential sensitivity.

The resulting sensitivity to sodium concentration was equal to -37.5 mV/dec [118], in reasonable agreement with the one reported in [119].

For this kind of measurement to be reliable, however, it is not sufficient that the response to the specific ion is modified: it is necessary to verify that the sensitivity of the gold sensing layer to other targets remained, as expected, unchanged after the functionalization. To investigate this property we repeated the measurements with a set of pH buffers ranging from 3 to 8 (Figure 3.21).

The data obtained has again been treated to find the differential cross-sensitivity of the sensing system. The results are plotted in Figure 3.22.

The measured cross-sensitivity, amounting to just 3 mV/pH, shows that this differential sensor

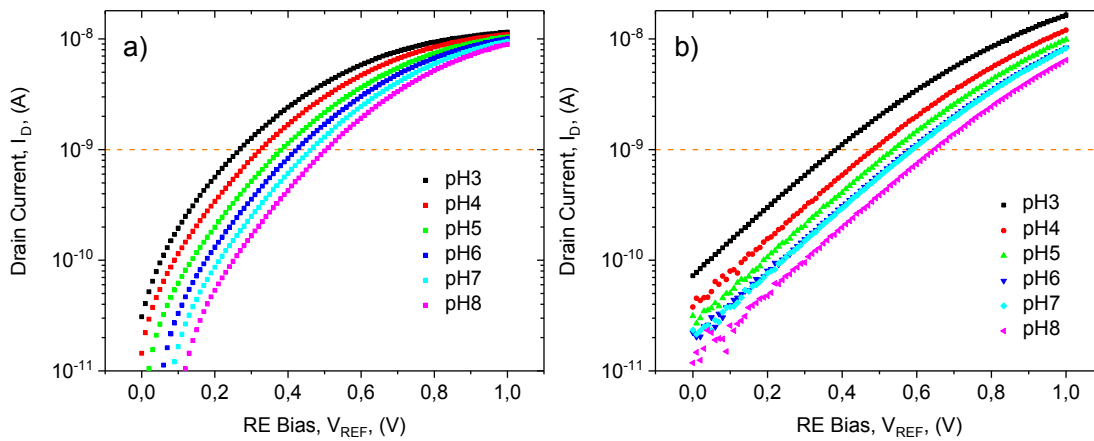


Figure 3.21 – Transfer characteristics response to variations in the pH of the analyte for a) a sensor whose gold gate has been functionalized with a sodium-sensitive SAM and b) a sensor with a clean gold gate.

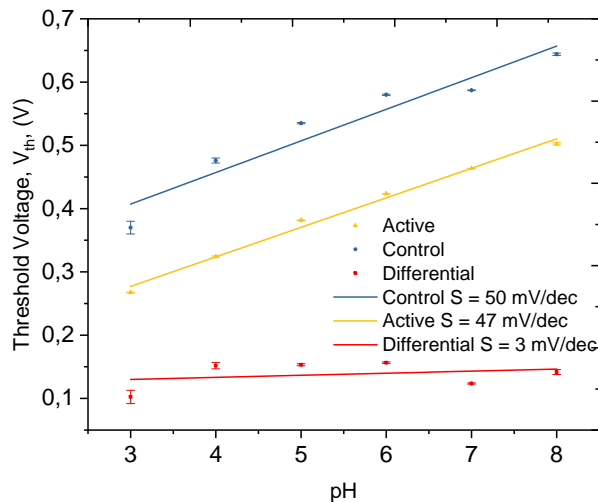


Figure 3.22 – Response of the functionalized and control sensors to the pH of the solution and extracted differential sensitivity. The near-zero value of the differential sensitivity demonstrates that the SAM functionalization doesn't affect the gold sensitivity to non-specific ions.

is able to selectively measure the concentration of sodium ions in a solution.

3.2.2 Ion-Selective Membranes

An alternative strategy to achieve selective ion-sensing, not requiring differential measurements, consists in drop-casting ISMs on the sensing areas. As described in [120], these membranes are made of a mix of bis(2-ethylhexyl) sebacate (DOS) and polyvinyl chloride (PVC).

The sensing mechanism of these membrane is vastly different from that of a SAM and, on top

of that, is also completely independent on the underlying material.

To understand how an ISM is able to sense the concentration of a target ion and discriminate it from competing species, it is necessary to recall the mechanism beneath the formation of a *phase boundary potential* between the membrane and the liquid under test (LUT) [121].

When a salt molecule approaches the interface between the two immiscible solvents, the positive and negative ions composing it can be subjected to non-equal solvation energies in the two phases, *i.e.* the positive ion could be more soluble in the membrane than its negative counterpart. The condition of charge neutrality can not be ignored in the bulk of the two phases, therefore the bulk molar concentrations of positive and negative ions need to remain equal. However, in a layer of just few nanometers of thickness across the phase interface, the different affinities of the two ions could create a *charge separation layer*, where an excess of cations is observed in the membrane side and an excess of anions can be found in the liquid side (Figure 3.23).

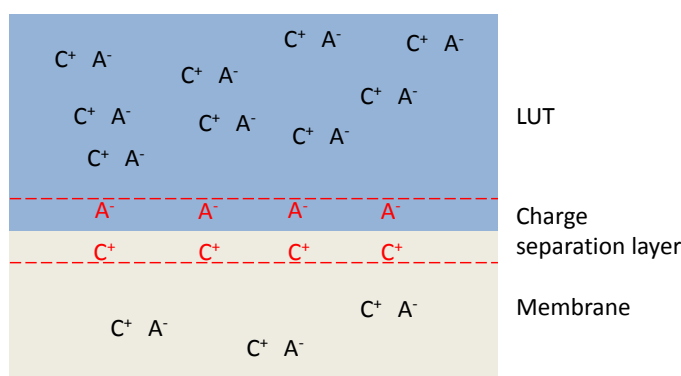


Figure 3.23 – Separation of positive (C⁺) and negative (A⁻) ions of a salt at the interface between two phases, according to their solubility.

It is important to clarify that, even though the solubility of a cation in the membrane is higher than that of its related anion, both positive and negative ions have much higher solubilities in the aqueous phase than in the organic membrane, and therefore the equilibrium concentration of salt will be much lower in the latter. To give some order of magnitude, in [121] it is reported that the transfer of nitrate ions from 1,2-dichloroethane to water is favored by 33.9 kJ/mol, which, according to the relation reported in [122], gives a concentration ratio in the water/organic phase of about 8×10^5 .

The bias generated at the phase interface by the charge separation (Electromotive Force, EMF) is described by Nernst law:

$$EMF = E^0 + \frac{k_B T}{q} \ln \frac{[C^+]_{LUT}}{[C^+]_{mem}}, \quad (3.1)$$

where E^0 is a constant dependent on the chemical properties of the ions and of the two phases and $[C^+]_{LUT}$ and $[C^+]_{mem}$ are, respectively, the cations concentrations in the LUT and in the organic membrane.

Increasing the concentration of salt in the liquid would not modify the value of EMF, because the solubility ratio would not be changed (unless extremely high concentrations are reached). As a consequence, any variation of $[C^+]_{LUT}$ will bring to a proportional variation of $[C^+]_{mem}$ and their ratio will remain constant.

In order to enable sensitivity to the salt concentration it is necessary to fix $[C^+]_{mem}$ to a definite value, as independent as possible on $[C^+]_{LUT}$.

Achieving this condition requires the addition of two more ingredients to the membrane. The first is a high molar concentration of hydrophobic anions such as a tetraphenylborate derivative which, because of the charge neutrality law, will enforce a high cation concentration in the membrane. These anions are usually called *ionic sites*. The second ingredient to add is an even higher molar concentration (conventionally twice as high as that of the ionic sites) of specific *ionophores*, able to selectively bind to the target ion in which we are interested. This second element will increase the solubility of the target ion in the membrane, making it the preferred cations for compensating the charge of the ionic sites (Figure 3.24)

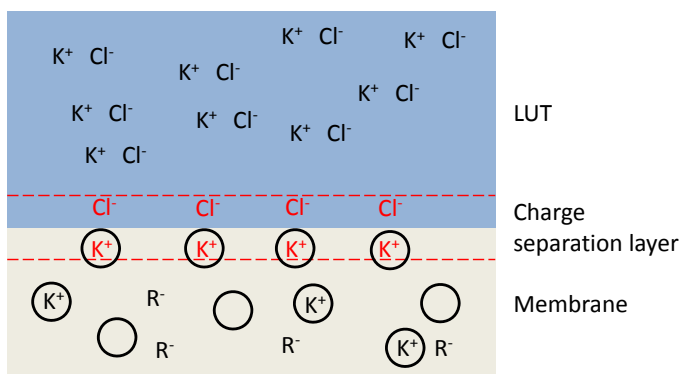


Figure 3.24 – ISM embedding ionic sites (R^-) and specific ionophores (black circles). In this figure, a specific salt (KCl) has been taken as an example to underline the role of the different elements.

From now on, we will consider potassium as our target ion and KCl as the salt employed, as a mean to simplify the explanations. The same concepts will however hold valid for any target cation.

If $[K^+]_{LUT}$ is increased or diminished, potassium ions will still be able to penetrate or leave the membrane, but, given their high starting concentration, their relative variation will be negligible and therefore the ratio $[K^+]_{LUT}/[K^+]_{mem}$ will vary. At the same time, if the concentration of another salt in the LUT is varied, a proportional variation will still follow in to the membrane, so that no effect on the EMF is observed.

This selectivity mechanism is the reason why we need a higher concentration of ionophores with respect to ionic sites. In a membrane with an excess of ionic sites, in fact, the ionophores would be saturated before complete charge compensation is achieved. As a consequence, the membrane would absorb and retain the remaining amount of cations needed for neutrality without any preference for the chosen target. High starting concentrations of competitor ions in the ISM would determine an EMF dependence on their concentration in the LUT, for

the same sensing mechanism explained above, so that cross-sensitivity would ensue and the selectivity would be compromised.

For clarity, let's consider from a mathematical point of view the case in which $[K^+]_{LUT}$ is multiplied by a factor C and $[Na^+]_{LUT}$ is multiplied by a factor D on a potassium-functionalized ISM.

The $[K^+]_{mem}$ will be considered constant for the reason explained above. The initial EMF can be defined as:

$$EMF_0 = E_K^0 + \frac{k_B T}{q} \ln \frac{[K^+]_{LUT}}{[K^+]_{mem}} + E_{Na}^0 + \frac{k_B T}{q} \ln \frac{[Na^+]_{LUT}}{[Na^+]_{mem}}. \quad (3.2)$$

The total EMF is given by the sum of the two independent contributions. Multiplying by a factor C the LUT concentration of K^+ and by a factor D that of Na^+ and waiting for equilibrium, the new EMF will be defined as:

$$EMF_1 = E_K^0 + \frac{k_B T}{q} \ln \frac{C[K^+]_{LUT}}{[K^+]_{mem}} + E_{Na}^0 + \frac{k_B T}{q} \ln \frac{D[Na^+]_{LUT}}{D[Na^+]_{mem}}. \quad (3.3)$$

The potential variation ΔV at the membrane interface will therefore be:

$$\begin{aligned} \Delta V &= EMF_1 - EMF_0 = \\ &= \cancel{E_K^0} - \cancel{E_K^0} + \frac{k_B T}{q} \left(\ln \frac{C[K^+]_{LUT}}{[K^+]_{mem}} - \ln \frac{[K^+]_{LUT}}{[K^+]_{mem}} \right) + \\ &+ \cancel{E_{Na}^0} - \cancel{E_{Na}^0} + \frac{k_B T}{q} \left(\ln \frac{D[Na^+]_{LUT}}{D[Na^+]_{mem}} - \ln \frac{[Na^+]_{LUT}}{[Na^+]_{mem}} \right). \end{aligned} \quad (3.4)$$

Employing the properties of the logarithms we can rewrite this equation as

$$\begin{aligned} \Delta V &= \frac{k_B T}{q} \left(\ln(C[K^+]_{LUT}) - \ln([K^+]_{mem}) - \ln([K^+]_{LUT}) + \ln([K^+]_{mem}) \right) = \\ &= \frac{k_B T}{q} \ln \frac{C[K^+]_{LUT}}{[K^+]_{LUT}} = \frac{k_B T}{q} \ln(C). \end{aligned} \quad (3.5)$$

Therefore the interface potential between the ISM and the LUT will depend only on the concentration of the specific ion for which it is functionalized and, provided a sufficient concentration of ionic sites, will show a Nernstian response of 59 mV/dec at room temperature.

An alternative explanation found in the literature [123] doesn't mention the necessity of ionic sites in the membranes and indicates the ionophores are the sole element needed for sensitivity and selectivity: the dipole formation due to the difference in solubility between the positive target ions (for which ionophores are provided) and their corresponding negative ions will reportedly determine the appearance of an interface potential, whose magnitude will depend on the ion concentration in the LUT. The lower solubility in the membrane of competing ions will determine formation of weaker non-specific dipoles, providing selectivity.

In this work, the sodium-selective membranes have been produced mixing together Na ionophore X (1% w/w), Sodium tetrakis[3,5-bis(trifluoromethyl)phenyl] borate (Na-TFPB) (0.55% w/w, for the ionic sites), PVC (33% w/w), and DOS (65.45% w/w). 100 mg of this mixture have been dissolved in 660 μl of tetrahydrofuran (THF). Similarly, the potassium-selective membranes were made of valinomycin (2% w/w, as ionophore), Sodium tetraphenylborate (Na-TPB) (0.5% w/w, for the ionic sites), PVC (32.7% w/w) and DOS. The same amount of mixture has been dissolved in 350 μl of cyclohexanone.

The structure of the ionophore used for potassium is shown in Figure 3.25.

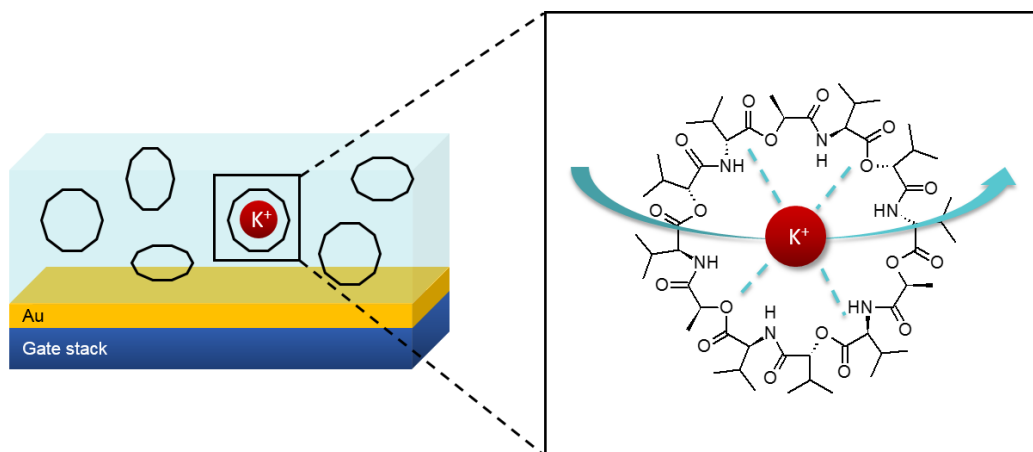


Figure 3.25 – ISM with ionophores for potassium.

In order to test the selectivity of the membranes towards non-specific ions, we have extracted the functionalized ISFET transfer characteristics not only with a set of known dilutions of the target ion, but also for a solution with a high concentration of a competitor specie (sodium for potassium-functionalized sensors and vice versa). In agreement with equation 3.5, the threshold voltage of the sensors will shift to more negative values for higher concentrations: we can evaluate the selectivity of the membranes measuring the ratio between the concentration of specific and non-specific ions needed to read the same threshold voltage variation (Figure 3.26).

As stated, the measurements made with an ISM don't need to be compared with a control device to extract the ion sensitivity (or, in case of a sensor already calibrated, the ion concentration value). The value of RE bias corresponding to a Drain current of 100 nA have been extracted and plotted, as a function of the target ion concentration in Figure 3.27.

It can immediately be noticed that the sensitivities to the target ion concentrations are now higher than what we achieved with the SAMs, and appear perfectly nernstian.

Having calibrated the sensors response to their respective target ions, we can calculate the target ion concentrations corresponding to the readings extracted for a 50 mM concentration of the competitor ion, shown in Figure 3.26.

For the sodium-functionalized sensor, the bias of the RE at which we achieve the flag I_D of 100 nA, measuring an analyte containing a 50 mM concentration of potassium, amounts to 0.276 V. The sodium concentration needed to extract the same V_{th} value is 1 mM, therefore

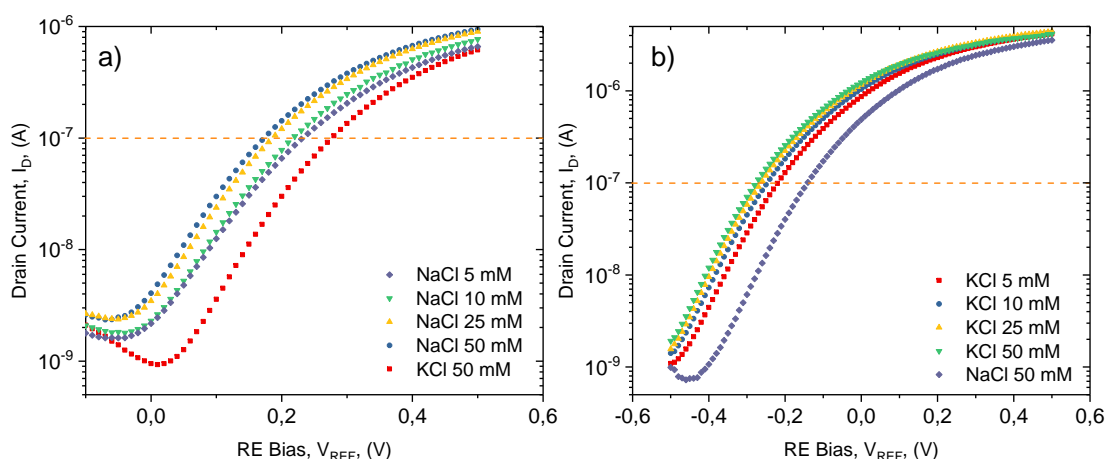


Figure 3.26 – Transfer characteristics response to variations of the sodium (a) or potassium (b) concentration in the analyte measured with the respective ISM. The results of a test with a high concentration of a competitor ion have also been reported.

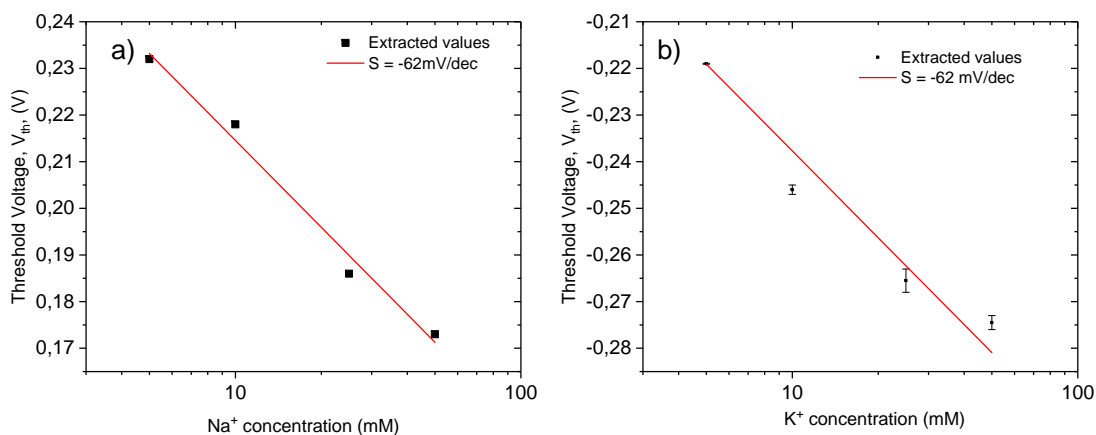


Figure 3.27 – Threshold voltage dependence of the sodium-selective sensor on the sodium concentration (a) and of the potassium-selective sensor on the potassium concentration (b). Data needed for the error bars of graph (a) have been lost.

the selectivity for this membrane amounts to 50.

We can evaluate the selectivity of the potassium-functionalized sensor in the same way, extracting a selectivity value of 172 [124].

A more in-depth testing of the selectivity of these same membranes has been later carried out by Dr. Junrui Zhang, employing as sensor his BEOL-modified foundry-made ISFETs [125]. This further testing consisted in measuring the response of ISMs to variations in the concentrations of a set of competing ions.

The results for both Na-functionalized and K-functionalized ISMs are shown in Figure 3.28. From these values, it appears clear that the ISMs, on top of being able to operate without a differential architecture, reducing the complexity and power consumption of the system, are also more sensitive and reliable with respect to a SAM of thiol chains functionalized with a

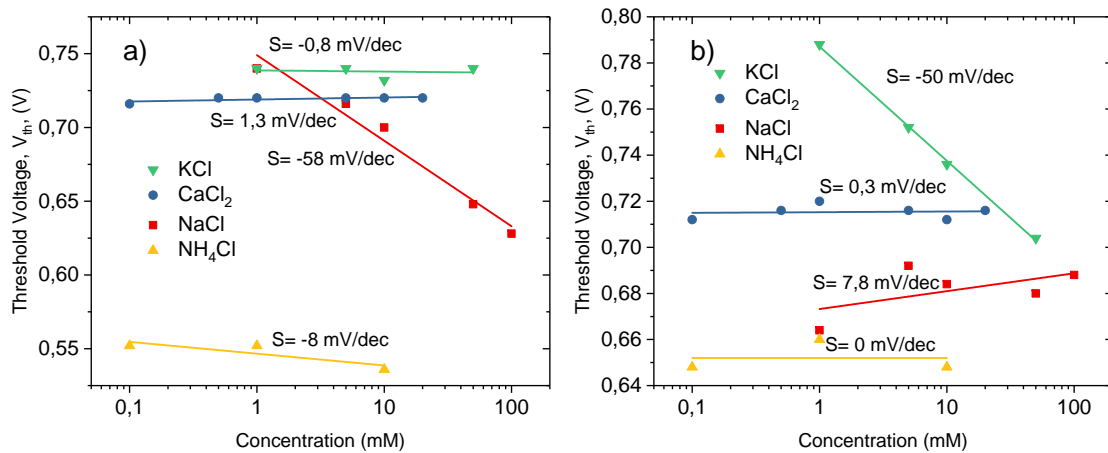


Figure 3.28 – Threshold voltage dependences of the sodium-functionalized (a) and potassium-functionalized (b) ISMs to their respective target ions and to competing species.

crowns ether. A last test for the ISMs consisted in measuring at the same time variation of Na^+ and K^+ concentrations in the same solution, with both membranes. The results are shown in Figure 3.29.

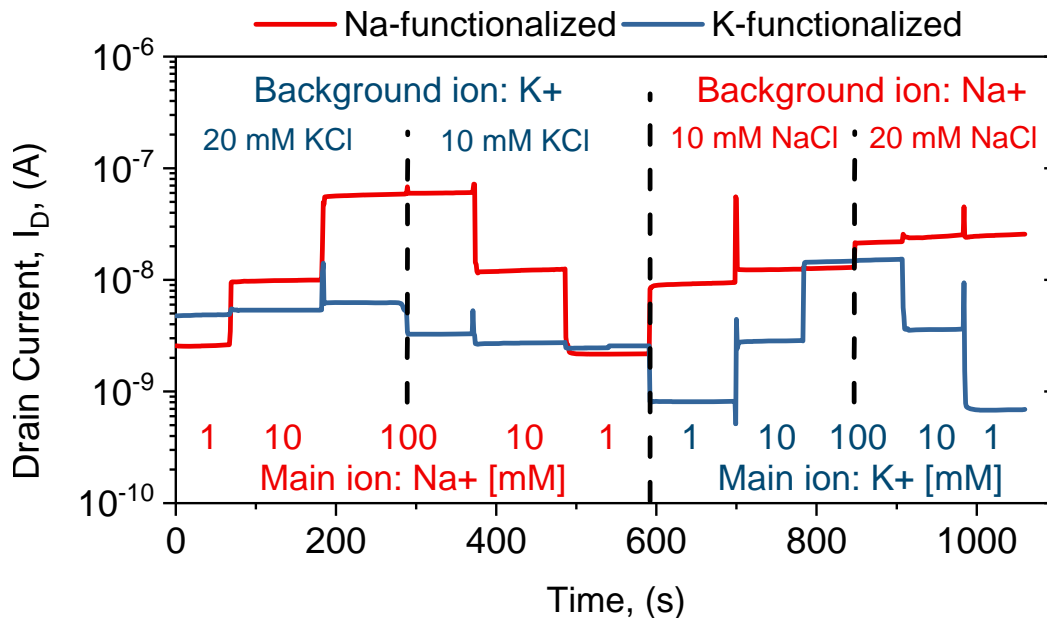


Figure 3.29 – Real-time monitoring of the concentration of sodium and potassium in a solution with a sodium-functionalized and a potassium-functionalized ISFET.

It is clear that, even when the concentrations of the two competing ions are changed at the same time, the ISMs are able to selectively sense only their ion of interest, with minimal responses to non-specific chemical signals. Furthermore, ISMs are easier to deposit locally (Figure 3.30), so that different sets of sensors can be individually functionalized on the same

chip.

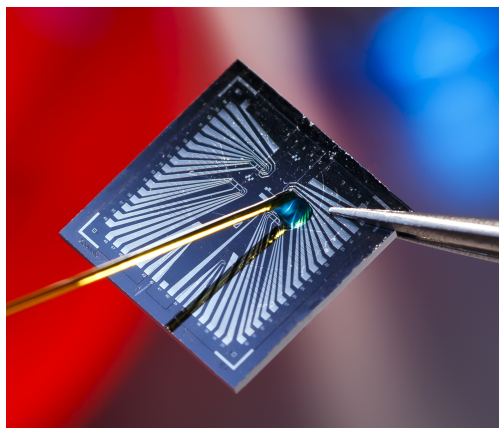


Figure 3.30 – Drop casting of the ISM on a set of sensors on the chip.

In the end, for our sensing system the employ of ISMs resulted definitely preferable. However, for applications in which the thickness of the membrane, amounting to several micrometers, would not be compatible with the microfluidics or other components of a device, the nanometric-thick SAMs should be considered.

3.3 Miniaturized Quasi Reference Electrode

The ion measurements shown so far have been performed with a commercial RE, consisting of an Ag/AgCl wire immersed in a 3 M dilution of KCl. The electrical contact between the analyte and the RE was achieved through a membrane, so that no liquid mixing could take place, as anticipated in subsection 1.3.2.

The employ of a commercial RE, however, is not suitable for the creation of a miniaturized fully integrated wearable system: it is therefore necessary to design a compact version of this element, compatible with wafer-level fabrication processes. This task has been tackled by Dr. Erick Garcia Cordero, Dr. Raffaele Cosimati, Dr. Fabien Wildhaber and MSc. Amira Muhech. As mentioned, in the commercial, bulky version of the AgCl RE, each component is meant to solve a portion of the specific issues related to the control of the potential of a liquid solution with a solid state electrode: the AgCl layer allows a reversible reaction at the interface with the liquid, able to discharge the built-up potential between the metal and the solution, the concentrated KCl solution, in which the electrode is immersed, saturates the dependence of the electrode potential on the chlorine concentration in the liquid and prevents the exhaustion of the AgCl layer and, finally, the membrane at the interface between the concentrated KCl solution and the analyte solution provides electrical connection, through the embedded salt bridges, to the liquid to be measured, while preventing physical mixing. When designing an alternative structure for the RE, each of these element has to be maintained or efficiently substituted, to keep its operability.

One of the simplest methods for miniaturization of a RE consists in abandoning the KCl

saturated solution entirely and putting the AgCl electrode in direct contact with the LUT. The potential drift due to the depletion of chlorine on the surface is mitigated (or rather delayed) by simply depositing a thicker layer of AgCl. This can be achieved by depositing a thick layer of silver by electroplating (which gives properties closer to that of bulk silver, allowing formation of a sensibly thicker layer of silver chloride), followed by chlorination in a FeCl₃ solution [64]. The first RE prototype for this project has been fabricated with a similar procedure, depositing 1 μm of silver by sputtering and chlorinating its surface by anodization in an FeCl₃ solution. A low current density of 2 mA/cm² has been employed to achieve smaller salt grain size, better adhesion and higher uniformity, in accordance with [126]. An SEM image showed that the process had generated an AgCl layer with a thickness of about 80 nm (Figure 3.31).

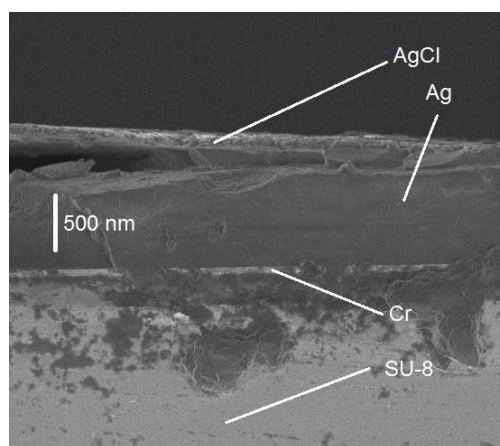


Figure 3.31 – AgCl formation on a 1 μm thick layer of silver sputtered on SU-8. The thin adhesion layer of chromium is also visible.

The stability of these devices has been tested with Open Circuit Potential (OCP) measurements against a commercial AgCl RE in a 3 M KCl solution. The duration of the test has been set to 10 hours. The results have shown both poor long-term stability (with a potential variation between 200 and 500 mV for the tested samples) and high noise characteristics, larger than 50 mV. It was concluded that RE fabricated with this procedure could only be operational for up to 4 hours.

It also has to be noted that a thicker layer of AgCl cannot completely make up for the removal of the KCl saturated solution, as the other function of this layer of liquid was to saturate the dependence of the electrode potential on the chlorine ion concentration in the LUT. The fabricated electrode, therefore, featured a further source of instability, which could affect the readings of the ISFETs. The term "Reference Electrode" is in fact improper for electrodes featuring a sensitivity to the chlorine ions: this kind of devices are generally referred to as *Quasi Reference Electrodes* (QRE).

For the reasons explained, the strategy of simply leaving the AgCl electrode in contact with the LUT has been abandoned.

An alternative strategy for the miniaturization of the RE has been proposed in [127]. Here the Ag layer had a thickness of only 180 nm and was chlorinated with the method described

3.3. Miniaturized Quasi Reference Electrode

before, but the dissolution of the AgCl layer was prevented by adding a membrane prepared with 79.1 mg of Polyvinyl butyral (PVB) and 50 mg of NaCl dissolved in 1 ml of methanol. This membrane acts in the same way as the KCl saturated solution, making the RE stable not only in time, but also for varying concentration of chlorine ions in the LUT, making the term "Quasi-Reference Electrode" arguably improper, as this system could be considered a definite RE.

Our second FD SOI ISFET batch had miniaturized REs (mREs) fabricated with this procedure: the appearance of the prototype with the saturated membranes is shown in Figure 3.32.

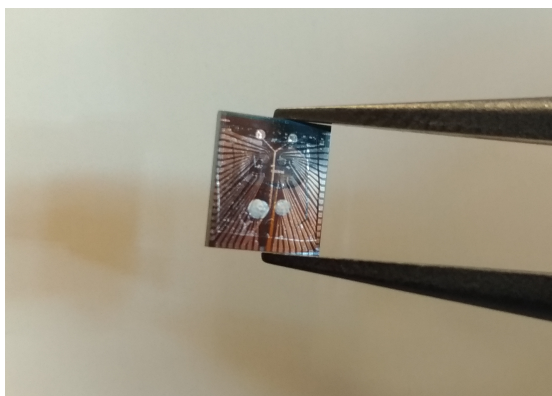


Figure 3.32 – ISM-functionalized chip featuring a pair of miniaturized RE on the bottom metal seed. The Cl^- -saturated membranes covering them are also visible.

The stability in time of this RE has been tested against that of a commercial RE (MI-16-702 Microelectrodes Inc.RE), employing an HP 4156A parameter analyzer (Hewlett-Packard JP, Tokyo, Japan). The results (Figure 3.33) showed that this new electrode presents no significant drift for up to 14 hours and its noise remained within ± 2.5 mV.

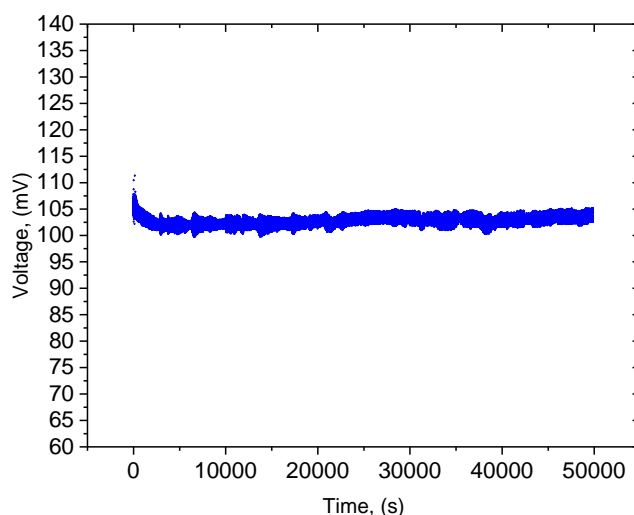


Figure 3.33 – Stability measurement of the membrane-coated miniaturized RE. Relevant potential drift is observed only after 14 hours.

3.4 Lab On SkinTM characterization

So far, each component of the Lab On Skin has been characterized individually and the measurements for ion concentration and pH have only been performed by data analysis on sets of transfer characteristics.

In order to enable real-time monitoring of the user's sweat, however, we need all of these components to operate together and to provide data which we can immediately relate to biological parameters.

It has to be noted that, at the current stage, the electrical connections for the readout of the chip is still implemented with ultra-low current point probes (Model # 73CT-CMIA/50 replaceable coax probes are mounted on DCP-150R probeholders, which are in turn mounted on DCM 200 Series micromanipulators), which are not compatible with the capillary microfluidics, forcing us to exclude it from the test until a suitable readout system will be introduced. The most straightforward method to extract readings in real-time from an ISFET consists in applying a constant bias on the RE and monitoring the Drain current, as explained in subsection 1.3.2. While this procedure is easily implemented for sensing the parameters of an unknown liquid on a calibrated sensors, the characterization itself of the system, including evaluation of the response time, is not straightforward: we need, in fact, to provide a continuous flow of solutions with known parameters with no gap between two consecutive ones.

This is achieved with a Low Pressure Stream Selector (Cheminert C25-3188), which allowed us to switch the liquid drawn by our syringe pump in withdrawal mode between five samples with five different pH/ion molar concentrations (Figure 3.34)

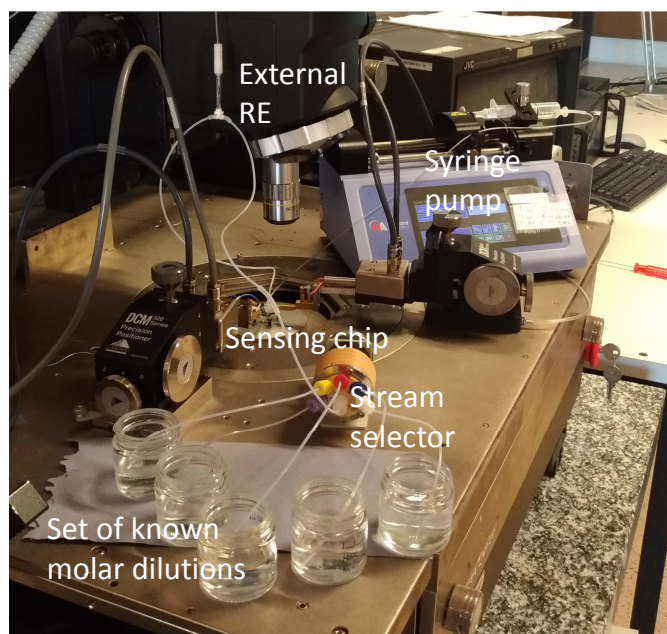


Figure 3.34 – Measurement setup for the characterization of the functionalized sensor in real-time measurement mode.

The results obtained for sodium and potassium samples are shown in Figure 3.35.

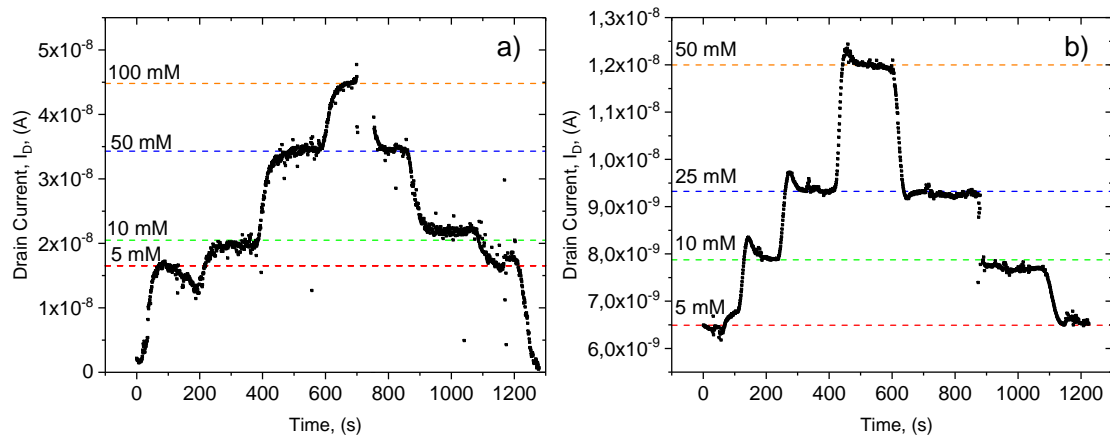


Figure 3.35 – Real-time measurement of (a) sodium and (b) potassium concentration in the LUT.

The response time measured here, amounting to about 40 seconds for sodium and to about 20 seconds for potassium, represents an upper limit of the actual time needed by our sensors to adjust its drain current to the new chemical composition, the actual sensor response time being probably lower. This is because, even though the flux of liquid in the microfluidics is completely laminar, so that no liquid mixing is expected, a gradient-driven diffusion of ions can in fact take place: as a consequence, the transition from one molar concentration to the next one is not completely abrupt.

The measured response time, however, is definitely compatible with the physiological evolution rate of chemical parameters in sweat.

So far we have demonstrated the capability of the ISFETs and ISM to operate together, but the reported measurements have been performed with an external flow-through RE and not with our miniaturized version. To check the operability of the ISFETs-ISM-mREs system, we have deposited a thin perimeter of PDMS on the chip surface (visible in Figure 3.32), to create a hydrophobic barrier able to confine a droplet of LUT on the center of the chip, in contact with both sensing areas and mREs. No liquid flow is provided in this case and the open system is no longer immune from evaporation, therefore measurements had to be performed in a short time to prevent variation of the target salt molar concentration.

The potassium sensitivity of one of our functionalized sensor, featuring an embedded mRE, has been measured according to this procedure and the results are shown in Figure 3.36.

The inset of Figure 3.36 (a) shows that the hysteresis of the sensor was limited to about 5 mV for a full V_{REF} sweep, making the measurements extremely reliable. Furthermore, the V_{th} dependence on the potassium molar concentration, shown in Figure 3.36 (b), resulted perfectly linear and nernstian. Real-time measurements have also been performed with this integrated sensor, but since, as stated, we were not able to use the PDMS stamp, fully continuous measurements couldn't be implemented. The procedure for the sensor characterization consisted therefore in measuring each solution in the same order as for the previous tests,

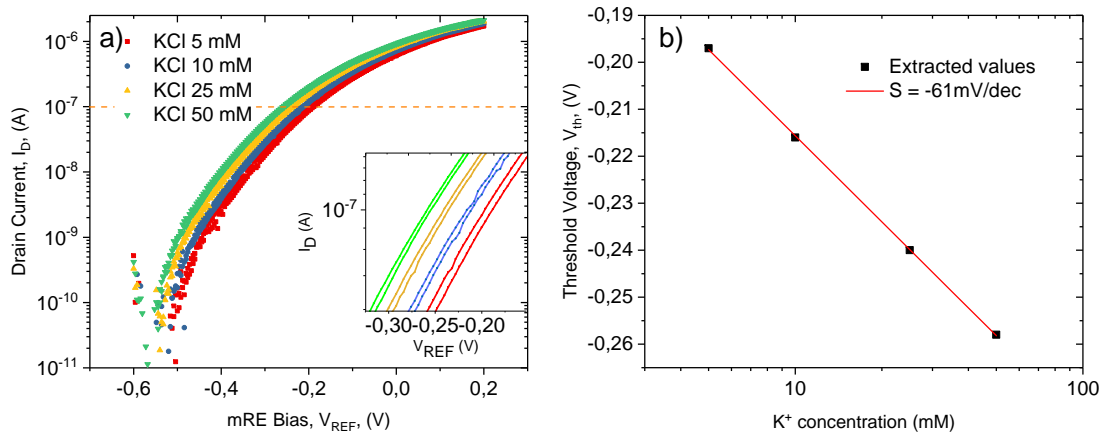


Figure 3.36 – (a) Transfer characteristics response to variation of the potassium concentration in the analyte, measured with the K-functionalized ISM and the embedded mRE. (b) Threshold voltage dependence of the integrated system on the potassium concentration.

quickly cleaning the chip between two measurements. We removed the few seconds of dry conditions from the data to facilitate the reading. The results are shown in Figure 3.37.

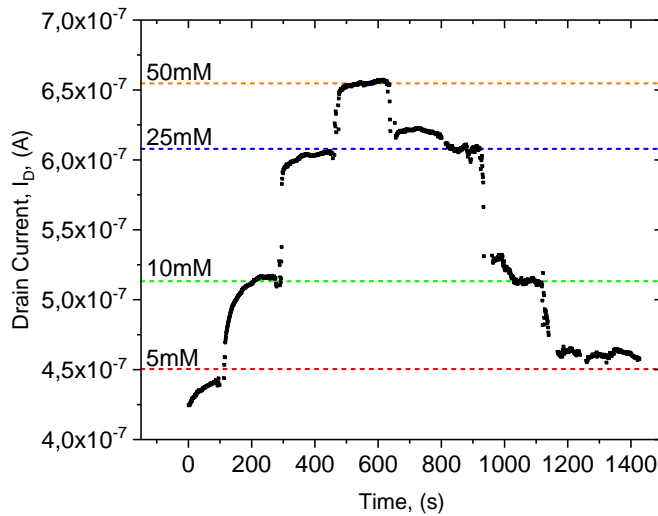


Figure 3.37 – Real-time measurement of potassium concentration in the LUT performed with the K-functionalized ISM and the embedded mRE.

It can be observed that the current levels related to a certain molar concentration are stable and mostly independent on the previously measured values, demonstrating that the integration of ISFETs, ISMs and mRE can in fact be employed for real-time measurements.

The various components of the LOS and their use are summarized with the diagram of Table 3.1.

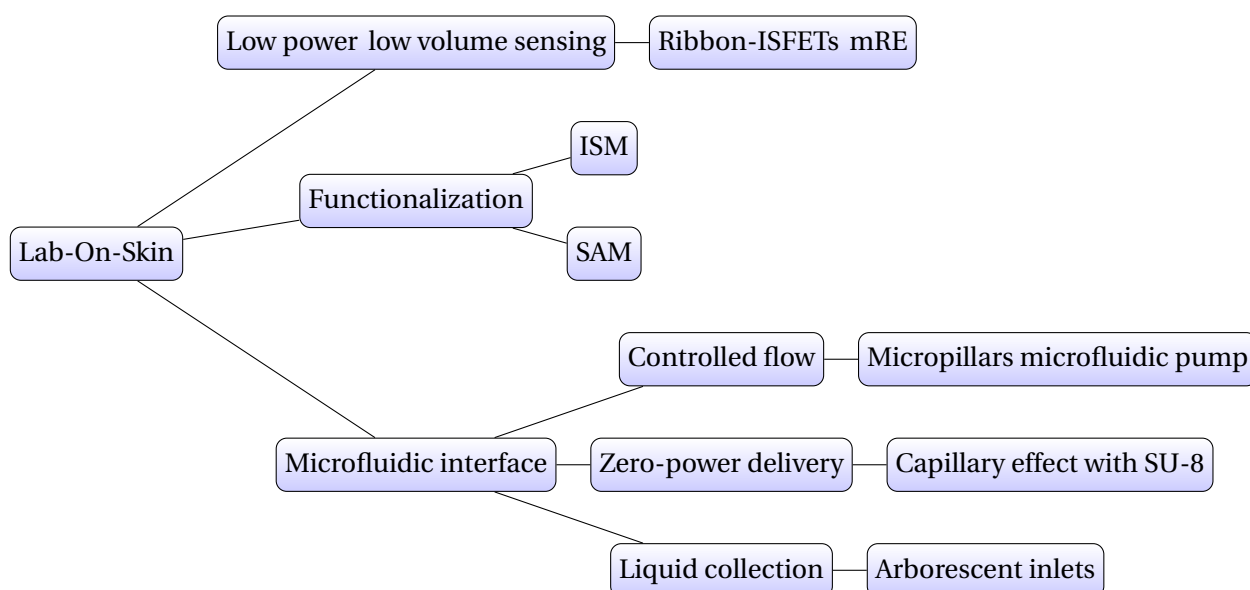


Table 3.1 – Lab-On-Skin diagram.

3.5 Summary

In this section, the most important achievements regarding the fabrication and monolithic integration on our ISFET chip of the other components of the Lab on SkinTM are outlined.

- **Technical outcomes:**

- Cleanroom fabrication of a passive SU-8 capillary microfluidics with the following properties:
 - * Channel thickness = 20 μm , channel width = 30 μm ;
 - * Arborescent inlets;
 - * Capillary pump based on pillars, imposing a flow rate of 4.2 nl/min.
- Definition of SAM for Na⁺ functionalization with the following properties:
 - * 15-crown-5 crown ether;
 - * -37.5 mV/dec differential sensitivity to Na⁺;
 - * -1 mV/pH cross sensitivity towards pH.
- Definition of two ISMs for Na⁺ and K⁺ functionalization with the following properties:
 - * Na ionophore X and valinomycin, respectively, as ionophores;
 - * -62 and -55 mV/dec sensitivity, respectively, to their specific ion;
 - * 50 and 172 selectivity, respectively, towards competing ions.
- Definition of a miniaturized RE with the following properties:
 - * Stability throughout the 14 hours of testing;

- * Noise limited to ± 2.5 throughout the 14 hours of testing;
- * No sensitivity to Cl^- concentration in the LUT.

- **Results highlights:**

In this chapter we have presented the design, fabrication and integration on chip of a set of technologies needed for wearable sweat monitoring.

The design and definition of a robust process flow for a SU-8 capillary microfluidics, featuring wide collection areas and a capillary pump able to control the sweat rate, is reported, highlighting the importance of the arborescent structure of the inlets and of the sizing and positioning of the pillars in the microfluidics pump.

Two different functionalization layers have been produced and characterized: a SAM for Na^+ sensing and two ISMs functionalized for Na^+ and K^+ . While the SAM showed the capability of selectively sensing the Na^+ concentration in the LUT employing a differential measurement, the two ISMs resulted superior in terms of sensitivity, selectivity and ease of integration on the chip and have therefore been selected as preferred functionalization layer.

A miniaturized RE has been fabricated on-chip to remove the necessity of employing cumbersome commercial RE, which can not be integrated in a wearable device. Encapsulation in an hydrophobic membrane allowed achieving long-term stabilization.

The full system has been tested with various pH buffers and known ion dilutions, showing the capability of monitoring in real time the chemical parameters of the LUT.

4 Negative Capacitance ISFET

As seen in subsection 1.3.1, Field-Effect Transistors are characterized by a lower limit to the amount of gate bias needed to switch them from an "ON" state to an "OFF" state or viceversa. In particular, it is not possible to increase or reduce by one order of magnitude the Drain current of a conventional MOSFET with a V_G variation lower than $\frac{k_B T}{q} \ln(10)$, equal to about 60 mV, at room temperature. This minimum value comes from the Boltzmann energy distribution of the electrons in the semiconductor, and is therefore completely independent on the design of the device. Such limitation, often referred to as *Boltzmann Tyranny*, is now widely regarded as the most immediate obstacle to the prosecution of Moore's Law. Even though the physical dimension of the devices could still be reduced, in fact, their supply voltage needs to remain the same, otherwise circuit designers would be forced to choose between not switching off completely the devices (high I_{OFF} , which would bring to high power consumption while they are not operating) or not switching them on completely (low I_{ON} , which implies slower computations). Having to operate smaller, more densely packed devices with the same bias brings the double issue of excessive power consumption and excessive heat generation of the FETs [128]. This limit in the SS of the transfer characteristics also affects the maximum current sensitivity S_{out} achievable by the ISFETs, limiting the I_D variation for a given ion-related ΔV_{th} . One of the solutions proposed to overcome this issue is the application of a *Negative Capacitance* (NC) booster integrated in the gate stack of transistors [129], which would allow steepening the SS of the devices without the need of employing an entirely different current injection principle, such as for the Tunnel FETs.

In this chapter we will first present a conceptual and mathematical understanding of the NC effect and its application to MOSFETs and, in particular, to our first batch of UTB FD SOI MOSFETs. Afterwards, the application of the same principle to ISFETs will be presented and discussed, supported by some modeling and experimental results.

4.1 Negative Capacitance for steep-slope switches.

The NC technology employs a specific class of materials which goes under the name of *ferroelectrics* (FE) [130]. Materials belonging to this group (such as PbTiO_3 , BaTiO_3 , Si-doped

Chapter 4. Negative Capacitance ISFET

HfO₂, Pb(Zr_xTi_{1-x})O₃ (PZT) etc.) are characterized by two separated stable polarization states. Applying a bias to these materials, it is possible to make them switch from one state to the other.

The rate of change in the polarization of such materials is described by the Landau-Khalatnikov equation [146].

$$\rho \frac{dQ_F}{dt} = - \frac{dU}{dQ_F}. \quad (4.1)$$

Here ρ (>0) represents the frictional inertia of the system, Q_F is the polarization charge and U is the free energy of the FE material, which, in second order approximation, can be written as:

$$U = \frac{\alpha_{FE}}{2} Q_F^2 + \frac{\beta_{FE}}{4} Q_F^4 - Q_F V_F, \quad (4.2)$$

where V_F is the voltage across the capacitor and α_{FE} and β_{FE} are anisotropy constants ($\alpha_{FE} < 0$) defined as:

$$\alpha_{FE} = - \frac{\sqrt{3}}{2} \frac{V_C}{Q_0} \quad \beta_{FE} = \frac{\sqrt{3}}{2} \frac{V_C}{Q_0^3}. \quad (4.3)$$

V_C and Q_0 represent, respectively, the coercive potential, *i.e.* the potential that can be applied before depolarization, and the remnant polarization charge, which is the charge still stored in the FE when the external bias drops to 0.

It is possible to visualize the two separated polarization states by plotting Equation 4.2 (Figure 4.1).

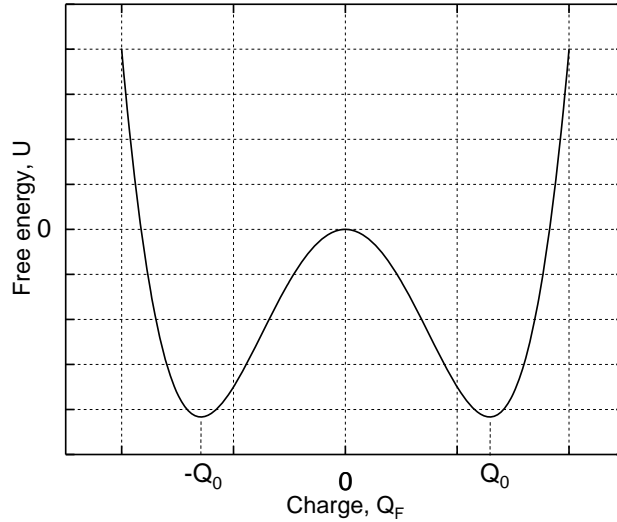


Figure 4.1 – Energy landscape of a ferroelectric material. The two local minimums correspond to the remnant polarization charge Q_0 .

It is easy to remark the two local minimums of the system, representing the stable conditions for the polarization. To switch from one state to the other, inducing the characteristic phase

4.1. Negative Capacitance for steep-slope switches.

transition of these materials, we need to overcome the energy difference between one stable state and the local maximum found for $Q_F=0$. To extract the dependence of V_F on the polarization charge of the FE capacitor (FE-Cap), we can take the derivative of equation 4.2 with respect to the polarization charge:

$$\frac{dU}{dQ_F} = \alpha_{FE}Q_F + \beta_{FE}Q_F^3 - V_F, \quad (4.4)$$

and, remembering equation 4.1,

$$-\rho \frac{dQ_F}{dt} = \alpha_{FE}Q_F + \beta_{FE}Q_F^3 - V_F, \quad (4.5)$$

from which we write

$$V_F = \rho \frac{dQ_F}{dt} + \alpha_{FE}Q_F + \beta_{FE}Q_F^3. \quad (4.6)$$

In steady-state condition we can ignore the time derivative and the $V_F(Q_F)$ function will have the shape shown in Figure 4.2.

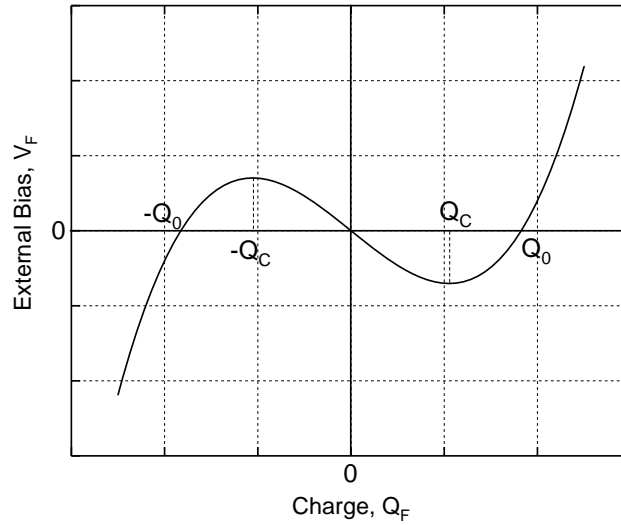


Figure 4.2 – Relation between the polarization charge of the ferroelectric and the external bias. Q_C is the coercive polarization charge, corresponding to the coercive potential.

Here, the local maximum and local minimum, corresponding to $\pm Q_C$, represent an important threshold for the system: they are in fact the points of maximum instability which, in Figure 4.1, correspond to the maximum steepnesses of the energy function between $-Q_0$ and Q_0 .

Inverting this graph, we obtain a visual representation of the dependence of the charge stored in the FE-Cap on the external bias, which is the very definition of "capacitance" (Figure 4.3).

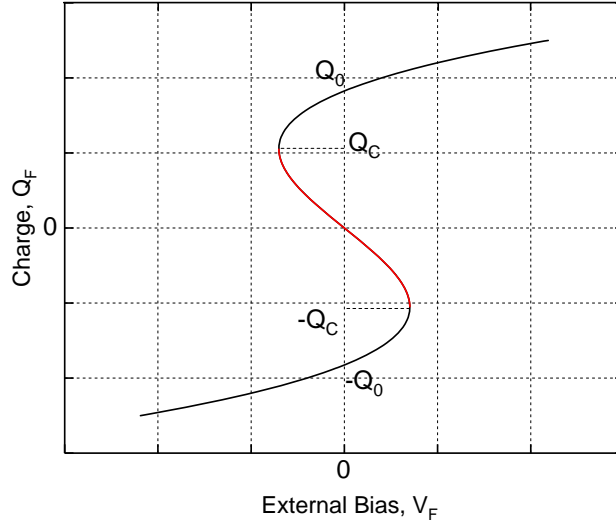


Figure 4.3 – Inverted $V_F(Q_F)$ characteristics. The red section points to the region where the capacitance is negative.

In the red section between $-Q_C$ and Q_C we observe that an increase in the external bias is related to a *decrease* of the stored charge in the FE-Cap, therefore the capacitance $C_{FE} = \delta Q_F / \delta V_F$ is, in fact, negative.

In real applications, however, this effect has proven elusive: as shown in Figure 4.1, the condition of zero Q_F corresponds to a local maximum in the energy landscape, therefore any small perturbation would push the system to one of the two stable phases, where it would just behave as a normal capacitor. For this reason, it is widely accepted that NC requires a stabilizing component.

The role of the stabilizing component is to turn the isolated FE-Cap into a part of a system whose *global* energy landscape shows a minimum for $Q_F=0$, so that the NC can be observed. This task can easily be trusted to a simple capacitor based on a conventional dielectric material. To understand the required parameters of this second capacitor we go back to equation 4.2 and remark that the local maximum is due to the negative coefficient α_{FE} of Q_F^2 .

The energy stored in a normal capacitor follows the relation

$$U_{CDE} = \frac{1}{2} \frac{Q_{DE}^2}{C_{DE}}, \quad (4.7)$$

where U_{CDE} is the energy of the dielectric capacitor and Q_{DE} and C_{DE} are, respectively, its stored charge and its capacitance. Since two capacitors in series always store the same amount of charge, we can assume that $Q_{DE} = Q_F$. The energy of the two-capacitor system will therefore be defined as

$$U = \left(\frac{\alpha_{FE}}{2} + \frac{1}{2C_{DE}} \right) Q_F^2 + \frac{\beta_{FE}}{4} Q_F^4 - Q_F V_F, \quad (4.8)$$

4.1. Negative Capacitance for steep-slope switches.

where the coefficient of Q_F^2 needs to be positive, yielding the condition

$$C_{DE} < -\frac{1}{\alpha_{FE}}. \quad (4.9)$$

Let's now consider the case in which this stabilizing capacitance is given by a conventional MOSFET with capacitance C_{MOS} : as a first order approximation, we could see this system as a standard MOSFET with a voltage amplification element (the FE-Cap) connected between its gate and the external bias source V_G [132] (Figure 4.4).

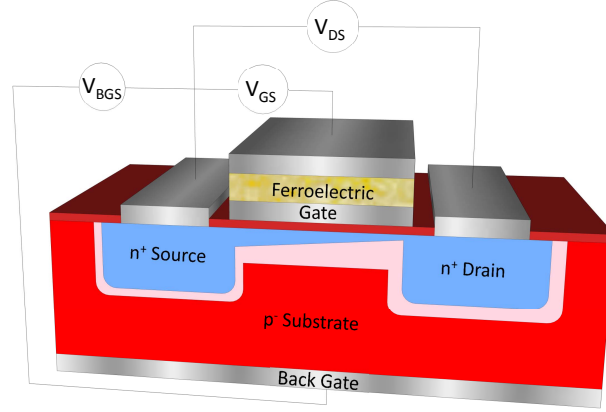


Figure 4.4 – Structure of a NC-MOSFET. The FE-Cap can be defined on top of the gate or be a completely separated element with an electrical connection to the gate metal.

The gain of this amplifier is defined as

$$A_V = \frac{\delta V_{MOS}}{\delta V_G}. \quad (4.10)$$

The formula describing this amplification can be extracted directly from the one of the capacitive voltage divider, and takes the form of

$$\delta V_{MOS} = \delta V_G \frac{C_{FE}}{C_{FE} + C_{MOS}} \rightarrow A_V = \frac{C_{FE}}{C_{FE} + C_{MOS}}. \quad (4.11)$$

The conditions for high absolute gain is that $|C_{FE}| > |C_{FE} + C_{MOS}|$. The gain will be higher as $|C_{FE}|$ nears the value of C_{MOS} .

It is also important to avoid a negative gain, as this would mean that the overall capacitance of the system is still negative, yielding instability and hysteresis. From this formula, we see that this condition is validated when the stabilizing capacitance C_{MOS} is smaller than the module of C_{FE} , in agreement with equation 4.9.

It is now possible to define the SS of the NC MOSFET as the conventional SS divided by the NC gain, therefore the NC SS will be written as:

$$SS_{NC} = SS_{MOSFET} \frac{1}{A_V} = \frac{k_B T}{q} \ln(10) \frac{C_D + C_{OX}}{C_{OX}} \frac{C_{FE} + C_{MOS}}{C_{FE}}, \quad (4.12)$$

where C_D is the depletion capacitance of the MOSFET and C_{OX} the capacitance of its oxide layer. Inserting the extended formula for C_{MOS} in equation 4.12 and performing simple mathematical steps we can get to the final formula

$$\begin{aligned}
 SS_{NC} &= \frac{k_B T}{q} \ln(10) \frac{C_{FE} C_{OX} + C_{FE} C_D + C_D C_{OX}}{C_{FE} C_{OX}} = \\
 &= \frac{k_B T}{q} \ln(10) \left(1 + \frac{C_D}{C_{OX}} + \frac{C_D}{C_{FE}} \right).
 \end{aligned}
 \tag{4.13}$$

Here we find the condition for the FE-Cap to reduce the SS of the MOSFET below the thermionic limit: $|C_{FE}|$ must be lower than C_{OX} , so that the overall capacitance of the gate stack is negative. Therefore, the overall condition for achieving an hysteresis-free NC MOSFET with a SS below the thermionic limit can be resumed as:

$$C_{MOS} < |C_{FE}| < C_{OX} \tag{4.14}$$

This condition takes the name of *capacitive matching*.

4.2 Experimental demonstration of Negative Capacitance with metal gate FETs.

An experimental study on the application of the NC effect to MOSFETs has been performed by Dr. Ali Saeidi [133] employing the devices from our first batch. The wide area of our devices, chosen to increase the SNR, as explained in subsection 1.3.3, is in fact also ideal for NC experiments, for the reason explained in this section.

The trend for MOSFET fabrication, as it is widely known, is pushing to extreme device miniaturization, which leads to extremely low capacitances. Preliminary experiments for the fabrication of FE-Cap able to operate in NC condition, instead, usually employ capacitors featuring wide areas (tens to thousands of μm^2) to facilitate external connections. As a consequence, achievement of the capacitive matching condition is hindered.

Our sensing gates, instead, featuring areas between 40 and 120 μm^2 , possess a sufficient capacitance to provide matching and, subsequently, steep-slope and hysteresis-free operation. Furthermore, while foundry-made State-of-Art MOSFETs for computing have minimized parasitic capacitances between the Gate and the Source/Drain contacts, our devices feature 3 μm long overlaps between the gate metal contact and the Source/Drain highly doped regions: while this parasitic capacitance could prevent fast switching (not needed for sensing), the presence of a fixed capacitor in parallel to the variable channel capacitance helps stabilizing the capacitive matching.

For this study, a polycrystalline $\text{Pb}(\text{Zr}_{0.43}\text{Ti}_{0.57})\text{O}_3$ FE-Cap has been used (Figure 4.5), with a surface of 20 $\mu\text{m} \times 20 \mu\text{m}$ and a thickness of 46 nm.

Its fabrication process started with the deposition by sputtering of a Pt(100 nm)/TiO₂(30 nm)

4.2. Experimental demonstration of Negative Capacitance with metal gate FETs.

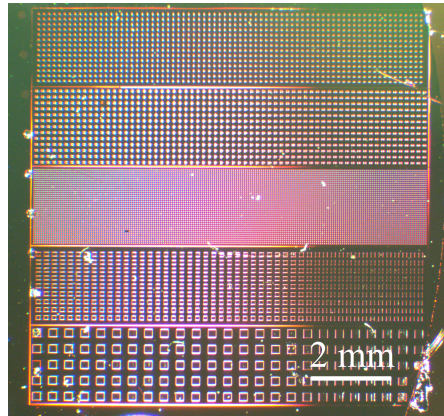


Figure 4.5 – Optical image of the polycrystalline PZT FE-Cap chip employed. Different sizes of FE-Cap are visible.

stack on a Si wafer featuring an oxide layer of 500 nm. The blanket deposition of PZT has been executed *via* chemical solution deposition root [137]. To define the capacitor areas, Pt pads are deposited on top of the PZT through lift-off and a *shadow masking* technique, in which a thin sheet of metal is placed into intimate contact with the substrate to protect the areas in which no deposition is needed. A hole in the PZT allowed connecting the bottom contact of the capacitor. The fabricated FE-Cap showed a relative permittivity between 220 and 240. Its Polarization-Voltage characteristics, is shown in Figure 4.6.

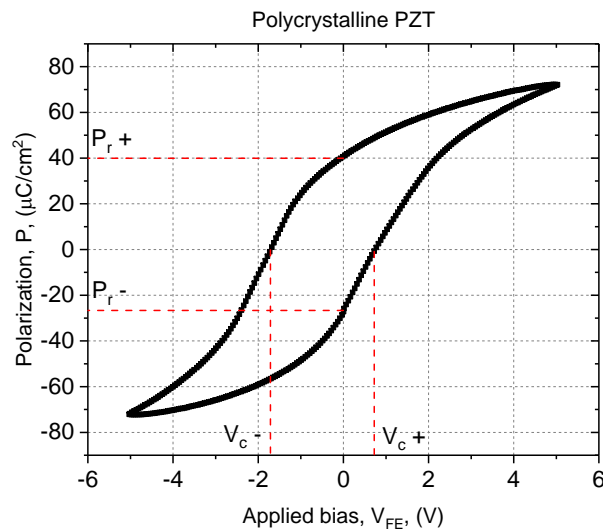


Figure 4.6 – P-V characteristics of the polycrystalline PZT FE-Cap.

It can be observed that the characteristics was not symmetric and showed a positive coercive voltage (V_c) of 0.7 V, while the negative one was -1.8 V. The positive remnant polarization (P_r) value was 40 $\mu\text{C}/\text{cm}^2$, the negative was -26 $\mu\text{C}/\text{cm}^2$.

It is worth noting that, while many studies employ monocrystalline FE materials to improve the FE-Cap quality at the expense of its integrability [138–140], the deposition of the poly-

Chapter 4. Negative Capacitance ISFET

crystalline PZT employed in this study can be easily included in a standard CMOS process flow. The setup employed to link the FE-Cap to the Gate of our devices and measure the full system as a single NCFET is schematically shown in Figure 4.7, together with the corresponding equivalent circuit.

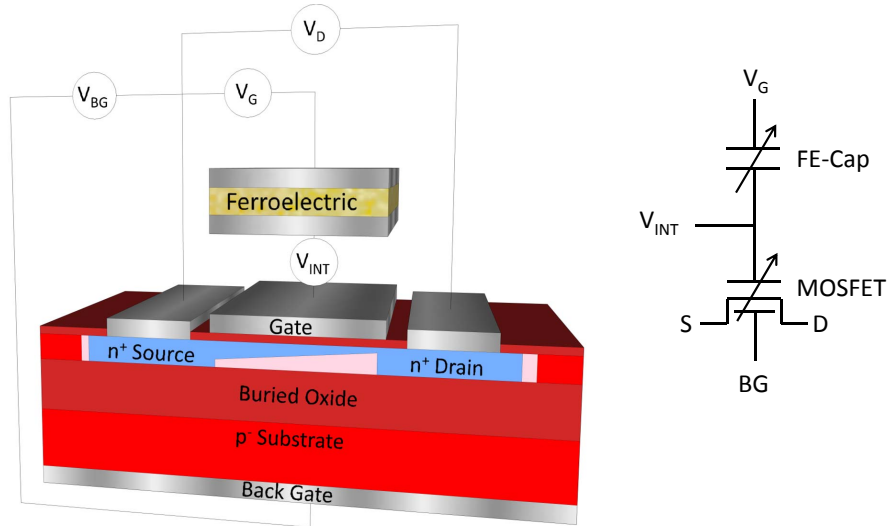


Figure 4.7 – Connection scheme and equivalent circuit of our NCFET. FE-Cap and MOSFET are two separate devices connected through micromechanical probes and BNC cables.

The bias on the internal gate of our MOSFET (V_{INT}) is measured to keep track of the NC gain, with negligible effects on the SS of the NCFET.

The variable capacitor C_S represents the capacitance of the silicon layer.

The transfer characteristics of our simple MOSFET and of the full NC system, where the gate bias is applied through the FE-Cap, are shown in Figure 4.8.

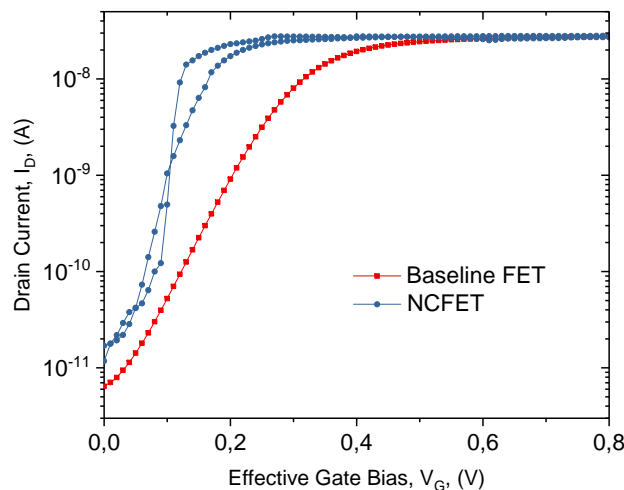


Figure 4.8 – Transfer characteristics of our MOSFETs in normal conditions and with the addition of the FE-Cap. The curve steepening due to the NC effect is clearly visible.

4.2. Experimental demonstration of Negative Capacitance with metal gate FETs.

In this image, the X axis (Gate Bias) represents the external bias, *i.e* the bias applied to the FE-Cap in the NC configuration or to the gate metal for the standard MOSFET configuration. It is evident that the SS of our devices is steepened by the insertion of the FE-Cap and the observed hysteresis is extremely low and mostly due to a slight difference in the SS between the forward and backward switch of the ferroelectric material.

To obtain a visual representation of the steepness improvement, we have plotted the SS of the two configuration as a function of the corresponding Drain current (Figure 4.9).

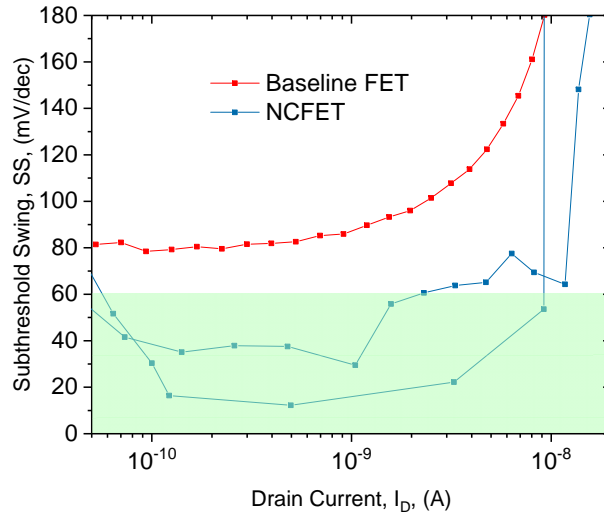


Figure 4.9 – Comparison of the SS of the conventional and NC MOSFETs. The NC configuration shows a sub-thermionic SS over more than two decades of current.

As can be observed, the SS remains below the conventional limit of 60 mV/dec over a relatively wide range of Drain currents, reaching values as low as 12 mV/dec in the steepest region, demonstrating the viability of the NC effect as a mean to tackle the Boltzmann Tyranny and prosecute Moore's law.

The reduced power consumption can be observed from the improved current efficiency g_m/I_D achieved by the NCFET (Figure 4.10).

The differential gain of the FE-Cap, $\delta V_{INT}/\delta V_G$, representing the steepening of the gate bias ramp achieved in the NC region, is plotted in Figure 4.11.

Comparing this curve with the transfer characteristics shown in Figure 4.8 we can notice that the gate bias in the region with the highest differential gain corresponds to the gate bias in which the NC MOSFET transfer characteristics achieves the minimum SS.

One last measurement which can be performed on this system is the relation between the internal polarization of the FE-Cap and the externally applied bias: since the MOSFET capacitance has stabilized the ferroelectric in the NC condition, an "S"-shaped relation similar to the one shown in Figure 4.3 should be observed.

The procedure to extract the P-V curve from a Ferroelectric consists in applying a positive triangular impulse followed without delay by a negative one. The current generated by these impulses is measured and integrated, in order to extract the polarization. In this work, the

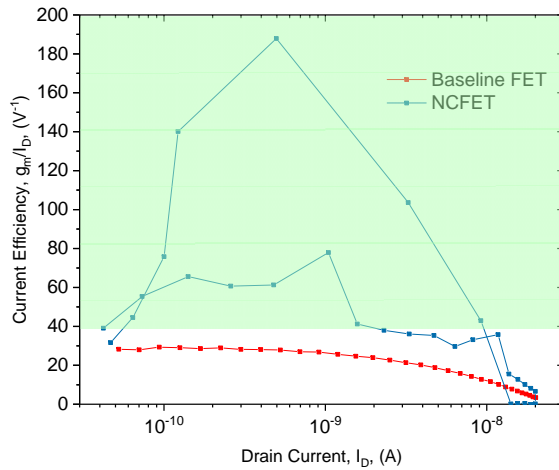


Figure 4.10 – Comparison of the current efficiency of the conventional and NC MOSFETs. The NC configuration shows an efficiency $> 40 \text{ V}^{-1}$ over more than two decades of current.

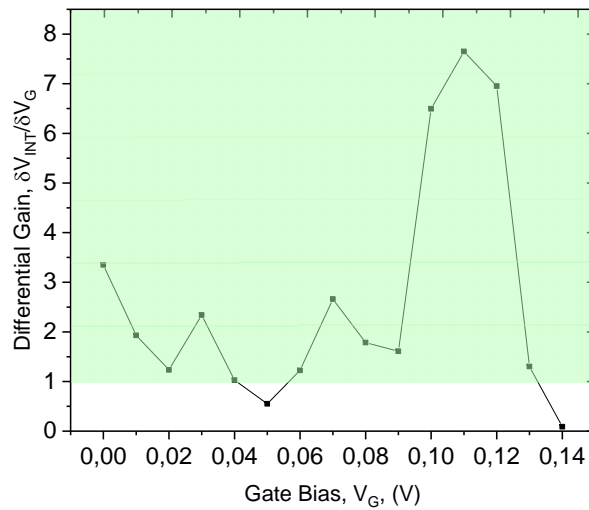


Figure 4.11 – Differential gain of the FE-Cap over the relevant V_G range for the SS. The average value is relevantly bigger than one.

measurement has been performed employing a, aixACCT: TF 2000. The result is reported in (Figure 4.12).

The P_{FE}/V_{FE} function shows negative slope in many regions, especially in the area inside the red ellipse. When this condition is verified, an increase in the externally applied bias determines a decrease in the internal polarization, so that the external effect can be seen as a negative capacitance. The performance improvements related to the NC effect are summarized in Table 4.1.

4.3. Application of the Negative Capacitance effect to ISFETs.

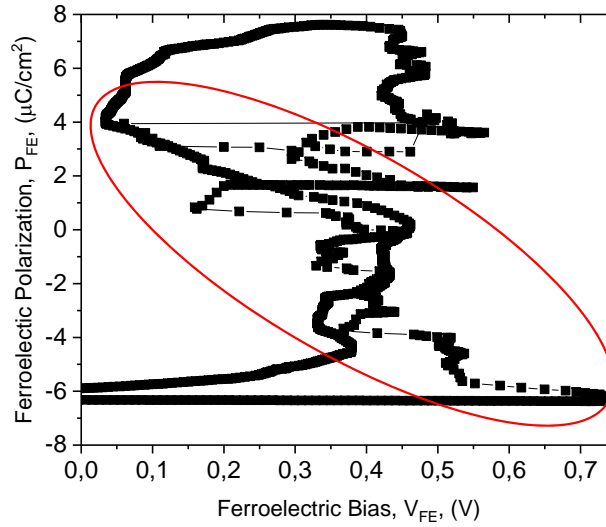


Figure 4.12 – Dependence of the polarization on the externally applied bias, measured during the NCFET operation. Negative capacitance is observed in the marked region.

	FET	NCFET
Average SS	80 mV/dec	20 mV/dec
Average g_m/I_D	29 V^{-1}	115 V^{-1}

Table 4.1 – FET performance Boost due to NC effect

4.3 Application of the Negative Capacitance effect to ISFETs.

As explained in subsection 1.3.2, the overall sensitivity S_{out} describing the relative variation of I_D due to a relative variation of $[\text{ion}^+]_{sol}$ is limited to 1 dec/dec, *i. e.* a tenfold variation in $[\text{ion}^+]_{sol}$ cannot vary I_D of a factor bigger than 10. This ceiling arises from the physical limits governing the two transduction relating $\Delta[\text{ion}^+]_{sol}$ to ΔI_D : the Nernst limit on the $\Delta V_{th}/\Delta[\text{ion}^+]_{sol}$ relation and the thermionic limit on the $\Delta I_D/\Delta V_{th}$ relation.

Having experimentally demonstrated the possibility of surpassing the second limit employing NC, we want to explore the possibility of improving the sensitivity of our devices using the same principle.

The insertion of a FE-Cap in the gate stack can be implemented in two different circuit nodes: between the RE and the external bias source or between the MOSFET and the liquid gate .

The first configuration allows applying the NC-related gain to the entire LUT, so that more devices can be operated with a single FE-Cap, and could therefore result the most convenient strategy for industrial fabrication of the proposed device. The second configuration, however, is maybe more straightforward, since the structure of the NC MOSFET is unchanged and we are simply employing the system as a sensor instead of as a switch, in a way completely analogous to what is done for ISFETs: if NC MOSFETs will become a widespread and fully

integrated technology, this implementation of the sensor will probably be favored. In this chapter both configurations will be implemented and studied. A 3D rendering of a possible implementation of the first case, together with its equivalent circuit, is shown in Figure 4.13.

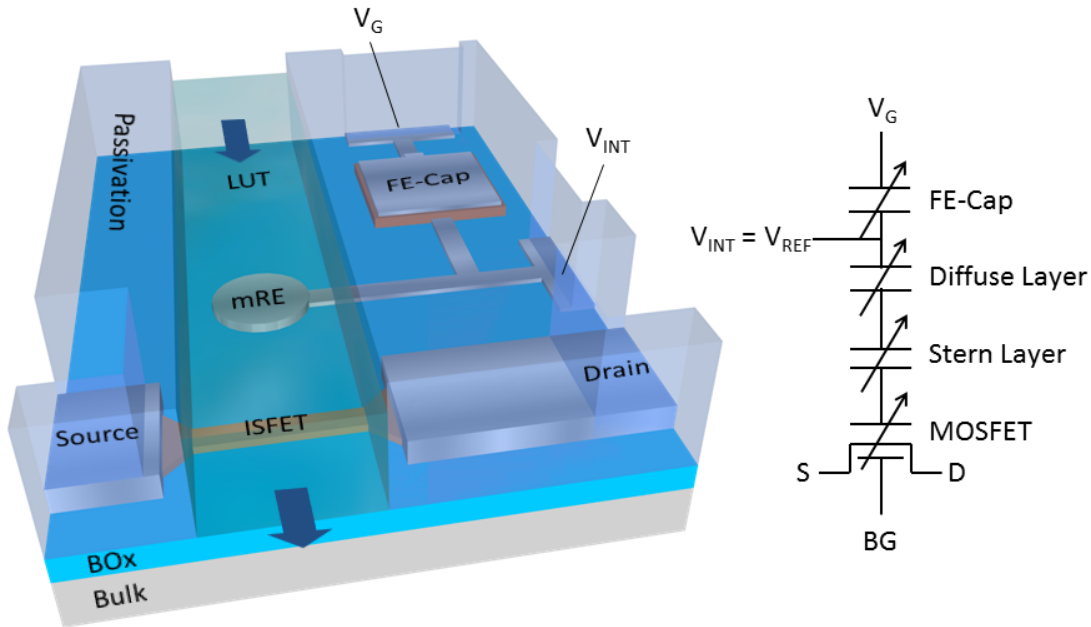


Figure 4.13 – First configuration of the introduced NC ISFET, with the corresponding equivalent circuit.

With respect to the equivalent circuit shown in Figure 4.7, in this one we can see two new elements, labeled Diffuse Layer and Stern Layer, which represent the capacitance of the two components of the liquid gate of our sensor, according to the Stern model introduced in subsection 1.3.2. The mathematical models describing their capacitance are quite complex, therefore the modeling of the equivalent circuit of this NC sensor needs to be studied carefully in order to achieve the required capacitive matching.

4.3.1 Modeling of the ISFET capacitance for matching

To formulate a model relating the density of liquid gate capacitance (C_{LG}) to the input values we can control (*i. e.* the RE bias and the pH and ion concentration in the LUT), we describe the liquid-Gate interaction according to the Stern model. We therefore consider the LUT to be composed of a thin layer of fixed molecules steadily bound on the surface of the sensing gate (the Stern layer) and a layer of liquid in which ions are free to move (the Diffuse layer). Each of these components can be seen as a separated capacitor and, since they are in series, from the point of view of the applied bias V_{REF} , we can calculate C_{LG} as the series of the two. On top of that, however, we will also need to consider the MOSFET used for sensing itself, to accurately describe the complete capacitive divider (Figure 4.14).

4.3. Application of the Negative Capacitance effect to ISFETs.

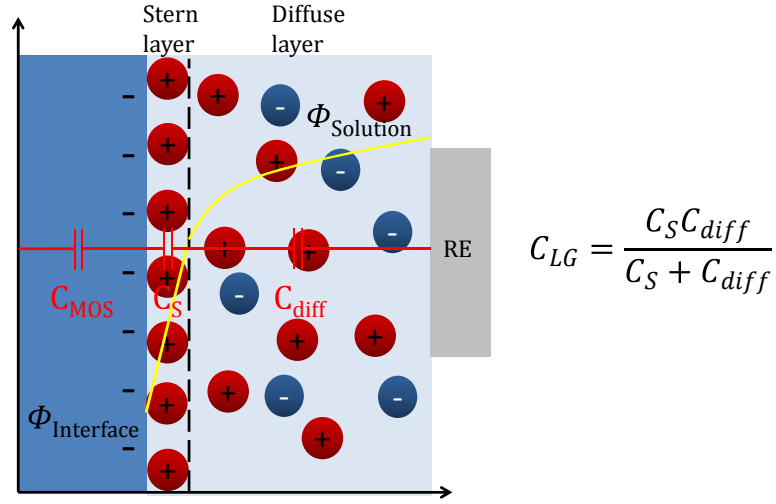


Figure 4.14 – Stern model used for the evaluation of C_{LG} .

A mathematical description of the density of capacitance of the Diffuse layer (C_{diff}) can be extracted from the Grahame equation [141], which relates the density of charge σ in the Outer Helmholtz Plane (OHP, the interface between the Stern and diffuse layers) with the potential V_{diff} across the diffuse layer:

$$\sigma = \sqrt{8\epsilon_r\epsilon_0k_B T n_0} \sinh\left(\frac{qV_{diff}}{2k_B T}\right), \quad (4.15)$$

where $k_B T$ is the thermal energy, q is the elementary charge, n_0 is the bulk density of ions, ϵ_r is the dielectric constant of the diffusion layer, assumed to be equal to 78.5, and ϵ_0 is the permittivity of vacuum.

Using the definition of density of capacitance, we can extract C_{diff} by taking the derivative of this equation with respect to V_{diff} :

$$C_{diff} = \frac{\delta\sigma}{\delta V_{diff}} = \sqrt{2\eta q^2 n_0 \epsilon_r \epsilon_0} \cosh(\eta q V_{diff}/2), \quad (4.16)$$

where η is the reciprocal of the thermal energy ($\eta = 1/k_B T$).

To evaluate the density of capacitance of the Stern layer (C_S), instead, we can follow the procedure reported in [142], in which C_S is related to the intensity of the electric field inside it. Their procedure started with the description of the polarization of water molecules in the Stern layer. In their model, a single water molecule is seen as a sphere with a point-like water dipole situated at its center. The permittivity of such spherical molecule is equal to n^2 , being n the optical refractive index of water. The polarization of the Stern layer can then be expressed as:

$$P = -n_{0w} p_0 \left(\frac{2+n^2}{3}\right) L(\gamma p_0 E \eta), \quad (4.17)$$

where n_{0w} is the bulk density of water molecules in the liquid, p_0 is the magnitude of the water external dipole moment, E is the electric field in the Stern layer, $\gamma = (2+n^2)/2$ and L is the Langevin function, defined as $L(u)=\coth(u)-1/u$.

Having defined this parameter, we can now write the equation for the dielectric constant of the Stern layer as:

$$\epsilon_S = n^2 + \frac{|P|}{\epsilon_0 E} = n^2 + \frac{n_{0w} p_0}{\epsilon_0} \left(\frac{2+n^2}{3} \right) \frac{L(\gamma p_0 E \eta)}{E}, \quad (4.18)$$

and, remembering that the Stern layer can be considered as a homogeneous dielectric with a constant electric field,

$$C_S = \frac{\epsilon_0 n^2 + n_{0w} p_0 \left(\frac{2+n^2}{3} \right) \frac{L(\gamma p_0 E \eta)}{E}}{b}. \quad (4.19)$$

To calculate numerically the series capacitance of these two layer, as said, we now need to relate them to the external parameters we are able to control.

A viable strategy would consist in writing both terms as function of the bias of the RE but, in order to do so, we must see how the free variables of these two equations (V_{diff} and E) are related to V_{REF} .

V_{diff} is the portion of V_{REF} which drops across the Diffuse Layer. Using the formula of the capacitive voltage divider we can therefore write:

$$V_{diff} = V_{REF} \frac{C_S C_{MOS}}{C_{diff} C_{MOS} + C_S C_{diff} + C_S C_{MOS}}. \quad (4.20)$$

To evaluate the electric field E in the Stern layer, we must first use the capacitive voltage divider formula to evaluate the potential V_S in that region. Making reference to the reported physics of the Stern Layer, we can then use V_S to evaluate E by simply dividing it by the layer thickness b .

$$E = \frac{V_{REF}}{b} \frac{C_{diff} C_{MOS}}{C_{diff} C_{MOS} + C_S C_{diff} + C_S C_{MOS}}, \quad (4.21)$$

It can be noticed that these definitions have made the values of C_{diff} and C_S dependent on themselves and each other, which will make necessary the employ of an iterative algorithm to achieve the solution.

To keep into account the influence of pH on the RE bias, the most rigorous procedure would be using the site-binding model [143], but such an accurate description of the ion-sensing mechanism is out of the scope of this model and would heavily impact its computational cost. We will therefore limit the complexity of the system by simply considering a phenomenological approach in which a bias $V_{pH} = V_{sens} \times (pH_{pzc} - pH)$, where V_{sens} is the threshold voltage variation due to a pH variation of one point and pH_{pzc} is the pH corresponding to the Point of Zero Charge of the sensing layer, is added to the RE bias. The MATLAB code used to compute the capacitance values of the liquid gate is reported in Appendix A.3.

4.3. Application of the Negative Capacitance effect to ISFETs.

Before showing the numerical results, a few considerations are reported here on the extracted relations between the capacitances and their free variables: first of all, we notice that C_{diff} depends on the hyperbolic cosine of $\eta q V_{diff}/2$. This function is ≈ 1 for argument values $\ll 1$ and grows exponentially with the absolute value of the argument. The constant coefficient $\eta q/2$ has a value of 19.4 V^{-1} at room temperature, meaning that values of V_{diff} bigger than few tens of mV could determine humongous C_{diff} values. In [141] this issue has been avoided by assuming $V_{diff} \ll V_T$, where V_T is the thermal voltage $k_B T/q \approx 25.85 \text{ mV}$ at room temperature, and therefore assuming that $\cosh(\eta q V_{diff}/2) \approx 1$. In this work, however, we decided to maintain the complete formula so that C_{diff} is accurately described for low values of V_{diff} . Excessively high values of C_{diff} are generally avoided thanks to the self-regulating nature of the capacitive divider: the higher is the capacitance of a certain component, in fact, the lower is the portion of bias dropping on it. Moreover, even in the case in which extremely high C_{diff} values are calculated, we don't observe nonphysically high results for C_{LG} , since in a capacitive series the smaller capacitor dominates.

The dependence of C_S on the free variable E , on the other hand, is defined in the factor $L(\gamma p_0 \eta)/E$. The Taylor expansion of the Langevin function is defined on the basis of that of the hyperbolic cotangent as

$$L(u) = \coth(u) - \frac{1}{u} = \frac{\sum_{i=0}^{+\infty} \frac{u^{2i}}{(2i)!}}{\sum_{i=0}^{+\infty} \frac{u^{2i+1}}{(2i+1)!}} - \frac{1}{u}, \quad (4.22)$$

therefore the first terms read

$$L(u) = \frac{u}{3} + \frac{u^3}{45} + \frac{2u^5}{945} + \dots \quad (4.23)$$

For $u \ll 1$, we see that higher order terms tend to zero, therefore the ratio $L(\gamma p_0 \eta)/E$ is constant with E as long as the argument of the Langevin function is small.

The value of the fixed coefficient $\gamma p_0 \eta$ amounts to $4.72 \times 10^{-9} \text{ m/V}$, therefore, unless extremely high electric fields are considered, C_S will not vary. This is coherent with the assumption that the Stern layer behaves like a dielectric.

Because of the interdependence of the capacitances of the various layers, our model requires to know the surface proportions between them: the bigger is a capacitor area, compared to the others, the higher will be its capacitance and the lower the potential drop on it. The presence of a liquid component and of several parasitic capacitances due to wiring, however makes it difficult to estimate the real physical size of these components: for this reason, the effective areas have been extracted by fitting the measured transfer characteristics of our standard ISFET employing the introduced liquid gate model and the industry-standard BSIM-IMG model for MOSFETs, in collaboration with the Indian Institute of Technology Kanpur. The comparison between the pH measurements and the model fitting are reported in Figure 4.15. Having defined the effective areas of the various capacitors, we employed our model to simulate the dependence of C_{diff} and C_S on the RE bias applied, considering a pH equal to the

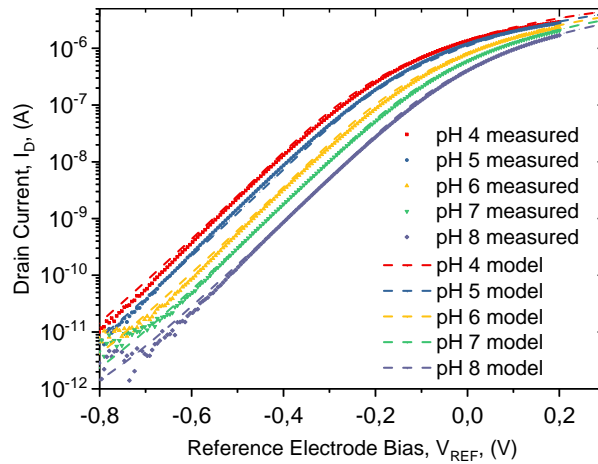


Figure 4.15 – Measured and simulated ISFET transfer characteristics at various pH values.

pH_{pzc} (9.1, in this simulation) and an ion concentration n_0 equal to $6 \times 10^{19} \text{ l}^{-1}$ (corresponding to $100 \mu\text{M}$). The result is shown in Figure 4.16.

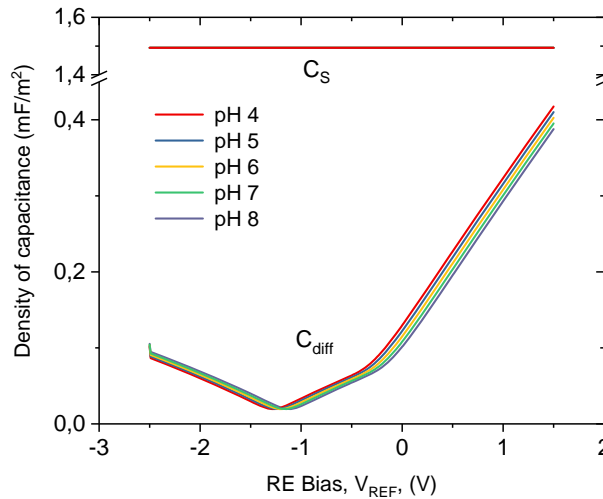


Figure 4.16 – Dependence of C_{diff} and C_S on the RE bias.

The shift given by the employ of different pH buffers is clearly visible. It can be noticed that, while equation 4.16 is clearly symmetric, such symmetry is not observed in this graph. This is due to the fact that the portion of V_{REF} dropping on the Diffuse layer will depend on all the capacitances composing this system, therefore the asymmetric nature of the MOSFET C-V characteristics affects this graph.

We can now consider the C-V function of our complete ISFET system, embedding both the FD SOI MOSFET and the liquid gate (Figure 4.17).

We can observe that the capacitance starts with a low value due to the depletion condition, with a minimum located in the bias range for which the diffuse Layer drops (cfr. Figure 4.16). As V_{REF} grows, approaching inversion condition, we note a remarkable capacitance increase.

4.3. Application of the Negative Capacitance effect to ISFETs.

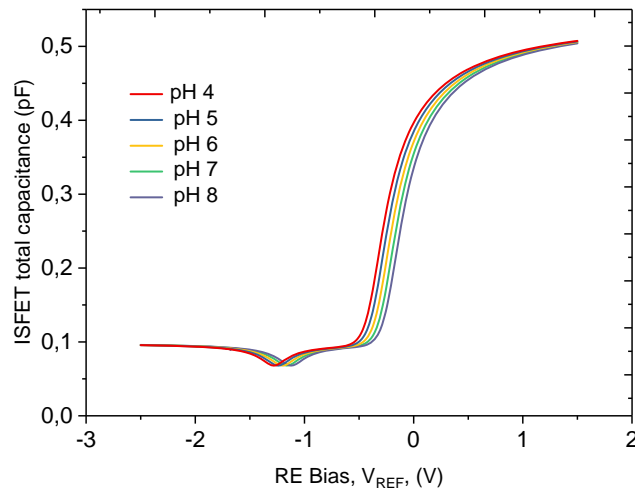


Figure 4.17 – C-V characteristics of the complete ISFET.

4.3.2 Experimental characterization of an NC ISFET

In this subsection we report the experimental results of pH sensing with the first introduced ferroelectric-ISFET configuration, and compare them with the transfer characteristics measured for conventional ISFETs.

The FE-Caps employed for this experiment were 46 nm thick single-crystalline PZT with an area of $100 \mu\text{m} \times 100 \mu\text{m}$. The fabrication procedure started with the growth of 20 nm of SrRuO_3 (SRO) on a DyScO_3 (DSO) substrate with (110) crystal orientation. Pulsed Laser Deposition (PLD) is employed for the epitaxial growth of the PZT. 50 nm thick Pt pads are then deposited on top by sputtering and lift-off with a shadow mask. The measured polarization curve, which resulted symmetrical, is shown in Figure 4.18.

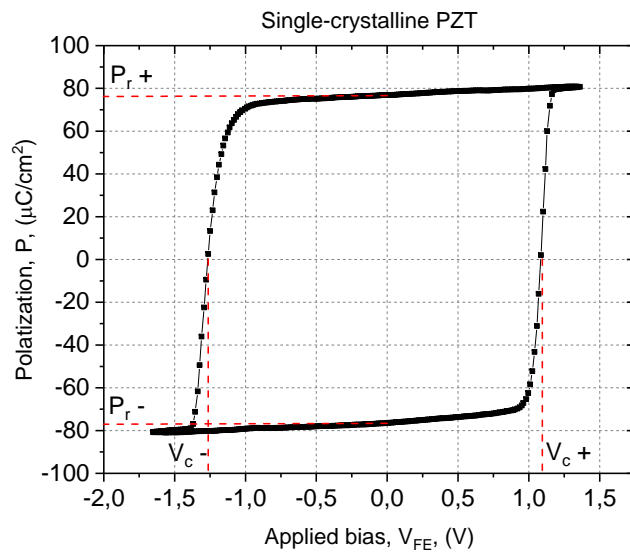


Figure 4.18 – P-V characteristics of the single-crystalline PZT FE-Cap.

Chapter 4. Negative Capacitance ISFET

The extracted V_c is equal to 1.25 V, while P_r is $78 \mu\text{C}/\text{cm}^2$.

Using two microprobes, the FE-Cap has been connected between the external bias source (parameter analyzer Agilent 4156A) and the commercial flow-through RE (MI-16-701 Microelectrodes Inc. RE) which applies the bias to the liquid gate. The resulting transfer characteristics has been extracted with a standard measurement mode in double sweep. The results are shown in Figure 4.19.

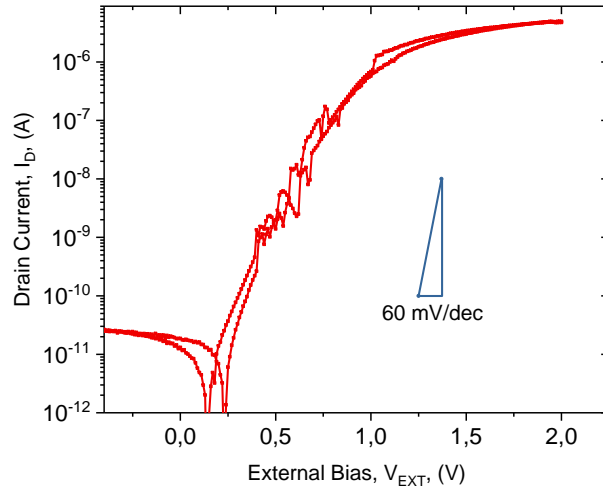


Figure 4.19 – NC ISFET transfer characteristics extracted at pH 7.

The measured characteristics shows extremely low hysteresis, sign of an efficient stabilization of the FE-Cap. It can be noticed that, with the exception of a few short current ranges, the SS remains above the thermionic limit of 60 mV/dec. The transfer characteristic comparison with the standard ISFET configuration, however, shows a non-negligible improvement on the overall steepness, as shown in Figure 4.20.

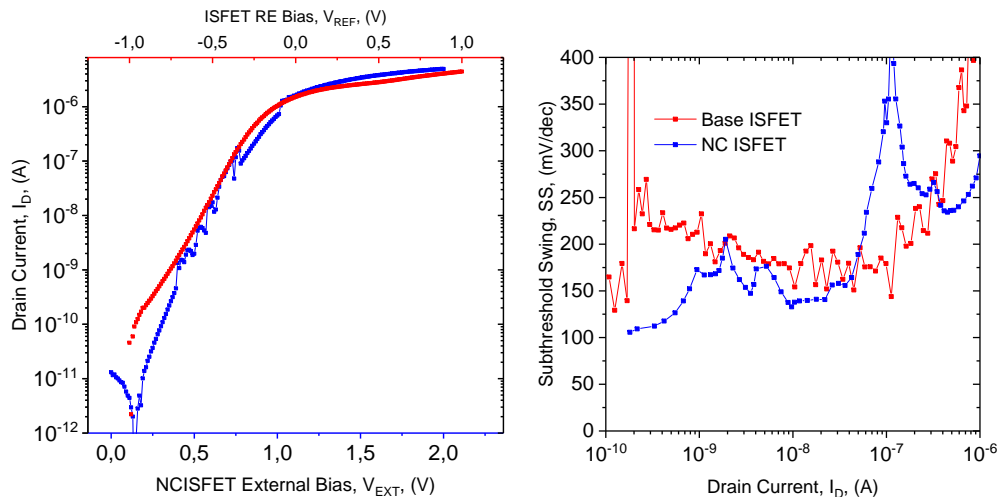


Figure 4.20 – Comparison of transfer characteristics and 10-points smoothed SS of standard and NC-boosted ISFETs.

4.3. Application of the Negative Capacitance effect to ISFETs.

The SS relative improvement amounts to 21%, so that, as explained in subsection 1.3.2, the I_D (pH) response S_{out} is boosted by a factor:

$$S_{out,NC}/S_{out} = \frac{\Delta V_{th}/SS_{NC}}{\Delta V_{th}/SS} = \frac{SS}{SS_{NC}} = \frac{SS}{(1 - 0.21)SS} \approx 1.27 \quad (4.24)$$

In analogy with the NC MOSFET study of section 4.2, we can also show the improvement in the current efficiency g_m/I_D (Figure 4.21).

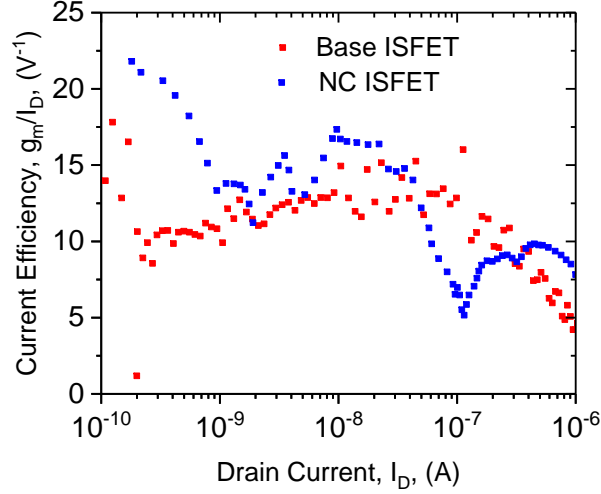


Figure 4.21 – Comparison of the current efficiency of standard and NC-boosted ISFETs.

The ISFET performance improvements related to the NC effect are summarized in Table 4.2.

	ISFET	NCISFET
Average SS	190 mV/dec	150 mV/dec
S_{out}	0.28	0.35
Average g_m/I_D	12 V^{-1}	15 V^{-1}

Table 4.2 – ISFET performance Boost due to NC effect

Where S_{out} , as reported in subsection 1.3.2, is an ideality parameter merging together the gate sensitivity and the gate coupling. As can be seen, the performance improvements, while inferior with respect to the ones of Table 4.1 are still relevant. The definitive proof that these improvements are actually due to the NC effect can be found measuring the differential gain $\delta V_{INT}/\delta V_{EXT}$ between the two sides of the FE-Cap (Figure 4.22).

The green area of the graph, as for Figure 4.11, represents the condition of differential gain bigger than one, which is the physical cause of the steeper SS and can only be determined by the NC condition in the FE-Cap. We can therefore confirm that the system we assembled is, in fact, the first experimental demonstration of a NC ISFET.

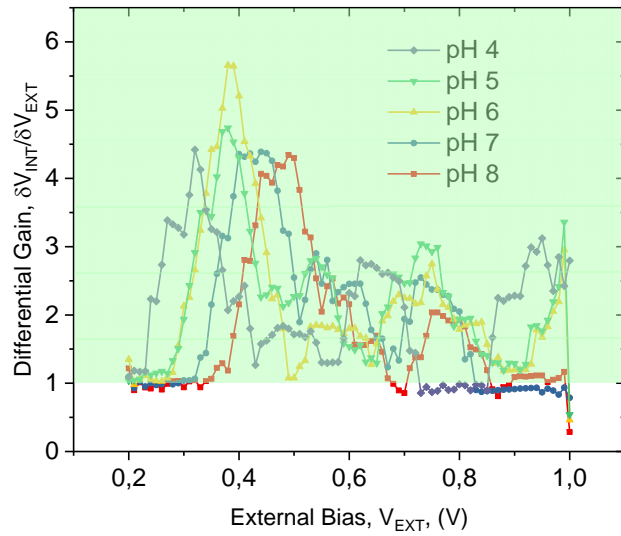


Figure 4.22 – Differential gain measured at the two sides of the FE-Cap.

It should be observed that the peak of the NC gain does not appear at a fixed bias but instead shifts to more positive values as pH is increased, showing the same behavior anticipated by our capacitance model in Figure 4.16 and 4.17. The peak will therefore intrinsically shift with pH in the same way as the transfer characteristics of the base sensor, guaranteeing that the maximum gain will always be found in the same portion of the curve, so that their shape is maintained regardless the pH value.

The stability of the system, and its consequent usability as a sensor, has been demonstrated by extracting the transfer characteristics with different pH buffers (three consecutive measurements for each pH value), in order to ensure that the V_{th} shifts are stable and only influenced by the pH of the LUT. The results are reported in Figure 4.23.

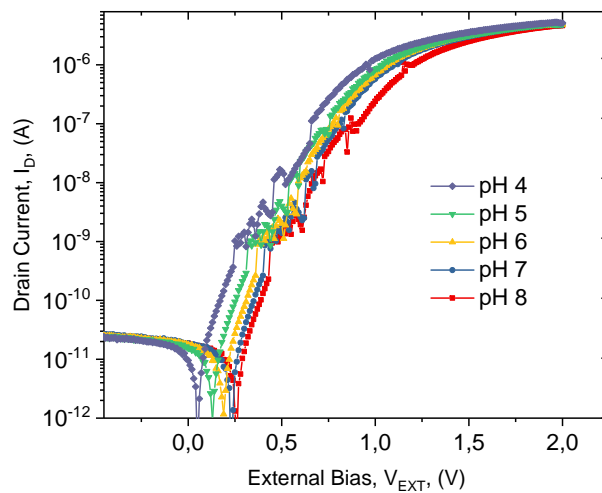


Figure 4.23 – Transfer characteristics extracted at various pH values for the NC ISFET.

4.3. Application of the Negative Capacitance effect to ISFETs.

As can be observed, the transfer characteristics showed a constant and repeatable shift with pH. The measured voltage sensitivity resulted identical to the one of their standard counterparts.

4.3.3 Pulsed measurements mode for improved NC

While the NC device reported in the previous subsection has proven capable of sensing pH and improving some figures of merit of its standard counterpart, its SS remained far greater than the thermionic limit of 60 mV/dec.

It has been reported [144] that, when a metal layer is present between the Ferroelectric layer and the stabilizing dielectric, NC effects can be reduced or entirely prevented by the current leakages, which can cause the discharge of the capacitors. This effect can be avoided if the gate bias is cycled faster than the time needed by this phenomenon to take place [145–147]. Pulsed measurement is a technique in which, instead of applying a DC bias to the system to characterize, the input bias is provided in short pulses and the electrical output is measured in the same interval. This technique, while helping reducing the heating effects on delicate devices, has two notable downsides: first of all, short pulses generate transient currents which are hardly shielded by the dielectric layers, with the consequence that a much higher gate leakage current could be measured, covering the lower part of the transfer characteristics. Secondly, shorter pulse determine lower integration time provided to the parameter analyzer to measure the output current, so that the limit of detection is shifted towards higher values. This second effect can be mitigated with the employ of remote amplifiers, which is a standard option with the parameter analyzer employed for this set of experiments (Keithley 4200A-SCS), but not entirely suppressed. In Figure 4.24 these effects are shown by measuring the transfer characteristics of the standard FD SOI MOSFET at various pulses duration.

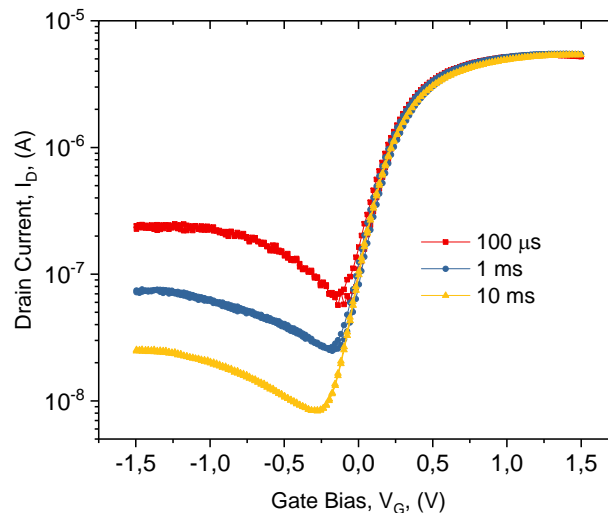


Figure 4.24 – Transfer characteristics of the FD SOI MOSFET extracted at various pulses duration.

The I_{OFF} here are higher than the foreseen limits of detection of the parameter analyzer at the

given pulses duration and tend to grow for more negative biases, pointing out that their high value are due to the increased gate leakage, in this case.

For this new set of experiments, we employed the second proposed NC ISFET configuration: we moved the FE-Cap location between the liquid gate and the gate contact of the FD SOI MOSFET, so that we can consider our device as a standard NCFET operated with a liquid gate. Employing the top electrode of a single FE-Cap as sensing layer, however, is not straightforward: while the sensing material remains the same (Pt), it is now difficult to limit the sensing area to a single FE-Cap capacitor, since the top electrode size is too reduced to host the entirety of our liquid gate; as a consequence, the surrounding devices would also be connected. We initially tried to solve this issue by defining a photoresist passivation of the chip, leaving an opening only for the FE-Cap of interest, but our tests showed that the contribution of the surrounding area was not completely shielded. Finally, in order to be able to connect to the liquid gate a single FE-Cap at a time, it has been necessary to create a second probe bridge connecting a Pt sensing electrode to the top contact of one of the FE-Caps. The obtained structure is equivalent to the integrated one of the 3D sketch of Figure 4.25

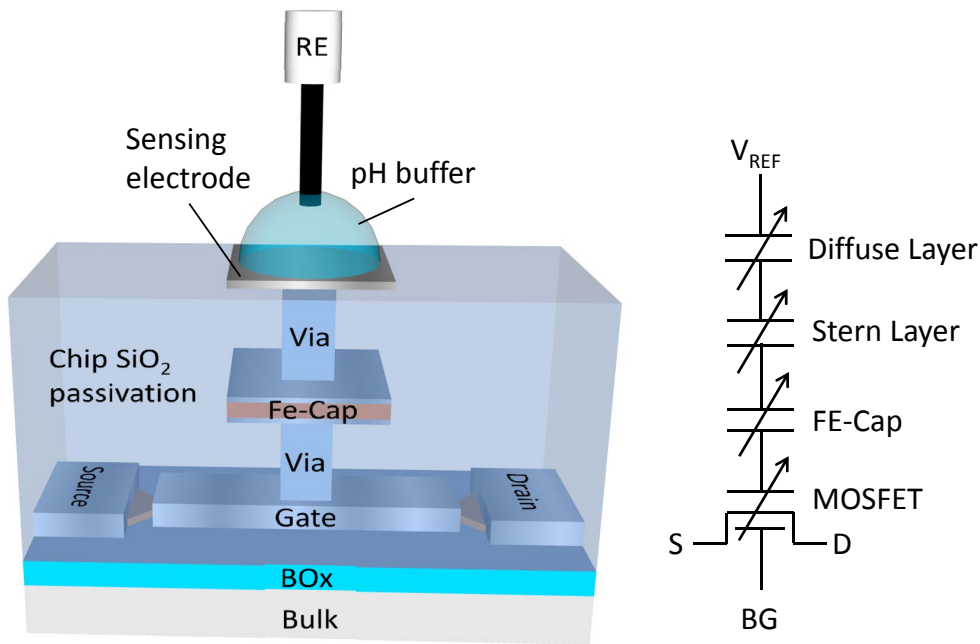


Figure 4.25 – Second configuration of the introduced NCISFET with the corresponding equivalent circuit.

Along with the single-crystalline PZT, two new sets of FE-Caps have been tested, made of Si-doped HfO_2 with two different annealing temperatures. Both sets have been produced by alternated ALD of HfO_2 (16 cycles), SiO_2 (1 cycle) and HfO_2 (16 cycles) again, repeated five times, resulting in a thickness of 16 nm. The final Si concentration is about 3%. The low-temperature annealing is performed by heating the deposited layer at 700°C for 60 s, while the high-temperature one employs 800°C for 20 s. While the first procedure guarantees lower leakages, the second ensures a more homogeneous Si distribution, and therefore a more

4.3. Application of the Negative Capacitance effect to ISFETs.

homogeneous layer. The respective P-V loops are shown in Figure 4.26.

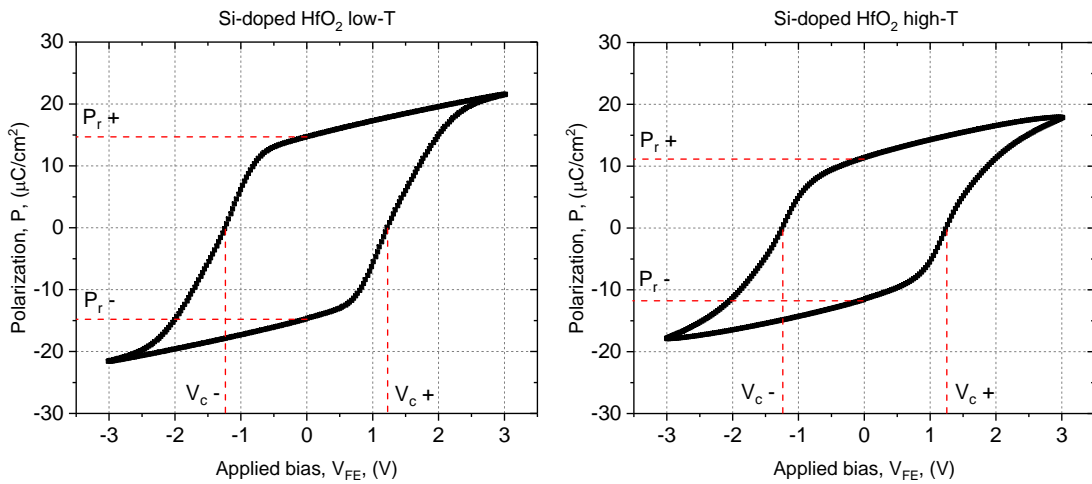


Figure 4.26 – P-V characteristics of the low (700°C) and high (800°C) temperature annealing Si-doped HfO₂ FE-Caps.

The parameters extracted from these curves are, as expected, quite similar, both showing a V_c of 1.2 V and a P_r of, respectively, 14.7 and 11.5 $\mu\text{C}/\text{cm}^2$. Since the duration of the pulse is expected to influence gate leakages, LOD, and NC effect, we started our measurements with the characterization of our device with a given capacitor (100 $\mu\text{m} \times 100 \mu\text{m}$ single-crystalline PZT) and a given pH buffer (pH 8) at different pulse duration, to determine the optimal one. The results are shown in Figure 4.27.

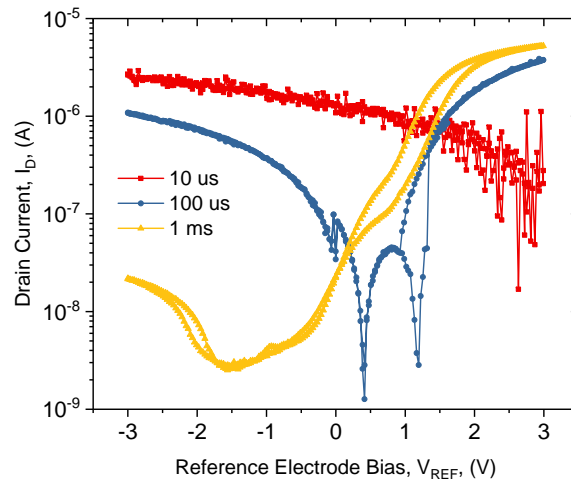


Figure 4.27 – Transfer characteristics of the NC-ISFET extracted at various pulse durations.

It can be observed that pulses duration of 1 ms yield an hysteretic curve without any relevant SS improvement, which can be a sign of the fact that the gate leakages still have enough time to discharge the capacitors, hindering the NC effect. At 10 μs , instead, we observed a drastically reduced gate control, which can be due to excessive gate leakages or to the impossibility of the

liquid gate to react fast enough to the bias variation. In between, at 100 μ s pulses duration, we are finally able to observe a steepening of the SS, which for one branch is reduced down to 27 mV/dec. The same effect has been observed for the other FE-Caps as well, therefore all the following experiments are performed employing this optimal value.

Our first observation, while electrically characterizing this setup, was the high instability of the transfer characteristics, which was shifting by tens of mV between two consecutive measurements. We were not able to precisely identify the cause of this shift in V_{th} , which has been observed both for the sub-thermionic and normal branch of the curve. The stable measurements achieved with the previous NC ISFET configuration suggest that the variability is not due to a non-stable response of the FE-Cap and a set of pH measurements performed in pulsed mode on a standard ISFET (Figure 4.28) showed that pulsed measurements are not intrinsically incompatible with pH measurements.

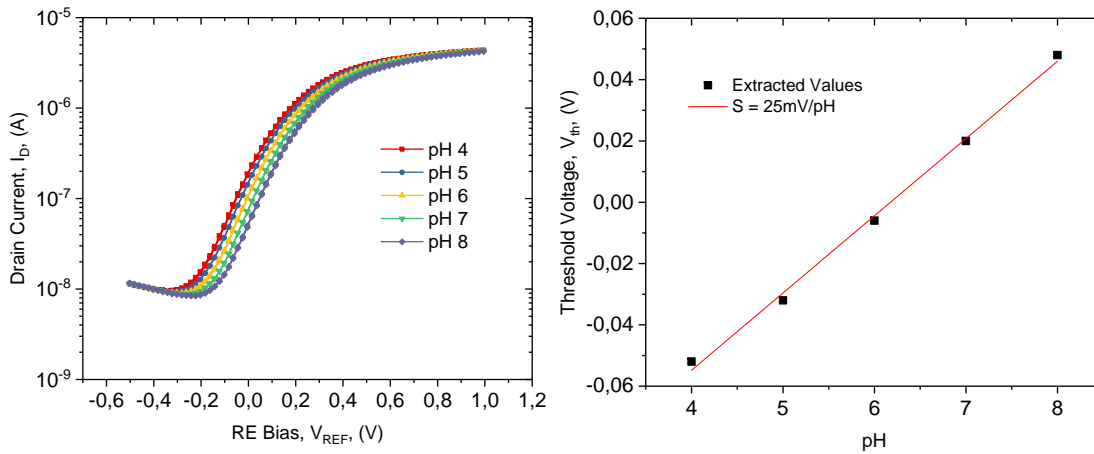


Figure 4.28 – Characterization of the pH response of a standard ISFET in Pulsed Mode.

The most reasonable explanation is therefore the high complexity of the employed measurement setup, which now embeds many parasitic capacitances and amplifiers, together with a liquid component (the pH buffer) and an electrical connection based on reversible chemical reactions (the RE), therefore we are likely to have parameters outside our control which are varying in time.

Stable and repeatable measurements of a single pH buffer have been however observed employing the low-temperature annealing Si-doped HfO₂ FE-Cap (Figure 4.29).

Even though this configuration has proven stable for consecutive measurements, we observed that simply removing and redepositing the drop of pH buffer would still cause a huge pH shift, making the pH measurements completely unreliable. In our experiment to evaluate the V_{th} shift with pH, we have been able to get stable results while repeating the measurement three time for each pH buffer, and changing the buffer we have also been able to observe a shift in the right direction (Figure 4.30) but when we finally repeated the pH 5 buffer measurement we obtained a curve completely off.

In the end, we concluded that our setup could not yield stable pH measurements but, given

4.3. Application of the Negative Capacitance effect to ISFETs.

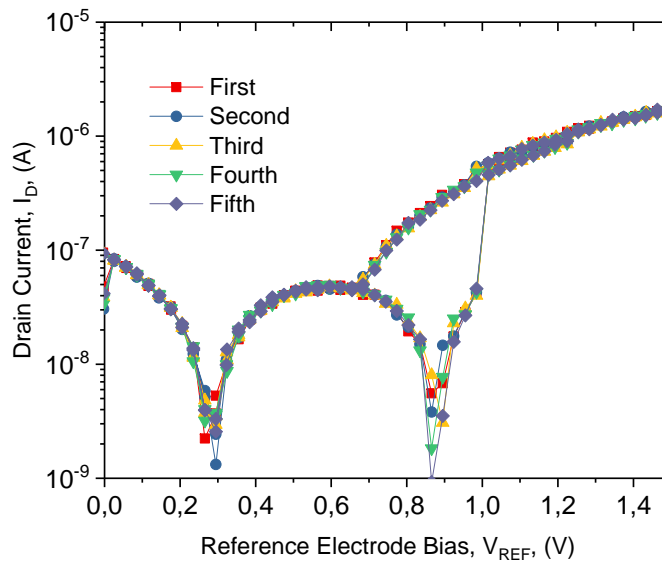


Figure 4.29 – Results of five consecutive transfer characteristics measurements employing the low-temperature annealing Si-doped HfO₂.

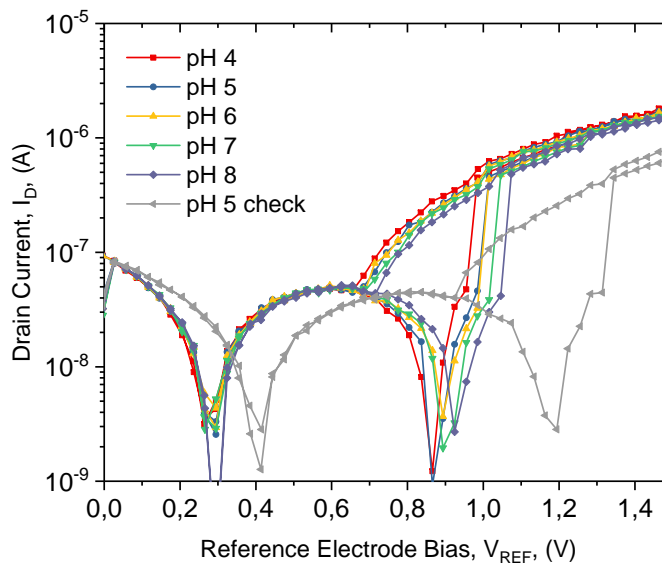


Figure 4.30 – Transfer characteristics of the NC ISFET extracted at different pH values, together with the failed consistency check.

the promising shape of the transfer characteristics, could be used to provide a definitive proof of concept of the feasibility of an NC-based super-steep switch embedding a liquid gate. Our best results to that end has been achieved with the setup embedding the high-temperature annealing Si-doped HfO₂, with which we have been able to achieve a sub-thermionic SS down to 20 mV/dec over two decades of current and an hysteresis of just 2 mV (Figure 4.31). In this graph, we observe a plateau at the I_D value of about 30 nA, which corresponds to the minimum current which can be measured at this pulse duration with our parameter analyzer,

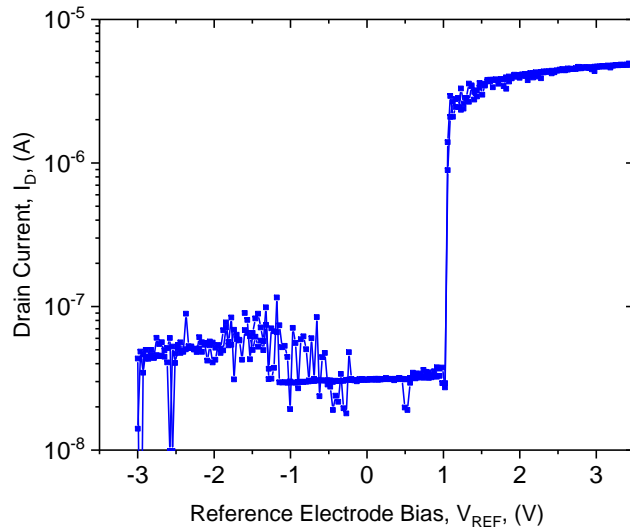


Figure 4.31 – Transfer characteristics of the high-temperature annealing Si-doped HfO₂ NC ISFET.

therefore it is likely that the sub-thermionic range of our curve would have been wider in absence of measurement issues.

These results show clearly that the NC effect has promising applications to ISFETs, which would be best exploited by a fully integrated device in which the Ferroelectric material is directly deposited on the gate dielectric, without any interlayer metal, so that the necessity of employing Pulsed Measurements to achieve strong SS steepening is removed.

4.4 NC ISFET complete modeling.

In this final section, we embed our model for the liquid gate capacitance in the compact model for NC ISFET simulation introduced in [148], creating the first ever complete NC ISFET model. Given the observed complexity of the system, we believe that this tool will prove useful for future implementations of this technology.

The model is based on the Landau-Devonshire theory of ferroelectric discussed in subsection 4.1 and makes use of the BSIM-IMG model for the description of the baseline FD SOI MOSFET. High computation efficiency is achieved deriving, for the two operating conditions of interest (weak inversion and strong inversion), an educated initial guess for the charge stored in the FE-Cap. This allows drastically reducing the computational cost of numerical approaches. The parameters of the high-temperature annealing Si-doped HfO₂ FE-Cap have been considered.

In analogy to what we did for the modeling of the baseline ISFET, we first extracted the effective areas of the various components of the NC ISFET by fitting the transfer characteristics of Figure 4.31. The result is shown in Figure 4.32.

As stated, the high OFF current value measured is due to the noise limit of the parameter

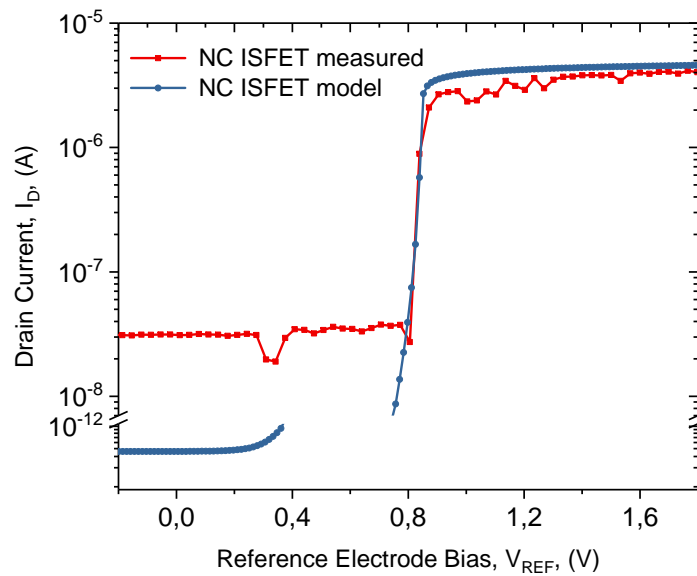


Figure 4.32 – Comparison between the transfer characteristics of the high-temperature annealing Si-doped HfO₂ NC ISFET and the obtained fitting with the NC ISFET model.

analyzer in pulsed mode; for this reason, this parameter has not been considered for fitting. The Y-axis of Figure 4.32 has been broken to better display the relevant areas of the two curves. The model can now be used to evaluate some relevant parameters for the design of the NC ISFET, such as its C-V characteristics and the potential drop across the FE-Cap as a function of the RE bias (Figure 4.33).

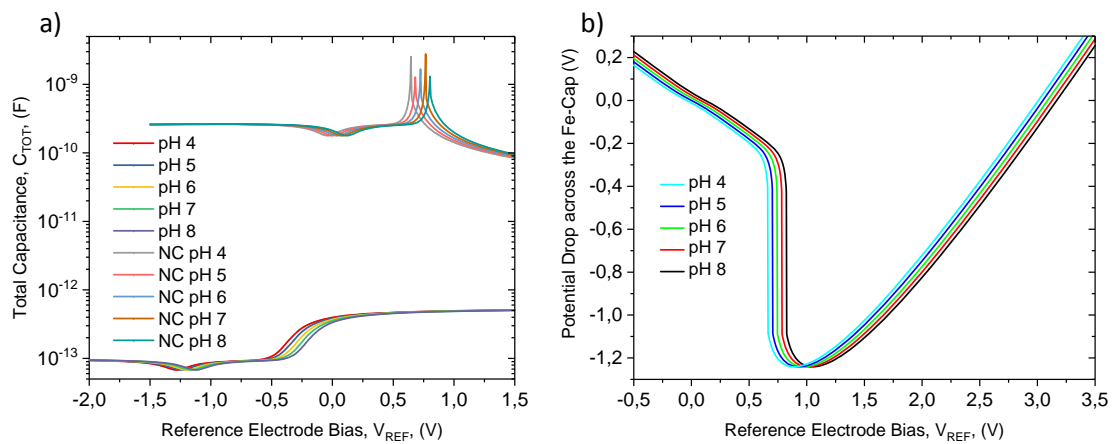


Figure 4.33 – a) Comparison between the total capacitance of the baseline ISFET and of its corresponding NC counterpart for different pH values. b) Potential drop across V_{REF} , showing a marked negative valley in response to positive RE biases.

It can be observed that the overall capacitance of the NC ISFET is orders of magnitude larger than that of the baseline device. As a consequence, the amount of bias required to generate charge in the device is drastically reduced. The bias response of the FE-Cap indicates that this

Chapter 4. Negative Capacitance ISFET

element is acting as a bias amplifier.

Knowing the voltage drop on the different elements of the NC ISFET allows us to define the band diagram of the system, allowing a comparison with the standard case in which no FE-Cap is included and obtaining a clear visualization of the advantages brought by the addition of this element (Figure 4.34).

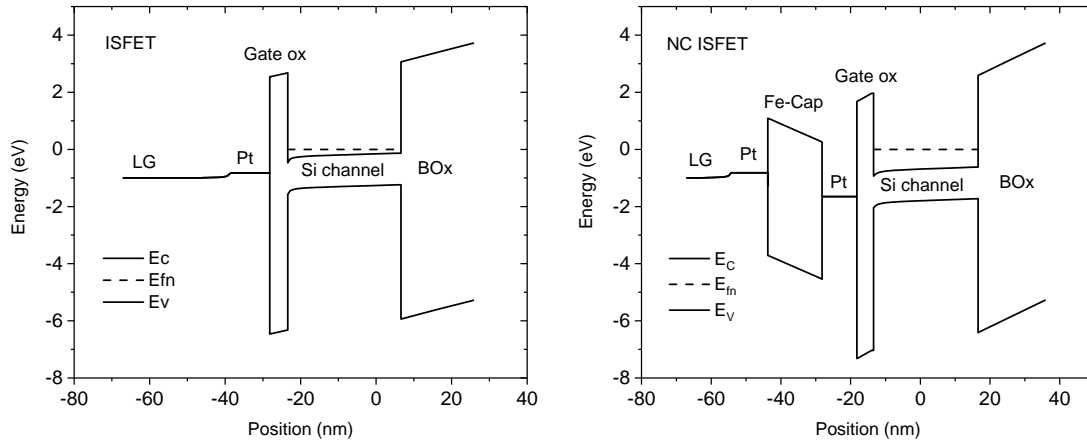


Figure 4.34 – Band diagram of ISFET and NC ISFET. The ferroelectric component increase the band bending in the silicon channel.

Finally, we can use this model to simulate the pH response of our NC ISFET without the instability observed in our proof of concept (Figure 4.35).

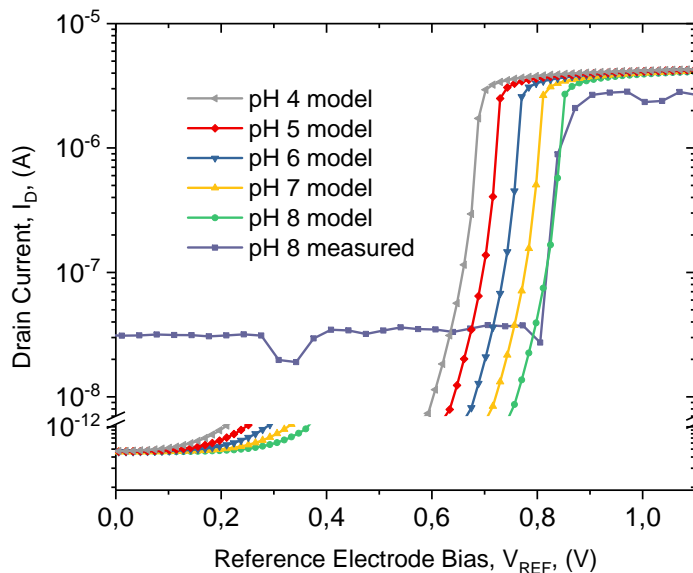


Figure 4.35 – NC ISFET transfer characteristics simulated for pH values ranging from 4 to 8.

Thanks to its steep SS of 20 mV/dec, the presented device could reach a current sensitivity of 2 dec/dec, therefore an overall ideality parameter S_{out} of 2. Moreover, if an HfO_2 layer was

employed for sensing instead of the platinum electrode, this value could be further increased to 3, meaning that the Drain current level would change of a factor 1000 per each pH point variations. Such superior performances could be exploited to detect and measure minimal variations in pH with higher precision, or to achieve equal precision with a less sophisticated read-out system. This would pave the way for highly reliable Point-of-Care or wearable applications.

It is important to underline a fundamental difference between the proposed NC ISFET and the existing strategies for signal amplification, such as double-gate ISFETs: while the existing strategies simply amplify the measurements and their superimposed noise together, without any advantage in terms of Signal-to-Noise Ratio, the dramatic increase of gate capacitance due to the addition of a negative component to the gate stack can drastically reduce the flicker noise [149], the same way as our wide sensing areas do. Optimization of the NC configurations can therefore deliver cleaner readings.

4.5 Summary

In this section, the most important achievements regarding the application of the Negative Capacitance effect to our sensors are outlined.

- **Technical outcomes:**

- Definition of a NC FET configuration with the following properties:
 - * Average SS reduced to 20 mV/dec from a starting value of 80 mV/dec;
 - * Average current efficiency increased to 115 V^{-1} from a starting value of 29 V^{-1} ;
 - * Peak differential NC gain across the FE-Cap larger than 7;
 - * Low hysteresis with crossing characteristics.
- Definition of a NC ISFET configuration characterized in DC mode with the following properties:
 - * Average SS reduced to 150 mV/dec from a starting value of 190 mV/dec;
 - * Average current efficiency increased to 15 V^{-1} from a starting value of 12 V^{-1} ;
 - * Peak differential NC gain across the FE-Cap larger than 4;
 - * High stability and repeatability of the measurements;
 - * Low hysteresis with crossing characteristics.
- Definition of a NC ISFET configuration characterized in pulsed mode with the following properties:
 - * Average SS reduced to 20 mV/dec from a starting value of 128 mV/dec;
 - * Average current efficiency increased to 115 V^{-1} from a starting value of 19 V^{-1} ;
 - * Negligible hysteresis equal to 2 mV;

- **Results highlights:**

In this chapter we have investigated the application of the Negative Capacitance effect

to ISFETs.

A mathematical model for the capacitance of the liquid gate has been introduced, in order to provide a basis for the capacitive matching. Two different NC ISFET configurations have been proposed and tested. The first configuration, characterized in DC mode, resulted sufficiently stable to allow pH measurements, and showed some measurable improvements in the current sensitivity with respect to the baseline ISFET. A substantial NC differential gain has also been measured across the FE-Cap. The second configuration, characterized in pulsed mode, resulted too unstable to allow pH measurements, but showed deep subthermionic SS and negligible hysteresis, demonstrating that, after optimization, NC ISFETs with current sensitivities S_{out} higher than unity could be producible.

The introduced model for liquid gate capacitance has been integrated in a compact model for NC FETs, resulting in the first mathematical model for NC ISFETs. After optimization of the model parameters with actual measurements, we have been able to use it to simulate some relevant device properties.

5 Conclusions and Outlook

In this final chapter, the contents and main achievements of this thesis are summarized, listing the final performances of the various implemented components. The ongoing work on the Lab On SkinTM will also be outlined, together with recommendations for future work on the proposed NC-ISFET.

5.1 Main achievements

Contents and main achievements of each chapter are reported here:

1. Introduction

The theoretical backgrounds on sweat, sweat-sensing, MOSFET and ISFET have been introduced. The advantages of ISFETs with respect to competing technologies are listed, especially in the frame of sweat analysis with minimal quantities of liquid. HfO₂ is presented as an ideal material for pH sensing, in terms of sensitivity, selectivity and long-term stability, while FD technology has been introduced for achieving a steep SS. Literature on the optimization of the SNR and LOD for sensing, together with considerations on the particular biomarkers in which we are interested in this work, have brought to the selection of the particular FD technology employed for the fabrication of our devices, which has been the ribbon-FET.

2. Technological development and characterization of the ribbon-ISFET

The geometrical and doping parameters of the ribbon-ISFET have been defined according to literature recommendations for high SNR and to TCAD simulations. The implantation parameters have been determined with the aid of simulation based on the Markov Chain Algorithm.

Hysteresis-free devices, with I_{ON}/I_{OFF} ratio as high as 10^6 , SS down to 64 mV/dec and negligible contact resistance have been obtained. Strong control on V_{th} through application of backgate bias has also been observed. The measured pH sensitivity amounted to 54 mV/pH for devices with the HfO₂ layer exposed and to 40 mV/pH for Pt-coated

devices. The measured SS value with a liquid gate was of 128 mV/dec.

3. **Lab On SkinTM: a fully integrated wearable sweat analyzer**

FD SOI ISFETs, capillary microfluidics, functionalization layers (both SAMs and ISMs) and miniaturized REs have been successfully integrated together, creating a device able to collect minimal quantities of sweat from the skin and to provide information about the individual concentrations of different biomarkers inside it.

The epoxy resin SU-8 has proven to be an excellent material for the fabrication of the capillary microfluidics, both from the point of view of the ease of fabrication and from the one of durability and performances. The capillary pumps have shown the capability of providing a sweat flow of just 4.2 nl/min, compatible with the rate of production at rest of a small (21 mm²) portion of skin. Fluorescent microscopy has shown the efficiency of the capillary inlets in collecting small droplets of sweat from an artificial skin prepared for testing purposes.

The SAM-based functionalization layers have shown the capability of changing the response of a sensing surface to the concentration of a specific ion while leaving unchanged the sensitivity toward others, allowing selective sensing through differential measurements. ISMs, however, have shown an even higher sensitivity to their target ions, often achieving a fully nernstian response, and also a fairly high selectivity with respect to competing species, all without needing the employ of differential measurements.

A miniaturized RE has been fabricated on the FD SOI ISFETs chips by sputtering and chlorination of a few micrometers of Ag on top of ad-hoc prepared Pt electrodes. A protective PVB membrane saturated in NaCl has ensured that the bias was stable in time (no drift observed over a 14 hours-long monitoring) and independent on the Cl⁻ concentration in the analyte (perfectly linear and nernstian ISFET sensitivity has been observed employing the miniaturized RE).

Real-time monitoring of the ion concentration in the LUT by continuous measurement of I_D at a given V_{REF} have shown both fast response and high repeatability.

4. **Negative Capacitance ISFET**

The possibility of employing the NC effect to steepen the SS of an ISFET, therefore improving its current sensitivity, has been explored.

Results on the successful application of a FE-Cap to our base ribbon FETs has been shown, to demonstrate the envisaged advantages. The SS has been reduced from 80 mV/dec to the deep sub-thermionic value of 20 mV/dec.

A model for the capacitance of the liquid gate has been proposed, to allow the choice of the correct FE-Cap parameters for achieving capacitive matching. Two different NC ISFET configurations, two different measurements modes (DC and pulsed) and three different sets of FE-Cap have been tested. The first configuration studied, measured in DC, allowed achieving stable measurements of pH and showed a differential NC gain bigger than 4, but the SS improvement amounted to just 21% with respect to the base device and the SS remained greater than the thermionic limit. The second configuration, characterized with pulsed measurements, while resulting unstable, has shown a SS of

just 20 mV for 2 decades of Drain current and negligible hysteresis. A NC model based on our liquid gate capacitance model has been tuned with our experimental results and provided further insight on the properties of the sensor.

5.2 Comparison with the State of Art

Comparing different wearable sensing technologies is sometimes not straightforward, given that different structures, strategies and technologies can be employed. In this section we try to resume the main differences between the introduced Lab On SkinTM and the other recently proposed technological solutions.

The main broad parameters which have been considered to determine the quality of a wearable sweat sensor are the power consumption (intended per sensor), the sensitivity to its target biomarkers (in mV/dec), the variety of biomarkers which can be sensed, the presence or not of a microfluidics able to continuously renew the sweat in contact with the sensors and the minimum sweat rate (MSR) needed to achieve readings (intended in nl/min per cm²).

This last parameter is particularly difficult to define, for devices not employing a microfluidics: if the system is open it is for example necessary to evaluate the evaporation rate, which is influenced by a number of parameters, while if the system is closed it would be relevant knowing how the old sweat is removed from the sensing area. For these reasons, in the works in which no microfluidics nor minimum sweat rate tested are specified, we will simply denote the value as "high", with the meaning that it is not compatible with at-rest conditions at normal atmospheric temperatures. The comparisons are summarized in Table 5.1,

ref.	sensor type	power	pH	Na	K	other	μ fluidics	MSR
[33]	colorimetric	N/A	N/A	-	-	lactate, glucose, creatinine, chloride	yes	200
[34]	electrode	not reported	-	25	-	-	no	high
[35]	electrode	not reported	-	64.2	61.3	glucose, lactate	no	3000
[37]	ISFET	750 nW	51.2	-	-	-	no	high
[38]	ISFET	50-300 nW	50	-	-	-	no	high
this work	ISFET	20 nW	40	62	55	-	yes	20

Table 5.1 – Lab On SkinTM comparison with the SOA

As can be seen, the sensitivities of our device to its target ions are excellent even when compared to the State of the Art. Furthermore, we demonstrate ultra-low power consumption per sensor and the only reported MSR required compatible with at-rest conditions. These advantages show the unique suitability of our system for continuous sweat monitoring of a subject in normal conditions.

Given the complete novelty of the NC ISFET proposed in Chapter 4, together with the fact that its development is still at the initial phase, it is not possible to directly compare it to similar devices. We can however report a brief comparison of our best NC ISFET transfer characteristics (Figure 4.31) with the ones reported in recent publications about standard NC MOSFET (Table 5.2).

ref.	SS	hysteresis	decades
[133]	20 mV/dec	(crossing)	2
[134]	56 mV/dec	40 mV (crossing)	2
[136]	19.6 mV/dec	0.48 V	5
[138]	11.3 mV/dec	4 V	9
this work	20 mV/dec	2 mV	2

Table 5.2 – NC ISFET comparison with the SOA

It appears clear that the addition of a liquid gate to the system does not pose an absolute limit to the employ of the NC effect to a MOSFET, and this technological improvement can therefore be transferred to ISFETs.

5.3 Outlook

A few issues still need to be addressed, in order to employ our sensor as a medical device. In this section, we report a list of recommendations for future work at short and long term, both for the Lab On SkinTM and for the introduced NC ISFET.

5.3.1 Technological improvements for the Lab On SkinTM

The following improvements should be considered for the next batch of sensors:

1. **Embedded temperature sensor:** On top of the diagnostic relevance of the skin temperature itself, knowledge of this parameter could help compensating its effect on the ISFET's readings. Temperature measurements could be achieved with minimal footprint in a number of way, ranging from resistive measurements on metal nanowires to a more complex and reliable diode circuit.

2. **Embedded flowmeter:** The physiological concentration of certain biomarkers in sweat depends on the sweat rate, therefore this parameter could help determining whether a detected variation is diagnostically meaningful or not. Furthermore, it would prevent meaningless readings before the microfluidics has been filled or in case it gets emptied for any reason.
3. **Further ISMs:** So far, only 2 different ISMs (functionalized for Na^+ and K^+) have been deposited on our sensing chip, but 2 more have already been tested (for Ca^{++} and NH_4^+) and many more could still be integrated. Next chip design should therefore provide a sufficient number of sensor sets to host a broad range of different membranes, so that many biomarkers can be tested at the same time. A drop-casting technique should also be implemented, in order to minimize the footprint of each functionalized area.
4. **Embedded computation:** In the current prototype, only the sensors are fabricated on the chip, while all the computation is performed by the external read-out circuit. A higher level of integration, in which the I_D integration is performed on-chip, could reduce both the footprint of the device and the added noise.
5. **Ribbon ISFETs and Nanowire ISFETs on the same chip:** While wide sensing areas provide the best SNR for sensing, future implementations could host on the same chip both ribbon and nanowire ISFETs: this strategy would expand the applications range of our device by enabling sensing of biomarkers at extremely low concentration ranges, such as cortisol, troponin and interleukin 6.

5.3.2 Technological improvements for the NC ISFET

The next steps in the implementation of NC on ISFETs are outlined below.

1. **Full integration of the system:** It has been observed how the parasitic capacitances of the cumbersome wiring have made the V_{th} of our prototype unstable. Future work should be focused on integrating the FE-Cap on the chip itself. The employ of a microfluidic system, such as the one introduced for the Lab On SkinTM could also help reducing the variabilities linked to the liquid gate.
2. **Removal of the metal layer between dielectric and ferroelectric:** Pulsed measurements had to be employed to prevent the gate leakages from destabilizing the NC effect. This measurement mode had adverse effects, such as increased instability, increased LOD and, furthermore, the necessity of complex biasing and read-out systems featuring remote amplifying units. An alternative to this strategy would be to deposit the ferroelectric material directly on the gate oxide.
3. **Integration of SAMs or ISMs in the system for selective sensing:** The sensor studied so far is only capable of sensing pH. To broaden its applications it would be desirable to enable selective ion sensing. In order to do so, however, models for the capacitance

of the SAMs and of the ISMs should be implemented. The thickness and uniformity of these layers, moreover, could become a critical parameter for the performances of the device and methods to accurately control these parameters will be needed.

5.3.3 Further functionalizations and new applications

So far, our sensors have only been functionalized for direct sensing of charged biomarkers. This technology enables applications for optimizing the training sessions of athletes or to promptly diagnose a small set of specific health conditions, such as renal failure or cystic fibrosis.

Adding functionalizations for complex biomolecules would drastically increase the application spectrum of the introduced device. Some of the possible applications are listed below.

- **Glucose functionalization for diabetes monitoring:** Glucose is not a charged biomarker, therefore it cannot be directly sensed by a potentiometric detector, such as an ISFET. The strategy used to enable sensing, in these cases, usually relies on the immobilization on the sensing areas of enzymes specific for the target biomolecule: after selective binding, these molecules promote a chemical reaction able to locally change the pH of the solution. For glucose sensing, β -D-glucose oxidase is used to promote the oxidation of the β -D-glucose and the consequent production of D-glucono- δ -lactone and hydrogen peroxide [150].
The ability to continuously monitor the glucose concentration in sweat would allow to indirectly monitor the one in blood as well, given their strict correlation, lifting diabetic patients from the need of continuous invasive testing.
- **Alcohol functionalization for intake monitoring:** Potentiometric sensing of alcohol in sweat yields highly accurate estimations of the corresponding blood concentration thanks to their strict correlation. Strategies for potentiometric sensing of alcohol can rely on enzymes (alcohol oxidase or alcohol dehydrogenase) [151] just like the ones for glucose.
Implementing this specific sensing in our device would allow monitoring the behavior of patients suffering from alcohol addiction, as well as providing data to users about the safety of driving or performing other potentially dangerous tasks.
- **Cortisol functionalization for stress monitoring:** Cortisol sensing in sweat has recently drawn a diffused interest, as its concentration, whose physiological values range between 20 and 500 nM, is an excellent indicator for stress levels. High levels of cortisol in sweat are symptoms of a condition which, in the short term, can adversely affect regulation of blood pressure, glucose level and metabolism of carbohydrates, while in the long term can have even more relevant effects, with insurgence of chronic diseases regarding hearth, kidneys, skeleton and immune system [152]. The methods for sensing this non-charged molecule are based on Molecularly Selective Membranes, which are produced by polymerization of functional monomer and cross-linker in presence of the

target molecule, which acts as a template. The produced membrane is permeable to other molecular and ionic species but gets clogged when it binds to its target molecule, reducing the sensitivity of the underlying potentiometric sensor to the charged species present in the analyte. The reversible binding allows monitoring increases and decreases of the target molecule concentration without the need of a washing step.

5.3.4 Concluding remarks

Sweat monitoring is an extremely promising field for healthcare and in time its applications range grows together with the reliability of its results.

In this thesis we have shown how full exploitation of this technique requires cooperation from different branches of science: Chapter 2 presented the fully CMOS-compatible fabrication of stable and reliable ribbon ISFETs featuring a wide sensing range (high I_{ON}/I_{OFF} ratio), negligible hysteresis and low contact resistance. Chapter 3 introduced the on-chip integration of the other necessary elements for sensing: our miniaturized capillary microfluidics which, thanks also to the reduced dimensions of the ribbon ISFETs, allows performing sweat monitoring with extremely reduced amounts of analyte, the miniaturized RE, which guarantees a stable bias without the employ of cumbersome commercial RE, and the two kinds of functionalization layers, which expand the application range of our system allowing selective sensing of specific ions.

Chapter 4 is a further demonstration of how ISFET technology can benefit from the continuous research made on MOSFET for computing technology: the Negative Capacitance introduced to decrease the SS of standard FETs has been successfully applied to our ISFETs, demonstrating the possibility of using this strategy to improve the current sensitivity of the sensors, possibly beyond the 1 dec/dec theoretical limit.

A Appendices

A.1 Appendix A

This appendix contains the scripts for the SDE and SDEVICE compilers used for the simulation of the ribbon-FET.

Definition of the device geometry in SDE:

```
1 (sdegeo:set-default-boolean "ABA") ;;new structures overwrite old
2 ;;structures
3
4 ;;setting definitions to be able to modify the structure
5 ;;making reference to external parameters in Structure Editor
6 (define ChanDop @ChanDop@)
7 (define SourceDop @SourceDop@)
8 (define DrainDop @DrainDop@)
9 (define Lg @Lg@)
10 (define Xjs @Xjs@)
11 (define Xjd @Xjd@)
12 (define Tbox @Tbox@)
13 (define Tbulk @Tbulk@)
14 (define Tfin @Tfin@)
15 (define Tgateox @Tgateox@)
16 (define COD 0.25)
17
18
19 ;;creating the device geometry
20
21 (sdegeo:create-rectangle (position 0 Tfin 0) (position Lg (+ Tfin (+
22 0.0025 Tgateox)) 0) "HfO2" "Gate_ox")
23
24 (sdegeo:create-rectangle (position 0 Tfin 0) (position Lg (+ Tfin 0.0025)
25 0) "SiO2" "Interlayer")
26
27 (sdegeo:create-rectangle (position 0 0 0) (position Lg Tfin 0) "Silicon"
28 "Channel")
29
30 (sdegeo:create-rectangle (position (- 0 (* 2 COD)) 0 0) (position (+ Lg (*
31 2 COD)) (- 0 Tbox) 0) "SiO2" "BOX")
32
33 (sdegeo:create-rectangle (position 0 0 0) (position (- 0 COD) Tfin 0)
```

Appendix A. Appendices

```
34 "Silicon" "Source")
35
36 (sdegeo:create-rectangle (position Lg 0 0) (position (+ Lg COD) Tfin 0)
37 "Silicon" "Drain")
38
39 ;;defining additional vertex for contacts
40
41 (sdegeo:insert-vertex (position (- 0 (/ COD 2)) Tfin 0))
42
43 (sdegeo:insert-vertex (position (+ Lg (/ COD 2)) Tfin 0))
44
45 (sdegeo:insert-vertex (position 0.01 (+ Tfin (+ 0.007 Tgateox)) 0))
46
47 (sdegeo:insert-vertex (position (- Lg 0.01) (+ Tfin (+ 0.0025 Tgateox)) 0))
48
49 ;;setting contacts
50
51 (sdegeo:define-contact-set "source" 4 (color:rgb 1 0 0) "##")
52
53 (sdegeo:define-contact-set "drain" 4 (color:rgb 1 1 0) "##")
54
55 (sdegeo:define-contact-set "gate" 4 (color:rgb 1 0 1) "##")
56
57 ;;(sdegeo:define-contact-set "backgate" 4 (color:rgb 1 1 1) "##")
58
59 ;;defining contacts
60
61 (sdegeo:set-current-contact-set "source")
62 (sdegeo:set-contact-edges (list (car (find-edge-id (position (- 0
63 (* COD 0.6)) Tfin 0)))) "source")
64
65 (sdegeo:set-current-contact-set "drain")
66 (sdegeo:set-contact-edges (list (car (find-edge-id (position (+ Lg
67 (* COD 0.6)) Tfin 0)))) "drain")
68
69 (sdegeo:set-current-contact-set "gate")
70 (sdegeo:set-contact-edges (list (car (find-edge-id (position (/ Lg 2)
71 (+ Tfin (+ 0.0025 Tgateox)) 0)))) "gate")
72
73 ;;(sdegeo:set-current-contact-set "backgate")
74 ;;(sdegeo:set-contact-edges (list (car (find-edge-id (position 0 (-
75 (- 0 Tbox) Tbulk) 0)))) "backgate")
76
77
78 ;;Reference/Evaluation Windows (S/C interface, D/C interface, source,
79 drain, channel, S+C)
80
81 (sdedr:define-refeval-window "Refwin.Source_Ch_intf" "Rectangle"
82 (position -0.005 0 0) (position 0.005 Tfin 0))
83
84 (sdedr:define-refeval-window "Refwin.Drain_Ch_intf" "Rectangle"
85 (position (- Lg 0.005) 0 0) (position (+ Lg 0.005) Tfin 0))
86
87 (sdedr:define-refeval-window "Refwin.Gate_ox" "Rectangle" (position
88 0 (+ Tfin Tgateox) 0) (position Lg (+ Tfin (* 2 Tgateox)) 0))
89
90 (sdedr:define-refeval-window "Refwin.Interlayer" "Rectangle" (position
91 0 Tfin 0) (position Lg (+ Tfin Tgateox) 0))
92
93 (sdedr:define-refeval-window "Refwin.Channel" "Rectangle" (position 0 0 0))
```

```

94   (position Lg Tfin 0))
95
96   (sdedr:define-refeval-window "Refwin.Source" "Rectangle" (position 0 0 0)
97     (position (- 0 COD) Tfin 0))
98
99   (sdedr:define-refeval-window "Refwin.Drain" "Rectangle" (position Lg 0 0)
100     (position (+ Lg COD) Tfin 0))
101
102   (sdedr:define-refeval-window "Refwin.BOX" "Rectangle" (position (- 0
103     (* 2 COD)) 0 0) (position (+ Lg (* 2 COD)) (- 0 Tbox) 0))
104
105   ;(sdedr:define-refeval-window "Refwin.Bulk" "Rectangle" (position (- 0
106     (* 2 COD)) (- 0 Tbox) 0) (position (+ Lg (* 2 COD)) (- (- 0 Tbox) Tbulk)
107     0))
108
109   ;;Doping
110
111   (sdedr:define-refeval-window "Baseline.Source" "Line" (position 1 Tfin 0)
112     (position (- 0 COD) Tfin 0))
113
114   (sdedr:define-refeval-window "Baseline.Drain" "Line" (position (- Lg 1)
115     Tfin 0) (position (+ Lg COD) Tfin 0))
116
117   (sdedr:define-constant-profile "CPDef.Silicon" "BoronActiveConcentration"
118     ChanDop)
119   (sdedr:define-constant-profile-material "PlaceCD.Silicon" "CPDef.Silicon"
120     "Silicon") ;;Base doping for the silicon
121
122   (sdedr:define-analytical-profile-placement "PlaceAP.Source" "Gauss.Source"
123     "Baseline.Source" "Both" "NoReplace" "Eval")
124
125   (sdedr:define-gaussian-profile "Gauss.Source"
126     "PhosphorusActiveConcentration" "PeakPos" 0 "PeakVal" SourceDop
127     "ValueAtDepth" ChanDop "Depth" 0.1 "Gauss" "Factor" Xjs)
128
129   (sdedr:define-analytical-profile-placement "PlaceAP.Drain"
130     "Gauss.Drain"
131     "Baseline.Drain" "Both" "NoReplace" "Eval")
132
133   (sdedr:define-gaussian-profile "Gauss.Drain"
134     "PhosphorusActiveConcentration" "PeakPos" 0 "PeakVal" DrainDop
135     "ValueAtDepth" ChanDop "Depth" 0.1 "Gauss" "Factor" Xjd)
136
137   ;;Definition of the refinement region (one for each zone,
138   ;;therefore no global one)
139
140   (sdedr:define-refinement-size "RefDef.gateox" 0.1 0.1 0.01 0.01 )
141   (sdedr:define-refinement-placement "PlaceRP.gateox" "RefDef.gateox"
142     (list "material" "HfO2" ))
143
144   (sdedr:define-refinement-size "RefDef.interlayer" 0.1 0.1 0.01 0.01 )
145   (sdedr:define-refinement-placement "PlaceRP.interlayer" "RefDef.interlayer"
146     (list "material" "SiO2" ))
147
148   (sdedr:define-refinement-size "RefDef.BOX" 0.3 0.3 0.3 0.03 )
149   (sdedr:define-refinement-placement "PlaceRP.BOX" "RefDef.BOX" "Refwin.BOX" )
150
151   (sdedr:define-refinement-size "RefDef.Bulk" 0.3 0.3 0.3 0.3 )
152   (sdedr:define-refinement-placement "PlaceRP.Bulk" "RefDef.Bulk"
153     "Refwin.Bulk" )

```

Appendix A. Appendices

```
154
155 (sdedr:define-refinement-size "RefDef.source" 0.02 0.02 (/ Tfin 4)
156 (/ Tfin 4) )
157 (sdedr:define-refinement-placement "PlaceRP.source" "RefDef.source"
158 "Refwin.Source" )
159
160 (sdedr:define-refinement-size "RefDef.drain" 0.02 0.02 (/ Tfin 4)
161 (/ Tfin 4) )
162 (sdedr:define-refinement-placement "PlaceRP.drain" "RefDef.drain"
163 "Refwin.Drain" )
164
165 (sdedr:define-refinement-size "RefDef.channel" 0.2 0.2 (/ Tfin 4)
166 (/ Tfin 4) )
167 (sdedr:define-refinement-placement "PlaceRP.channel" "RefDef.channel"
168 "Refwin.Channel" )
169
170 ;;Mesh creation
171
172 (sde:set-meshing-command "snmesh -a -c boxmethod")
173 (sde:build-mesh "snmesh" "-a -c boxmethod" "n@node@msh")
174
175 ;;Saving band structure, commands and structure
176
177 (sdeio:save-tdr-bnd (get-body-list) "n@node@_bnd.tdr")
178 (sdedr:write-cmd-file "n@node@msh.cmd")
179 (sde:save-model "n@node@dvs.sat")
```

Simulation of the device characteristics in SDEVICE:

```
1 File{
2   * input files:
3   Grid= "n@node|-1@msh.tdr"
4   * output files:
5   Plot= "@tdrdat@"
6   Current="n@node@_CDop=@ChanDop@_SDop=@SourceDop@_DDop=@DrainDop@_Lg=@Lg@
7   _Xjs=@Xjs@_Xjd=@Xjd@.plt"
8   Output= "@log@"
9
10 }
11 Electrode{
12   { Name="source" Voltage=0.0 WorkFunction=5.5 }
13   { Name="drain" Voltage=0 WorkFunction=5.5 }
14   { Name="gate" Voltage=0 WorkFunction=5.5 }
15   * { Name="backgate" Voltage=@Vbg@ WorkFunction=4 }
16 }
17
18 Physics{
19   eQCvanDort
20   EffectiveIntrinsicDensity( OldSlotboom )
21   Mobility(
22     DopingDep
23     eHighFieldsaturation( GradQuasiFermi )
24     hHighFieldsaturation( GradQuasiFermi )
25     Enormal
26   )
27   Recombination(
28     SRH( DopingDep ElectricField ( Lifetime = Schenk ) )
29   )
30 }
31
```

```

32 Plot{
33   *--Density and Currents , etc
34     eDensity hDensity
35     TotalCurrent/Vector eCurrent/Vector hCurrent/Vector
36     eMobility hMobility
37     eVelocity hVelocity
38     eQuasiFermiPotential hQuasiFermiPotential
39     eQuasiFermiEnergy hQuasiFermiEnergy
40
41   *--Fields and charges
42     ElectricField/Vector Potential SpaceCharge
43
44   *--Doping Profiles
45     Doping DonorConcentration AcceptorConcentration
46
47   *--Generation/Recombination
48   *   SRH   eBand2BandGeneration hBand2BandGeneration
49
50   *--Driving forces
51     eGradQuasiFermi/Vector hGradQuasiFermi/Vector
52     eParallel hEparallel eENormal hENormal
53
54   *--Band structure/Composition
55     BandGap BandGapNarrowing Affinity
56     ConductionBand ValenceBand NonLocal
57 }
58
59 CurrentPlot
60 {
61   eDensity( Integrate(Region="Channel") )
62   eDensity( Integrate(Region="Source") )
63   eDensity( Integrate(Region="Drain") )
64 }
65 Math {
66   Extrapolate
67   Derivatives
68   RelErrControl
69   Digits=6
70   ErRef(electron)=1e10
71   ErRef(hole)=1e10
72   Notdamped=50
73   Iterations=40
74   RhsMin=1e-20
75   RhsMax=1e20
76   RhsFactor=1e20
77   Number_of_Threads = 8
78   Method = ILS
79   CurrentPlot (Digits = 6)
80   CurrentPlot (IntegrationUnit = um)
81 }
82
83 Solve {
84   NewCurrentPrefix = "ignore_n@node@"
85   Coupled(Iterations=100 ) { Poisson }
86   Coupled(Iterations=100 ) { Electron }
87   Coupled(Iterations=100 ) { Poisson Electron }
88   Coupled(Iterations=100 ) { Poisson Electron Hole }
89
90   Quasistationary (
91   DoZero

```

Appendix A. Appendices

```
92     InitialStep=0.01 MaxStep=0.1 MinStep=1.e-5
93     Goal { Name="drain" Voltage=@Vd@ }
94     { Coupled
95       { Poisson Electron Hole }
96
97     NewCurrentFile="n@node@_Vds_1_"
98
99     Quasistationary (
100     DoZero
101     InitialStep=0.01 MaxStep=0.01 MinStep=1.e-5
102     Goal { Name="gate" Voltage=@Vg@ }
103     )
104
105     { Coupled
106       { Poisson Electron Hole }
107       Plot( FilePrefix="n@node@_Vd_1_" Time=(Range=(0 1) Intervals=8)
108         noOverwrite )
109     }
110     Save( FilePrefix="Vds_1_" )
111 }
```

A.2 Appendix B

This appendix contains the scripts for the SPROCESS compiler used for the simulation of the implantation and annealing processes.

```
1  set SDdose      @dose@
2
3  set SDenergy   @energy@
4
5  set oxmask     @OxideMaskThickness@
6
7
8  pdbSet ImplantData MonteCarlo 1
9
10 pdbSet MCImplant model sentaurus.mc
11
12
13 #--- 2D Grid definition -----
14
15 line x location=0.0 spacing= 1<nm> tag=OxideTop
16
17 line x location=20<nm> spacing=3<nm> tag=OxideBottom
18
19
20 line y location=0.0 spacing= 5<nm> tag=OxideLeft
21
22 line y location=2<um> spacing=5<nm> tag=OxideRight
23
24
25 #--- Initial simulation domain -----
26
27 region Oxide xlo=OxideTop xhi=OxideBottom ylo=OxideLeft yhi=OxideRight
28
29
30 #--- Initialize the simulation -----
31
```



```

32  init concentration=1e15<cm-3> field=Boron wafer.orient=100
33
34
35  #--- MGOALS settings for automatic meshing in newly generated layers -
36
37  mgoals min.normal.size=3<nm> max.lateral.size=0.2<um> normal.growth.ratio=1.4
38
39
40  #graphics configure= "xyshow=Phosphorous*"
41
42  #graphics on
43
44
45  #---Mask Definition-----
46
47  mask name=implant_mask segments = { -1<nm> 500<nm> 1500<nm> 2001<nm> }
48
49  deposit Si type=isotropic thickness=30<nm>
50  deposit oxide type=isotropic thickness=1.3<nm>
51  deposit oxide type=isotropic thickness=$oxmask
52
53  etch oxide type=anisotropic thickness=$oxmask mask=implant_mask
54
55
56  #--- Implanting P -----
57
58  # Analytic implantation models use the simple Gaussian and Pearson as
59
60  # well as the advanced dual Pearson functions. The implantation damage with
61  # analytic models is
62
63  # calculated according to the Hobler model
64
65  implant Phosphorus energy=$SDenergy dose=$SDdose tilt=7<degree> rotation=0<degree
66  > ion.movie
67
68  etch oxide type=anisotropic thickness=$oxmask
69
70  # The MC method uses a statistical approach to the
71  # calculation of the penetration of implanted ions into the target and
72  # accumulation of crystal
73
74  # damage based on the binary collision approximation
75
76  #--- Plotting out the "As implanted" profile -----
77
78  struct tdr=n@node@_2Dimplant
79
80  SetPlxList
81
82  #--- Rapid Thermal Annealing -----
83
84  diffuse temperature= 300<C> time= 2.6<s> N2 ramprate= 115<C/s>
85  diffuse temperature= 600<C> time= 600.0<s> N2
86  diffuse temperature= 600<C> time= 3.5<s> N2 ramprate= 115<C/s>
87  diffuse temperature= 900<C> time= 20.0<s> N2
88  diffuse temperature= 900<C> time= 60.0<s> N2 ramprate= -11.7<C/s>

```

```

89
90 #--- Plotting out the "Annealed" profile -----
91
92 struct tdr=n@node@_2Danneal
93
94 SetPlxList { Damage }

```

A.3 Appendix C

This appendix contains the MATLAB scripts used for the simulation of Double Layer capacitance of the liquid gate.

```

1 function [Clg,Cs,Cdl] = Iterative_C(Vref,pH,n0)
2 b=4e-10; %m
3 Beta=2.43e20; %J^-1
4 e0=1.6e-19; %C
5 epsr=78;
6 eps0=8.854e-12; %F/m
7 n=1.33; %refractive index water
8 n0w=3.35e28; %m^-3 bulk density of molecules of water
9 p0=1.03e-29; %C*m dipole momentum of a molecule of water (3.1D)
10 gamma=(2+n^2)/2;
11 A=sqrt(2*Beta*e0^2*n0*epsr*eps0);
12 %Cmos=0.97e-4; %F/m^2
13 Cmos=0.97e-3; %F/m^2
14 %Cmos=0.97e-2; %F/m^2
15 %Cmos=0.97;
16 Cs=1; %initial guess values Stern Layer
17 %Cs=1.743;
18 Cdl=1; %initial guess values Diffuse Layer
19 %Cdl=0.0052;
20 Clg=Cs*Cdl/(Cs+Cdl); %initial guess values Liquid Gate
21 Vph=6e-2*(7-pH); %adapt if sensitivity < 60 mV/dec
22 Cs0=eps0*n^2;
23 K=n0w*p0*((2+n^2)/3);
24 % To compute pH influence -----
25 %Nsil=3e18; %per m^-2
26 %Ka=15.8; %mol/l
27 %Kb=6.31e-8;
28
29 %Ka=3.2; %mol/l
30 %Kb=3.2e-5;
31 %Hb=10^(-pH); %mol/l
32 %Vg=Vref*Clg/(Clg+Cmos);
33
34 %VphEv=zeros(4,1);
35
36
37 %-----
38 err=1;
39 count=0;
40 while err>1e-4
41     %if (-2*Beta*Vg*e0)>20
42     % Vph=(e0/Clg)*Nsil;
43     %else
44     %Vph=(e0/Clg)*Nsil*((Hb^2*10^(-2*Beta*Vg*e0)-Ka*Kb)/(Hb^2*10^(-2*Beta*Vg*
45     e0)+Ka*Hb*10^(-Beta*Vg*e0)+Ka*Kb))

```

```

45     %      Vph=(e0/Clg)*Nsil*((Hb^2*10^(-2*Beta*Vph*e0)-Ka*Kb)/(Hb^2*10^(-2*Beta*
      Vph*e0)+Ka*Hb*10^(-Beta*Vph*e0)+Ka*Kb))
46     % Vph=(e0/Clg)*Nsil*((Hb^2-Ka*Kb)/(Hb^2+Ka*Hb+Ka*Kb))
47     %end
48     VrefTot=Vref+Vph;
49     Vg=VrefTot*Clg/(Clg+Cmos);
50     Vs=VrefTot*Cdl*Cmos/(Cdl*Cmos+Cs*Cdl+Cs*Cmos);
51     %Phi=Vg+Vs %smaller than VrefTot
52     Phi=VrefTot*Cs*Cmos/(Cdl*Cmos+Cs*Cdl+Cs*Cmos);
53     E=Vs/b;
54     Cdl=A*cosh(Beta*e0*Phi/2);
55     L=coth(gamma*p0*E*Beta)-1/(gamma*p0*E*Beta);
56     Cs=(Cs0+K*L/E)/b;
57     if abs(VrefTot)<1e-5
58         Cs=(Cs0+K*gamma*p0*Beta/3)/b;
59     end
60     Clg_new=Cs*Cdl/(Cs+Cdl);
61     err=abs((Clg-Clg_new))/Clg;
62     Clg=Clg_new;
63     count=count+1;
64     if Cdl>100
65         Cdl =100;
66     end
67     if count>200
68         disp('Did not converge')
69         Clg=0;
70         Cdl=0;
71         break
72     end
73 end
74 count;
75 %Clg=Clg*Cmos/(Clg+Cmos);

```


Bibliography

- [1] Paradiso, R. Wearable health care system for vital signs monitoring. In *4th International IEEE EMBS Special Topic Conference on Information Technology Applications in Biomedicine*, 283-286 (IEEE, 2003)
- [2] Choi, S., & Jiang, Z. A novel wearable sensor device with conductive fabric and PVDF film for monitoring cardiorespiratory signals. *Sensors and Actuators A: Physical* **128(2)**, 317-326 (2006)
- [3] Maurer, U., Rowe, A., Smailagic, A., & Siewiorek, D. P. eWatch: a wearable sensor and notification platform. In *Wearable and Implantable Body Sensor Networks, 2006. BSN 2006. International Workshop*, 4 (IEEE, 2006)
- [4] Chung, W. Y., Lee, Y. D., & Jung, S. J. A wireless sensor network compatible wearable u-healthcare monitoring system using integrated ECG, accelerometer and SpO₂. In *Engineering in Medicine and Biology Society, 2008. EMBS 2008. 30th Annual International Conference of the IEEE*, 1529-1532 (IEEE, 2008)
- [5] Liu, T., Inoue, Y., & Shibata, K. Development of a wearable sensor system for quantitative gait analysis. *Measurement* **42(7)**, 978-988 (2009)
- [6] Lorincz, K., Chen, B. R., Challen, G. W., Chowdhury, A. R., Patel, S., Bonato, P., & Welsh, M. Mercury: a wearable sensor network platform for high-fidelity motion analysis. *SenSys* **9**, 183-196 (2009)
- [7] Zhang, J., Ser, W., Yu, J., & Zhang, T. T. A novel wheeze detection method for wearable monitoring systems. In *2009 International Symposium on Intelligent Ubiquitous Computing and Education*, 331-334 (IEEE, 2009)
- [8] Sardini, E., & Serpelloni, M. Instrumented wearable belt for wireless health monitoring. *Procedia Engineering* **5**, 580-583 (2010)
- [9] Garbarino, M., Lai, M., Bender, D., Picard, R. W., & Tognetti, S. Empatica E3—A wearable wireless multi-sensor device for real-time computerized biofeedback and data acquisition. In *Wireless Mobile Communication and Healthcare (Mobihealth), 2014 EAI 4th International Conference*, 39-42 (IEEE, 2014)

Bibliography

- [10] Orengo, G., Lagati, A., & Saggio, G. Modeling wearable bend sensor behavior for human motion capture. *IEEE Sensors Journal* **14(7)**, 2307-2316 (2014)
- [11] Yang, C. M., Yang, T. L., Wu, C. C., Hung, S. H., Liao, M. H., Su, M. J., & Hsieh, H. C. Textile-based capacitive sensor for a wireless wearable breath monitoring system. In *2014 IEEE International Conference on Consumer Electronics (ICCE)*, 232-233 (IEEE, 2014)
- [12] Maria, A. R., Pasca, S., & Strungaru, R. Heart rate monitoring by using non-invasive wearable sensor. In *2017 E-Health and Bioengineering Conference (EHB)*, 587-590 (IEEE, 2017)
- [13] Parsons, K. Maintaining health, comfort and productivity in heat waves. *Global Health Action* **2(1)**, 2057 (2009)
- [14] Kreyden, O. P., Böni, R., & Burg, G. Hyperhidrosis and botulinum toxin in dermatology **30**. *Karger Medical and Scientific Publishers* (2002)
- [15] Wilke, K., Martin, A., Terstegen, L., & Biel, S. S. A short history of sweat gland biology. *International journal of cosmetic science* **29(3)**, 169-179 (2007)
- [16] Taylor, N. A., & Machado-Moreira, C. A. Regional variations in transepidermal water loss, eccrine sweat gland density, sweat secretion rates and electrolyte composition in resting and exercising humans. *Extreme physiology & medicine* **2(1)**, 4 (2007)
- [17] Buono, M. J., Lee, N. V., & Miller, P. W. The relationship between exercise intensity and the sweat lactate excretion rate. *The Journal of Physiological Sciences* **60(2)**, 103-107 (2010)
- [18] Hamouti, N., Del Coso, J., Ortega, J. F., & Mora-Rodriguez, R. Sweat sodium concentration during exercise in the heat in aerobically trained and untrained humans. *European journal of applied physiology* **111(11)**, 2873-2881 (2011)
- [19] Sonner, Z., Wilder, E., Heikenfeld, J., Kasting, G., Beyette, F., Swaile, D., Sherman, F., Joyce, J., Hagen, J., Kelley-Loughnane, N., & Naik, R. The microfluidics of the eccrine sweat gland, including biomarker partitioning, transport, and biosensing implications. *Biomicrofluidics* **9(3)**, 031301 (2015)
- [20] Lee, H., Song, C., Hong, Y. S., Kim, M. S., Cho, H. R., Kang, T., Shin, K., Choi, S. H., Hyeon, T. & Kim, D. H. Wearable/disposable sweat-based glucose monitoring device with multistage transdermal drug delivery module. *Science advances* **3(3)**, e1601314 (2016)
- [21] Vairo, D., Bruzzese, L., Marlinge, M., Fuster, L., Adjriou, N., Kipson, N., Brunet, P., Cautela, J., Jammes, Y., Mottola, G., Ruf, J., Guieu, R., Fenouillet, E., & Burtey, S. Towards Addressing the Body Electrolyte Environment via Sweat Analysis: Pilocarpine Iontophoresis Supports Assessment of Plasma Potassium Concentration. *Scientific reports* **7(1)**, 11801 (2017)
- [22] Sakharov, D. A., Shkurnikov, M. U., Vagin, M. Y., Yashina, E. I., Karyakin, A. A., & Tonevitsky, A. G. Relationship between lactate concentrations in active muscle sweat and whole blood. *Bulletin of experimental biology and medicine* **150(1)**, 83-85 (2016)

- [23] Buono, M. J. Sweat ethanol concentrations are highly correlated with co-existing blood values in humans. *Experimental physiology* **84**(2), 401-404 (2016)
- [24] Huang, C. T., Chen, M. L., Huang, L. L., & Mao, I. F. Uric acid and urea in human sweat. *Chinese Journal of Physiology* **45**(3), 109-116 (2002)
- [25] Abellán-Llobregat, A., Jeerapan, I., Bandodkar, A., Vidal, L., Canals, A., Wang, J., & Moral-lon, E. A stretchable and screen-printed electrochemical sensor for glucose determination in human perspiration. *Biosensors and Bioelectronics* **91**, 885-891 (2017)
- [26] Emaminejad, S., Gao, W., Wu, E., Davies, Z. A., Nyein, H. Y. Y., Challa, S., Ryan, S. P., Fahad, H. M., Chen, K., Shahpar, Z., Milla, C., Javey, A., Davis, R. W. & Talebi, S. Autonomous sweat extraction and analysis applied to cystic fibrosis and glucose monitoring using a fully integrated wearable platform. *Proceedings of the National Academy of Sciences* **114**(18), 4625-4630 (2017)
- [27] Czarnowski, D., Gorski, J., Józwiuk, J., & Boroń-Kaczmarska, A. Plasma ammonia is the principal source of ammonia in sweat. *European journal of applied physiology and occupational physiology* **65**(2), 135-137 (1992)
- [28] Lieberman, J. Cyclic fluctuation of sweat electrolytes in women: Effect of polythiazide upon sweat electrolytes. *JAMA* **195**(8), 629-635 (1966)
- [29] Morgan, R. M., Patterson, M. J., & Nimmo, M. A. Acute effects of dehydration on sweat composition in men during prolonged exercise in the heat. *Acta Physiologica Scandinavica* **182**(1), 37-43 (2004)
- [30] Lacher, J. W., & Schrier, R. W. Sweating treatment for chronic renal failure. *Nephron* **21**(5), 255-259 (1978)
- [31] Ďurč, P., Foret, F., Pokojová, E., Homola, L., Skříčková, J., Herout, V., Dastyh, M., Vinohradská & Kubáň, P. New approach for cystic fibrosis diagnosis based on chloride/potassium ratio analyzed in non-invasively obtained skin-wipe sweat samples by capillary electrophoresis with contactless conductometric detection. *Analytical and bioanalytical chemistry* **409**(14), 3507-3514 (2017)
- [32] Benito-Lopez, F., Coyle, S., Byrne, R., Smeaton, A., O'Connor, N. E., & Diamond, D. Pump less wearable microfluidic device for real time pH sweat monitoring. *Procedia Chemistry* **1**(1), 1103-1106 (2009)
- [33] Koh, A. *et al.* A soft, wearable microfluidic device for the capture, storage, and colorimetric sensing of sweat. *Science Translational Medicine* **8**(366), 366ra165-366ra165 (2016)
- [34] Rose, D. P., Ratterman, M. E., Griffin, D. K., Hou, L., Kelley-Loughnane, N., Naik, R. R., Hagen, J. A., Papautsky, I. & Heikenfeld, J. C. Adhesive RFID sensor patch for monitoring of sweat electrolytes. *IEEE Transactions on Biomedical Engineering* **62**(6), 1457-1465 (2015)

Bibliography

- [35] Gao, W., Emaminejad, S., Nyein, H. Y. Y., Challa, S., Chen, K., Peck, A., Fahad, H., Ota, H., Shiraki, H., Kiriya, D., Javey, A., Brooks, G. A., Davis, R. W. & Lien, D. H. Fully integrated wearable sensor arrays for multiplexed in situ perspiration analysis. *Nature* **529(7587)**, 509 (2016)
- [36] Zhang, J. Wearable System for for Real-Time Sensing of Biomarkers in Human Sweat. (2019)
- [37] Nakata, S., Arie, T., Akita, S., & Takei, K. Wearable, flexible, and multifunctional healthcare device with an ISFET chemical sensor for simultaneous sweat pH and skin temperature monitoring. *ACS sensors* **2(3)**, 443-448 (2017)
- [38] Douthwaite, M., Moser, N., Koutsos, E., Yates, D., Mitcheson, P., & Georgiou, P. A CMOS ISFET array for wearable thermoelectrically powered perspiration analysis. In *Biomedical Circuits and Systems Conference (BioCAS)*, 54-57 (IEEE, 2016)
- [39] Schaller, R. R. Moore's law: past, present and future. *IEEE spectrum* **34(6)**, 52-59 (1997)
- [40] Bergveld, P. Development of an ion-sensitive solid-state device for neurophysiological measurements. *IEEE Transactions on Biomedical Engineering* (**1**), 70-71 (1970)
- [41] Kittel, C. Introduction to Solid State Physics, 7th edition. (2007)
- [42] Reif, F. Statistical thermal physics *Mcgraw-Hill Kogakusha* (1965)
- [43] Adan, A. O., & Higashi, K. OFF-State leakage current mechanisms in bulkSi and SOI MOSFETs and their impact on CMOS ULSIs standby current. *IEEE Transactions on Electron Devices* **48(9)**, 2050-2057 (2001)
- [44] Tsividis, Y., & McAndrew, C. Operation and Modeling of the MOS Transistor **2** *Oxford university press* (1999)
- [45] Cheung, K. P. On the 60 mV/dec@ 300 K limit for MOSFET subthreshold swing. In *Proceedings of 2010 International Symposium on VLSI Technology, System and Application*, 72-73 (IEEE, 2010)
- [46] Colinge, J. P. Subthreshold slope of thin-film SOI MOSFET's. *IEEE Electron Device Letters* **7(4)**, 244-246 (1986)
- [47] Balestra, F., & Brini, J. SOI MOSFET in weak inversion and weak accumulation. *Electronics Letters* **23(5)**, 211-213 (1987)
- [48] Sturm, J. C. Performance advantages of submicron silicon-on-insulator devices for ULSI. In *MRS Online Proceedings Library Archive*, 107, 1987)
- [49] Wouters, D. J., Colinge, J. P., & Maes, H. E. Subthreshold slope in thin-film SOI MOSFETs. *IEEE Transactions on Electron Devices* **37(9)**, 2022-2033 (1990)

-
- [50] Colombo, L., Chambers, J. J., & Niimi, H. Gate dielectric process technology for the sub-1 nm equivalent oxide thickness (EOT) era. *16(3)*51-55 *INTERFACE-PENNINGTON* (2007)
- [51] Helmholtz, H. V. Ueber einige Gesetze der Vertheilung elektrischer Ströme in körperlichen Leitern, mit Anwendung auf die thierisch-elektrischen Versuche. *Annalen der Physik* **165(7)**, 353-377 (1853)
- [52] Gouy, L. G. Sur la Constitution de la Charge Electrique a la Surface d'un Electrolyte. *J. de Physique* **4,9**, 457-468 (1910)
- [53] Chapman, D. L. A contribution to the theory of electrocapillarity. *The London, Edinburgh, and Dublin philosophical magazine and journal of science* **25(148)**, 475-481 (1913)
- [54] Stern, O. Zur theorie der elektrolytischen doppelschicht. *Zeitschrift für Elektrochemie und angewandte physikalische Chemie* **30(21-22)**, 508-516 (1924)
- [55] Yates, D. E., Levine, S., & Healy, T. W. Site-binding model of the electrical double layer at the oxide/water interface. *Journal of the Chemical Society, Faraday Transactions 1: Physical Chemistry in Condensed Phases* **70**, 1807-1818 (1974)
- [56] Bergveld, P. Thirty years of ISFETOLOGY: What happened in the past 30 years and what may happen in the next 30 years. *Sensors and Actuators B: Chemical* **88(1)**, 1-20 (2003)
- [57] Van Hal, R. E. G., Eijkel, J. C., & Bergveld, P. A novel description of ISFET sensitivity with the buffer capacity and double-layer capacitance as key parameters. *Sensors and Actuators B: Chemical* **24(1-3)**, 201-205 (1995)
- [58] Endresen, L. P., Hall, K., Høye, J. S., & Myrheim, J. A theory for the membrane potential of living cells. *European Biophysics Journal* **29(2)**, 90-103 (2000)
- [59] Bousse, L., De Rooij, N. F., & Bergveld, P. Operation of chemically sensitive field-effect sensors as a function of the insulator-electrolyte interface. *IEEE Transactions on Electron Devices* **30(10)**, 1263-1270 (1983)
- [60] Bergveld, P., Van Hal, R. E. G., & Eijkel, J. C. The remarkable similarity between the acid-base properties of ISFETs and proteins and the consequences for the design of ISFET biosensors. *Biosensors and bioelectronics* **10(5)**, 405-414 (1995)
- [61] Shinwari, M. W., Zhitomirsky, D., Deen, I. A., Selvaganapathy, P. R., Deen, M. J., & Landheer, D. Microfabricated reference electrodes and their biosensing applications. *Sensors* **10(3)**, 1679-1715 (2010)
- [62] Kang, J. W., & Cho, W. J. Achieving Enhanced pH Sensitivity Using Capacitive Coupling in Extended Gate FET Sensors with Various High-K Sensing Films. *Solid-State Electronics* (2018)

Bibliography

- [63] Zafar, S., D'Emic, C., Afzali, A., Fletcher, B., Zhu, Y., & Ning, T. Optimization of pH sensing using silicon nanowire field effect transistors with HfO₂ as the sensing surface. *Nanotechnology* 405501 (2011)
- [64] Polk, B. J., Stelzenmuller, A., Mijares, G., MacCrehan, W., & Gaitan, M. Ag/AgCl micro-electrodes with improved stability for microfluidics. *Sensors and Actuators B: Chemical* **114(1)**, 239-247 (2006)
- [65] Kaisti, M. Detection principles of biological and chemical FET sensors. *Biosensors and Bioelectronics* **98**, 437-448 (2017)
- [66] Chin, Y. L., Chou, J. C., Sun, T. P., Chung, W. Y., & Hsiung, S. K. A novel pH sensitive ISFET with on chip temperature sensing using CMOS standard process. *Sensors and Actuators B: Chemical* **76(1-3)**, 582-593 (2001)
- [67] Schlesinger, R., Bruns, M., Becht, R., Dosenbach, S., Hoffmann, W., & Ache, H. J. ISFETs with sputtered sodium alumino-silicate glass membranes. *Fresenius' journal of analytical chemistry* **354(7-8)**, 852-856 (2006)
- [68] Constandinou, T. G., Georgiou, P., Prodromakis, T., & Toumazou, C. A CMOS-based lab-on-chip array for the combined magnetic stimulation and opto-chemical sensing of neural tissue. In *Cellular Nanoscale Networks and Their Applications (CNNA), 2010 12th International Workshop*, 1-6 (IEEE, 2010)
- [69] Sohbaty, M., & Toumazou, C. Dimension and shape effects on the ISFET performance. *IEEE Sensors Journal* **15(3)**, 1670-1679 (2015)
- [70] Liu, Y. Engineering robust cmos isfet smart sensor systems. 2012)
- [71] Khanna, V. K. Remedial and adaptive solutions of ISFET non-ideal behaviour. *Sensor Review* **33(3)**, 228-237 (2013)
- [72] Song, E., Lee, Y. K., Li, R., Li, J., Jin, X., Yu, K. J., Xie, Z., Fang, H., Zhong, Y., Du, H., Fang, G., Kim, Y., Yoon, Y., Alam, M., Mei, Y., Huang, Y., Rogers, J., & Zhang, J. Transferred, ultrathin oxide bilayers as biofluid barriers for flexible electronic implants. *Advanced Functional Material* **28(12)**, 1702284 (2018)
- [73] Dak, P., Seo, W., Jung, B., & Alam, M. A. A Physics-Based (Verilog-A) Compact Model for DC, Quasi-Static Transient, Small-Signal, and Noise Analysis of MOSFET-Based pH Sensors. *IEEE Transactions on Electron Devices* **64(3)**, 1285-1293 (2017)
- [74] Rajan, N. K., Brower, K., Duan, X., & Reed, M. A. Limit of detection of field effect transistor biosensors: Effects of surface modification and size dependence. *Applied Physics Letters* **104(8)**, 084106 (2014)
- [75] Bedner, K., Guzenko, V. A., Tarasov, A., Wipf, M., Stoop, R. L., Rigante, S., Brunner, J., Fu, W., David, C., Calame, M., Schönenberger, C., & Gobrecht, J. Investigation of the

- dominant 1/f noise source in silicon nanowire sensors. *Sensors and Actuators B: Chemical* **191**, 270-275 (2014)
- [76] Nair, P. R., & Alam, M. A. Performance limits of nanobiosensors. *Applied physics letters* **88(23)**, 233120 (2006)
- [77] Gagniuc, P. A. Markov chains: from theory to implementation and experimentation. (20177)
- [78] Rigante, S. High-K Dielectric FinFETs on Si-Bulk for Ionic and Biological Sensing Integrated Circuits. 2014)
- [79] Smith, A. J., Gwilliam, R. M., Stolojan, V., Knights, A. P., Coleman, P. G., Kallis, A., & Yeong, S. H. Enhancement of phosphorus activation in vacancy engineered thin silicon-on-insulator substrates. *Journal of Applied Physics* **106(10)**, 103514 (2009)
- [80] Golden, J., Miller, H., Nawrocki, D., & Ross, J. Optimization of bi-layer lift-off resist process. *CS Mantech Technical Digest* (2009)
- [81] Moritz, H. Optical single layer lift-off process. *IEEE Transactions on Electron Devices* **32(3)**, 672-676 (1985)
- [82] Williams, K. R., Gupta, K., & Wasilik, M. Etch rates for micromachining processing-Part II. *Journal of microelectromechanical systems* **12(6)**, 761-778 (2003)
- [83] Köllensperger, P. A., Karl, W. J., Ahmad, M. M., Pike, W. T., & Green, M. Patterning of platinum (Pt) thin films by chemical wet etching in Aqua Regia. *Journal of Micromechanics and Microengineering* **22(6)**, 067001 (2012)
- [84] Cardinaud, C., Peignon, M. C., & Tessier, P. Y. Plasma etching: principles, mechanisms, application to micro-and nano-technologies. *Applied Surface Science* **164(1-4)**, 72-83 (2000)
- [85] Glöersen, P. G. Ion beam etching. *Journal of Vacuum Science and Technology* **12(1)**, 28-35 (1975)
- [86] Delabie, A., Bellenger, F., Houssa, M., Conard, T., Van Elshocht, S., Caymax, M., Heyns, M., & Meuris, M. Effective electrical passivation of Ge (100) for high-k gate dielectric layers using germanium oxide. *Applied physics letters* **91(8)**, 082904 (2007)
- [87] Deal, B. E., & Grove, A. S. General relationship for the thermal oxidation of silicon. *Journal of Applied Physics* **36(12)**, 3770-3778 (1965)
- [88] Rigante, S., Scarbolo, P., Wipf, M., Stoop, R. L., Bedner, K., Buitrago, E., Bazigos, A., Bouvet, D., Calame, M., Schönenberger, C., & Ionescu, A. M. General relationship for the thermal oxidation of silicon. *Journal of Applied Physics* **36(12)**, 3770-3778 (1965)

Bibliography

- [89] George, S. M. Atomic layer deposition: an overview. *Chemical reviews* **110(1)**, 111-131 (2009)
- [90] Waits, R. K. Planar magnetron sputtering. *Journal of Vacuum Science and Technology* **15(2)**, 179-187 (1978)
- [91] Kern, W. In *Thin film processes II (Vol. 2)*, 79-129 (Elsevier, 2012)
- [92] Gaillardin, M., Martinez, M., Paillet, P., Andrieu, F., Girard, S., Raine, M., Marcandella, C., Duhamel, O., Richard, N., & Faynot, O. Impact of SOI substrate on the radiation response of ultrathin transistors down to the 20 nm node. *IEEE Transactions on Nuclear Science* **60(4)**, 2583-2589 (2013)
- [93] Suyama, S., Okamoto, A., & Serikawa, T. Electrical Conduction and Dielectric Breakdown in Sputter-Deposited Silicon Dioxide Films on Polysilicon. *Journal of The Electrochemical Society* **135(12)**, 3104-3106 (1988)
- [94] Sze, S. M., & Ng, K. K. In *Physics of semiconductor devices*, (John Wiley & Sons, 2006)
- [95] Tao, M., Agarwal, S., Udeshi, D., Basit, N., Maldonado, E., & Kirk, W. P. Low Schottky barriers on n-type silicon (001). *Applied physics letters* **83(13)**, 2593-2595 (2003)
- [96] Reith, T. M., & Schick, J. D. The electrical effect on Schottky barrier diodes of Si crystallization from Al-Si metal films. *Applied physics letters* **25(9)**, 2593-2595 (1974)
- [97] <https://warwick.ac.uk/fac/sci/physics/current/postgraduate/regs/mpagswarwick/ex5/devices/hetrojunction/ohmic/>
- [98] Learn, A. J. Evolution and current status of aluminum metallization. *Journal of The Electrochemical Society* **123(6)**, 894-906 (1976)
- [99] Guo, H. Electrical Properties of Junction Structure in Silicon Devices (Doctoral dissertation, University of Pittsburgh). 2018)
- [100] O'Donnell, S. J., Bartling, J. W., & Hill, G. Silicon inclusions in aluminum interconnects. In *Reliability Physics Symposium, 1984. 22nd Annual*, 9-16 (IEEE, 1984)
- [101] Finetti, M., Ostojica, P., Solmi, S., & Soncini, G. Aluminum-Silicon ohmic contact on shallow n+/p junctions. *Solid State Electronics* **23**, 255-257 (1980)
- [102] Nogami, T., Takahashi, S., Oami, M., Kaneko, Y., & Haida, O. Suppressed Si precipitation at an AlSi/Si contact by the presence of thin SiO₂ film on the Si substrate. *Semiconductor science and technology* **9(11)**, 2138 (1994)
- [103] Muta, H. Electrical properties of platinum-silicon contact annealed in an H₂ ambient. *Japanese Journal of Applied Physics* **17(6)**, 1089 (1978)

- [104] Boberg, G., Stolt, L., Tove, P. A., & Norde, H. Contact resistance measurements of platinum-silicide and chromium contacts to highly doped n and p silicon. *Physica Scripta* **24(2)**, 405 (1981)
- [105] Hauber, J., Frank, W., & Stolwijk, N. Diffusion and solubility of platinum in silicon. *Materials Science Forum* **38**, 707-712 (1989)
- [106] Larrieu, G., Dubois, E., Wallart, X., Baie, X., & Katcki, J. Formation of platinum-based silicide contacts: Kinetics, stoichiometry, and current drive capabilities. *Journal of Applied Physics* **94(12)**, 7801-7810 (2003)
- [107] Garcia-Cordero, E., Guerin, H., Muhech, A., Bellando, F., & Ionescu, A. M. Heterogeneous integration of low power pH FinFET sensors with passive capillary microfluidics and miniaturized Ag/AgCl quasi-Reference Electrode. In *2016 46th European Solid-State Device Research Conference (ESSDERC)*, 452-455 (IEEE, 2016)
- [108] Hillel, D., & Hatfield, J. L. *Encyclopedia of Soils in the Environment (Vol. 3)*. (Elsevier, 2005)
- [109] Jokinen, V., & Franssila, S. Capillarity in microfluidic channels with hydrophilic and hydrophobic walls. *Microfluidics and Nanofluidics* **5(4)**, 443-448 (2008)
- [110] Law, K. Y. Definitions for hydrophilicity, hydrophobicity, and superhydrophobicity: getting the basics right. *Journal of Physical Chemistry Letters, Guest commentary* (2014)
- [111] Otitoju, T. A., Ahmad, A. L., & Ooi, B. S. Superhydrophilic (superwetting) surfaces: a review on fabrication and application. *Journal of industrial and engineering chemistry* **47**, 19-40 (2017)
- [112] Lorenz, H., Despont, M., Fahrni, N., LaBianca, N., Renaud, P., & Vettiger, P. SU-8: a low-cost negative resist for MEMS. *Journal of Micromechanics and Microengineering* **7(3)**, 121 (1997)
- [113] Nemani, K. V., Moodie, K. L., Brennick, J. B., Su, A., & Gimi, B. In vitro and in vivo evaluation of SU-8 biocompatibility. *Materials Science and Engineering: C* **33(7)**, 4453-4459 (2013)
- [114] Test, A. D. *Critical surface tension and contact angle with water for various polymers. Diversified Enterprises, Claremont, USA* (2009)
- [115] Zimmermann, M., Schmid, H., Hunziker, P., & Delamarche, E. Capillary pumps for autonomous capillary systems. *Lab on a Chip* **7(1)**, 119-125 (2007)
- [116] Garcia-Cordero, E., Wildhaber, F., Bellando, F., Longo, J., Fernández-Bolaños, M., Guerin, H., & Ionescu, A. M. Embedded passive nano-liter micropump for sweat collection and analysis. In *2018 IEEE Micro Electro Mechanical Systems (MEMS)*, 1217-1220 (IEEE, 2018)

Bibliography

- [117] Ulman, A. Formation and structure of self-assembled monolayers. *Chemical reviews* **96(4)**, 1533-1554 (1996)
- [118] Bellando, F., Garcia-Cordero, E., Wildhaber, F., Longo, J., Guérin, H., & Ionescu, A. M. Lab on skin™: 3D monolithically integrated zero-energy micro/nanofluidics and FD SOI ion sensitive FETs for wearable multi-sensing sweat applications. In *2017 IEEE International Electron Devices Meeting (IEDM)*, 18-1 (IEEE, 2017)
- [119] Wipf, M., Stoop, R. L., Tarasov, A., Bedner, K., Fu, W., Wright, I. A., Martin, C. J., Constable, E. C., Calame, M., & Schönenberger, C. Selective sodium sensing with gold-coated silicon nanowire field-effect transistors in a differential setup. *ACS nano* **7(7)**, 5978-5983 (2013)
- [120] Morf, W. E. The principles of ion-selective electrodes and of membrane transport (Vol. 2). (Elsevier, 2012)
- [121] Bühlmann, P., & Chen, L. D. Ion-selective electrodes with ionophore-doped sensing membranes. *Supramolecular Chemistry: From Molecules to Nanomaterials* **5**, 2539-2579 (2012)
- [122] Vaes, W. H., Urrestarazu Ramos, E., Verhaar, H. J., Cramer, C. J., & Hermens, J. L. Understanding and estimating membrane/water partition coefficients: Approaches to derive quantitative structure property relationships. *Chemical research in toxicology* **11(8)**, 847-854 (1998)
- [123] <https://nanohub.org/resources/30736/>.
- [124] Garcia-Cordero, E., Bellando, F., Zhang, J., Wildhaber, F., Longo, J., Guerin, H., & Ionescu, A. M. Three-Dimensional Integrated Ultra-Low-Volume Passive Microfluidics with Ion-Sensitive Field-Effect Transistors for Multiparameter Wearable Sweat Analyzers. *ACS nano* **12(12)**, 12646-12656 (2018)
- [125] Zhang, J. R., Rupakula, M., Bellando, F., Cordero, E. G., Longo, J., Wildhaber, F., Herment, G., Guérin, H., & Ionescu, A. M. All CMOS Integrated 3D-Extended Metal Gate ISFETs for pH and Multi-Ion (Na⁺, K⁺, Ca²⁺) sensing. In *2018 IEEE International Electron Devices Meeting (IEDM)*, 12-1 (IEEE, 2018)
- [126] Huang, I. Y., Huang, R. S., & Lo, L. H. Improvement of integrated Ag/AgCl thin-film electrodes by KCl-gel coating for ISFET applications. *Sensors and Actuators B: Chemical* **94(1)**, 53-64 (2003)
- [127] Emaminejad, S., Gao, W., Wu, E., Davies, Z. A., Nyein, H. Y. Y., Challa, S., Ryan, S. P., Fahad, H. M., Chen, K., Shaphar, Z., Milla, C., Javey, A., Davis, R. W., & Talebi, S. Autonomous sweat extraction and analysis applied to cystic fibrosis and glucose monitoring using a fully integrated wearable platform. *Proceedings of the National Academy of Sciences* **114(18)**, 4625-4630 (2017)

- [128] Theis, T. N., & Solomon, P. M. It's time to reinvent the transistor!. *Science* **327(5973)**, 1600-1601 (2010)
- [129] Salahuddin, S., & Datta, S. Use of negative capacitance to provide voltage amplification for low power nanoscale devices. *Nano letters* **8(2)**, 405-410 (2008)
- [130] Salahuddin, S. Review of negative capacitance transistors. In *2016 International Symposium on VLSI Technology, Systems and Application (VLSI-TSA)*, 1-1 (IEEE, 2016)
- [131] Khan, A. I., Radhakrishna, U., Chatterjee, K., Salahuddin, S., & Antoniadis, D. A. Negative capacitance behavior in a leaky ferroelectric. *IEEE Transactions on Electron Devices* **63(11)**, 4416-4422 (2016)
- [132] Yeung, C. W., Khan, A. I., Salahuddin, S., & Hu, C. Device design considerations for ultra-thin body non-hysteretic negative capacitance FETs. In *2013 Third Berkeley Symposium on Energy Efficient Electronic Systems (E3S)*, 1-2 (IEEE, 2013)
- [133] Saeidi, A., Jazaeri, F., Bellando, F., Stolichnov, I., Luong, G. V., Zhao, Q. T., Mantl, S., Enz C. C., & Ionescu, A. M. Negative capacitance as performance booster for tunnel FETs and MOSFETs: An experimental study. *IEEE Electron Device Letters* **38(10)**, 1485-1488 (2017)
- [134] Zhou, J., Han, G., Li, Q., Peng, Y., Lu, X., Zhang, C., Zhang, J., Sun, Q., Zhang, D. W., & Hao, Y. Ferroelectric HfZrO_xGe and GeSn PMOSFETs with Sub-60 mV/decade subthreshold swing, negligible hysteresis, and improved I_{ds}. In *2016 IEEE International Electron Devices Meeting (IEDM)*, 12-2 (IEEE, 2016)
- [135] Dasgupta, S., Rajashekhar, A., Majumdar, K., Agrawal, N., Razavieh, A., Troler-Mckinstry, S., & Datta, S. Sub-kT/q Switching in Strong Inversion in PbZr_{0.52}Ti_{0.48}O₃ Gated Negative Capacitance FETs. *IEEE Journal on Exploratory Solid-State Computational Devices and Circuits* **1**, 43-48 (2015)
- [136] Ko, E., Lee, J. W., & Shin, C. Negative capacitance FinFET with sub-20-mV/decade subthreshold slope and minimal hysteresis of 0.48 V. *IEEE Electron Device Letters* **38(4)**, 418-421 (2017)
- [137] Pellegrini, N., Frattini, A., Steren, C. A., Rapp, M. E., Gil, R., Trbojevich, R., Gonzales Oliver, C. J. R., & De Sanctis, Y. O. Chemical solution technique to prepare perovskite PZT and PLZT thin films and powders. *Integrated Ferroelectrics* **30(1-4)**, 111-119 (2000)
- [138] Khan, A. I., Chatterjee, K., Duarte, J. P., Lu, Z., Sachid, A., Khandelwal, S., Ramesh, R., Hu, C., & Salahuddin, S. Negative capacitance in short-channel FinFETs externally connected to an epitaxial ferroelectric capacitor. *IEEE Transactions on Electron Devices* **37(1)**, 111-114 (2016)
- [139] Gao, W., Khan, A., Marti, X., Nelson, C., Serrao, C., Ravichandran, J., Ramesh, R., & Salahuddin, S. Room-temperature negative capacitance in a ferroelectric-dielectric superlattice heterostructure. *Nano letters* **14(10)**, 5814-5819 (2014)

Bibliography

- [140] Appleby, D. J., Ponon, N. K., Kwa, K. S., Zou, B., Petrov, P. K., Wang, T., Alford, N. M., & O'Neill, A. Experimental observation of negative capacitance in ferroelectrics at room temperature. *Nano letters* **14**(7), 3864-3868 (2014)
- [141] Martinoia, S., & Massobrio, G. A behavioral macromodel of the ISFET in SPICE. *Sensors and Actuators B: Chemical* **62**(3), 182-189 (2000)
- [142] Velikonja, A., Gongadze, E., Kralj-Iglic, V., & Iglic, A. Charge dependent capacitance of Stern layer and capacitance of electrode/electrolyte interface. *International Journal of Electrochemical Science* **9**(10), 5885-5894 (2014)
- [143] Venema, P., Hiemstra, T., & van Riemsdijk, W. H. Comparison of different site binding models for cation sorption: description of pH dependency, salt dependency, and cation-proton exchange. *Journal of Colloid and Interface Science* **181**(1), 45-59 (1996)
- [144] Hoffmann, M., Pešić, M., Slesazeck, S., Schroeder, U., & Mikolajick, T. On the stabilization of ferroelectric negative capacitance in nanoscale devices. *Nanoscale* **10**(23), 10891-10899 (2018)
- [145] Ng, K., Hillenius, S. J., & Gruverman, A. Transient nature of negative capacitance in ferroelectric field-effect transistors. *Solid State Communications* **265**, 12-14 (2017)
- [146] Khan, A. I., Radhakrishna, U., Chatterjee, K., Salahuddin, S., & Antoniadis, D. A. Negative capacitance behavior in a leaky ferroelectric. *IEEE Transactions on Electron Devices* **63**(11), 4416-4422 (2016)
- [147] Hoffmann, M., Fengler, F. P., Herzig, M., Mittmann, T., Max, B., Schroeder, U., Negrea, R., Lucian, P., Slesazeck, S., & Mikolajick, T. Unveiling the double-well energy landscape in a ferroelectric layer. *Nature* **565**(7740), 464 (2019)
- [148] Pahwa, G., Dutta, T., Agarwal, A., & Chauhan, Y. S. Compact model for ferroelectric negative capacitance transistor with MFIS structure. *IEEE Transactions on Electron Devices* **64**(3), 1366-1374 (2017)
- [149] Zagni, N., Pavan, P., & Alam, M. A. Two-dimensional MoS₂ negative capacitor transistors for enhanced (super-Nernstian) signal-to-noise performance of next-generation nano biosensors. *Applied Physics Letters* **114**(23), 233102 (2019)
- [150] Shul'ga, A. A., Sandrovsky, A. C., Strikha, V. I., Soldatkin, A. P., Starodub, N. F., & El'Skaya, A. V. Overall characterization of ISFET-based glucose biosensor. *Sensors and Actuators B: Chemical* **10**(1), 41-46 (1992)
- [151] Rotariu, L., Bala, C., & Magearu, V. New potentiometric microbial biosensor for ethanol determination in alcoholic beverages. *Analytica chimica acta* **513**(1), 119-123 (2004)
- [152] Parlak, O., Keene, S. T., Marais, A., Curto, V. F., & Salleo, A. Molecularly selective nanoporous membrane-based wearable organic electrochemical device for noninvasive cortisol sensing. *Science advances* **4**(7), eaar2904 (2018)

Francesco BELLANDO

Avenue du Silo 10, 1020 Renens Switzerland
Mobile phone +41 789541467 (Swiss) +39 3343211663 (Italian)
Date of birth 13.04.1989
francesco.bellando@gmail.com
<https://www.linkedin.com/in/francesco-bellando-2971a615a>.

Strengths

- EPFL engineer
- 4 years cleanroom experience
- Problem solving abilities
- Trilingual (Italian, English and French)



PROFESSIONAL EXPERIENCES

Research Engineer at EPFL NanoLab and start-up Xsensio, Lausanne, Switzerland

- 2015-present**
- Study, design, simulation, fabrication and characterization of an Ion-Sensitive Field Effect Transistor (**ISFET**)-based chip for sweat analysis.
 - **Optimization** of the Process Flow to improve yield, gaining robustness towards process variabilities of a non-industrial cleanroom.
 - **Excellent electric performances** of the fabricated devices.
 - Active contribution to the **design** of the complete system and to the **troubleshooting** of issues in areas ranging from **electronics** to **microfluidics** to **chemistry**.

Scientist at EPFL NanoLab, Lausanne, Switzerland

- 2015**
April-June
- **Study of viable solutions** for fabricating a simulated TFET structure, with severe constraints on precision and material safety of the process.
 - In the short time provided, a full **set of tests** has been performed, highlighting weak points of the initially envisaged Process Flow and proposing alternative solutions based on the results obtained.

EDUCATION




Ph.D. in Nanoelectronics at EPFL NanoLab, Lausanne, Switzerland

- 2015-present**
- “UTBSOI ISFET-based sensing chip for real-time sweat analysis in low sweating conditions”

Master of Science in Nano-engineering at Politecnico di Torino

- 2008-2015**
- Major in Nanotechnologies for the Information and Communication Technologies.
 - Minor in Physics engineering.
 - Master Thesis for exchange student at EPFL.
 - Final GPA: 110/110.

TECHNICAL SKILLS AND COMPETENCES

Cleanroom	Photolithography, Polyimide, Ion Beam Etching (IBE), plasma etching, wet etching, gas etching, lift-off, sputtering, evaporation, Atomic Layer Deposition (ALD), thermal annealing, Scanning Electron Microscope (SEM), optical microscopy, ellipsometry, reflectometry, profilometry.
Software	Semiconductor FEA: Sentaurus TCAD; Microfluidics simulation: Comsol; Device characterization: IC-CAP; Data analysis: Origin, Matlab; Design of the devices: L-Edit; 3D Modeling: Sketchup; Text editor, presentations, miscellaneous: L ^A T _E X, Office.
Languages	 Italian: Mother tongue;  English: C2;  French: C1.
Others	Oral presentations to international audiences and board meeting, design of a complete fabrication Process Flow, device characterization, interns coaching, assistance to practice classes, creative problem solving.

PROJECTS

EPFL NanoLab, Lausanne, Switzerland

- October 2014-
March 2015**
- Design, simulation and fabrication of a **zero-power capillary microfluidics** for a sensing chip.
 - In less than six months, a full system, **cheap, quick to produce and fully compatible** with the sensor for which it was meant has been designed and fabricated.
 - The **strategy introduced** has been **patented** and used, so far, in four papers, and is now one of the **core technologies** of the Xsensio start-up.

Istituto Nazionale di Ricerca e Metrologia, INRiM, Torino, Italy

- 2011-2012**
- Collaboration for the characterization of a **laser comb** for metrology purposes.
 - **Data analysis.**
 - Design and fabrication of a **tunable optical filter** and introduction of a **new strategy** allowing **reducing the number of operational amplifiers** needed.

PERSONAL INTERESTS

Books (both reading and writing, mostly novels), movies, traveling, cooking, fitness, solving puzzles.

PATENTS

1. Ionescu, M. A., Guerin, H., García, C. E., & Bellando, F. (2018). **Bio-fluid Collection and Sensing Device, System and Method.** U.S. Patent Application No. 15/453,920.
2. Zhang, J., Bellando, F., García Cordero, E.A. & Ionescu, M.A. (2018). **Field effect transistor device and method for sensing ions and biomarkers in a fluid.** U.S. Patent Application No 62/688,413.

List of Publications

Garcia-Cordero, E., Guerin, H., Muhech, A., **Bellando, F.**, & Ionescu, A. M. Heterogeneous integration of low power pH FinFET sensors with passive capillary microfluidics and miniaturized Ag/AgCl quasi-Reference Electrode. In *2016 46th European Solid-State Device Research Conference (ESSDERC)*, 452-455 (IEEE, 2016)

Saeidi, A., Jazaeri, F., **Bellando, F.**, Stolichnov, I., Luong, G. V., Zhao, Q. T., Mantl, S., Enz C. C., & Ionescu, A. M. Negative capacitance as performance booster for tunnel FETs and MOSFETs: An experimental study. *IEEE Electron Device Letters* **38(10)**, 1485-1488 (2017)

Saeidi, A., Jazaeri, F., **Bellando, F.**, Stolichnov, I., Enz, C. C., & Ionescu, A. M. Negative capacitance field effect transistors; capacitance matching and non-hysteretic operation. In *2017 47th European Solid-State Device Research Conference (ESSDERC)*, 78-81 (IEEE, 2017).

Bellando, F., Garcia-Cordero, E., Wildhaber, F., Longo, J., Guérin, H., & Ionescu, A. M. Lab on skin™: 3D monolithically integrated zero-energy micro/nanofluidics and FD SOI ion sensitive FETs for wearable multi-sensing sweat applications. In *2017 IEEE International Electron Devices Meeting (IEDM)*, 18-1 (IEEE, 2017)

Garcia-Cordero, E., Wildhaber, F., **Bellando, F.**, Longo, J., Fernández-Bolaños, M., Guerin, H., & Ionescu, A. M. Embedded passive nano-liter micropump for sweat collection and analysis. In *2018 IEEE Micro Electro Mechanical Systems (MEMS)*, 1217-1220 (IEEE, 2018)

Zhang, J. R., **Bellando, F.**, Garcia Cordero, E. A., Mazza, M., Fernandez-Bolanos Badia, M., & Ionescu, A. M. Low power analog frontend for ISFET sensor readout. In *Proceedings of IMCS 2018, 17th International Meeting on Chemical Sensors, 15-19 July 2018, Vienna, Austria*, (2018)

Garcia-Cordero, E., **Bellando, F.**, Zhang, J., Wildhaber, F., Longo, J., Guerin, H., & Ionescu, A. M. Three-Dimensional Integrated Ultra-Low-Volume Passive Microfluidics with Ion-Sensitive

Bibliography

Field-Effect Transistors for Multiparameter Wearable Sweat Analyzers. *ACS nano* **12(12)**, 12646-12656 (2018)

Zhang, J. R., Rupakula, M., **Bellando, F.**, Cordero, E. G., Longo, J., Wildhaber, F., Herment, G., Guérin, H., & Ionescu, A. M. All CMOS Integrated 3D-Extended Metal Gate ISFETs for pH and Multi-Ion (Na⁺, K⁺, Ca²⁺) sensing. In *2018 IEEE International Electron Devices Meeting (IEDM)*, 12-1 (IEEE, 2018)

Zhang, J., Rupakula, M., **Bellando, F.**, Garcia Cordero, E., Longo, J., Wildhaber, F., Herment, G., Guérin, H., & Ionescu, A. M. Sweat Biomarker Sensor Incorporating Picowatt, Three-Dimensional Extended Metal Gate Ion Sensitive Field Effect Transistors. *ACS sensors* **4(8)**, 2039-2047 (2019)

Rupakula, M., Zhang, J., **Bellando, F.**, Wildhaber, F., Convertino, C., Schmid, H., Moselund, K., & Ionescu, A. M. Monolithically integrated catalyst-free High Aspect Ratio InAs-On-Insulator (InAsOI) FinFETs for pH sensing. In *ESSDERC 2019-49th European Solid-State Device Research Conference (ESSDERC)*, 106-109 (IEEE, 2019).